Luminescent Gold and Copper Nanoclusters for Theranostic Applications

By

Upashi Goswami

Roll No. 126153007

A Thesis

Submitted in Partial Fulfilment of the Requirements for the Degree of

DOCTOR OF PHILOSOPHY

at the

Indian Institute of Technology Guwahati

Centre for Nanotechnology

Indian Institute of Technology Guwahati

Guwahati- 781039, Assam, India

June, 2018

Luminescent Gold and Copper Nanoclusters for Theranostic Applications

A thesis by ***Upashi Goswami***

Thesis Supervisors,

Prof. Siddhartha Sankar Ghosh and Prof. Arun Chattopadhyay

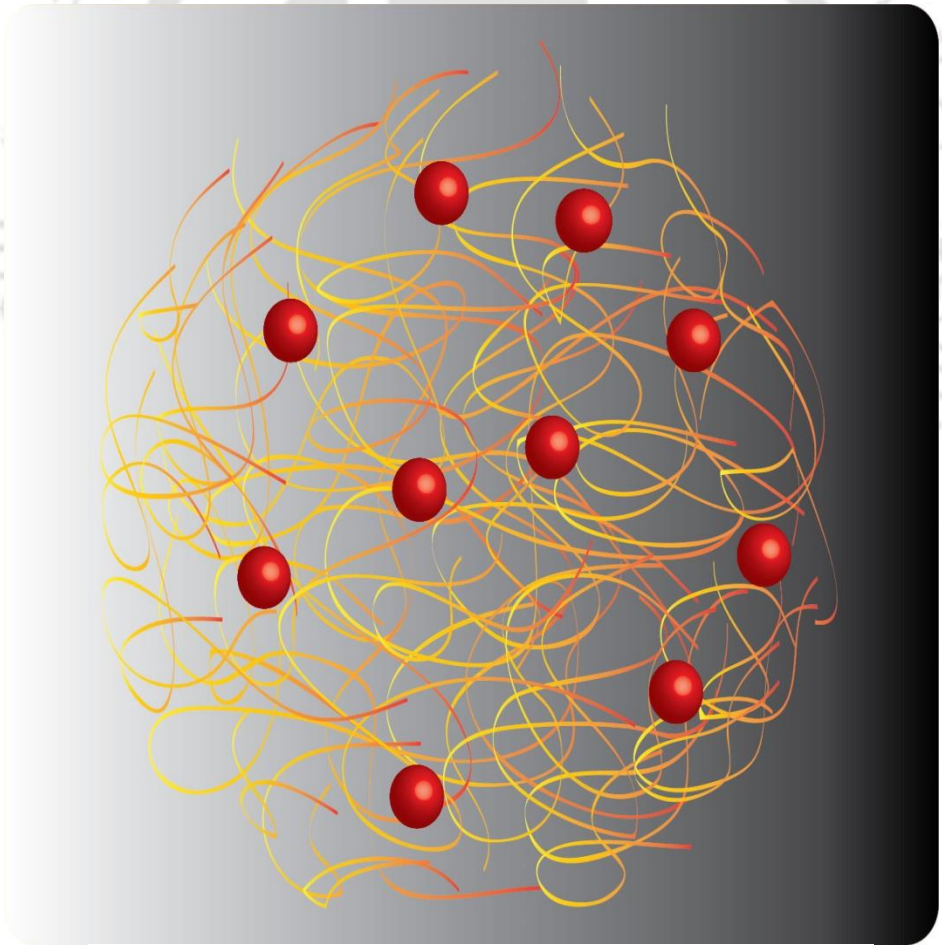

Centre for Nanotechnology

IIT Guwahati, Assam, India.

DECLARATION

I hereby declare that the results and discussions embodied in the thesis titled "***Luminescent Gold and Copper Nanoclusters for Theranostic Applications"*** is the outcome of research work carried out by me under the supervision of ***Prof. Siddhartha Sankar Ghosh*** and ***Prof. Arun Chattopadhyay***, **Centre for Nanotechnology**, **Indian Institute of Technology Guwahati**, **Guwahati**, **Assam**, **India** for the award of the degree of Doctor of Philosophy. To the best of my knowledge and belief, the present thesis has not been submitted for any degree, diploma, associateship etc. of any Institute or University elsewhere.

Date:

Place: Guwahati

Upashi Goswami
Centre for Nanotechnology
IIT Guwahati, Guwahati-781039
Assam, India

भारतीय प्रौद्योगिकी संस्थान गुवाहाटी
INDIAN INSTITUTE OF TECHNOLOGY GUWAHATI

CERTIFICATE

This is to certify that the thesis entitled ***"Luminescent Gold and Copper Nanoclusters for Theranostic Applications"*** being submitted to the **Indian Institute of Technology Guwahati** by ***Upashi Goswami*** (Roll No. **126153007**) for the award of the degree of **Doctor of Philosophy** in ***Nanotechnology*** is a bonafide record of research work carried by her. The information and data reported by her are solely the results of her original findings. She has meticulously carried out the investigations and followed the guideline of the laboratory. This work has not been submitted elsewhere for any degree or diploma.

Prof. Siddhartha Sankar Ghosh

Thesis Supervisor

Department of Biosciences and Bioengineering, Indian Institute of Technology, Guwahati, Guwahati-781039, Assam, India

Prof. Arun Chattopadhyay

Thesis Supervisor

Department of Chemistry, Indian Institute of Technology, Guwahati, Guwahati-781039, Assam, India

Dedicated to my Parents and Sister

ACKNOWLEDGEMENT

As it says, all beautiful things come to an end at one point, it's very difficult to put in words all the enriching experiences and learning of all these years together. For me, it's been a long association with IITG, as first one an half year I was working as a JRF in a project followed by PhD. In this course of time I met many people whose encouragement and support have really helped me in my progress. I always believe that there is a lot to learn from every individual and each one of them has in some or the other way contributed in growing me as an individual. This journey would have been difficult without the support of these lovely people around me.

Firstly, I would like to convey my sincere gratitude to my supervisors, Prof. Siddhartha Sankar Ghosh and Prof. Arun Chattopadhyay for giving me this wonderful opportunity to be a part of their group. I am highly obliged for their encouragement, support, constructive criticism, knowledgeable discussions, and indispensable advices. They have always encouraged me to pursue things of my interest, which have really helped me to improve my ground as a researcher. Their every morning visits have taught me that irrespective of all sorts of work, regularity and punctuality play a very crucial role in overall development. In their visits, Arun Sir always used to ask "Anything New"??, and came up with very innovating ideas which have motivated me to think out of the box and made me realise that nothing is impossible, as all ideas can be implemented with passion, sincerity and hard work. Ghosh Sir has always helped me in executing the ideas and his suggestions have helped a lot in polishing the research work. He has been a constant support in my entire journey and pushed to get the best out me. Along with their guidance they have provided us enormous lab facilities and funding's because of which it has been comparatively comfortable to carry out research work.

I extend my thanks to my doctoral committee members, Dr. Biplab Bose (Chairman) and to the other committee members Dr. Chandan K. Jana and Dr. Lal Mohan Kundu for continuously evaluating my thesis work and for giving valuable ideas and suggestions for its improvement. I also thank Prof. Anumita Paul for her support and help.

I would like to thank Central Instrumental Facility (CIF), Centre for Excellence in Nanoelectronics & Theranostic Devices (CENTD) and DBT Programme Support (Centre for Excellence) for providing me with the much needed instrumental facilities. I would like to acknowledge all the staff members of Centre of Nanotechnology and CENTD for treating me like a friend rather than a mere student. Special mention to Mr. Kaustubh Acharyya, Mr.

Paran Dutta, Mrs. Pranjoli Das and Mr. Indrajit Talukdar for their help both professionally and personally. Special mention to Indrajit Sir for carrying out all the TEM experiments with so much patience and fulfilling all my demands to get the best images.

Next, I take this opportunity to thank Dr. Kohila , Dr. Chokolingam and Dr. Amaresh Kumar Sahoo for teaching me all the basic techniques of research with so much ease and patience. Thank you Amaresh Da for all your guidance and support throughout and for being a supportive senior and a friend. I also thank my seniors Dr. Pallab Sanpui, Dr. Amit Jaiswal, Dr. Shilpa Sharma and Dr. Aditi Banerjee for all the love and support.

I have been fortunate to work with various people from different academic backgrounds and it's been a great learning experience to work with each one of them. Thank you to all my collaborators Dr. Palashuddin, Dr. Rama, Dr. Devendra, Dr. Archita, Dr. Asif, Dr. Anushree, Srestha, Dr. Madhumita, Kafeel, Rajender, Bedika and Mahmuda. This list will be incomplete without mentioning the names of my IASST collaborators Dr. Raghuram Kandimalla and Dr. Sanjeeb Kalita .It's been a wonderful learning opportunity in their expertise and work in in vivo systems. Big thanks to both of them; I thoroughly enjoyed their company.

I sincerely thank my group members Dr. Sunil, Dr. Bandhan, Deepanjalee, Dr. Madhumita, Anitha, Kasturi, Debashree, Neha, Anil, Srirupa, Rajeeb, Muktashree, Dr. Satya, Uday, Shilaj, Sabhyasachi, Ayan, Kafeel, Srestha, Mihir, Chirantan, Srimonto and Manideepa for providing me a healthy work environment. Special thanks to my lovely juniors Anil, Srirupa, Rajeeb and Debashree for their help and support during my crucial days.

Besides research IITG has given me a friend for a lifetime- Namami. This wouldn't have been possible without her support. I thank her from the bottom of my heart for always being there through thick and thin, and lending ears to all my problems. She has been a constant support and has helped me in keeping my fun and natural side alive with timeless discussions, help, love and care. Being a national level player she has inspired me to balance between work and passion of your interest. I will treasure all the moments I have spent with her and there is a long way to go. I will also cherish my friendship with Anushree, who has not only helped me in my research work but has contributed a lot in overall work. Thank you Anushree for your encouragement and help. In the last 2 years I always have a guest in my room. Thank you Srestha for your regular visits and deep discussions. I thoroughly enjoyed your company and you will always remind me of "Biryani". On serious note you have taught me how execution and proper planning can help in achieving your targets easily both professionally and personally. It gives me immense pleasure to work with Dr.

Madhumita Das. She always inspires me that there is no boundary in learning new things. Being a medical practitioner her thirst for research is incredible and because of her I have been fortunate to work with real patient samples. At the same time I would like to thank my friends from IITG, Aditi Didi , Sharbani, Tamanna, Indrani, Emlin, Gayatri Mam, Ujjwol, Thomas, Anamika, Amit, Nilanjan, Mitradeep, Akhtar and many more. Here I like to thank my dance group members specially Anwesha mam for keeping my love for dance alive. It's a stress buster thing for me and I have made some beautiful friends Chandita, Shivani, Sunanda, Prerona, Jinat, Niharika, Soumi, Anjali and many more.

Next I would like to thank my friend Aashita for always being there. She has been my constant support and she's the only one who calls me regularly to ask about my wellbeing. Thank you Aashi for your unconditional love and support. I am blessed with some very good friends and all of them were there whenever I needed them. Thank you Shaishav, Aditi, Sakshi, Momina, Meenakshi Priyanka, Ranjita and Debarchana for always being there. Special mention to my cousin brother Mani and Suman for their encouragement and constant moral support. You guys have been my pillar of strength. I express my gratitude to my family for all their love and support. My heartfelt thanks to Mi for all her love and affection.

Last but not the least; I thank my parents for all their encouragement, love, comfort and support. Thank you for giving me the best possible education and teachings which have helped me in overcoming difficult situations. They have always taught me to be self-sufficient and have imparted that with hard work, simplicity, sincerity and dedication everything can be achieved. Many thanks to my sister Shreya for her love and encouragement. Though being younger to me, sometimes she plays a role of elder sister. Thank you for understanding me and supporting me. I owe everything whatever I have earned in these years to my parents and sister. I thank almighty for gifting me with such wonderful people.

It will be incomplete without mentioning the beautiful green campus of IITG abundant in nature's gift. It was indeed a lovely and pleasant stay in this lush green campus.

Upashi Goswami

TABLE OF CONTENTS

Thesis Abstract

Luminescent Gold and Copper Nanoclusters for Theranostic Applications

By

Upashi Goswami

Submitted to the Indian Institute of Technology Guwahati in June, 2018 in Partial Fulfillment of the Requirements for the Degree of Doctor of Philosophy in Centre for Nanotechnology

Recent advances in nanobiotechnology and its intregation with chemistry, biology, biochemistry and medicine have given new horizons of luminescent nanoscale particles such as semiconductor quantum dots (QDs), dye-doped nanoparticles, lanthanide-doped nanoparticles and carbon nanodots. In recent years, due to facile synthesis, significant quantum yields, tunable fluorescence emission, large Stokes shifted emission and high photo stability; metal nanoclusters have emerged as new nanoscale materials with multitude of promising applications in various disciplines.

The present thesis emphasizes on synthesis and development of different types of metal nanoclusters (Au and Cu) and their potential applications in bactetial enumeration / detection, distinction of kanamycin resistant bacteria, white light emission and in the development of theranostic nanomedicines for cancer treatment. The present thesis is divided into six chapters.

Chapter 1 of the thesis provides introduction and insights of luminescent metal nanoclusters, which are composed of several to a few hundred metal atoms and have garnered worldwide consideration due to their extraordinary physical, electrical, optical and chemical properties. Further the chapter elaborates various applications of metal nanoclusters in the field of bacterial detection, enumeration, distinction of antibiotic resistant strains, white light emission, electro chemical biosensing, bioimaging, therapeutics, and in the fields of theranostics for cancer therapy. The scopes and salient features of the current work have been described. **Chapter 2** introduces a new facile method of luminescent gold nanocluster (Au

NC) synthesis on the surface of bacteria for detection, counting and strain differentiation. The limit of detection (LOD) was 740 ±14 CFU/mL for the Gram negative and was 634 ±16 CFU/mL for the Gram positive bacteria. Brief treatment with lysozyme could differentiate the Gram strains based on their luminescence intensities. The current method could also detect bacterial contaminants from water sources and kanamycin resistant strains rapidly. This quick synthesis of Au NCs on bacterial template attributes an easy and rapid method for enumeration, detection of bacterial contaminants and kanamycin resistant strains. Next aim was to use bacteria along with mercaptopropionic acid (MPA) and gold chloride for white light generation. Thus, **Chapter 3** reports the synthesis of gold nanoclusters using green fluorescent protein (GFP)-expressing bacteria as the stabilizer. Combining the blue and green fluorescence of GFP-expressing bacteria and orange luminescence of the nanoclusters, white light emission associated with appreciable quantum yield, color rendering index and correlated color temperature was achieved. The above works highlighted the use of novel templates (bacteria) for synthesis of Au NCs which strive us to look for other templates and use it as carrier or nanodrug for cancer therapy. With advent of metal nanoclusters its use as cancer theranostics is in demand because of its bright luminescence property, low photobleaching, non-cytotoxicity and can be formulated into luminescent drug delivery carriers. **Chapter 4** illustrates the combination therapy for cancer treatment using a plant based drug artesunate (ART) and a naturally available short chain fatty acid sodium butyrate (NaB) to reduce the side effects associated with regular chemotherapeutic drugs. With the heterogenecity of tumor microenvironment, combinational therapies have found an edge over monotherapy owing to high toxicity and drug resistance associated with chemotherapeutic drugs. The polymer PEG containing luminescent nanoparticles were synthesized based on Au NCs and negatively charged drug NaB, where NaB and PEG in the presence of Au NCs formed spherical drug encapsulated composite nanoparticles (PEG-Au NC-NaB-NPs). The results demonstrated enhanced therapeutic activity in case of combination therapy with PEG-Au NC-NaB-NPs and ART as opposed to their individual doses. The synergy of action was attained and was confirmed by combination index (CI). The mechanism of cell death was also studied in detail where elevated generation of

reactive oxygen species (ROS) with combination therapy of PEG-Au NC-NaB-NPs and ART was obtained that resulted in dysfunction of mitochondrial membrane potential which was confirmed by JC-1 staining. Further, it was found that SB and ART triggered inhibition of histone deacetylase (HDACi) and DNA fragmentation, leading to cell death as corroborated with histone deacetylase assay (HDAC) and terminal deoxynucleotidyl transferase dUTP nick end labeling (TUNEL) assay. The efficacy of combination therapy observed in *in vitro* system inspired trials for *in vivo* mice bearing Dalton's lymphoma ascites (DLA) tumors where significant reduction of tumor volume and viable tumor cell count with increased survival percentage and life span was observed. Thus this chapter reports a new platform for combination therapy using a plant derived antimalarial drug ART and a small fatty acid chain SB with enhanced synergistic therapeutic activity and provided a promising combination for an effective and enhanced cancer therapy. The next objective was for targeted cancer therapy where **Chapter 5** demonstrates novel synthesis of transferrin (Tf)-templated luminescent blue copper nanoclusters (Tf-Cu NCs). They are further formulated into spherical Tf-Cu NC–doxorubicin nanoparticles (Tf-Cu NC–Dox NPs) based on electrostatic interaction with doxorubicin (Dox). The as-synthesized Tf-Cu NC–Dox NPs are explored for bioimaging and targeted drug delivery to delineate high therapeutic efficacy. Förster resonance energy transfer (FRET) within the Tf-Cu NC–Dox-NPs exhibited striking red luminescence, wherein the blue luminescence of Tf-Cu NCs (donor) is quenched due to absorption by Dox (acceptor). Interestingly, blue luminescence of Tf-Cu NCs is restored in the cytoplasm of cancer cells upon internalization of the NPs through overexpressed transferrin receptor (TfR) present on the cell surface. Finally, gradual release of Dox from the NPs leads to the generation of its red luminescence inside the nucleus. The biocompatible Tf- Cu NC–Dox NPs displayed superior targeting efficiency on TfR overexpressed cells (HeLa and MCF-7) as compared to the cells expressing less TfR (HEK-293 and 3T3-L1). Combination index (CI) revealed synergistic activity of Tf-Cu NCs and Dox in Tf-Cu NC–Dox NPs. *In vivo* assessment of the NPs on TfR positive Daltons lymphoma ascites (DLA) bearing mice revealed significant inhibition of tumor growth rendering prolonged survival of the mice.

Glossary of Acronyms

a.u.	Arbitaray Units
Au NC	Gold Nanoclusters
Ag	Silver
Au	Gold
AIEE	Aggregation induced emission enhancement
AFM	Atomic Force Microscopy
ART	Artesunate
AST	Aspartate transaminase
ALT	Alanine transaminase
ALP	Alkaline phosphatase
ACT	Artemisinin-based combination therapy
BSA	Bovine Serum Albumin
BHI	Brain–Heart Infusion
Cu	Copper
Cu NCs	Copper nanoclusters
CpG	Cytosine-phosphate-guanine
CFU	Colony forming unit
CLSM	Confocal Laser Scanning Microscope
CIE	Commission internationale de I'elcairage
CCT	Correlated color temperature
CRI	Color rendering index
CT	Computed Tomography
CI	Combination index
DHLA	Dihydrolipoic Acid
DPA	D-Penicillamine

DMSO	Dimethyl Sulphoxide
DLA	Dalton's lymphoma ascites
Dox	Doxorubicin
DCFH-DA	2, 7-Dichlorofluoresceindiacetate
EtBr	Ethidium bromide
EDX	Energy dispersive X-ray spectrum
ESIPT	Excited state intermolecular proton transfer
FESEM	Field-Emission Scanning Electron Microscopy
FA	Folic Acid
Fe	Iron
5-FU	5 Flurouracil
FRET	Förster resonance energy transfer
GFP	Green Fluorescent protein
GSH	Glutathione
HAT	Histone acetyltransferases
HDAC	Histone deacetylases
HEK-239	Human Embryonic Kidney Cells
HDACi	Histone deacetylase inhibitors
HeLa	Human cervical cancer cell line
JC-1	5, 5', 6, 6'-tetrachloro-1,1',3,3'- tetraethylbenzimi--dazolylcarbocyanine iodide
LFT	Liver functions tests
LEDs	Light Emitting Device
LOD	Limit of Detection
MRI	Magnetic Resonance Imaging
MPA	Mercapto-propionic acid
MALDI-TOF	Matrix assisted laser desorption/ionisation - time of flight

MCF-7	Human breast cancer cell line
3T3-L1	Mouse embryo fibroblast cell line
Ni	Nickel
NIR	Near infrared region
NCs	Metal nanoclusters
NaB	Sodium Butyrate
NB	Nutrient Broth
NOAEL	No observed adverse effect level
OVA	Ovalbumin
PEG	Polyethylene Glycol
Pt	Platinum
PAMAM	Polyamidoamine
PPI	Poly (propylene imine)
PDT	Photodynamic Therapy
PLN	Polymer Lipid hybrid nanoparticle
PET	Position Emission Tomography
PTX	Paclitaxel
PCR	Polymerase chain reaction
PEG -Au NC-NaB-NPs	PEG-Gold nanoclusters –sodium butyrate nanoparticles
PBS	Phosphate Buffered Saline
QY	Quantum Yield
ROS	Reactive Oxygen Species
QDs	Quantum Dots
RBC	Red Blood Cell
SGOT	Serum glutamic oxaloacetic transaminase
SGPT	Serum glutamic pyruvate transaminase

SLN	Solid Lipid nanoparticle
Tf	Transferrin
TfR	Transferrin receptors
TFA	Trifluroacetic acid
TEM	Transmission Electron Microscope
TUNEL	Terminal deoxynucleotidyl transferase dUTP nick end labelling
TdT	Terminal deoxynucleotidyl transferase
TPP	Tripolyphosphate
WLE	White Light Emitting
WBC	White Blood Cell
XPS	X-ray photoelectron spectroscopy

Chapter-1

Introduction and Literature Review

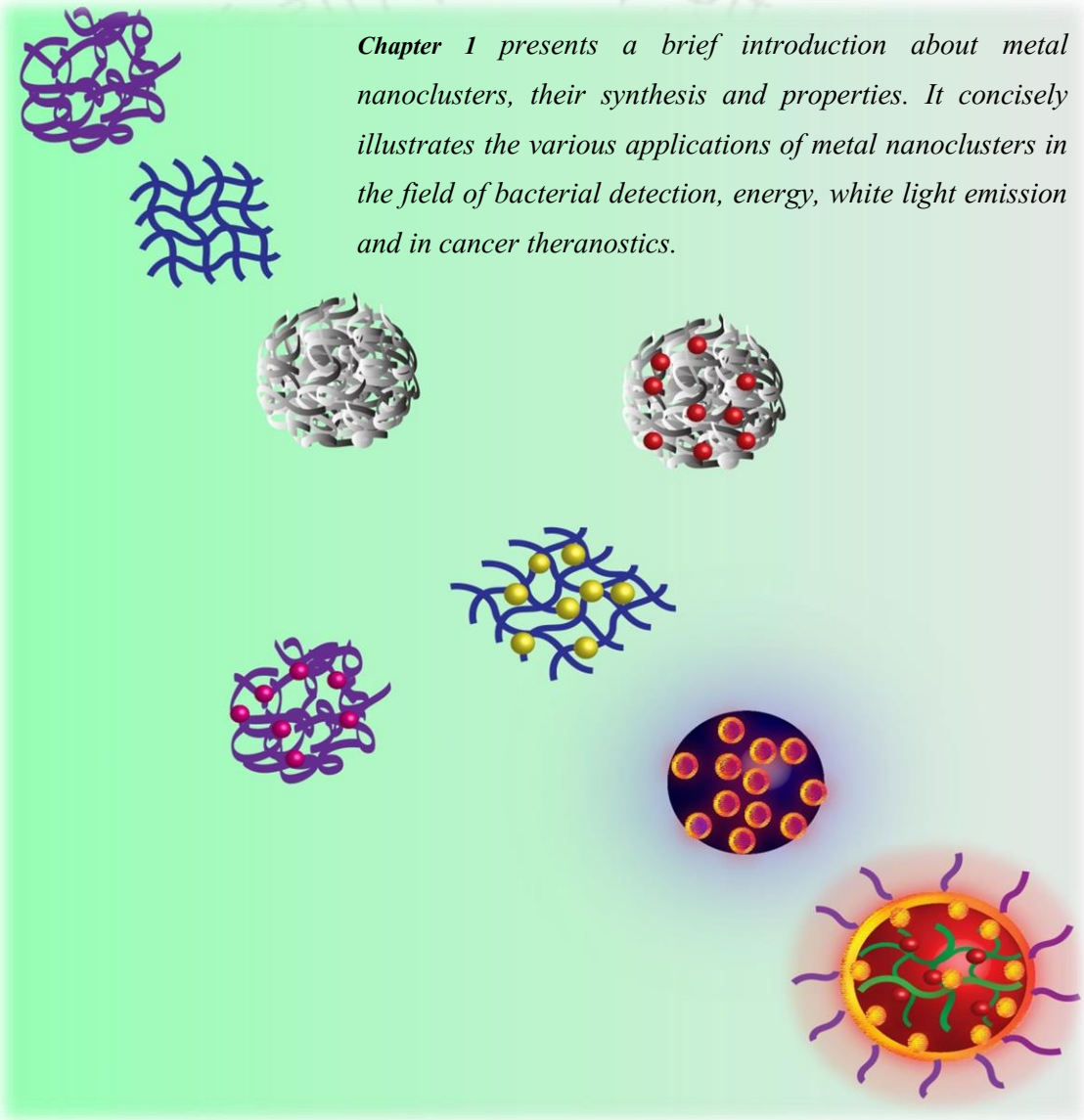

Chapter 1 *presents a brief introduction about metal nanoclusters, their synthesis and properties. It concisely illustrates the various applications of metal nanoclusters in the field of bacterial detection, energy, white light emission and in cancer theranostics.*

Chapter 1

1.1. Introduction

Nanoscience and nanotechnology is a multidisciplinary technology bestowed to work at the atomic, molecular and supramolecular levels (on a scale of 1–100 nm) and to assemble into objects, hierarchically along several length scales, with essentially new properties and functions. Owing to its small size, the nanoscale particles including metals, metal oxides, and semiconductors, exhibits high surface to volume ratios with distinct physical, chemical, optical, electrical, and biological properties[1–6]having widespread applications in the fields of optoelectronics,[7,8] catalysis,[9,10] sensors,[11] white light emission,[12,13] bioimaging,[14–16] biosensing,[15,16] medicine,[17,18] nanobiotechnology.[19] Nanobiotechnology applied the nanoscale principles and techniques to create new biomaterials which extensive applications in the field of biology and biomedical healthcare, such as diagnostic (imaging), detection of pathogens, biosensing, nanomedicine, drug delivery, gene delivery and tissue engineering.[20]

1.2. Nanoparticles

With advancement in the field of nanotechnology various types of nanoparticles varying in size, shape, compositions, and functionalities have been developed. They are broadly classified into inorganic nanoparticles, organic nanoparticles, dendrimers and carbon nanotubes. Inorganic nanoparticles comprise of metal gold, silver, copper (Au, Ag, Cu), iron oxides, quantum dots, silica and calcium phosphate, with size ranging from 2 - 100 nm and exhibits size- and shape-dependent plasmonic properties.[2–4] Organic nanoparticles include liposomes, polymer micelles, polymer nanoparticles and dendrimers.[4] Due to size confinement of their electronic states, semiconductor nanoparticles, commonly known as quantum dots (QDs) have discrete electronic states and hence display size-dependent absorption and emission features.

1.3 Metal Nanoclusters (NCs)

Metal nanoclusters (NCs) are new class of flurogenic functional materials, usually containing few hundreds of metal atoms or less with a core size below 2 nm. It represents an intermediate state of matter, between individual atoms and their corresponding bulk dimensions **(Figure 1.1)**[21,22] Due to small size (<2 nm) the continuous energy band breaks into discrete energy levels and exhibit molecule like properties and possess distinct electrical, optical and chemical properties distinct from larger metal nanoparticles. This results in HOMO–LUMO transition, tunable luminescence emission, enhanced quantum yields, large Stokes shift, high photostability.[20,23] Therefore, because of all these unique attributes metal nanoclusters generate pronounced potential and have been extensively exploited for applications in the fields of bacterial detection and enumeration,[20] catalysis,[24] light harvesting materials,[25] white light emission,[12,13] biology,[20] biomedicine,[26,27] chemical sensors,[28] and therapeutics.[20,29,30] NCs of gold (Au), silver (Ag), copper (Cu), platinum (Pt) have been studied in detail and have been extensively used in various disciples.[12,24,28,31,32,33,34]Whereas, recently nanoclusters of transition metals such as iron (Fe), nickel (Ni) have gained attention and have opened a new prospect of nanomaterial science.

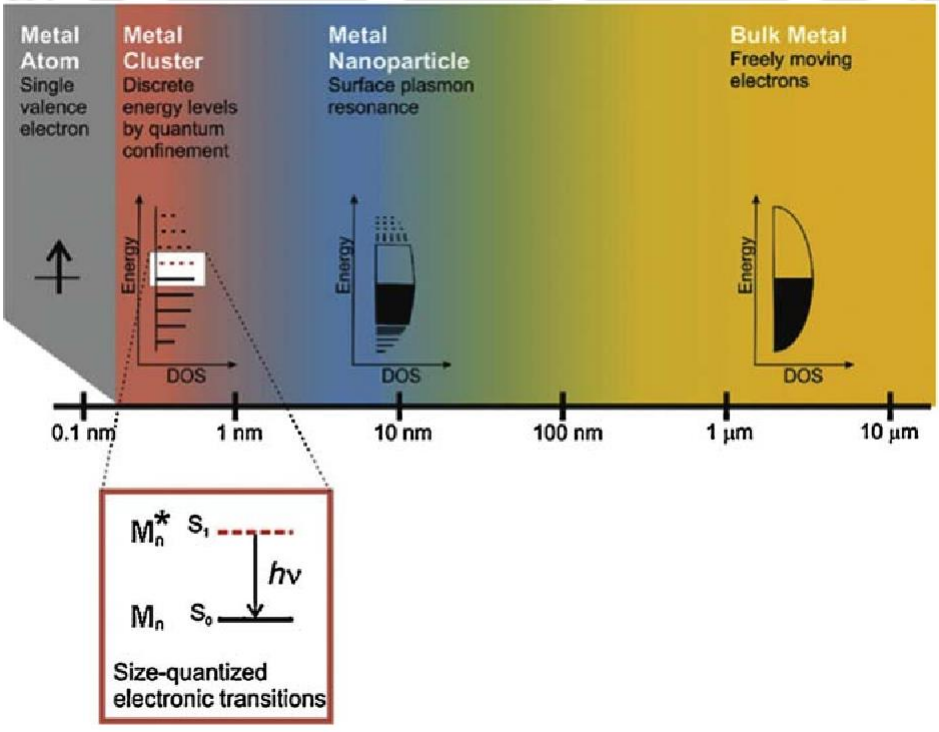

Figure1.1. The effects of size on the various properties of nanoscale particles like bulk metal, metal nanoparticles and metal nanoclusters.[Reprinted with permission from **reference 35**. Copyright 2011 Royal Society of Chemistry].

1.3.1. Development of Luminescent Metal NCs

For synthesis of highly luminescent water soluble metal nanoclusters with enhanced quantum yield various approaches have been established. Generally for synthesis of nanoclusters, reduction of metal ions in aqueous solution with suitable reducing agents, templates, surface protecting capping agents were required.[28,30,32,36] Without suitable template or surface protecting agents, it resulted in formation of large nanoparticles, as nanoclusters because of high surface energy have tendency to aggregate. Therefore, choosing suitable templates or scaffolds for stabilization of clusters from aggregation is a pivotal role for synthesis of highly luminescent metal NCs.[23,33,37,38,39] At the same time factors like electron energy quantization effect, metal–ligand interaction, surface effect and metal core charge state plays an important role in attaining high yield metal nanoclusters.[23,36] The most common method for synthesis of metal NCs are based on template and stabilizer ligands surrounding the NC core and are broadly classified as- thiol protected metal NCs and template based metal NCs which include polymer, protein/peptide, DNA and dendrimers as templates. Briefly few of the strategies of synthesis of metal NCs are discussed below.

1.3.2 Strategies for Metal NCs synthesis

1.3.2(a). Synthesis of Thiol Protected Metal NCs

Small molecules containing thiol (-SH) are some of the most common stabilizers for metal NCs synthesis. Au and Ag have very strong affinity towards thiols. Different –SH containing ligands such as glutathione (GSH),[40–42] tiopronin,[43] phenylethylthiolate,[44] thiolate α-cyclodextrin,[45,46] 3-mercaptopropionic acid,[47,48] dihydrolipoic acid (DHLA),[49–52] dodecanethiol[53] and D-penicillamine (DPA),[54,55] *etc*. has been extensively used for luminescent metal NCs synthesis precisely Au, Ag and Cu with high quantum yield.[34]

1.3.2(b). Template-Based Synthesis Methods

(i) Dendrimers: Dendrimers are synthetic polymers having branched star-shaped macromolecules with nanometer-scale dimensions and act as hosts for guest molecule. Polyamidoamine (PAMAM) and poly (propylene imine) (PPI) dendrimers are commonly used for synthesis of metal Au, Cu and Ag NCs.[56–60]

(ii) Polymers: Polymers are widespread macromolecule with abundant functional groups like carboxylic acids, hydroxyl, epoxy, amines etc. The polymers used for synthesis of metal NCs are poly (methacrylic acid),[57] polyethylene imine (PEI),[59] polyglycerol-block-poly (acrylic acid) copolymers,[61] poly(N-isopropylacrylamide-acrylic acid-2-hydroxyethylacrylate) and chitosan.[47]

(iii) Biomolecules: Biomolecules are used as attractive tools for nanocluster synthesis owing to their rich structure consisting of various functional groups such as amine, thiol, hydroxyl, and carboxyl. At the same time some of the biomolecules can act as both reducing and protecting agents. [23,37] Different types of biomolecules mainly peptides, proteins and DNA have been extensively used for the synthesis of metal nanoclusters,[39,62,63]

***Proteins and Peptides as Templates*:** Biological macromolecules like proteins [38]and peptides[39] are rich in functional groups, such as carboxyl, thiol and amino groups and thus are efficient templates or scaffolds for the synthesis of metal NCs.[23,37] The large molecular masses of proteins along with abundant binding sites are effective for binding and reducing metal ions and thus play a vital role in NCs stabilization efficiently. Based on these unique attributes Bovine Serum albumin BSA[64,65] have been comprehensively used as template for the synthesis of different types of metal NCs. With its success various other proteins, such as lysozyme, [66,67]horseradish peroxidase,[68] lactoferrin,[69] transferrin,[70,71] insulin,[72] trypsin[73] and ovalbumin[74] were used predominantly for synthesis of varied types of metal NCs (Au, Ag, Pt, Cu).

Similar to proteins peptides are polymeric biomolecules, whose composition, sequence, and length can be selectively designed mainly through synthetic chemistry have been widely used as templates for synthesis of metal

NCs. Precisely, the amine and thiol groups of peptides can be utilized for the protection and functionalization of metal NCs. GSH which is tripeptide are extensively used for the synthesis of various luminescent metal NCs (Au, Ag, Pt, and Cu NC). [34,39,62,63]At the same time many synthetic peptides are designed specifically based on their substrate recognition properties and requisite activity for the synthesis of metal NCs and are gaining lots of attention owing to its exceptional properties.[34,39]

***DNA oligonucleotides as Templates*:** The interactions of metal cations with DNA which is a polynucleotide consisting of nitrogen-containing nucleobase (i.e. guanine , adenine, thymine or cytosine) along with deoxyribose and a phosphate group have been studied predominantly for metal NCs synthesis.[75] It has been used for the synthesis of Au, Ag and Cu NCs extensively.[23,33] At the same time there is a report of Ag NCs generating different emission colors like blue, green, yellow NIR using single stranded DNA as its template.[76]

1.3.3. Gold Nanoclusters (Au NCs)

Au NCs (size <2 nm) due to its stable chemical property, facile synthesis, and nontoxicity has received enormous attention and are the most broadly studied material. Au NCs typically composed of a few to 100 gold atoms and are associated with intriguing molecular like properties such as strong photoluminescence in the visible to near-infrared (NIR) region, quantized charging, HOMO–LUMO transition, molecular magnetism, molecular chirality, long lifetime, large Stokes shift, photostability, biocompatibility and do not exhibit surface plasmon resonance (SPR).[24,28,32]Different methods like microwave assisted, sonochemical, photoreductive, etching based, electrostatically-induced reversible phase-transfer and template based synthesis of Au NCs are widely studied[28,32,77–79] as illustrated in **Figure 1.2**. Among these the most common strategy to prepare Au NCs involves ligand and template assisted wet chemical reduction technique which uses reducing and capping agents to reduce the precursors of Au^{3+} to Au^{+} and then finally to Au(0).[77] Various types of proteins (BSA, lysozyme, transferrin, trypsin, lactoferrin etc.)[64,67,69,70,80] peptides (GSH),[39,63] polymers (PAA, PTMP-PMAA etc.)[56,59,61] were used for Au NCs synthesis. At the same time it is well established

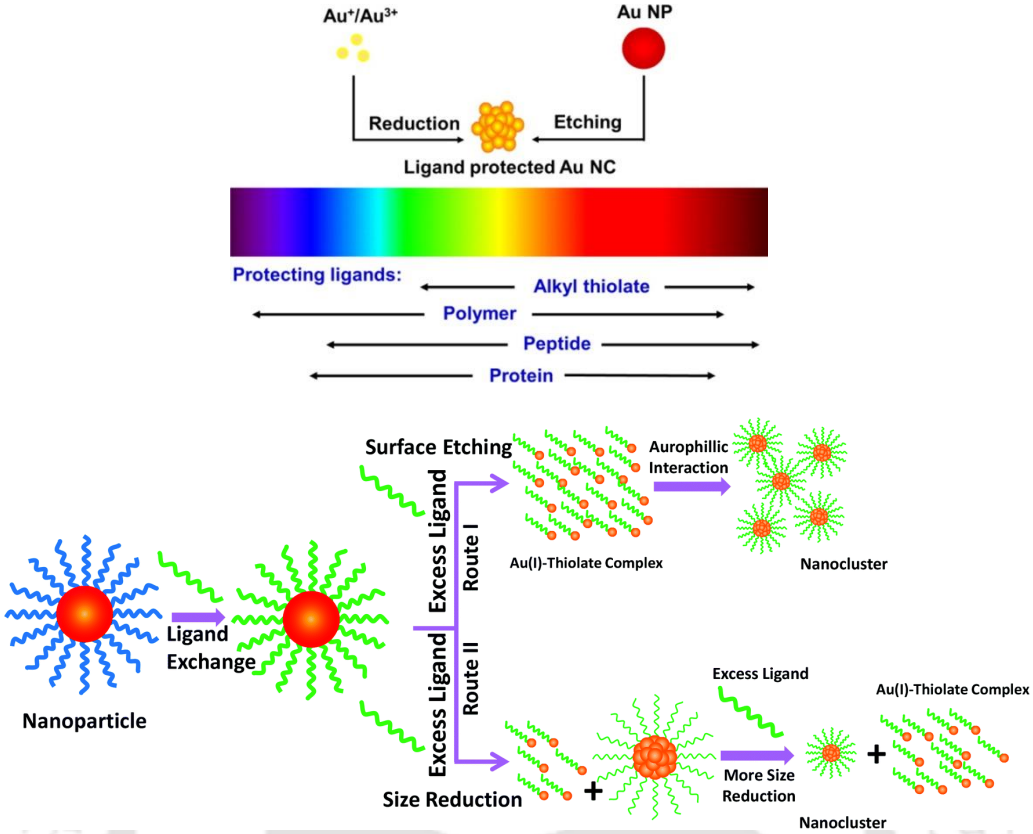

Figure1.2. Illustration of synthetic strategies of synthesis of luminescent Au NCs and effects of ligands in its luminescence property. Reprinted with permission from **reference 77 and 23**. Copyright 2015 American Chemical Society and Copyright 2014 Royal Society of Chemistry respectively].

that thiol containing compounds acts as a capping agent primarily because of their strong affinity towards Au and forms Au–S bond with Au atoms/ions. Glutathione (GSH) which is a tripeptide and a naturally available thiol containing molecule has been used for synthesis of Au NCs.[39,63] Many other thiol containing groups like dodecanethiol, D-penicillamine (DPA), lipoic acid, mercaptopropionic acid, tiopronin, phenylethylthiolate etc. have been utilized for the preparation of monolayer-protected fluorescent Au NCs.[32,78] The surface ligands play a vital role in influencing the luminescence property by preventing it from aggregation in the following ways:

- Charge transfer from the surface ligands to the gold core by forming Au-S bonds
- Direct donation of electrons from ligand (electron rich atoms or groups) to Au core.

1.3.4 Copper Nanoclusters (Cu NCs)

Newly emerging ultra-small copper nanoclusters (Cu NCs) comprising of a few to a hundred copper (Cu) atoms have received great attention due to their atomic precision, easy access, water solubility, ease of functionalization, low cost, good optical and rich catalytic properties.[81] Additionally low cost of Cu NCs along with its tuneable luminescence property makes them a better option for various multidisciplinary applications.[42,49,54] However with considerable efforts in recent years a promising improvement has been made to overcome the intrinsic tendency of Cu NCs towards oxidation.[42]

The most commonly used method for the synthesis of Cu NCs is the wet chemistry process where Cu NCs are formed by the reduction of Cu (II) ions to Cu atoms in solution. Than clustering of Cu atom takes place in association with suitable template, stabilizer and reducing agents.[82] This synthesis method can be further categorised into ligand assisted methods, template-assisted methods, electrochemical synthesis, and etching methods.[82,83] Selection of suitable ligand is an important step as it is a fundamental component for generating high yields luminescent Cu NCs and protects it from aggregation and oxidation.[82,83] Ligands contain specific functional groups which have affinity towards copper and prevents nanoparticle formations by protecting them from aggregation by either charge or steric effects.[82] Thiolate ligands like GSH,[42,84] penicillamine,[54] phenylethanethiol,[85] dihydrolipoic acid,[49,50] mercaptobenzoic acids,[86] cysteamine[82] etc are some of the common ligands used for Cu NCs synthesis which resulted in enhanced PL properties and prevents it from aggregation.

In template assisted method, first the Cu (II) ions bind with suitable template having specific structure and with the help of reducing agents it is reduced into Cu atoms and clusters on the template, forming Cu NCs.[82] Template provides the steric protection and prevents it from oxidation and aggregation. Broadly the templates used for Cu NCs are polymers, DNA, proteins and peptides.[82,83] Illustrations of essential steps for the synthesis of Cu NCs taking protein as a template are depicted in **(Figure 1.3)**. Examples of some of the polymers employed for synthesis of high yield Cu NCs are poly (amidoamine)

(PAMAM), [58]poly (propylene imine),[82] poly (methacrylic acid),[87] pentaerythritol tetrakis 3-mercaptopropionate, Poly (ethylene glycol),[88] lipoic acid [49,50] etc. Similarly ssDNA,[89] dsDNA,[90] proteins like bovine serum albumin (BSA),[65] lysozyme,[66] transferrin,[71] trypsin,[73] are widely used for Cu NCs synthesis.

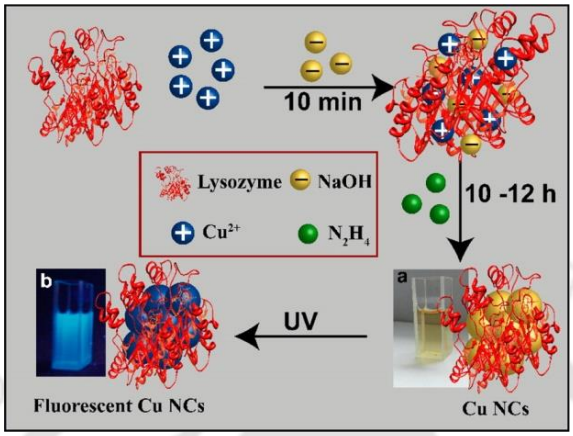

Figure 1.3. Illustration of essential steps for the synthesis of Cu NCs taking protein as a template. [Reprinted with permission from **reference 66.** Copyright 2014 American Chemical Society].

1.4 Applications of metal NCs (Au and Cu NCs)

Metal nanoclusters have widespread applications in the field of healthcare, environment and energy.[36] Uses of metal NCs in the field of therapeutics,[20] bioimaging,[77] light emitting devices (LEDs)[12,13] and as theranostics[29,91] are illustrated below **(Figure 1.4).**

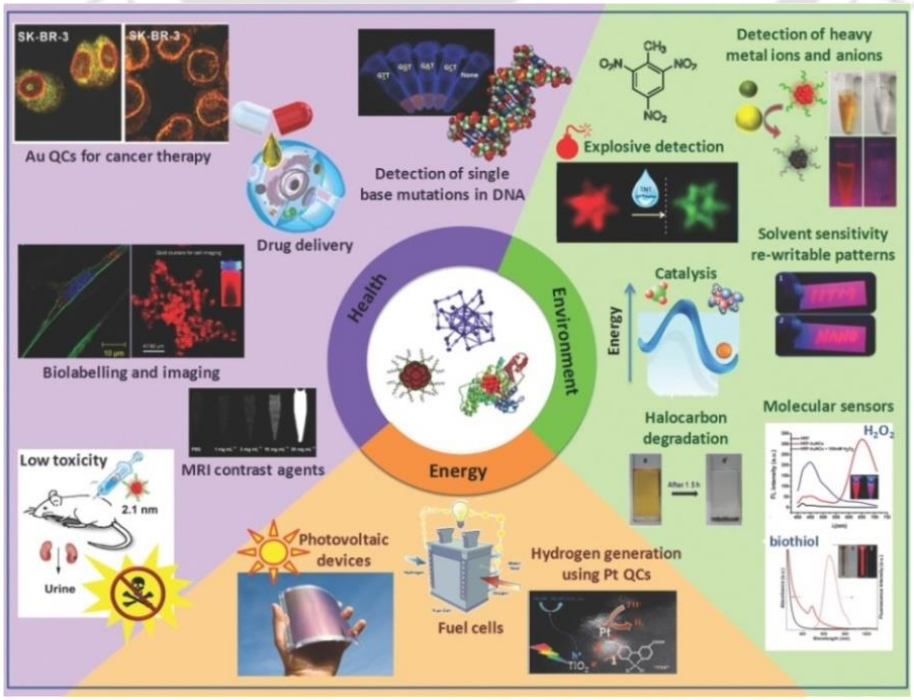

Figure1.4. Applications of metal nanoclusters on major domains: energy, environment, and biology. [Reprinted with permission from reference 36. Copyright 2014 John Wiley and Sons].

1.4.1 Metal NCs in Therapeutics

Metal nanoclusters with therapeutic applications:

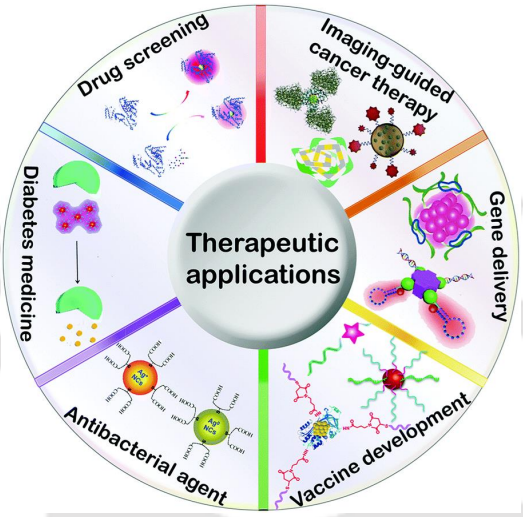

Figure 1.5 Therapeutic applications of metal nanoclusters. [Reprinted with permission from **reference 20**. Copyright 2015 Royal Society of Chemistry].

1.4.1(a) Cancer Therapy : Metal nanoclusters owing to its good optical properties shows great potential for applications in cancer treatment where detection, diagnosis and therapy can be achieved. Metal NCs like Au NCs and Cu NCs modified into multifunctional theranostic nanocomposite[92,47,49] have been extensively studied for bioimaging,[77,66] targeted drug delivery,[69,71,93] chemotherapy,[49,93] immune therapy,[94] stem cell therapy,[95] hormone therapy and recombinant protein cancer therapy.[96,97] In addition, luminescence intensity of NCs has employed as potent intracellular thermometer for temperature detection in living cells.[98] In fact metal NCs has also found an application as radiosensitizers for cancer radiotherapy,[99] photodynamic therapy (PDT)[100] and photo thermal therapy as well.[101,102]

1.4.2 (b) Gene Therapy : A nanocarrier that incorporates desirable characteristics into a single gene delivery system have shown great potential to improve gene therapy owing to its well-defined physicochemical properties, improved DNA packaging capacity and enhanced targeted delivery to tumors with high degree of molecular diversity. Many novel nanocarriers incorporating metal

NCs have been applied in the field of gene delivery for combating genetic diseases and cancer.[20,47] Further multifunctional probe (Ag NCs) has been designed comprising of cell-specific aptamer for their promising application for siRNA delivery and tracking.[103]

1.4.3 (c) Vaccine Development: Immunotherapy has been commonly used for treatment of various types of viral diseases such as those associated with human papilloma virus (HPVs), cytomegalovirus (CMV) and Epstein Bar virus (EBV). In recent times immunotherapy with advancement of research in use of monoclonal antibodies, have gained much importance for treatment of some types of cancer like bladder cancer, cervical cancer and breast cancer. There are reports of synthesis of Ag NCs and Au NCs on DNA supplemented with cytosine-phosphate-guanine dinucleotide (CpG) motif and ovalbumin (OVA) conjugated with CpG oligonucleotide respectively. These acted as self-vaccines with combinatory effects of enhanced immune response and cell imaging. [20]

1.4.4 (d) Antimicrobial agent : Development of rapid, accurate, and simultaneous bacterial identification method is in great demand to overcome the total time taken for diagnostics and hence quick treatment. In this regard, metal NCs of Au, Ag and Cu having bright luminescence, good stability, and excellent water solubility, has been extensively studied for reduction of overall time taken for their identification. Several protein based NCs were explored as sensing probes for broad-band labelling of pathogenic bacteria including both Gram-positive and Gram negative bacteria.[20] At the same time it can effectively inhibit the antibiotic-resistant bacteria, including pan-drug-resistant *Acinetobacter baumannii* and vancomycin resistant *Enterococcus faecalis* with least toxicity to the cells.[104] NCs have enhanced therapeutic activity than NPs which has been studied with Au NCs in case of both Gram positive and Gram negative bacteria. It reveals that along with membrane disruptions, Au NCs induce intracellular metabolic imbalance through intracellular ROS generation and thus the consequent killing effect **(Figure 1.6)**.[31] Additionally, surface functionalization of the Au NCs has been used for the receptor specific detection of pathogenic as well as environmental bacteria with enhanced selectivity.

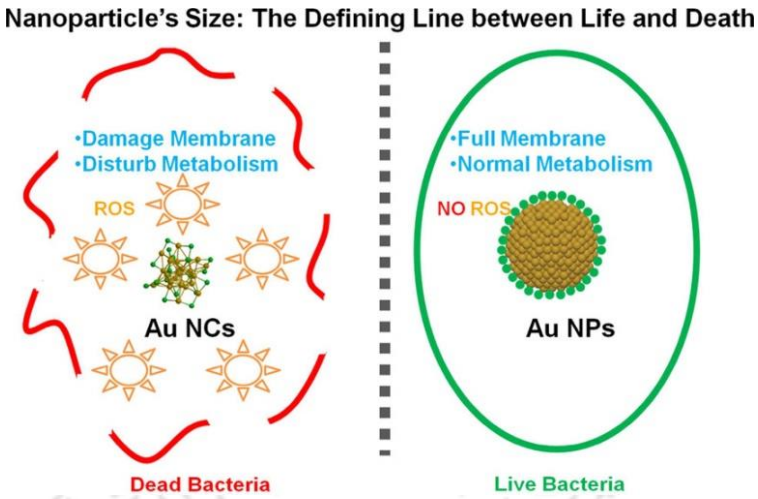

Figure 1.6. Antibacterial mechanism of Au NPs and Au NCs on bacteria. [Reprinted with permission from **reference 31**. Copyright 2017 American Chemical Society].

1.4.2. Metal NCs as Light Emitting Devices

Metal NCs comprising of several tens of metal atoms in its core surrounded by organic ligands on its surface, where charge transfer takes place from ligand-to-metal or ligand-to-metal–metal. The charge transfer results in active absorption and emission due to which metal NCs have been exploited in the field of electroluminescent devices. Cu NCs and Au NCs have been commonly used for generation of white light emitting devices.[12,13]

1.4.3 Metal NCs as Theranostics

Advancement of metal nanoclusters with its distinct characteristics, has offered an opportunity to draw diagnosis and therapy (theranostics) closer in various biological applications.[29,91,105] Theranostics, is the combination of diagnosis and therapy, have garnered lots of interest owing to its specificity towards individualized therapies for cancer treatment through a single agent. A highly potent and tailored theranostic agent could be established with ingenious combinations modalities where the intrinsic luminescence of the noble metal core can be utilized for imaging, and its unique optical properties could be exploited for various cancer therapies.[20,29,91] Specifically metal NCs synthesized on biomolecule serve as an effective theranostic agent for cancer therapy and their advantages are as follows:

- Small size for effective delivery and renal clearance.
- Bright luminescence with good quantum yield for diagnostics and monitoring bio distribution *in vivo.*
- Rich surface chemistry for binding specific biological moieties with ligands used for stabilization of metal NCs.
- Large surface to volume ratio of metal NCs serves as a reservoir for loading multiple drugs and genes.

Cancer is manifested by various sequential mutations in cells, characterized by uncontrolled cell growth and eventually leading to death. The most widely used regimens for treatments include surgical intervention, radiation and chemotherapy, which are associated with severe side effects and often kills normal cells as well.[106,107,108] Though chemotherapy has achieved improved therapeutic effects involving small molecular anticancer drugs but is often associated with non-specificity, rapid clearance, poor solubility and drug resistance.[109] Nanotheranostic research has experienced a great paradigm shift in last few years with the advent of remarkable outcomes based on diagnosis and treatment of cancer.[29,91,105] The nanoparticle based delivery system has some advantages:

- High dose improved delivery of less water soluble drug into cancer cells.
- Protection of the drug from degradation and hydrolysis due to harsh tumor microenvironment.
- Targeted delivery of the drugs for maximum efficacy and reducing the systemic side effects.
- Controlled, slow and prolong release of drugs of particular doses at specific time points.
- Improved pharmacokinetics and drug tissue distribution.
- Combination therapy can be attained by loading multiple types of drugs /diagnostic agents which could help to overcome multidrug resistance.

Thus, nanocarriers have been introduced for drug delivery purpose as a favourable solution for improved cancer therapy and to combat various problems

associated with direct administration of chemotherapeutic drugs.[92,110] Designing of a good delivery system (nanocarrier) is one of the important prospect for proper encapsulation of therapeutic agents into it for improved and target specific drug delivery.[111]

1.4.4. Nanocarriers for drug Delivery

Based on Ferrari's classification theranostic nanoparticle (nanocarrier) should comprise of mainly three parts:

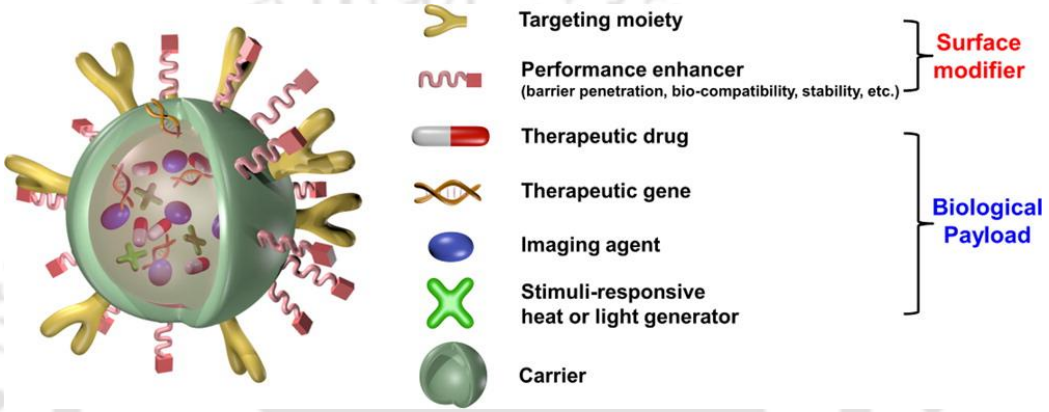

Figure1.7. Schematic illustration of multifunctional nanocomposites with essential features required for the effective delivery of therapeutic agents. [Reprinted with permission from **reference 29**. Copyright 2015 American Chemical Society].

Biomedical payload – These are basically agents which includes metal NCs,[28,47,49] QDs,[112] MRI contrast agents, CT contrast agents, anticancer drugs,[113] DNA,[33,76] and small interfering RNA[114] and have specific role or activity.

- ***Carrier***- Carriers incorporated with some essential properties allows proper loading or binding of all biological payloads for its specific and efficient delivery to the desired target site.[92,110] At the same time it provides physical protection to the payloads from degradation and helps in steady release. For fast and active clinical application, the nanocarrier should have following characteristics:
  - It should be biocompatible, well characterized and multifunctional.
  - Uptake specificity on cancer cells over normal cells.
  - Soluble or dispersible in water.

- Efficient encapsulation and release of the drugs inside the cancerous cells.
- Extended circulating half-life, a lower rate of accumulation, and a long shelf life.
- Preferential internalization by the tumor cells, either through active (targeting ligands) or passive pathway (mainly size, EPR effect).

❖ ***Surface modifier*** – To provide enhanced additional properties like long circulation time (e.g. PEG),[115] barrier-penetrating ability, and target-specific binding (e.g. receptors)[70,71,93,116] various surface modifiers are attached on the surface of the carrier.

Nanocarriers are mainly categorized as- (i) organic nano carriers (e.g. lipids or polymers),[47,117] which include solid lipid NP (SLN), liposomes, polymeric NP,[115,117] polymeric micelles[118] and more recently polymer–lipid hybrid NP (PLN) micelles,[119,120] dendrimers[92,121] and (ii) inorganic nanocarrier (e.g. metals or metal oxides) such as Au, Ag, Cu, Pt, silica etc.; which have been studied in details for various chemotherapeutic drug delivery.[92] Pre-clinical and detailed studies of some of the nanoparticle drug delivery system have already been conducted and transformed into notable nanoparticle formulations as clinical drug products (Table 1).

Table 1.1. Some of the examples of nanoparticle drug formulations approved by FDA in clinical practice and under clinical trials.

Trade Name	Formulation	Drug	Application	Phase of development
Abraxane	albumin-bound nanoparticle	Paclitaxel	Metastatic breast cancer	Approved
Caelyx	PEGylated liposome	Doxorubicin	Metastatic breast and ovarian cancer, Kaposi sarcoma	Approved
DaunoXome	Liposome	Daunorubicin	Kaposi sarcoma	Approved
DepoCyt	Liposome	Cytarabine	Lymphoma	Approved

Doxil	Liposome	Doxorubicin	Kaposi sarcoma	Approved
Genexol-PM	Polymeric micellar nano-particle	Paclitaxel	Breast cancer	Approved
Marqibo	Liposome	Vincristine sulfate	Lymphoblastic leukemia	Approved
Oncaspar	PEGylated asparaginase	Asparaginase	Acute lymphoblastic leukemia	Approved
CYT-6091	Gold nanoparticle	Tumor necrosis factor a	Pancreatic cancer, melanoma, softtissue sarcoma, ovarian, and breast cancer	Phase I/II
AuroLase	Gold nanoparticle	Doxorubicin	Solid tumor	Phase I
C-dots	PEG-coated SiO2		Melanoma	IND approved
TKM-080301	Lipid nanoparticle	siRNA	Liver cancer	Phase I

[Reprinted with permission from **reference 111**. Copyright 2014 John Wiley and Sons].

1.4.4 (a) <u>Polymer Based Nanocarrier</u> : Having excellent biocompatibility, biodegradability, and structural versatility, polymer-based nanomaterials have shown enormous growth as a drug delivery vehicle.[115,122] These are nontoxic and at permissible concentration, as over time it naturally degrades into carbon dioxide and water in the body. Chitosan and protein based luminescent nanocarrier (Au, Ag, Cu) has been employed for drug (doxorubicin, cisplatin, paclitaxel, 5-FU etc.) and gene delivery.[47,49,92,122] Some of the nanocarriers synthesized with polymers like polyethylene glycol (PEG), poly (D,L-lactic acid), poly (D,L-glycolic acid) and poly (ε- caprolactone) have already been approved for clinical practice.[115,122]New progress has been made in incorporating imaging modalities like MRI contrasting agents , radioactive substances for radionuclide

imaging via positron emission tomography PET, single photon emission computed tomography SPECT into therapeutic polymeric nanocarriers for combination therapy.[115]

1.4.4(b) <u>Combination Therapy for Synergistic Activity</u> : Chemotherapy (monotherapy) is often associated with severe side effects and increased drug resistance.[107,108,109] In this regard, combination therapy which targets and prevents several important pathways may help in overcoming multi drug resistance and results in enhanced synergistic therapy **(Figure 1.8a)**.[123] Combinatory strategies involved the coadministration or codelivery of two or more drugs with different pharmacological mechanism have gained enormous success in combating cancer due to enhanced synergistic therapeutic efficacy, decreased unwanted side effects, low toxicity and long-term prognosis.[106,123,124] Some of the drugs mostly used in combinations are paclitaxel (PTX) with 5-fluoroucacil,[123] cisplatin with doxorubicin,[125] paclitaxel (PTX) with doxorubicin[126] etc.[127] However, nanocarriers are mostly preferable for loading numerous therapeutics into a single entity for parallel delivery as it provides better drug solubility, reduced systemic toxicity, long circulation, systemic and controllable release.[92,110] Several nanocarriers involving polymers (liposome, PEG, PLGA etc.) and metals (Au, silica) have shown promising results as in combination therapy as described in **Table 1.1** through a single vehicle.[111] Additionally with the help of complex nature of nanocarrier, delivery of both hydrophobic and hydrophilic drug to the targeted site simultaneously have also been achieved.[124]

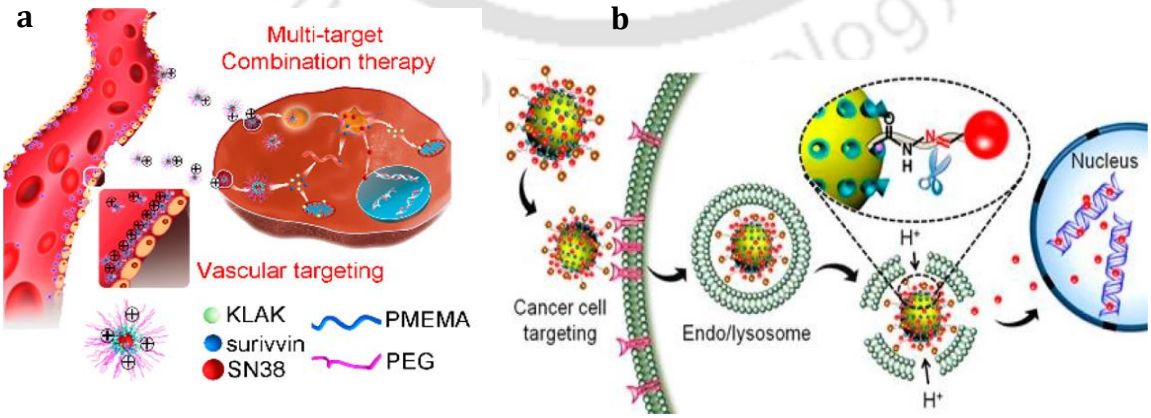

Figure 1.8 Multifunctional nanoparticles for (a) multi target combination therapy. [Reprinted with permission from **reference 123**. Copyright 2017 American Chemical

Society] and (b) targeted cancer therapy [Reprinted with permission from **reference 131.** Copyright 2015 American Chemical Society].

1.4.4(c) Targeted Delivery: With advancement of nanoscience and nanotechnology multifunctional pharmaceutical nanosystems are employed for high efficiency target specific drug delivery to the tumor site while sparing the normal cells.[69,70,71,93] This has resulted in combating the undesirable toxicity caused to the normal tissues following treatment and helps in overcoming non-specific biodistribution, drug resistance, and unwanted adverse effect. For enriched targeted drug delivery, nanocarriers are modified with targeting ligands, [69,70,71,93] monoclonal antibodies[128] and aptamers[129,130] that are specifically targeted to the receptors or antigens overexpressed on the surface of cancer cells as described in **Table 1.2.** Thus, targeting the receptors provides a promising active targeting strategy for efficient drug/gene delivery for enhanced cancer therapy[131] as represented in **(Figure 1.8b)**.

Table 1.2 Examples of some nanocarriers with targeting agents for specific targeting of overexpressed receptors in cancer cells.

Targeting agent	Platform	Receptor
FA	Silica Nanoparticles	FA
Tf	Polymeric Nanoparticles	TfR
cRGD	Micelles	$\alpha_v\beta_3$
Hyaluronic acid	Silica Nanoparticles	CD44
Galactosamine	Polymeric Nanoparticles	Asialoglycoprotein receptor
Anti- HER-2	Magnetic Nanoparticles	HER-2 receptor
LA	Silica Nanoparticles	Asialoglycoprotein receptor
Anisamide	Polymeric Nanoparticles	Sigma receptors

[Reprinted with permission from reference **116**. Copyright 2016 Royal Society of Chemistry].

1.5. Key areas and scopes

With the pursuit of literature review in the field of synthesis and characterisation of metal nanoclusters and its applications as theranostics, following scopes were identified as potential research area:

- Development of newer metal NCs using novel bio template for luminescence based bacterial detection and enumeration, thereby reducing the overall time taken for its treatment.
- Development of the novel metal NCs for distinction of antibiotic resistant bacteria.
- Exploring the application of novel metal nanoclusters in the field of energy (white light emission).
- Designing biocompatible biopolymer and drug based theranostic nanocarries for enhanced *in vitro and in vivo* combination therapy for cancer.
- Formulation of targeted luminescent nanodrug for synergistic cancer therapy *in vitro and in vivo*.

1.6. Significance and the salient features of the present study

The significance and salient features of the present study are summarised below:

- New facile method of synthesis of luminescent gold nanoclusters (Au NCs) has been developed taking bacteria as template.
- The method is new, easy, rapid, non-toxic and low cost approach and applied for detection and enumeration of Gram positive and Gram negative bacteria.
- Luminescence of Au NCs showed relationship with number of bacteria. Detection of bacteria in the water samples was possible by the luminescence of Au NCs.

- Distinguishing between kanamycin resistant bacteria from non-resistant strains was accomplished using luminescent Au NCs.
- Bacteria templated Au NCs was employed for white light emission.
- Luminescent PEG coated drug encapsulated composite nanoparticles (PEG-Au NC-NaB-NPs) were developed for combination therapy.
- The role of ART and NaB in DNA damage and HDAC inhibition resulting in cell death was observed both *in vitro* and *in vivo.*
- Multifunctional targeted nanoparticulate system or nanodrug employing stable blue emitting transferrin stabilised copper nanoclusters in combination with the drug doxorubicin as precursors (Tf-CuNC-Dox-NPs) has been formulated for diagnostic imaging, targeted drug delivery assisted via FRET and therapy for *in-vitro* as well as *in-vivo*.
- The nanodrug exhibited enhanced targeting efficacy on overexpressed TfR cells as compared with TfR less expressive cells for detection and therapy.
- A real time Förster resonance energy transfer (FRET) from Tf-Cu NCs as a donor to Dox as an acceptor was observed and was used for cellular tracking, drug release and imaging.
- Nanodrug showed enhanced therapeutic effect on mice bearing Daltons Lymphoma Ascites (DLA) tumor, with survivability for 50 days.

1.7. References

(1) McConnell, W. P.; Novak, J. P.; Brousseau, L. C.; Fuierer, R. R.; Tenent, R. C.; Feldheim, D. L. *J. Phys. Chem. B.* **2000**, *104* (38), 8925–8930.

(2) Kelly, K. L.; Coronado, E.; Zhao, L. L.; Schatz, G. C. *J. Phys. Chem. B.***2003**, *107* (3), 668–677.

(3) Eustis, S.; El-Sayed, M. A. *Chem. Soc. Rev.* **2006**, *35* (3), 209–217.

(4) Anu Mary Ealia, S.; Saravanakumar, M. P. A *IOP Conference Series: Materials Science and Engineering* **2017**, *263*, 32019.

(5) Li, Y.; Wang, Y.; Huang, G.; Gao, J.*Chem. Rev.* **2017**, DOI: 10.1021/acs.chemrev.8b00195.

(6) Roco, M. C. *Curr. Opin. Biotechnol.* **2003**, *14* (3), 337–346.

(7) Pita, M.; Krämer, M.; Zhou, J.; Poghossian, A.; Schöning, M. J.; Fernández, V. M.; Katz, E. *ACS Nano* **2008**, *2* (10), 2160–2166.

(8) Liao, J.; Blok, S.; van der Molen, S. J.; Diefenbach, S.; Holleitner, A. W.; Schönenberger, C.; Vladyka, A.; Calame, M. *Chem. Soc. Rev.* **2015**, *44* (4), 999–1014.

(9) Stratakis, M.; Garcia, H. *Chem. Rev.* **2012**, *112* (8), 4469–4506.

(10) Gawande, M. B.; Goswami, A.; Felpin, F. X.; Asefa, T.; Huang, X.; Silva, R.; Zou, X.; Zboril, R.; Varma, R. S. *Chem. Rev.* **2016**, *116* (6), 3722–3811.

(11) Li, M.; Gou, H.; Al-Ogaidi, I.; Wu, N. *ACS Sustain. Chem. Eng.* **2013**, *1* (7), 713–723.

(12) Bhandari, S.; Pramanik, S.; Khandelia, R.; Chattopadhyay, A. *ACS Appl. Mater. Interfaces* **2016**, *8*, 6–11.

(13) Wang, Z.; Chen, B.; Susha, A. S.; Wang, W.; Reckmeier, C. J.; Chen, R.; Zhong, H.; Rogach, A. L. *Adv. Sci.* **2016**, 1600182.

(14) Wolfbeis, O. S. *Chem. Soc. Rev.* **2015**, *44* (14), 4743–4768.

(15) Selvan, S. T.; Yang Tan, T. T.; Kee Yi, D.; Jana, N. R. *Langmuir* **2010**, *26* (14), 11631–11641.

(16) Jiang, S.; Win, K. Y.; Liu, S.; Teng, C. P.; Zheng, Y.; Han, M.-Y. *Nanoscale* **2013**, *5* (8), 3127.

(17) Sapsford, K. E.; Algar, W. R.; Berti, L.; Gemmill, K. B.; Casey, B. J.; Oh, E.; Stewart, M. H.; Medintz, I. L. *Chem. Rev.***2013**, *113* (3), 1904–2074.

(18) Dreaden, E. C.; Alkilany, A. M.; Huang, X.; Murphy, C. J.; El-Sayed, M. A. *Chem. Soc. Rev.* **2012**, *41* (7), 2740–2779.

(19) Pelaz, B.; Jaber, S.; De Aberasturi, D. J.; Wulf, V.; Aida, T.; De La Fuente, J. M.;

Feldmann, J.; Gaub, H. E.; Josephson, L.; Kagan, C. R.; Kotov, N. A.; Liz-Marzán, L. M.; Mattoussi, H.; Mulvaney, P.; Murray, C. B.; Rogach, A. L.; Weiss, P. S.; Willner, I.; Parak, W. J. *ACS Nano* **2012**, *6* (10), 8468–8483.

(20) Tao, Y.; Li, M.; Ren, J.; Qu, X. *Chem. Soc. Rev.***2015**, *44*, 8636–8663.

(21) Jin, R. *Nanoscale* **2010**, *2* (3), 343–362.

(22) Jin, R. **2015**, *Chem. Rev.* **2016**, *15*, 1549–1565.

(23) Goswami, N.; Zheng, K.; Xie, J. *Nanoscale* **2014**, *6* (22), 13328–13347.

(24) Li, G.; Jin, R. *Acc. Chem. Res.* **2013**, *46* (8), 1749–1758.

(25) Stamplecoskie, K. G.; Kamat, P. V. *J. Am. Chem. Soc.* **2014**, *136*, 11093−11099**.**

(26) Webb, J. A.; Bardhan, R. *Nanoscale* **2014**, *6*, 2502-2530.

(27) Fan, Z.; Fu, P. P.; Yu, H.; Ray, P. C. *J. Food Drug Anal***. 2014**, *22* (1), 3–17.

(28) Sun, J.; Jin, Y. *J. Mater. Chem. C.* **2014**, *2*, 8000–8011.

(29) Lim, E.; Kim, T.; Paik, S.; Haam, S.; Huh, Y.; Lee, K. *Chem. Rev.* **2015**, *115*, 327−394.

(30) Song, X.; Goswami, N.; Yang, H.; Xie, J. Analyst, **2016**, *141*, 3126–3140.

(31) Zheng, K.; Setyawati, M. I.; Leong, D. T.; Xie, J. *ACS Nano* **2017**, *11*, 6904−6910.

(32) Qu, X.; Li, Y.; Li, L.; Wang, Y.; Liang, J.; Liang, J. Fluorescent Gold Nanoclusters : Synthesis and Recent Biological Application. **2015**, *2015*.

(33) Pandya, A.; Lad, A. N.; Singh, S. P.; Shanker, R. *RSC Adv.* **2016**, *6*, 113095–113114.

(34) Metal, H. F.; Induced, E.; Phase, R. *ACS Nano* **2011**,11, 8800–8808.

(35) Ras, R. H. A. *Nanoscale*, **2011**, *3*, 1963–1970**.**

(36) Mathew, A.; Pradeep, T. Noble Metal Clusters : Applications in Energy , Environment , and Biology. **2014**, 1017–1053.

(37) Yu, Y.; Mok, B. Y. L.; Loh, X. J.; Tan, Y. N. *Adv. Healthcare Mater.* **2016**, *5*, 1844–1859.

(38) Somoza, A.; Cortajarena, A. L. *Biomacromolecules* **2015,** *16*, 3836−3844.

(39) Online, V. A.; Feng, J.; Huang, H.; Zhou, D.; Cai, L.; Tu, Q.; Wang, A. *J. Mater. Chem. C,* **2013,** *1*, 4720–4725.

(40) Yuan, X.; Tay, Y.; Dou, X.; Luo, Z.; Leong, D. T.; Xie, *J. Anal. Chem.* **2013**, *85*, 1913−1919.

(41) Uptake, T.; Clearance, H. R.; Zhang, X.; Luo, Z.; Chen, J.; Song, S.; Yuan, X.;

Shen, X.; Wang, H. *Sci. Rep.* **2015**, *5*,1–7.

(42) Das, N. K.; Ghosh, S.; Priya, A.; Datta, S.; Mukherjee, S. *J. Phys. Chem. C* **2015**, *119*, 24657−24664.

(43) Huang, T.; Murray, R. W. *J. Phys. Chem. B.* **2001**, *3290*, 12498–12502.

(44) Lee, D.; Donkers, R. L.; Wang, G.; Harper, A. S.; Murray, R. W.; Hill, C.; Carolina, N. *J. Am. Chem. Soc.* **2004**, 126, 6193-6199.

(45) Yan, C.; Liu, C.; Abroshan, H.; Li, Z.; Qiu, R.; Li, G. *Phys. Chem. Chem. Phys.* **2016**, *18*, 23358–23364.

(46) Simas, A. B. C.; Aguiar, L. C. S. *J. Mater. Chem*. **2011**, *21*, 13516–13523.

(47) Sahoo, A. K.; Banerjee, S.; Ghosh, S. S.; Chattopadhyay, A. *ACS Appl. Mater. Interfaces* **2014**, *6*, 712−724.

(48) Zhu, H.; Yu, T.; Xu, H.; Zhang, K.; Jiang, H.; Zhang, Z.; Wang, Z.; Wang, S. *ACS Appl. Mater. Interfaces* **2014**, *6*, 21461−21467.

(49) Ghosh, R.; Goswami, U.; Ghosh, S. S.; Paul, A.; Chattopadhyay, A. *ACS Appl. Mater. Interfaces* **2015**, *7,* 209–222.

(50) Li, D.; Chen, Z.; Wan, Z.; Yang, T.; Wang, H.; Mei, X. *RSC Adv.* **2016**, *6*, 34090–34095.

(51) Adhikari, B.; Banerjee, A. *Chem. Mater*. **2010**, *22*,4364–4371.

(52) Jiang, J.; Conroy, C. V; Kvetny, M. M.; Lake, G. J.; Padelford, J. W.; Ahuja, T.; Wang, G. *J. Phys. Chem. C* **2014,** *118*, 20680−20687.

(53) Ang, T. P.; Chin, W. S. *J. Phys. Chem. B* **2005**, *109,* 22228-22236.

(54) Ruiyi, L.; Huiying, W.; Xiaoyan, Z.; Xiaoqing, L.; Xiulan, S.; Zaijun, L. *New J. Chem.* **2015**, *40*, 732–739.

(55) Gerthsen, D.; Nienhaus, G. U. *Nanoscale* **2011**, *3*, 2009–2014.

(56) Bauer, B. J.; Akpalu, Y. A.; Jackson, C. L.; Amis, E. J. *Macromolecules* **2000**, *33*, 6042–6050.

(57) Díez, I.; Pusa, M.; Kulmala, S.; Jiang, H.; Walther, A.; Goldmann, A. S.; Müller, A. H. E.; Ikkala, O.; Ras, R. H. A. *Angew. Chem. Int. Ed*. **2009**, *48*, 2122–2125.

(58) Zhao, M.; Sun, L.; Crooks, R. M. *J. Am. Chem. Soc.* **1998**, *7863* (21), 4877–4878.

(59) Duan, H.; Nie, S. **2007**, *J. Am. Chem. Soc.* **2007**, *129,* 2412–2413.

(60) Sun, X.; Dong, S.; Wang, E. *Macromolecules* **2004**, *37*, 7105–7108.

(61) Chen, Y.; Zheng, X.; Wang, X.; Wang, C.; Ding, Y.; Jiang, X. *ACS Macro Lett.* **2014**, *3*, 74 -76.

(62) Huang, H.; Li, H.; Wang, A.; Zhong, S.; Fang, K.; Feng, J. *The Analyst* **2014**, *139*, 6536–6541.

(63) Wen, Q.; Gu, Y.; Tang, L.; Yu, R.; Jiang, J. *Anal. Chem.* **2013,** *85*,11681−11685.

(64) Gu, X. Le; Benjamin, H.; Jung, G.; Hollemeyer, K.; Trouillet, V.; Schneider, M. J. *Phys. Chem. C* **2011**, *115*, 10955–10963.

(65) Wang, C.;Wang, C.; Xu, L.; Cheng, H.; Lin,Q.; Jhang, C. *Nanoscale* **2014**, *6*, 1775–1781.

(66) Ghosh, R.; Sahoo, K. A.;Ghosh, S. S.; Chattopadhyay. A *ACS Appl. Mater. Interfaces* **2014**, *6*, 3822−3828.

(67) Chen, T.; Tseng, W. *Small* **2012**, *12*, 1912–1919.

(68) Wen, F.; Dong, Y.; Feng, L.; Wang, S.; Zhang, S.; Zhang, X. *Anal. Chem.***2011**, *83*,1193–1196.

(69) Xavier, P. L.; Chaudhari, K.; Verma, K.; Pal, K. *Nanoscale*, **2010**, *2*,2769–2776.

(70) Gu, X. Le; Daum, N.; Schneider, M. *Nanotechnology* **2011**,*22*, *275103*.

(71) Zhao, T.; He, X.; Li, W.; Zhang, Y. *J. Mater. Chem. B,* **2015**, *3*, 2388–2394.

(72) G.; Liu, C.; Wu, H.; Hsiao, Y.; Lai, C.; Shih, C.; Peng.Y.;Tang, K.;Chang, H.;Chien,Y.; Hsiao,J.; Cheng, J.; Chou,P. *Angew. Chem. Int. Ed.* **2011**,*50* 7056–7060.

(73) Feng, J.; Chen, Y.; Han, Y.; Liu, J.; Zhang, H.; Chen, X. *ACS Omega.* **2017**, 2, 9109−9117.

(74) Wang, L.; Qiao, J.; Qi, L.; Xu, X.; Li, D. *chem.scichina.com* **2015**, *58* (9), 1508–1514.

(75) New, S. Y.; Lee, S. T.; Su, X. D. *Nanoscale* **2016**, *8*, 17729–17746.

(76) Richards, C. I.; Choi, S.; Hsiang, J.; Antoku, Y.; Vosch, T.; Bongiorno, A.; Tzeng, Y.; Dickson, R. M. *J. Am. Chem. Soc.* **2008**, *8*, 5038–5039.

(77) Chen, L.; Wang, C.; Yuan, Z.; Chang, H. *Anal. Chem.***2015**, *87*, 216−229.

(78) Zheng, Y.; Lai, L.; Liu, W.; Jiang, H.; Wang, X. *Adv. Colloid Interface Sci.* **2017**, *242*, 1–16.

(79) Cui, M.; Zhao, Y.; Song, Q. *Trends Anal. Chem.* **2014**, *57*, 73–82.

(80) Liu, J.; Chen, J.; Yan, X. *Anal. Chem.* **2013**, *85*, 3238−3245 .

(81) Guo, Y.; Cao, F.; Lei, X.; Mang, L.; Cheng, S. *Nanoscale*, **2016**, *8,* 4852–4863.

(82) Wang, Z.; Chen, B.; Rogach, A. L. Nanoscale Horiz. **2017**, *2*, 135–146.

(83) Liu, X.; Astruc, D. *Coord. Chem. Rev.* **2018**, *359*, 112–126.

(84) Jia, X.; Li, J.; Wang, E. *Small* **2013**, *22*, 3873–3879.

(85) Ganguly, A.; Chakraborty, I.; Udayabhaskararao,T.; Praddep,T. *J Nanopart Res* **2013**, DOI 10.1007/s11051-013-1522-8.

(86) Lin, Y.;Chen, P.; Yuan, Z.; Ma, J.; Chang, H.*ChemComm*.**2015**,*51*,11983–11986.

(87) Zhang, H.; Huang, X.; Li, L.; Zhang, G.; Hussain, I.*ChemComm* **2012**, 567–569.

(88) Barthel, M. J.; Angeloni, I.; Petrelli, A.; Avellini, T.; Scarpellini, A.; Bertoni, G.; Armirotti, A.; Moreels, I.; Pellegrino, T.; Al, B. E. T. *ACS Nano***2015**,12, 11886–11897.

(89) Jia, X.; Li, J.; Han, L.; Ren, J.; Yang, X.; Wang, E.*ACS Nano* **2012**, 4, 3311–3317.

(90) Wang, H.; Zhang, H.; Chen, Y.; Huang, K.; Liu, Y. *Sens. Actuator B-Chem.* **2015**, *220*, 146–153.

(91) Yu, Y.;Mok,Y.L.B.;Loh,X.; Tan,Y.;T. *Adv. Healthcare Mater.* **2016**,*5*,1844–1859.

(92) Ang, C. Y.; Tan, S. Y.; Zhao, Y. R *Org. Biomol. Chem.* **2014**, *12* (27), 4776.

(93) Zhou, F.; Feng, B.; Yu, H.; Wang, D.; Wang, T.; Liu, J.; Wang, S.; Zhang, P.; Zhang, Z.; Li, Y. *Theranostics* **2016**, *6* (5), 679-687.

(94) Shao, K.; Singha, S.; Clemente-casares, X.; Tsai, S.; Yang, Y. N. *ACS Nano* **2014**, *9*,16-30.

(95) Rao, W.; Wang, H.; Han, J.; Zhao, S.; Dumbleton, J.; Agarwal, P.; Zhang, W.; Zhao, G.;Yu, J.; Lu, X.; He, X.*ACS Nano* **2015**, *6*, 5725–5740.

(96) Ghoshal, A.; Goswami, U.; Sahoo, A. K.; Chattopadhyay, A.; Ghosh, S. S. *ACS Biomater. Sci. Eng.* **2015**, *1,* 1256−1266.

(97) Ghoshal, A.; Goswami, U.; Raza, A.; Chattopadhyay, A.; Ghosh, S. S. *RSC Adv.* **2016**, *6,* 85763–85772.

(98) Shang, L.; Stockmar, F.; Azadfar, N.; Nienhaus, G. U. *Angew. Chem. Int. Ed.* **2013**, *52* (42), 11154–11157.

(99) Zhang, X. D.; Chen, J.; Luo, Z.; Wu, D.; Shen, X.; Song, S. S.; Sun, Y. M.; Liu, P. X.; Zhao, J.; Huo, S.; Fan, S.; Fan, F.; Liang, X. J.; Xie, J. *Adv Healthc Mater.* **2014**, *3* (1), 133–141.

(100) Roy, D.; Steyer, G. J.; Gargesha, M.; Stone, M. E.; Wilson, L. *Biomaterials* **2009**, *292* (3), 342–351.

(101) Katla, S. K.; Zhang, J.; Castro, E.; Bernal, R. A.; Li, X. *ACS Appl. Mater. Interfaces* **2018**, *10* (1), 75–82.

(102) Pan, N. U.; Khandelia, R.; Sanpui,P.; Das, S.; Paul,A.; Chattopadhyay, A. *ACS Appl. Mater. Interfaces* **2017,** *9*, 19495–19501.

(103) Li, J.; Wang, W.; Sun, D.; Chen, J.; Zhang, P.-H.; Zhang, J.-R.; Min, Q.; Zhu, J.-J. s

Chem. Sci. **2013**, *4* (9), 3514–3521.

(104) Chen, W.-Y.; Lin, J.-Y.; Chen, W.-J.; Luo, L.; Wei-Guang Diau, E.; Chen, Y.-C. *Nanomedicine* **2010**, *5* (5), 755–764.

(105) Kim, T. H.; Lee, S.; Chen, X. *Expert Rev. Mol. Diagn.* **2013**, *13* (3), 257–269.

(106) Zhang, J.; Liang, Y.; Lin, X.; Zhu, X.; Yan, L.; Li, S.; Yang, X. *ACS Nano* **2015**, 9, 9741–9756.

(107) Park, N. H.; Cheng, W.; Lai, F.; Yang, C.; Sessions, P. F. De; Periaswamy, B.; Chu, C. W.; Bianco, S.; Liu, S.; Venkataraman, S.; Chen, Q.; Yang, Y. Y.; Hedrick, J. L. *J. Am. Chem. Soc.* **2018,** *140*, 4244–4252.

(108) Holohan, C.; Schaeybroeck, S. Van; Longley, D. B.; Johnston, P. G. C. *Nature Publishing Group* **2013**, *13* (10), 714–726.

(109) Liang, X.; Chen, C.; Zhao, Y.; Wang, P. C. *Methods Mol Biol*. **2010**, *596* (3), 467–488.

(110) Peer, D.; Karp, J. M.; Hong, S.; Farokhzad, O. C.; Margalit, R.; Langer, R. *Nat Nanotechnol* .**2007**, *2*, 751–760.

(111) Sun, T.; Zhang, Y. S.; Pang, B.; Hyun, D. C.; Yang, M.; Xia, Y. *Angew. Chem. Int. Ed.* **2014**, *53*, 12320–12364.

(112) Walling,M.A.;Novak,J.A.;Shepard,J.R.E. *Int. J.Mol. Sci.* **2009**, *10* (2), 441–491.

(113) Article, R.; Singh, D.; Gupta, N.; Kumar, S. *World J. Pharm. Pharm.* Sci. **2014**, *3* (10), 336–351.

(114) Lin, G.; Chen, C.-K.; Yin, F.; Yang, C.; Tian, J.; Chen, T.; Xu, G.; He, C.; Lin, M. C.-M.; Wang, J.; Lu, F.; Wang, X.; Yong, K.-T. *J. Mater. Chem. B* **2017**, *5* (18), 3327–3337.

(115) Luk, B. T.; Zhang, L. *ACS Appl. Mater. Interfaces* **2014**, *6*, 21859−21873.

(116) Dai, L.; Liu ,J.; Luo, Z.; Li, M.; Cai, K. *J. Mater. Chem. B,* **2016**, *4*, 6758–6772.

(117) Khan, M.; Ong, Z. Y.; Wiradharma, N.; Attia, A. B. E.; Yang, Y. Y. *Adv Healthc. Mater.***2012**, *1* (4), 373–392.

(118) Mao, J.; Li, Y.; Wu, T.; Yuan, C.; Zeng, B.; Xu, Y.; Dai, L.*ACS Appl. Mater. Interfaces* **2016**, *8* (27), 17109–17117.

(119) Zhang, L.; Chan, J. M.; Gu, F. X.; Rhee, J.; Wang, A. Z.; Radovic-moreno, A. F.; Alexis, F.; Langer, R.; Farokhzad, O. C. S *ACS nano* **2008**, *2* (8), 1696–1702.

(120) Krishnamurthy, S.; Vaiyapuri, R.; Zhang, L.; Chan, J. M. *Biomater. Sci.* **2015**, *3* (7), 923–936.

(121) Caminade, A.-M.; Turrin, C.-O. *J. Mater. Chem. B* **2014**, *2* (26), 4055–4066.

(122) Hu, C.-M. J.; Fang, R. H.; Luk, B. T.; Zhang, L. *Nanoscale* **2014**, *6* (1), 65–75.

(123) Yan, X.; Yu, Q.; Guo, L.; Guo, W.; Guan, S.; Tang, H.; Lin, S.; Gan, Z. *ACS Appl. Mater. Interfaces* **2017**, *9*, 6804−6815.

(124) Ma, Y.; Liu, D.; Wang, D.; Wang, Y.; Fu, Q.; Fallon, J. K.; Yang, X.; He, Z.; Liu, F. *Mol. Pharmaceutics* **2014**, *11*, 2623−2630.

(125) Wu, H.; Jin, H.; Wang, C.; Zhang, Z.; Ruan, H.; Sun, L.; Yang, C.; Li, Y.; Qin, W.; Wang, C. *ACS Appl. Mater. Interfaces* **2017**, *9*, 9426−9436.

(126) Liu, Y.; Fang, J.; Kim, Y. J.; Wong, M. K.; Wang, P. *Mol. Pharm.* **2014**, *11* (5), 1651–1661.

(127) Jiang, T.; Mo, R.; Bellotti, A.; Zhou, J.; Gu, Z. *Adv. Funct. Mater.* **2014**, *24*, 2295–2304.

(128) Goodall, S.; Jones, M. L.; Mahler, S. *J. Chem. Technol. Biotechnol.***2015**, *90* (7), 1169–1176.

(129) Liu, Q.; Jin, C.; Wang, Y.; Fang, X.; Zhang, X.; Chen, Z.; Tan, W. *NPG Asia Mater.* **2014**, *6* (4), e95-10.

(130) Lao, Y. H.; Phua, K. K. L.; Leong, K. W. *ACS Nano* **2015**, *9* (3), 2235–2254.

(131) Chen, W. H.; Lei, Q.; Luo, G. F.; Jia, H. Z.; Hong, S.; Liu, Y. X.; Cheng, Y. J.; Zhang, X. Z. *ACS Appl. Mater. Interfaces* **2015**, *7* (31), 17171–17180.

Chapter-2

In situ Synthesis of Luminescent Au Nanoclusters on Bacterial Template for Rapid Detection, Quantification and Distinction of Kanamycin Resistant Bacteria

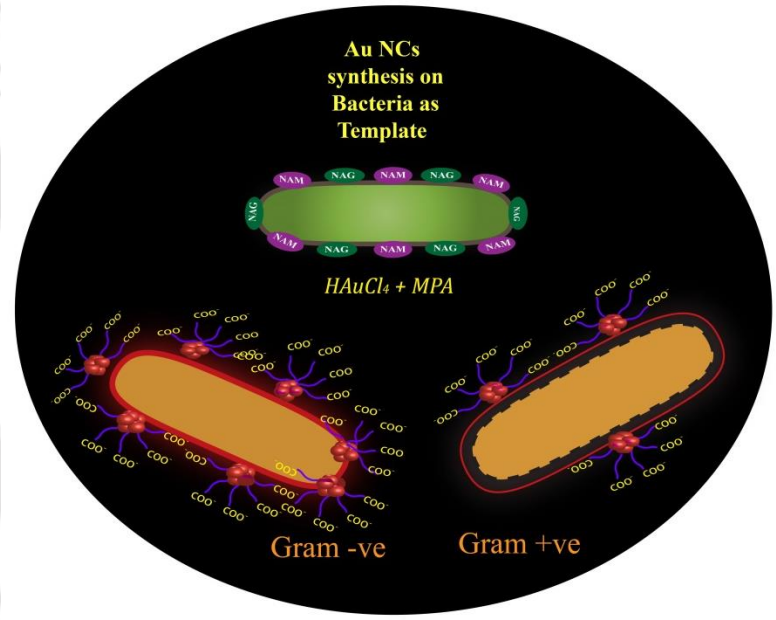

***In Chapter 2**, novel facile synthesis of luminescent gold nanoclusters (Au NCs) using bacteria as its template has been reported. The luminescence property of the as-synthesized Au NCs was probed for bacterial detection, enumeration and strain differentiation of Gram positive and Gram negative bacteria. Further, it was employed to detect bacterial contaminants from water sources and kanamycin resistant strains.*

https://pubs.acs.org/doi/abs/10.1021/acsomega.8b00504

Chapter -2

2.1. Introduction

Rapid and easy detection of numerous drug resistant bacteria is a burgeoning field of research in the recent time. New methods and tools based on the advanced biochemical techniques such as, PCR,[1-4]mass spectroscopy,[5] immunological assays / micro array,[1,6] enzyme assays,[7] have been adopted for bacterial detection. However, along with the time constraints and cost, these methods employ prolonged steps for sample preparation. Detection of antibiotic resistant bacteria using optical methods, [8] standard disk diffusion assays and E-test at various antibiotic concentrations on strips require more than 24 h.[9]

Nanotechnology based solutions have gained much attention owing to unique physiochemical properties due to small size over the conventional methods for bacterial detection.[10] Many nanoparticle-based detection methods require functional conjugation of suitable probes,[11,12] ligands[13-15] antibodies[16] and aptamers.[17] Recent progress in this field has led to the evolution of 'lab on a chip' for multiplex analysis with heightened sensitivity. Among this diversity of methods, the luminescence based methods are fascinating due to rapid response time, easy operation and sensitivity.[18-20] However, organic fluorophores employed in the routine exercises, have several limitations, which decline their widespread applications. Further, all nanoparticle (NPs) based detections involve two-way systems- first the synthesis of desired functionalized NPs and then the detection, and thus the overall process is time-consuming (12-14 h for bacterial growth only, synthesis and detection separately). In fact the optical determination of antibiotic resistant strains involves extended procedure of synthesis and purification of fluorophore.[8] However, metal nanoclusters (NCs) have been reported to overcome the inherent limitations of the conventional organic dyes. [21] In the size dominion of (< 2 nm), the NPs do not support surface plasmon resonance, which is the common phenomenon associated with the metal NPs; however they exhibit bright luminescence due to discretization of the continuous electronic states of metal. The synthesis of the metal NCs offers huge challenge in its stabilization due to its

ultra-small size, which often results agglomerations of the NCs or formation of plasmonic NPs. Macromolecules provide essential template for stabilization of the NCs. A great repertoire of studies has employed bio -macromolecules, such as, proteins, small molecules, and DNA as template for synthesis of the NCs that are useful for bioimaging and sensing applications.[21-24]A recent report has demonstrated the synthesis of the gold nanoclusters (Au NCs) inside cancer cells for the use of bioimaging.[25] Synthesis of Au NCs was reported using *Escherichia coli* enoyl-acyl ACP reductase, an enzyme commonly known as FabI.[26]Other reports of bacterial detection using Au NCs showed a long synthesis and detection procedure.[27, 28] Hence, the use of entire bacteria as template for the synthesis of NCs could be explored to utilize luminescence of the NCs for bacterial detection. Herein a one-way procedure of bacterial detection by synthesizing highly luminescent Au NCs on bacterial cells by slightly modifying the reaction concentrations of mercaptopropionic acid (MPA) and gold chloride from already established protocol has been reported.[29] For the present work the reaction mixture was exposed to (50 °C) heating for 2 min, which is less than pasteurization. Interestingly, the luminescence intensity of the Au NCs changes with the number of bacteria, offering a quick method to enumerate the number of bacteria present in the samples. The method is very versatile, where both Gram positive and Gram negative bacteria were used to synthesize Au NCs and at the same time this method can be employed for the detection of bacterial contamination in various water sources (samples) based on its luminescence. Further with increase in number of antibiotic resistant bacteria the present method can also be employed to detect antibiotic resistant strains in short time where distinctive difference can be observed in 6h. Therefore, the current investigation emphasizes on the development of a simple, fast detection method for 'point of care' diagnosis and prognosis, based on the luminescence property of the Au NCs on bacterial surface.

2.2. Outline of the present work

Herein, a new facile method of fluorescent gold nanoclusters (Au NCs) synthesis on the surface of bacteria for detection, counting and strain differentiation has

been introduced. The limit of detection (LOD) was 740 ±14 CFU/mL for the Gram negative and was 634 ±16 for the Gram positive bacteria. Brief treatment with lysozyme could differentiate the Gram strains based on their fluorescence intensities. The current method could also detect bacterial contaminants from water sources and kanamycin resistant strains rapidly. This quick synthesis of Au NCs on bacterial template attributes an easy and rapid method for enumeration, detection of bacterial contaminants and kanamycin resistant strains.

2.3. Experimental Section

2.3.1. Materials

Gold chloride (17 wt. % solution of $HAuCl_4$ in dilute HCl; 99.99%) and 3-Mercaptopropionic acid of high purity were obtained from Sigma-Aldrich Chemicals, U.S.A. Nutrient broth (NB), Brain–Heart Infusion (BHI), growth media were procured from HI Media, Mumbai, India. Water used in all the experiments was high purity Milli-Q grade water (>18 MΩ cm^{-1}, Millipore).

2.3.2. Bacterial Strains

Four bacterial strains were chosen as template for cluster synthesis and detection, which included two Gram-positive strains: *Bacillus cereus* MTCC 1305, *Enterococcus faecalis* MTCC 439 and two Gram-negative strains: *Escherichia coli* MTCC 433, *Pseudomonas aeruginosa* MTCC 2488 strains. *Enterococcus faecalis* MTCC 439 was grown in BHI at 37° C at 220 rpm for 12 h and all the other strains were grown in NB medium keeping the conditions intact.

2.3.3. Synthesis of Au NCs

The serial dilution was conducted on overnight grown bacteria after centrifugation in de-ionized water. On that 90µL (10 mM) of $HAuCl_4$ along with 30 µL (0.11M) of MPA was added and thoroughly mixed keeping the pH constant at 7.The samples were heated at 50 °C (less than pasteurization temperature) for 2 min followed by cooling. Bright luminescence was observed under UV trans illuminator (Excitation 305 nm).The luminescence peak was obtained at 582 nm

on excitation at 320 nm on Au NCs synthesized bacteria, which was not there in case of control bacteria.

2.4. Characterization

2.4.1. Luminescence Measurements

All luminescence data were obtained from Flurolog-3, Horiba JovinYvon, Edison, NY, USA. For this purpose, first the overnight grown bacterial culture was harvested by centrifuging at 10,000 rpm for 1 min. The cell pellet was redisposed in de- ionised water. The absorbance value of each bacterial strain is noted at 595 nm in UV- Vis spectrophotometer and is kept constant for all the strains. To carry out detection of bacteria, serial dilutions from 10^6 - 10^2 were made and synthesis was carried out in these, keeping all the reaction conditions intact. Further, before synthesis 100 µl from each set was spread on agar plate to obtain colonies and kept for overnight incubation at 37 °C. The number of colonies obtained is related with luminescence of each set of bacteria as luminescence obtained is directly proportional to bacterial number. The luminescence spectra obtained directs the Au NCs formation on the bacterial surface, which was not the characteristic peak of control bacteria. Luminescence spectra with different bacterial concentration of two Gram positive (*Bacillus cereus* MTCC 1305, *Enterococcus faecalis* MTCC 439) and two Gram negative strains (*Escherichia coli* MTCC433, *Pseudomonas aeruginosa* MTCC 2488) are shown. To find out the slope between different bacteria the logarithm of number of bacteria Log (N) CFU/mL with normalized emission intensity was plotted which exhibited a linear relation for both Gram positive and Gram negative (where I_f = Final emission intensity I_i = Initial emission intensity.

2.4.2. X- Ray Photoelectron Spectroscopy (XPS)

To find out the electronic state of Au NCs, X- Ray Photoelectron Spectroscopy was carried out in PHI 5000 Versa Probe II scanning XPS microprobe. For this, synthesized Au NCs on bacterial surface was taken and pellet was collected by

centrifuging at 10,000 rpm for 1 min. The pellet was dried by lyophilisation and measurements were taken.

2.4.3. Matrix-Assisted Laser Desorption Ionization Time of Flight Mass Spectroscopy (MALDI-TOF-MS) Analysis

MALDI –TOF analysis was carried out in Applied Bio systems 4800 Plus MALDI TOF/TOF Analyser where sinapinic acid was used as a matrix for the samples. The matrix was prepared by dissolving sinapinic acid (10 mg) in a mixture of 1 mL of 50 % acetonitrile (ACN) and 0.05% of trifluroacetic acid (TFA) and were mixed in the ratio of 1:2 (volume ratio) with Au NCs synthesized bacteria carefully and then spotted.

2.4.4. Confocal Laser Scanning Microscopy and Deconvulation microscopy Analysis

For CLSM studies, first the overnight grown bacteria (*Escherichia coli* MTCC 433) were taken centrifuged (10,000 rpm for 1 min) and serially diluted in Milli-Q water followed by Au NCs synthesis. After synthesis it was centrifuged again to remove the unreacted materials and pellet was fixed with 4% formaldehyde. From this, 60 µL of samples were taken and drop cast on a clean glass slide and was covered with a coverslip. The prepared samples were observed under CLSM (Zeiss microscope LSM 880) with λ_{ex} 405 nm. For Delta Vision Deconvolution Microscope (GE Healthcare) imaging was carried out in agar pads which were prepared with 0.6% agar in LB medium, where 10µL of Au NCs synthesized bacteria were drop casted for imaging.

2.4.5. Transmission Electron Microscopy (TEM)

To analyse the size of Au NCs, high resolution TEM (JEM-2100, JEOL, Japan) was used, which operates at an accelerating voltage of 200 kV. For TEM analysis, the sample as mentioned above was prepared, centrifuged and washed with water to remove the residual media, gold and MPA and analysed by adding 8.0 µL of the sample on carbon-coated copper grid . After complete drying the samples were taken for measurements.

2.4.6. Quantum Yield

The photoluminescence quantum yield of flurophore Au NCs synthesized on bacteria was determined relative to the reference of quantum yield of known compound quinine sulphate. The sample and a reference sample are excited at same wavelength keeping same slits and bandwidths and hence QY is calculated by using the formula:

$$QY = \frac{QY_r\, m}{m_r}\frac{n}{n_r}$$

Where, m denotes the slope of the plot of integrated fluorescence intensity vs. absorbance, n is the refractive index. The reference fluorophore i.e. quinine sulphate solution is represented by suffix r .For the experiment the same solutions were used to record both UV-Vis spectra (Perkin Elmer LS 45) and fluorescence emission .The absorbance value was kept less than 0.01 to minimize re-absorption effects. The refractive index of solvent (water) is 1.33 and quantum yield of the standard (QY_r) is 0.54.

2.4.7. Cell Viability MTT Assay

To study the cell viability of Au NCs synthesized bacteria MTT assay was carried out after 24 h of treatment on HEK-293 cells. Briefly, 1× 10^4 cells were seeded in each well of 96 well plates and were incubated overnight for attachment. After this treatments were given at varied concentrations for 24 h, in triplicates. Thereafter, MTT was added in each well and the formed formazon was dissolved in DMSO. The absorbance of formazan, was then measured at 550 nm with background reference measured at 655 nm in Multiplate Reader (Tecan). The cell viability was calculated as:

$$\%\ \text{of Cell Viability} = \frac{(A_{550} - A_{655})_{sample}}{(A_{550} - A_{655})_{control}} \times 100$$

2.5. Results and Discussion

The Au NCs were synthesized using bacteria as its template by slightly modifying the previous established protocol.[29] Overnight grown bacteria was collected by centrifugation and then re-dispersed in water at different dilution. To this bacterial solution, 0.01 M mercaptopropionic acid (MPA) and 10 mM gold solution ($HAuCl_4$) were added followed by heating at 50 ^{0}C for 2 min. The schematic representation of Au NCs synthesized bacteria and its role in enumeration, differentiation between Gram positive and Gram negative bacteria and kanamycin resistant strains has been explicated in **(Figure 2.1)**.

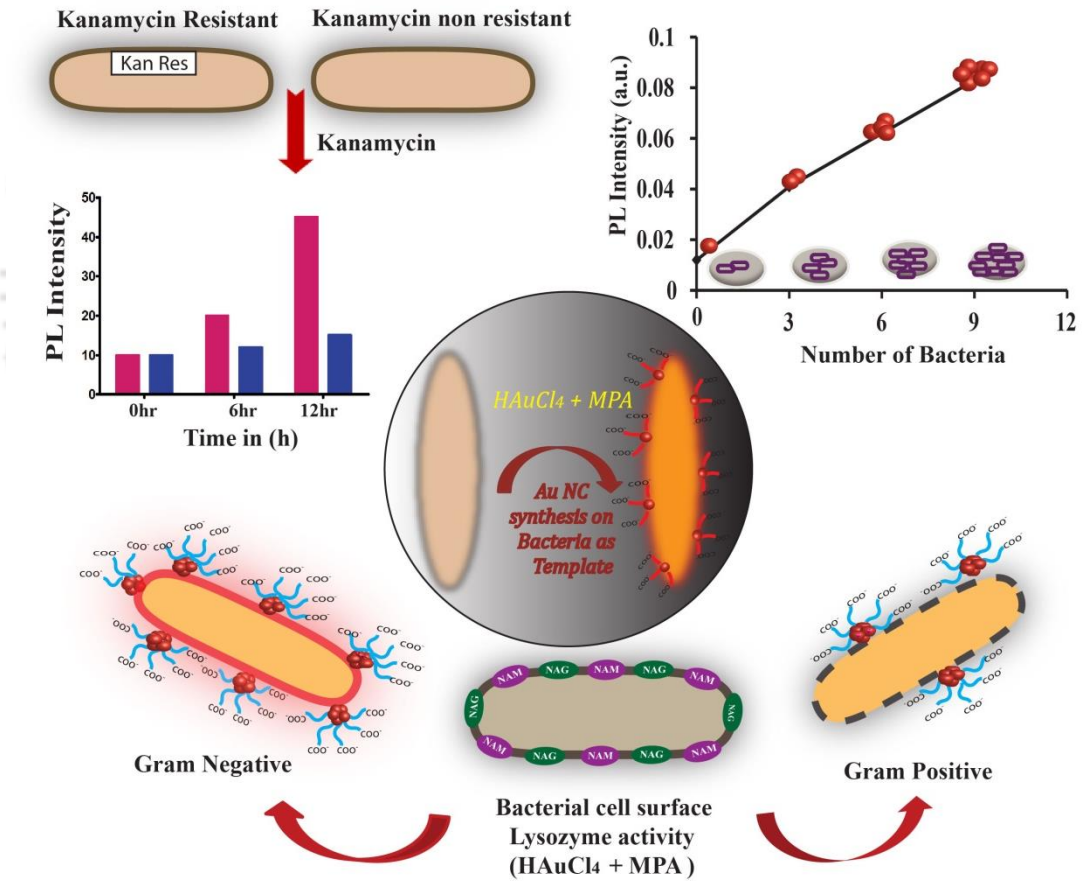

Figure 2.1. Schematic representation of Au NCs synthesized on bacteria and their role in enumeration, and differentiation between Gram positive and Gram negative bacteria and kanamycin resistant strains.

The formation of the Au NCs was confirmed by the fluorescence spectroscopy by observing the luminescence peak at 580 nm after the formation of Au NCs **(Figure 2.2a)**; however, the plasmon peak around 520 nm, which is a typical signature of the gold nanoparticles (Au NPs) was not seen in UV-Vis spectroscopy **(Figure 2.2b)**.The control bacteria i.e., without Au NCs synthesis has no peak in the red region, whereas after synthesis of the Au NCs strong luminescence was observed at 580 nm when excited at 320 nm **(Figure 2.2a)**.

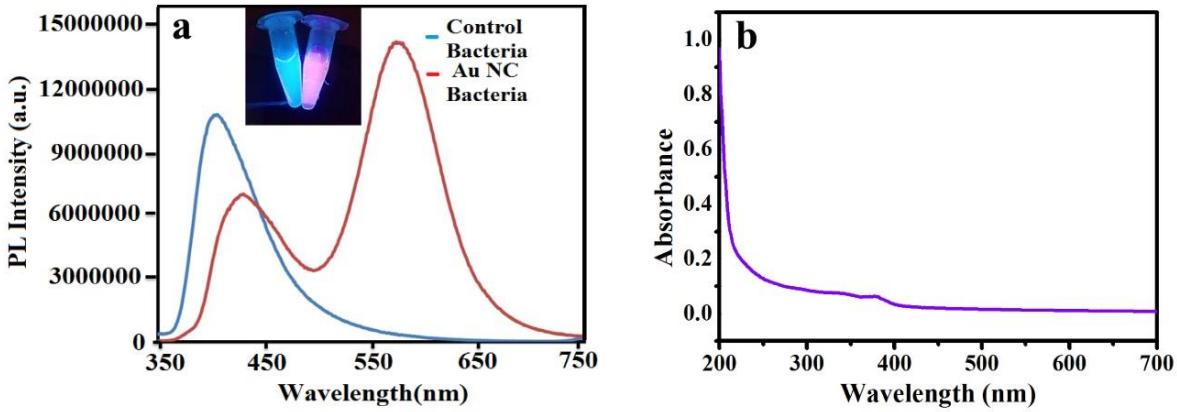

Figure 2.2. (a) Luminescence spectra of control bacterium and Au NCs synthesized on bacterium along with the inset image (b) UV-Vis spectra of Au NCs synthesized on bacterium.

Interestingly, the luminescence intensity gradually increases with bacterial numbers as depicted in **(Figure 2.3)** and the same phenomenon could be visualized in the inset of **(Figure 2.3).** This experiment was

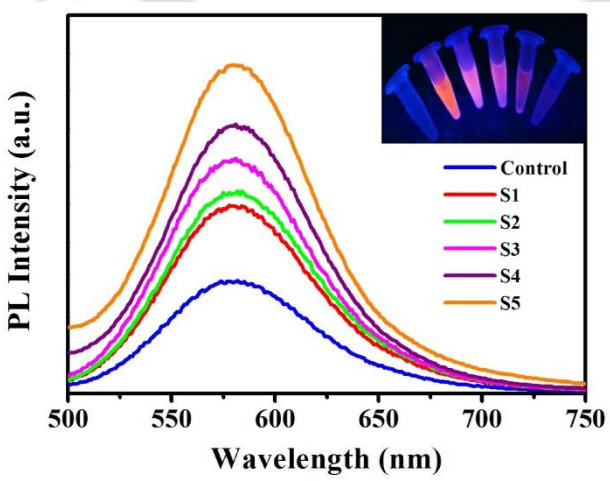

Figure 2.3. (a) Plot of luminescence intensity versus wavelength in the presence of increasing number of bacteria in the medium of synthesis. Control: Au NCs

synthesized (with $HAuCl_4$ and MPA) in absence of bacteria. S1, S2, S2, S4 and S5 correspond to bacterial number in the medium 0.74×10^3, 0.74×10^4, 0.74×10^5, 0.74×10^6 and 1.48×10^6, respectively.

performed with two Gram positive (*Bacillus cereus* MTCC 1305, *Enterococcus faecalis* MTCC 439) and two Gram negative strains (*Escherichia coli* MTCC 433, *Pseudomonas aeruginosa* MTCC 2488), where luminescence increased with the number of bacteria **(Figure 2.4)**.

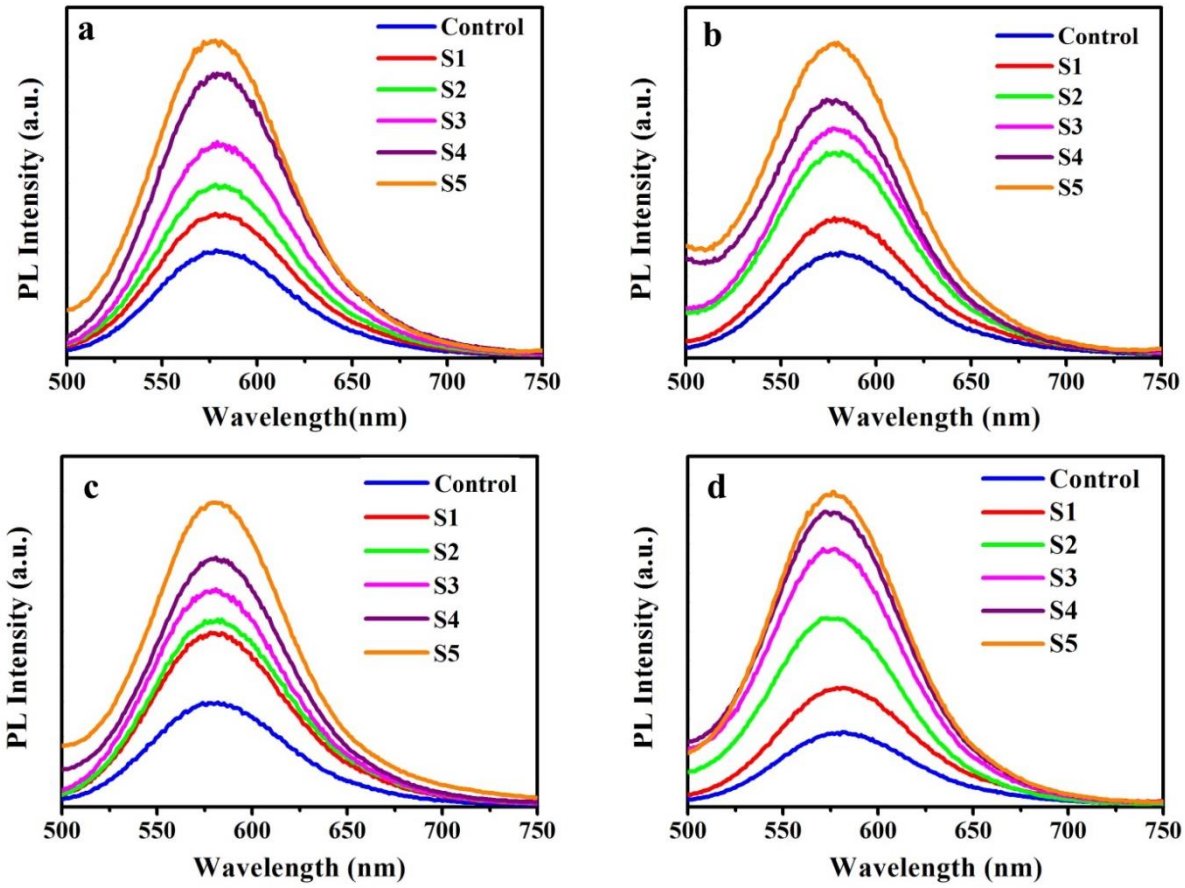

Figure 2.4. Increase in luminescence intensity of Au NCs synthesized on bacteria with increase in number of bacterial cells when excited at 320nm. (a) *Bacillus cereus* MTCC 1305 (b) *Enterococcus faecalis* MTCC 439 (c) *Escherichia coli* MTCC 433 and (d) *Pseudomonas aeruginosa* MTCC 2488.

The luminescence of Au NCs originates from ligand to metal charge transfer where MPA and gold salts forms –S–Au complexes. Also, it may be speculated that attachment of ligand stabilized Au NCs on the bacterial cell wall lead to the restricted motion of the ligands. This might have led to lowering of non-radiative transitions and energy loss thus increasing the

luminescence quantum yield. This observation is consistent with the literature reports of aggregation induced emission enhancement (AIEE) and other such enhancements of photoluminescence.[30,31]Here (MPA) served as the surface passivizing agent for the Au NCs and was responsible for optical and colloidal stability of Au NCs by forming –S–Au bonds. Whereas, bacterial cell wall served as template for the synthesis of Au NCs, possibly interacted with the carboxyl groups (-COOH) of MPA and ultimately produced stable luminescent Au NCs. Hence Au NCs stability was imparted through interactions with the surface proteins of bacterial cell wall. To confirm the formation of Au NCs, X-ray photoelectron spectroscopy (XPS) was performed, which exhibited peaks at 82.62 eV and 86.27 eV corresponding to the Au (4f5/2, 4f7/2) **(Figure2.5)**.

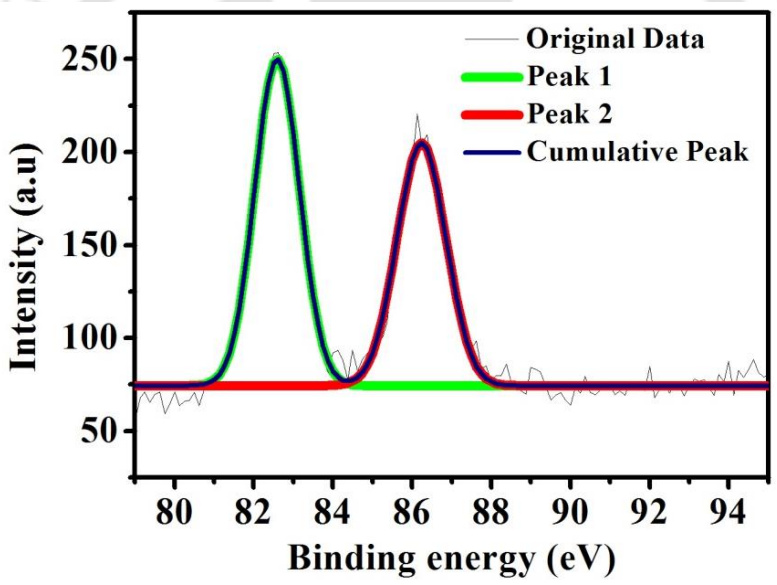

Figure 2.5. XPS spectrum of Au NCs synthesized on *Escherichia coli* MTCC 433.

At the same time matrix assisted laser desorption/ionisation - time of flight (MALDI-TOF) based mass spectrometric measurements (using sinapinic acid as the matrix) analysis of as-synthesized sample revealed suggestive information about formation of Au_{19} and Au_{22} atomic clusters **(Figure 2.6 a-d).** The peaks (m/z) were obtained at 5807, 5788, 5385, 5382, and 6332, which were assigned to 19, 19, 19, 19, 22 atoms of gold, respectively. However, stabilizing ligands were also considered for the calculation of masses, which were calculated to be [Au_{19}+MPA_{19}+3Na-

3H], [Au_{19}+MPA_{18}+7 Na - 8 H], [Au_{19} +MPA_{15}+ 3Na - 4H], [$Au_{19}MPA_{15}$+3Na-3H], and [Au_{22}+ MPA_{19}] respectively. Whereas no such peak was observed in control bacteria **(Figure 2.6 e)**.

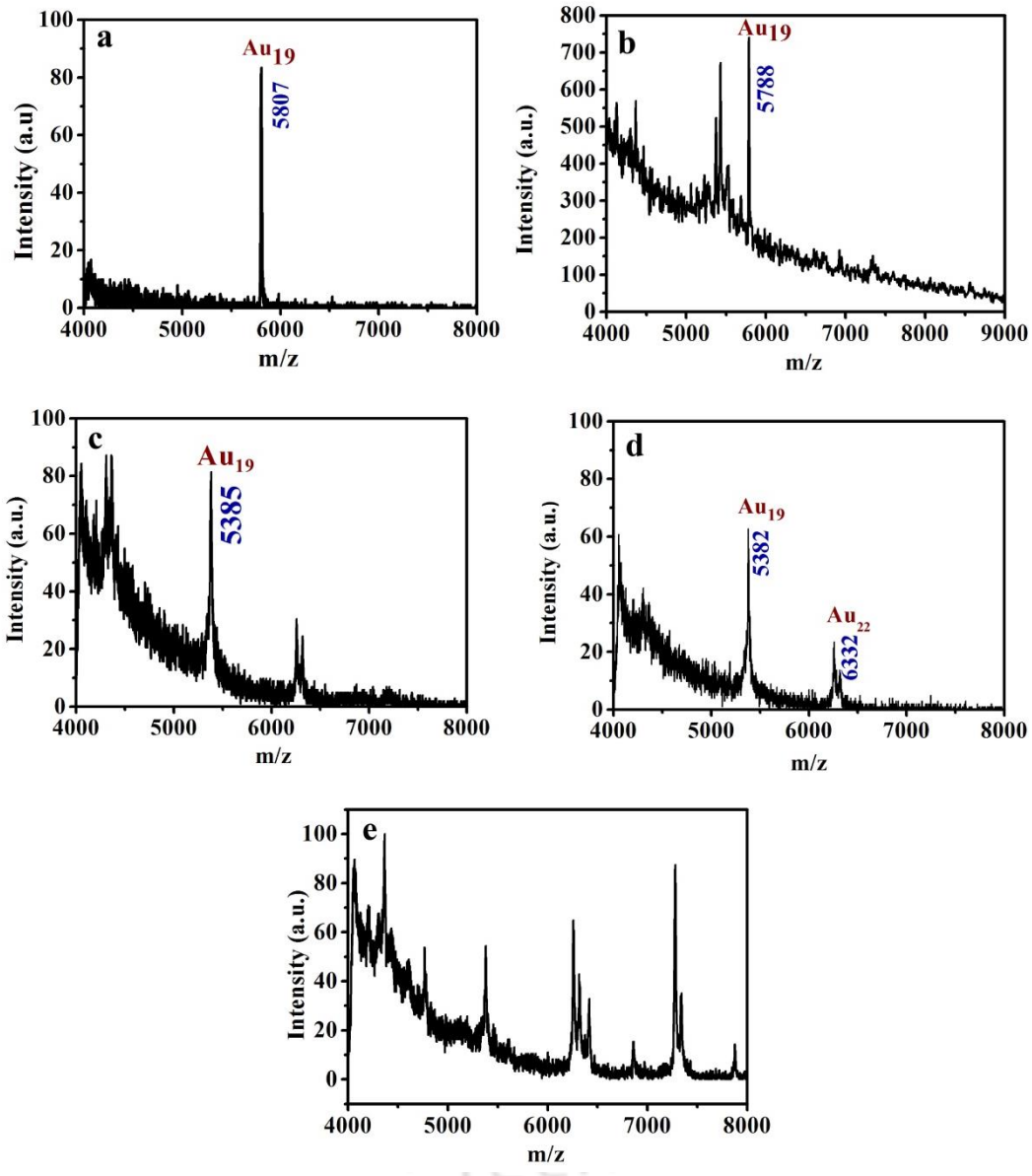

Figure 2.6 MALDI-TOF spectrum of Au NCs synthesized on *Escherichia coli* showing peaks at 5807, 5788 ,5385 , 5382, 6332 which corresponds to 19 and 22 atoms of gold, **(a-d)** Results of the experiments carried out at different times and **(e)** MALDI -TOF MS spectra of control bacteria.

Au NCs formation on bacterial surface was also observed under confocal laser microscopy, where the bright yellow orange luminescence was observed on the surface of bacteria (**Figure 2.7 a**) on exciting it with 405 nm. The bright field image of the same was shown in **(Figure 2.7 b)**.

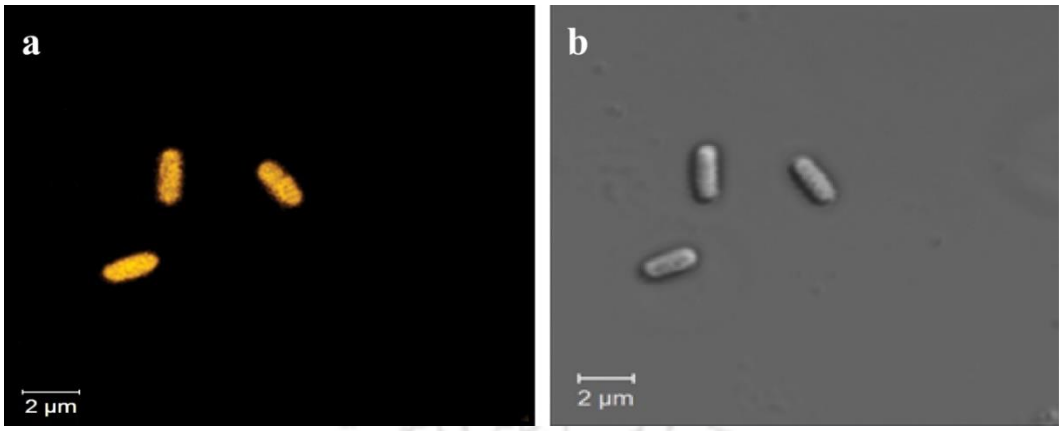

Figure 2.7. (a) CLSM image of Au NCs synthesized on bacterium *Escherichia coli* MTCC 433and **(b)** Bright field image of the same bacterium (i.e., treated with precursors for the synthesis of Au NCs).

TEM image clearly depicted the presence of Au NCs on the bacterial surface **(Figure 2.8 a-c)**. For TEM analysis, as-synthesized bacterial sample was drop cast into the TEM grid after centrifuging at 8,000 rpm for 5 min to remove the unreacted materials and re-dispersed into deionized water. The Au NCs were prominent on the magnified image of the highlighted bacterial surface **(Figure 2.8 b and c)**, while surface of the control bacteria remained clear as illustrated in **(Figure 2.8 e and f)**.

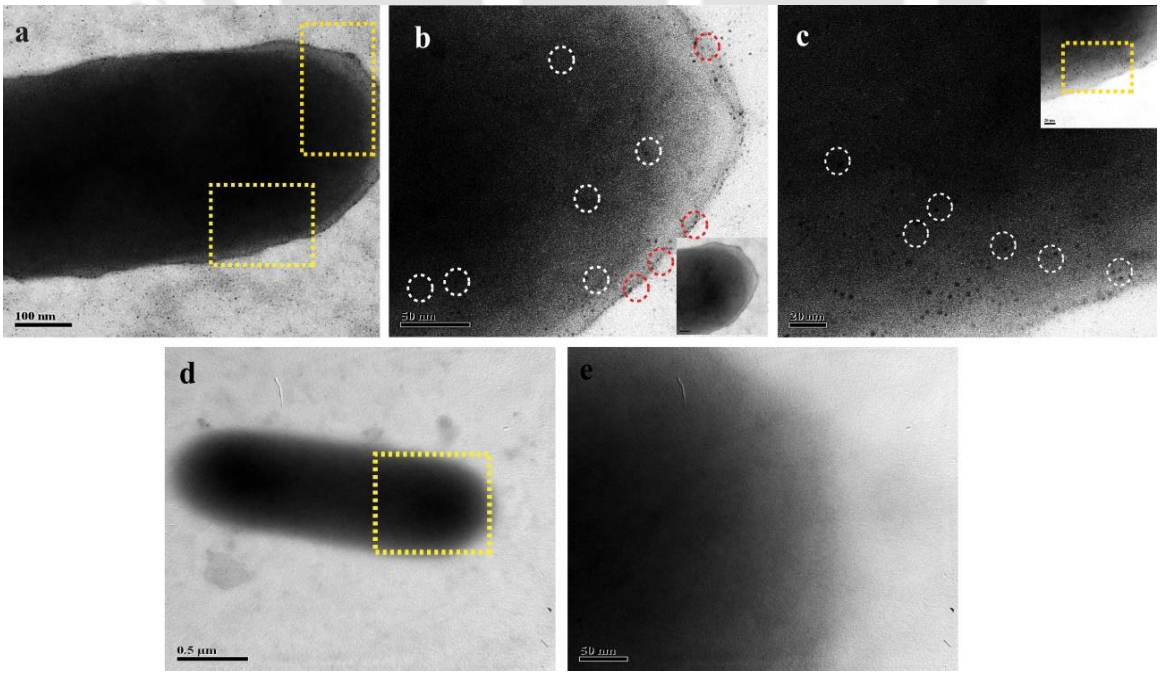

Figure 2.8 TEM images of Au NCs synthesized on a Gram negative (*Escherichia coli*

MTCC 433) bacterium. **(a)** Au NCs synthesized bacterium, the portion to be magnified was marked in yellow. **(b and c)** Magnified image of the same sample clearly showing the formation of the Au NCs on the surface, some of the Au NCs are highlighted by white and red circles. **(d)** TEM image of control Gram negative bacterium (*Escherichia coli* MTCC 433) i.e. without Au NCs synthesis and the portion to be magnified is marked in yellow and **(e)** Magnified image of the same sample.

The magnified TEM image of Au NCs synthesized on bacteria revealed that the average particle size was found to be less than 2nm. The energy dispersive X-ray spectrum (EDX) was also performed during TEM analysis, which confirmed the presence of the metal Au (0) **(Figure 2.9)** on Au NCs synthesized on bacterium. However, the EDX spectrum of control bacterium does not reveal the same **(Figure 2.10)**.

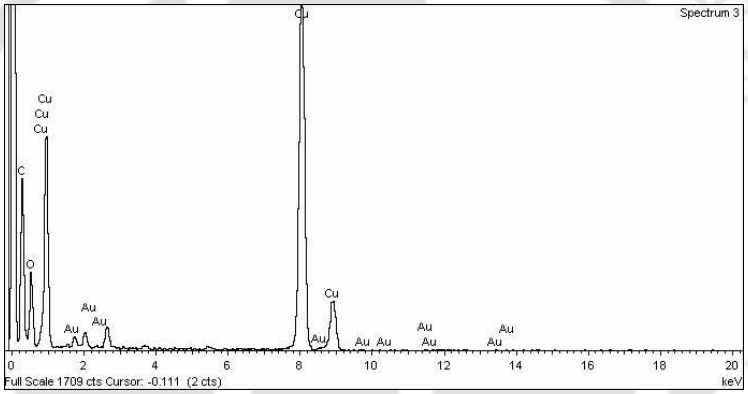

Figure 2.9. EDX of Au NCs synthesized bacterium *Escherichia coli* MTCC 433.

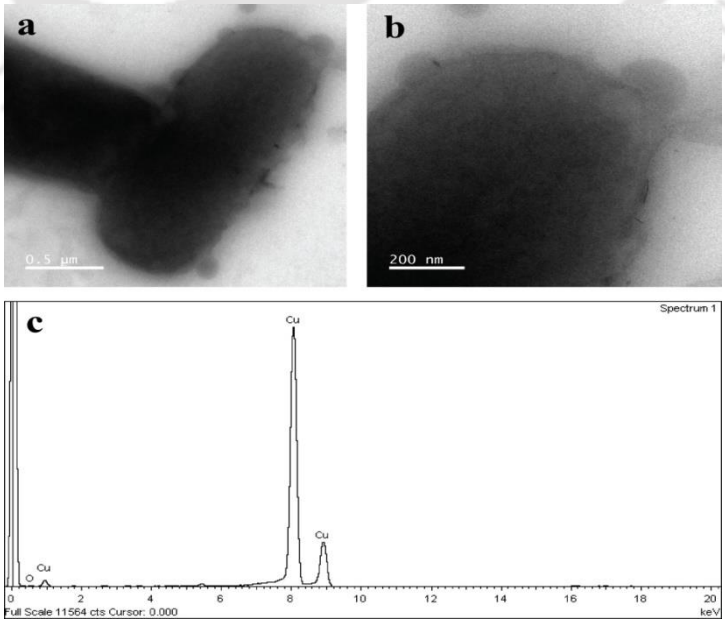

Figure 2.10. (a) TEM image of control *Escherichia coli* (i.e., bacterium without Au NCs). (b) Magnified image of the same bacterium. (c) Energy dispersive X-ray spectrum (EDX) of the same bacterium.

Further to enlighten the role of bacteria for Au NCs synthesis few control experiments were performed. Au NCs produced without bacteria were not stable for longer time. To check the stability of Au NCs without bacteria, time dependent measurements were carried out by probing the luminescence of control Au NCs (without bacteria) and Au NCs synthesized on bacteria. It was found that luminescence of the control significantly declined within 60 min whereas in 60 min there was slight reduction in the luminescence of Au NCs synthesized on bacteria **(Figure 2.11 a and b)**.At the same time luminescence of Au NCs on bacteria was much higher as compared to the control **(Figure 2.11 c)**.

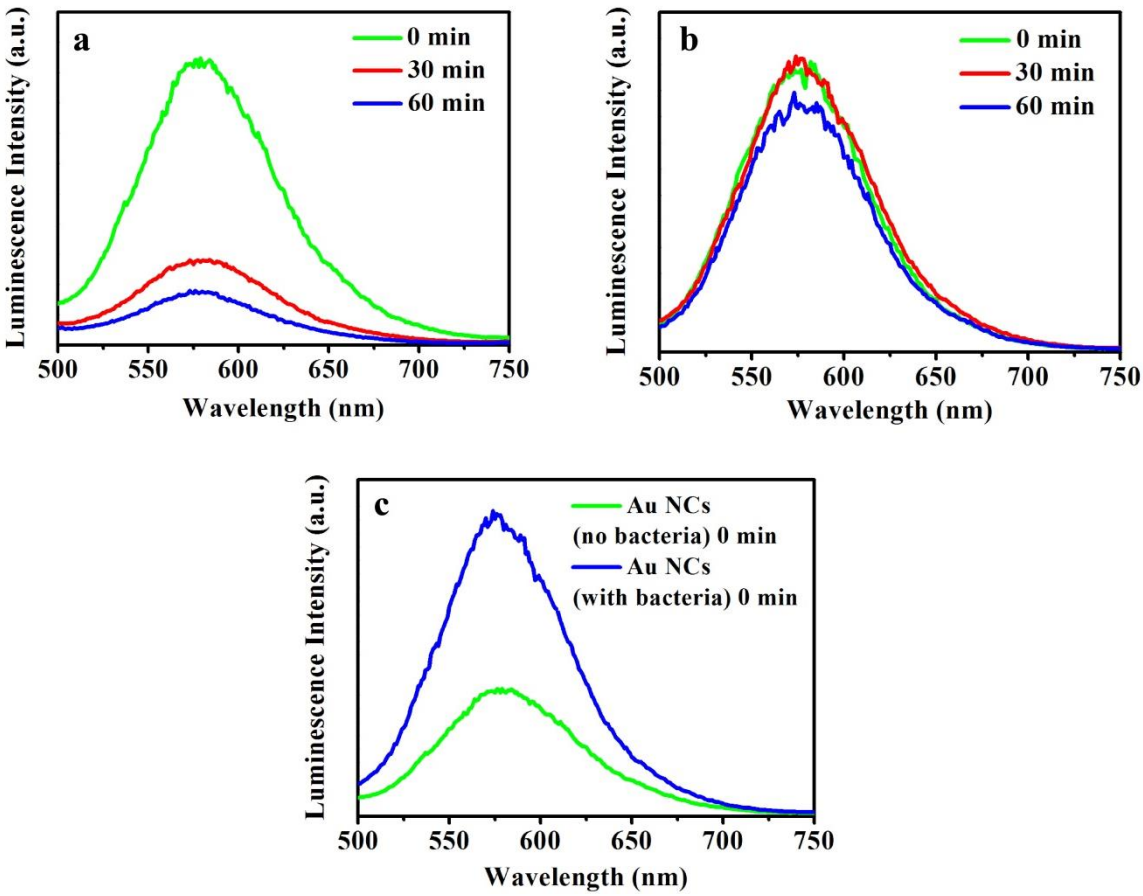

Figure 2.11. (a) Luminescence of control (without bacteria) with precursors of Au NCs ($HAuCl_4$ and MPA) at different time points. (b) Luminescence of Au NCs synthesized on bacteria at different time points. (c) Luminescence of control Au

NCs (without bacteria) and Au NCs synthesized on bacteria at 0 min with same concentration of precursors ($HAuCl_4$ and MPA).

Importantly, emission intensity of Au NCs was found to be gradually augmented with increasing number of both Gram positive and Gram negative bacteria. This offers plausibility to count the number of bacteria present in the test sample. For this purpose, the bacterial strains were grown in the culture media for 12 h. The cells were collected by centrifugation at 6000 rpm for 5 min, and the pellets were re-suspended in water. The Au NCs were synthesized using the same reaction condition by varying the numbers of bacteria and were prepared by serial dilutions (10^2, 10^3, 10^4, 10^5 and 10^6) of the original stock of the bacteria. It was observed that by keeping the concentration of the gold salt and MPA fixed, the emission intensity of the Au NCs increased with the number of the respective bacterial strains while maintaining an identical reaction condition. Since, the emission intensity of the Au NCs varied based on the number of bacteria present in the test sample, thus it was used to correlate with the number of bacteria. The increased luminescence intensity was normalized with respect to the initial value (luminescence intensity of control i.e., MPA and $HAuCl_4$ only) and plotted with Log of CFU/mL of bacteria (where I_f = Final emission intensity I_i = Initial emission intensity) and the linear relationship was observed. The experiments were carried out on two Gram positive bacteria (*Bacillus cereus* MTCC 1305 *Enterococcus faecalis* MTCC 439) and two Gram negative bacteria (*Escherichia coli* MTCC 433 *Pseudomonas aeruginosa* MTCC 2488) (**Figure 2.12 a-d**) .Interestingly, the results revealed that the slope values were different for Gram positive and Gram negative bacteria. The linearity of the plot observed herein, signified that the emission of Au NCs synthesized on the surface of bacteria was directly dependent on the Log number of CFU/mL for respective strains of Gram positive and Gram negative bacteria. The difference in the slope could possibly due to the variation in the cell wall compositions of the Gram positive and Gram negative bacteria, where it might have acted as scaffolds for Au NCs synthesis. To find out the exact number of bacteria, a standard plate count method was followed and the values were obtained after

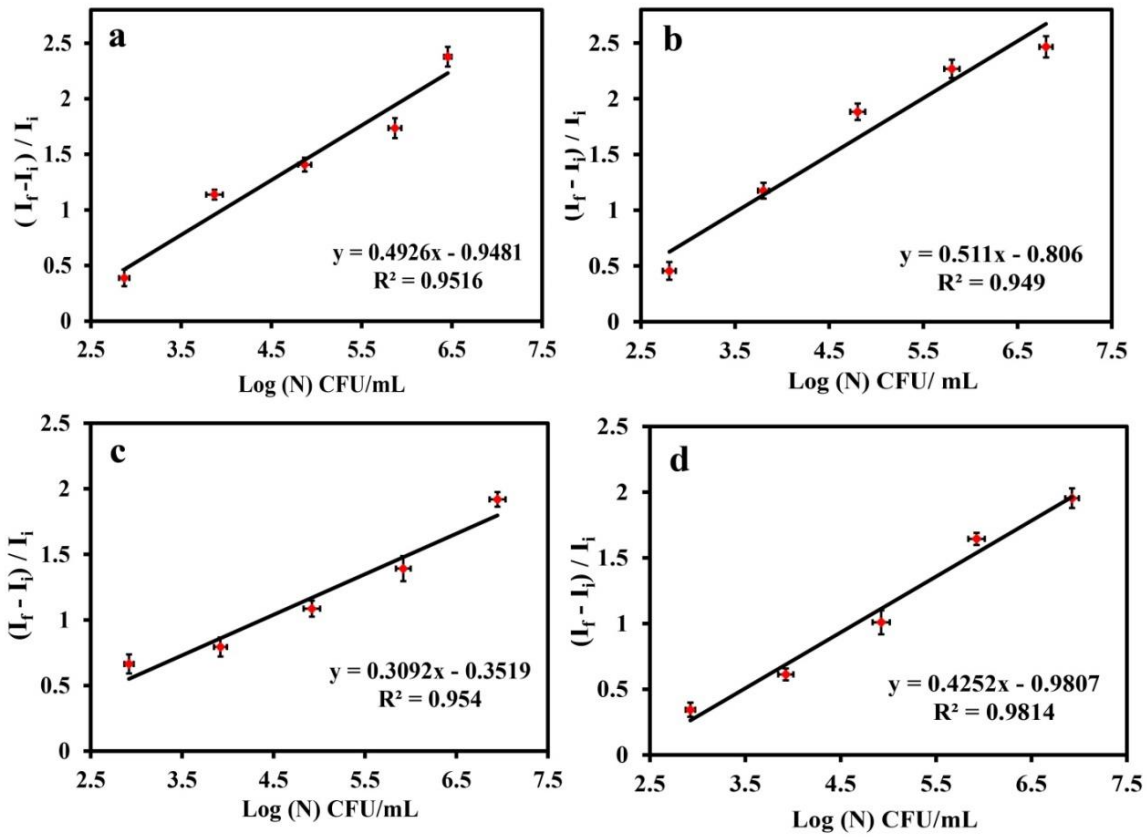

Figure 2.12. Relative increase in the luminescence intensity with log number of bacteria (CFU/mL^{-1}).**(a)** *Bacillus cerius* MTCC 1305, (b) *Enterococcus faecalis* MTCC 439, (c) *Escherichia coli* MTCC 433 and (d) *Pseudomonas aeruginosa* MTCC 2488. Here I_f = final emission intensity and I_i = initial emission intensity. Data are represented by taking average ± SD of three individual experiments.

multiplication with the corresponding dilution factors. For this the same amount of bacteria (by following serial dilution method) used for Au NCs synthesis were grown in the agar plate to find out the exact number of bacteria (CFU/mL). The average limit of detection (LOD) was found to be 634 ±16 and 740 ±14 CFU/mL, for Gram positive and Gram negative bacteria respectively. The quantum yield of Au NCs synthesized on bacteria was found to be 1.6% **(Figure 2.13)**. Thus, the interaction between the clusters and the functional groups on bacterial surface was evident to correlate the luminescence intensity of bacteria and finally, validates the direct relation of PL enhancement with number of bacteria used for Au NCs synthesis. Further, the restriction of the motion of the stabilizing ligand,

upon binding with the cell wall, might have prevented the loss of energy into non-radiative pathways and enhancing the luminescence quantum yield.

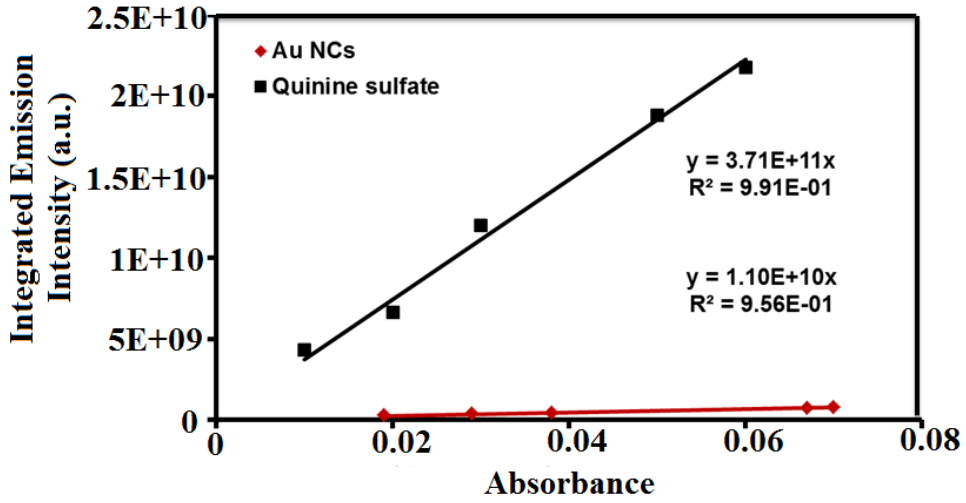

Figure 2.13. Quantum yield of Au NCs synthesized on bacteria.

The outer layer of the cell walls of both Gram positive and Gram negative bacteria contains peptidoglycan, though the thickness is significantly higher in Gram positive than the outer membrane (OM) of Gram negative bacteria. It has been reported that phosphoryl group present in the linkage unit along with two sugars of teichoic acid are covalently linked with the sugars of peptidoglycan layer, which are the active cation binding sites. In contrast Gram negative bacteria have an extra outer membrane along with peptidoglycan layer, which contains phospholipids, lipoproteins, lipopolysaccharides and proteins, where phosphoryl groups are present in phospholipids in the same fashion as teichoic acid. Negative charge of the cell wall could play a major role in metal adsorption, as reported by the molecular stimulation techniques.[32]

Additionally, the intrinsic properties of bacterial cell wall composition were investigated to distinguish between the Gram positive and the Gram negative strains. It is evident from TEM images that primarily outer layer i.e., peptidoglycan of the cell wall was serving as scaffold for the Au NCs, which can be tuned for bacterial strain selectivity. Thus the role of bacterial cell wall in the stabilization of Au NCs, both Gram positive and Gram

negative bacteria were treated with lysozyme (1 mg/mL) for various time periods (0, 20 and 30 min). It is to be noted here that lysozyme used here is only to degrade the cell wall of bacteria, [33] which had been removed from the medium following treatment. Thereafter, the cells were collected, washed with PBS and were used as templates for Au NC synthesis maintaining the same reaction condition and precursors (i.e., $HAuCl_4$ and MPA). The results revealed that the emission intensity of Au NCs synthesized after lysozyme treatment in case of Gram positive bacteria was low as compared to that of lysozyme treated-Gram negative bacteria at both the time points, indicating the possibility of the role of bacterial cell wall as a scaffold for Au NCs (**Figure 2.14**). It is well-known that both Gram positive and Gram negative bacteria have peptidoglycan as cell wall components; however, its thickness is different in Gram positive than Gram negative bacteria. Gram positive bacteria have thick peptidoglycan layer, which is known to be sensitive towards lysozyme.[33] Whereas, Gram negative bacteria have two layered wall structures with thinner peptidoglycan layer, which is covered by outer membrane comprising of phospholipids, lipoproteins, lipopolysaccharides, proteins and thus is prevented or less affected by lysozyme action. Hence, on lysozyme treatment, the cell wall of Gram positive bacteria degraded fast and therefore the luminescence of the product Au NCs was less in comparison to that of Au NCs formed in the presence of lysozyme-treated Gram negative bacteria. Thus the method offered the scope of distinguishing Gram positive and Gram negative bacteria based on the luminescence of Au NCs. Here, the control stands for Au NCs synthesis on Gram positive and Gram negative bacteria without treatment with lysozyme, which has been converted to 100% for comparison with the treated groups (lysozyme treatment at two time points), respectively.

At the same time the current method was employed to test the presence of bacteria (bacterial contaminants) in water for its practicability. Water from three different sources, namely, laboratory waste water, river

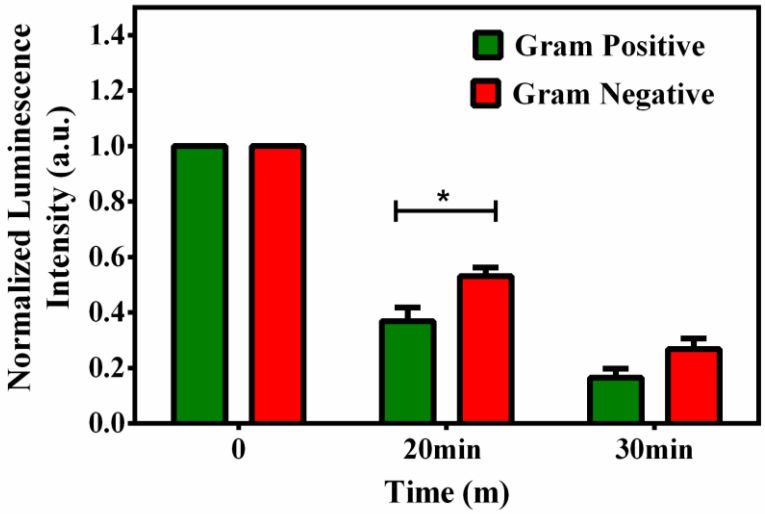

Figure 2.14. (a) Luminescence intensity of Au NCs synthesized after lysozyme treatment on both Gram positive (*Bacillus cereus*) and Gram negative (*Escherichia coli*) bacteria at different time interval (0, 20 and 30 min).

water, and pond water, along with a control group (i.e. Milli-Q grade water), were collected. To detect bacteria in water samples, Au NCs were synthesized as mentioned earlier using water from different sources. The luminescence peak was observed with all the water samples except in the control group **(Figure 2.15)**. Subsequently, the presence of bacteria was confirmed by agar plate colony count method, where no colonies were observed with Milli-Q water and the highest numbers of colonies were found in the laboratory waste water, as the number of bacteria was highest in that case. Thus, the probe for bacterial detection i.e. the luminescence property of Au NCs synthesized on bacteria is directly proportional to number of bacteria in the system.

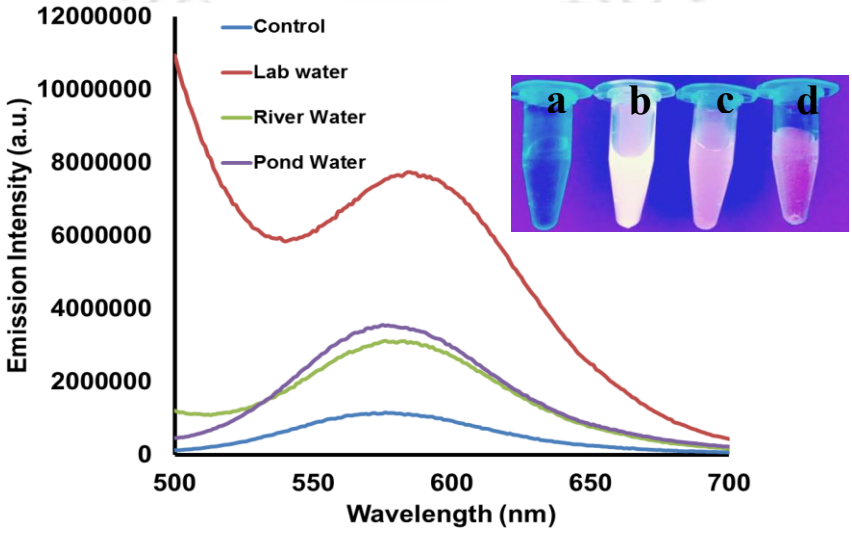

Figure 2.15. Luminescence spectra of bacteria in four different water samples i.e. control (Milli-Q water), lab waste water, river water, pond water.

Further, the luminescence of Au NCs on bacteria was explored to find out the antibiotic resistant strains as well. To circumvent the threat of antibiotic resistance bacteria via early detection, the current method was used to find out the antibiotic resistant strain based on the luminescence intensity of Au NCs synthesized on bacteria. It is to be noted here that mostly antibiotic discs were used to find out antibiotic resistant strains which takes 10-12 h to form colonies. For this application pet-28a (DH5-α), pEGFP-N1 (DH5-α) which are kanamycin antibiotic resistant strains and Gram positive *Bacillus cereus* MTCC 1305 and Gram negative *Escherichia coli* MTCC 433 bacteria non-kanamycin resistant, were chosen. First the respective strains of bacteria (5×10^6) with kanamycin (10 µL of 50 mg/mL) and then at different time points (0, 3, 6, 9 and 12 h) bacteria were collected by centrifugation, which was followed by Au NCs synthesis. Remarkably, after 6 h significant difference in the emission of Au NCs was observed in case of kanamycin resistant strains (pet-28a and pEGFP-N1) in comparison to the non-kanamycin-resistant strains (**Figure 2.16**). This is mainly because kanamycin inhibits the growth of non-resistant bacteria (Gram positive *Bacillus cereus* MTCC 1305 and Gram negative *Escherichia coli* MTCC 433) whereas resistant strains grow with time. As already mentioned

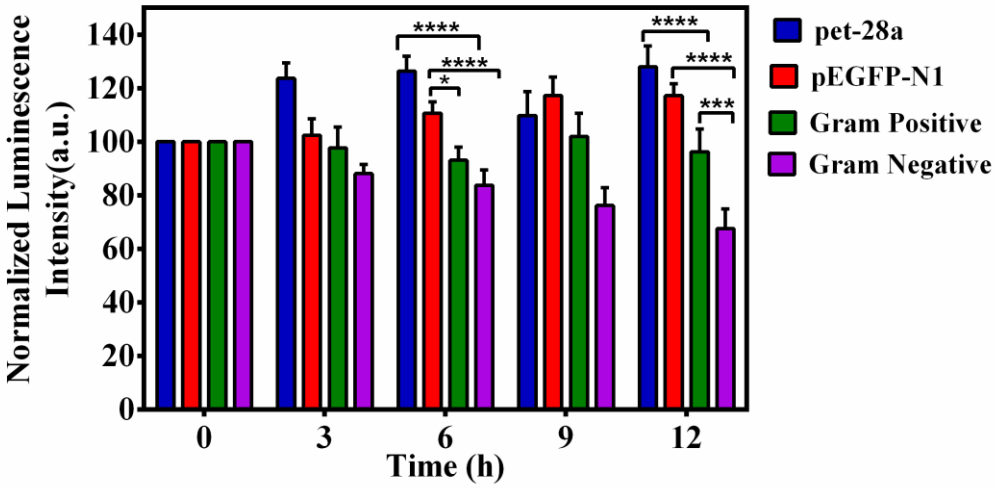

Figure 2.16. Normalized luminescence intensity of Au NCs synthesized on different strains of bacteria. Pet-28a and pEGFP-N1 are antibiotic (kanamycin)

resistant strain and Gram positive (*Bacillus cereus* MTCC 1305*)* and Gram negative (*Escherichia coli* MTCC 433) are wild strains. Plot was generated by average ± SD of three individual experiments. The ANOVA test revealed the statistical significance, which is represented by '*' ($p < 0.05$), '***' ($p < 0.001$), and '****' ($p < 0.0001$).

before, the linearity of the plots indicated that the emission of Au NCs synthesized directly depended on the Log number of CFU/mL of bacteria. Hence, the current method can be employed to find out kanamycin resistant strains within 6 h based on Au NCs synthesized on bacterial surface where emission of Au NCs is directly proportional to number of bacteria. Hence, the overall time for detection has been drastically reduced as Au NCs synthesis was possible at all the respective time points while growing the bacteria. Therefore, the luminescence of Au NCs was useful for detection of bacteria in a very short time, while normally bacterial detection needs at least 12 h for its growth followed by different procedures of detection. At the same time, cellular cytotoxicity of the Au NCs synthesized on bacteria was also checked following incubation with HEK-293 cells for 24 h and was found to be non-toxic **(Figure 2.17)**.

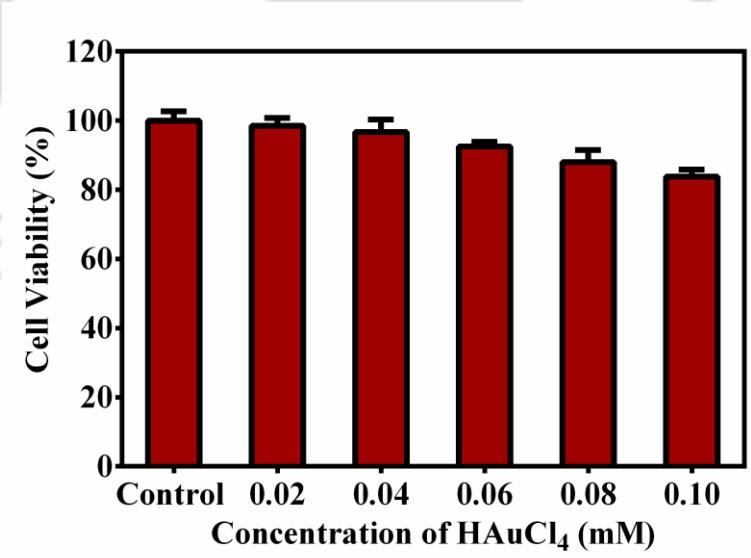

Figure 2.17. MTT assay of Au NCs synthesized on bacteria (at various concentrations) on HEK-293 cells performed following incubation for 24 h.

The AFM analysis was also performed to monitor the structural changes on the surface of bacteria (Gram negative *Escherichia coli* MTCC 433). It has been found that the bacterial surface was rough and indented after

synthesis of Au NCs, as compared to the control bacteria (**Figure 2.18 a and b**). The surface roughness and indentation of the bacteria after Au NCs synthesis were quantified using Gwiyddion software analysis **(Table A2.1, Appendix)**.

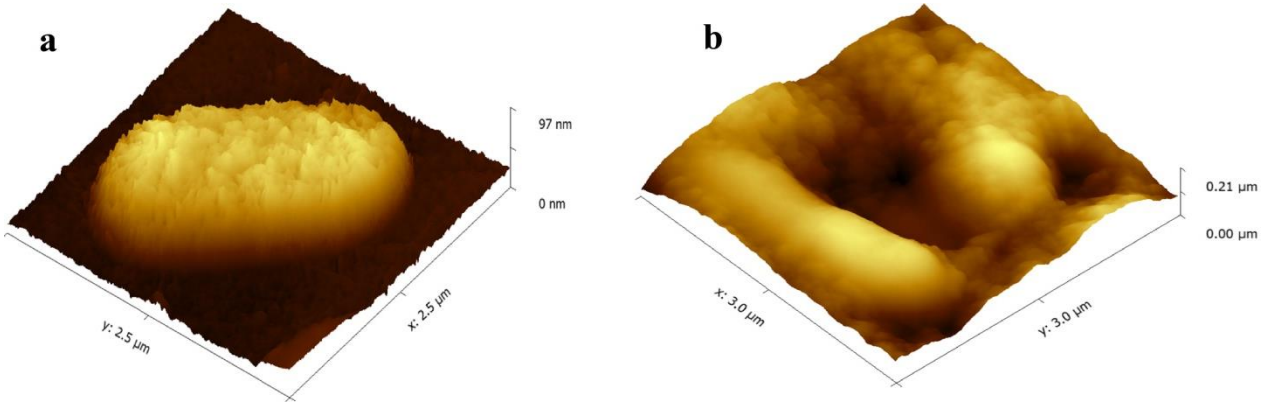

Figure 2.18. AFM image of **(a)** Au NCs synthesized bacteria and **(b)** Control bacteria.

2.6 Conclusions

In summary, a new method of synthesis of Au NCs using bacteria as template has been developed. The luminescence property of the as-synthesized Au NCs was probed for bacterial detection and counting. This method was applied to analyse bacterial contamination in water from various sources. Furthermore, the method distinguished between kanamycin resistant bacterial strains using fluorescence of Au NCs on the bacteria. The major advantage of this method is to detect bacteria with in short time as direct synthesis on bacteria can be used for detection as opposed to available routine detection techniques. Thus, the current method is a new, easy, rapid, non-toxic and possibly low cost approach for detection, enumeration of Gram positive and Gram negative, kanamycin resistant strains and bacterial contamination in water sources.

2.7 References

1. Chung, H. J.; Castro, C. M.; Im, H.; Lee, H.; Weissleder, R. *Nat. Nanotechnol.* **2013**, *8* (5), 369–375.

2. Adzitey, F.; Huda, N.; Ali, G. R. R. *3 Biotech* **2013**, *3* (2), 97–107.

3. Noble, R. T. *J Water Health.* **2005**, *3* (4), 381–392.

4. Gopinath, S. C. B.; Tang, T.-H.; Chen, Y.; Citartan, M.; Lakshmipriya, T. *Biosens. Bioelectron*. **2014**, *60*, 332–342.

5. Anhalt, J. P.; Fenselau, C. *Anal. Chem*. **1975**, *47* (2), 219–225.

6. Delehanty, J. B.; Ligler, F. S. *Anal. Chem.* **2002**, *74* (21), 5681–5687.

7. Magliulo, M.; Simoni, P.; Guardigli, M.; Michelini, E.; Luciani, M.; Lelli, R.; Roda, A. *J. Agric. Food Chem.* **2007**, *55* (13), 4933–4939.

8. Khan, S.; Sallum, U. W.; Zheng, X.; Nau, G. J.; Hasan, T. Rapid Optical Determination of β-Lactamase and Antibiotic Activity. *BMC Microbiol.* **2014**, *14* (1), 84.

9. Macia, M. D.; Borrell, N.; Perez, J. L.; Oliver, A. *Antimicrob. Agents Chemother*. **2004**, *48* (7), 2665–2672.

10. Ray, P. C.; Khan, S. A.; Singh, A. K.; Senapati, D.; Fan, Z. *Chem. Soc. Rev.* **2012**, *41* (8), 3193.

11. Disney, M. D.; Zheng, J.; Swager, T. M.; Seeberger, P. H. *J. Am. Chem. Soc.* **2004**, *126* (41), 13343–13346.

12. Chen, W.; Li, Q.; Zheng, W.; Hu, F.; Zhang, G.; Wang, Z.; Zhang, D.; Jiang, X. *Angew. Chem. Int. Ed.* **2014**, *53* (50), 13734–13739.

13. Phillips, R. L.; Miranda, O. R.; You, C.-C.; Rotello, V. M.; Bunz, U. H. F. *Angew. Chem. Int. Ed.* **2008**, *47* (14), 2590–2594.

14. Miranda, O. R.; Li, X.; Garcia-Gonzalez, L.; Zhu, Z.-J.; Yan, B.; Bunz, U. H. F.; Rotello, V. M. *J. Am. Chem. Soc.* **2011**, *133* (25), 9650–9653.

15. Hayden, S. C.; Zhao, G.; Saha, K.; Phillips, R. L.; Li, X.; Miranda, O. R.; Rotello, V. M.; El-Sayed, M. A.; Schmidt-Krey, I.; Bunz, U. H. F. *J. Am. Chem. Soc.* **2012**, *134* (16), 6920–6923.

16. Zhao, X.; Hilliard, L. R.; Mechery, S. J.; Wang, Y.; Bagwe, R. P.; Jin, S.; Tan, W. *Proc. Natl. Acad. Sci. U.S.A.* **2004**, *101* (42), 15027–15032.

17. Shen, H.; Wang, J.; Liu, H.; Li, Z.; Jiang, F.; Wang, F.B and Yuan,Q. *ACS Appl. Mater. Interfaces* **2016**, *8*, 19371–19378.

18. Tseng, Y.-T.; Chang, H.-T.; Chen, C.-T.; Chen, C.-H.; Huang, C.-C. *Biosens. Bioelectron.* **2011**, *27* (1), 95–100.

19. Sahoo, A. K.; Sharma, S.; Chattopadhyay, A.; Ghosh, S. S. *Nanoscale* **2012**, *4* (5), 1688.

20. Wu, S.; Duan, N.; Shi, Z.; Fang, C.; Wang, Z. *Anal. Chem* .**2014**, *86* (6), 3100–3107.

21. Wang, H.-H.; Lin, C.-A. J.; Lee, C.-H.; Lin, Y.-C.; Tseng, Y.-M.; Hsieh, C.-L.; Chen, C.-H.; Tsai, C.-H.; Hsieh, C.-T.; Shen, J.-L.; Chan, W.-H.; Chang, W. H.; Yeh, H.-I. *ACS Nano* **2011**, *5* (6), 4337–4344.

22. Couleaud, P.; Adan-Bermudez, S.; Aires, A.; Mejías, S. H.; Sot, B.; Somoza, A.; Cortajarena, A. L. *Biomacromolecules* **2015**, *16* (12), 3836–3844.

23. Yang, J.; Xia, N.; Wang, X.; Liu, X.; Xu, A.; Wu, Z.; Luo, Z. *Nanoscale* **2015**, *7* (44), 18464–18470.

24. Yuan, Z.; Chen, Y.-C.; Li, H.-W.; Chang, H.-T. *Chem. Commun.* **2014**, *50* (69), 9800.

25. Wang, J.; Zhang, G.; Li, Q.; Jiang, H.; Liu, C.; Amatore, C.; Wang, X. *Sci. Rep.* **2013**, *3*.

26. Ding, H.; Li, H.; Liu, P.; Hiltunen, J. K.; Wu, Y.; Chen, Z.; Shen, J. *MicrochimicaActa* **2014**, *181* (9-10), 1029–1034.

27. Chan, P.-H.; Ghosh, B.; Lai, H.-Z.; Peng, H.-L.; Mong, K. K. T.; Chen, Y.-C. *PLoS ONE* **2013**, *8* (3), e58064.

28. Mukherji, R.; Samanta, A.; Illathvalappil, R.; Chowdhury, S.; Prabhune, A.; Devi, R. N. *ACS Appl. Mater. Interfaces* **2013**, *5* (24), 13076–13081.

29. Goswami, U.; Basu, S.; Paul, A.; Ghosh, S. S.; Chattopadhyay, A. *J. Mater.Chem. C* **2017**, *5*, 12360–1236.

30. Ren, Y.; Lam, J. W. Y.; Dong, Y.; Tang, B. Z.; Wong, K. S. *J. Phys. Chem. B* **2005**, *109* (3), 1135–1140.

31. Leung, N. L. C.; Xie, N.; Yuan, W.; Liu, Y.; Wu, Q.; Peng, Q.; Miao, Q.; Lam, J. W. Y.; Tang, B. Z. *Chem. Eur. J.* **2014**, *20* (47), 15349–15353.

32. Johnson, K. J.; Cygan, R. T.; Fein, J. B. *Geochim. Cosmochim. Acta* **2006**, *70* (20), 5075–5088.

33. Salazar, O.; Asenjo, J. A. *Biotechnol. Lett.* **2007**, *29* (7), 985–994.

Appendix of Chapter- 2: A2

Table S1. Surface roughness and indentation of statistics of control bacteria and bacteria after Au NCs synthesis quantified using Gwiddion software analysis.

Statistical Quantities of Control
File: D:\NEW\Controlled 433_00006.gwy
Data channel: Topography
Selected area: 512 × 512 at (0, 0) px
2.500 × 2.500 at (0.000, 0.000) µm
Mask in use: No
Minimum: 0.000 nm
Maximum: 97.177 nm
Average value: 37.644 nm
Median: 21.206 nm
Ra (Sa): 24.024 nm
Rms (Sq): 26.386 nm
Rms (grain-wise): 26.386 nm
Skew: 0.6956
Kurtosis: -1.223
Surface area: 6.589594 µm^2
Projected area: 6.250000 µm^2
Variation: 1.5874 µm^2
Entropy: -16.806
Entropy deficit: 0.77403
Inclination θ: 0.14 deg
Inclination φ: 80.17 deg

Statistical Quantities of treated
File: D:\NEW\bac_00003_1_2d.tif
Data channel: Detail 4
Selected area: 309 × 309 at (0, 0) px
3.018 × 3.018 at (0.000, 0.000) µm
Mask in use: No
Minimum: 0.00 nm
Maximum: 208.00 nm
Average value: 113.82 nm
Median: 113.89 nm
Ra (Sa): 34.56 nm
Rms (Sq): 41.44 nm
Rms (grain-wise): 41.44 nm
Skew: -0.06817
Kurtosis: -0.7388
Surface area: 9.410890 µm^2
Projected area: 9.105778 µm^2
Variation: 2.0591 µm^2
Entropy: -15.619
Entropy deficit: 0.038534
Inclination θ: 0.44 deg
Inclination φ: -91.88 deg

Chapter-3

White Light Emission from Gold Nanoclusters Embedded Bacteria

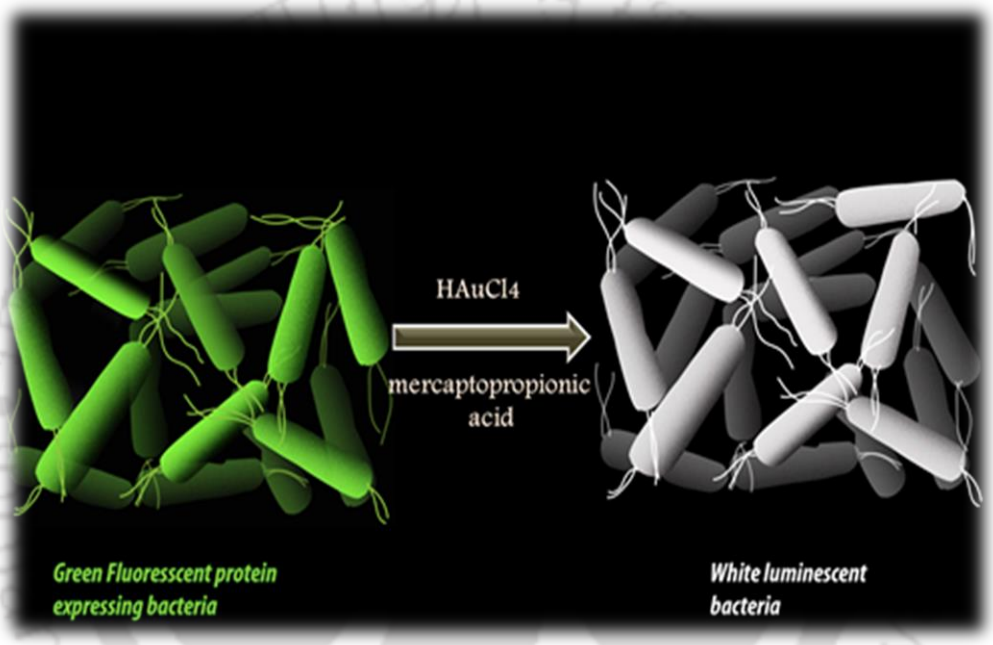

In Chapter 3, *the unprecedented synthesis of gold nanoclusters using green fluorescent protein (GFP)-expressing bacteria as the stabilizer has been reported. Combining the blue and green fluorescence of GFP-expressing bacteria and orange luminescence of the nanoclusters, white light emission associated with appreciable quantum yield, colour rendering index and correlated colour temperature was achieved.*

http://pubs.rsc.org/en/content/articlelanding/2017/tc/c7tc04554a#!div

Chapter 3

3.1. Introduction

With increasing global consumption, energy-demanding conventional incandescent lights are being phased out in favour of devices utilizing more efficient advanced light-emitting materials.[1–4] For example, current stress on the development of luminescent quantum dots, carbon dots and metal atom based nanoclusters (NCs) as potent light-emitting nanoscale materials is driven by achievable high emission/quantum efficiency, and control over chromaticity, color rendering indices and correlated color temperature. In this regard, white light-emitting (WLE) materials providing energy efficiency are an area of research where new ideas could make a potential difference to the technology and devices.[5–7] The importance of white light-emitting materials lies in their potential as the chief component in displays and light-emitting devices (LEDs).[8] A general strategy that has been widely employed to achieve white light emission is ''mixing'' of red, green and blue light-emitting components, which eventually suffers from an inherent limitation of distortion in color chromaticity, self-absorption and color ageing.[9]

A way out of this limitation could be based on the development of multi-component (primarily inorganic) composite materials, which would emit white light as a combination of base colors from the components. This may not only improve the efficiency, but also would lead to devices with high spatial resolutions. For example, if inorganic nanocrystals (such as ZnS) could be surface functionalized with inorganic complexes – in addition to being doped with cations such as Mn^{2+} – the overall emission from the single nanoparticle could be white light.[10] In addition, the color and other indices could be tuned not only based on the dopants but also on the concentration and nature of complex (es) present on the surface. On the other hand, organic nanomaterial based white light-emitting sources such as carbon quantum dots and graphene are also under focus for development.[11] Moreover, single organic molecules have been recently reported

to emit white light based on fundamental principles like aggregation-induced emission.[12] Excited state intermolecular proton transfer (ESIPT) has also emerged as an effective strategy for white light emission from a single fluorophore.[13]

Recent interests in luminescent bacterial species have heralded important advancements in understanding the molecular mechanisms of living systems. For example, photoluminescent green, yellow and red fluorescent proteins expressed in bacteria, cells and even in animals have contributed greatly as probes for cellular events.[14] Interestingly, bioluminescent bacteria have recently been used to illuminate the streets of Paris as a demonstration of futuristic sustainable lighting.[15] This has been achieved by filling up transparent cases with bacteria along with their means of survival i.e., sugar and oxygen. The commercial success of this endeavour would further provide impetus to establishing ''bio lights'' as an alternative to traditional means of light emission. At the same time, these luminescent bacteria can be utilized for establishing the mechanism of drug delivery. For the ease of synthesis and environmental friendliness, biosynthesis of such emitters may be the best way forward. On the other hand, for stability and ease of tunability of color indices, inorganic components may be essential.

Luminescent atomic clusters – especially of noble metals –could be of great significance with regard to generation of light. Their size, by dint of being in the range of the Fermi wavelength of electrons, confers them with quantized energy levels, which depend on the number of constituent atoms.[16] Using colloidal chemistry routes, these clusters could easily be synthesized – with uniform size – in a liquid medium. The luminescent properties of the clusters could be modified using appropriate stabilizing ligands during synthesis or by the formation of an assembly.[17] Importantly, while there have been a growing number of reports on their utility as probes for sensing and assays, focus on their usage as potent light-emitting materials is yet to begin. In this regard, generation of white light-emitting materials would be of great interest. It may be remarkable if the light-emitting materials could be obtained using biochemical routes involving prokaryotic cells, which are rather easy to culture in the laboratory. This is even more appropriate, given the abundance of proteins present on the bacterial cell wall, which are not

only useful for stabilizing luminescent atomic clusters, but also likely to contribute to the overall luminescence through their blue emissions.

3.2. Outline of the Present Work

Herein, the synthesis of gold nanoclusters (Au NCs) on the cell wall of green fluorescent protein (GFP)-expressing bacteria leading to efficient white light emission has been reported. The blue and green emission from GFP-expressing bacteria in combination with orange luminescence from the synthesized Au NCs on the former led to an overall white luminescence from the bacterial cell (upon excitation at 320 nm) with near-to-perfect chromaticity coordinates of white light and appreciable quantum yield. Additionally, confocal laser scanning microscopy (CLSM) investigations revealed that white light emission from a single bacterium could be observed following the synthesis of NCs.

3.3. Experimental Section

3.3.1. Materials

Tetrachloroauric acid (17 wt. % solution of $HAuCl_4$ in dilute HCl; 99.99%) and 3-mercaptopropionic acid were purchased from Sigma-Aldrich Chemicals, U.S.A. Growth media for different bacteria i.e. nutrient broth (NB) for *Bacillus cereus* MTCC 1305, brain–heart infusion (BHI) for *Enterococcus faecalis* MTCC 439 and Luria-Bertani broth (LB) for GFP and *Escherichia coli* MTCC 433 were procured from Hi Media, Mumbai, India. Milli-Q grade water (>18 MΩ cm−1, Millipore) water was used for all the experiments.

3.3.2. Bacterial Strains

The generation of white light has been achieved with two Gram negative and two Gram positive bacteria. Gram negative bacteria *Escherichia coli* MTCC 433 and GFP-expressing *Escherichia coli* were grown in Luria-Bertani broth (LB) under ambient condition (37°C at 220 rpm for 12 h). Whereas Gram positive *Bacillus cereus* MTCC 1305 and *Enterococcus faecalis* MTCC 439 bacteria were grown in nutrient broth (NB) and brain heart infusion Broth (BHI) media respectively under similar conditions.

3.3.3. Synthesis of Au NCs on Bacteria

The dispersion containing bacteria (grown overnight) were centrifuged at 10,000 rpm for 2 min. The so obtained pellet was washed with de-ionized water and redispersed in water. The dispersed bacteria were serially diluted to obtain bacterial concentrations of 2×10^6, 10^6,10^5 and 10^4. In order to synthesise Au NCs on bacterial template, 18µL $HAuCl_4$ (10 mM) and 6µL of 0.11M MPA were added to a dispersion containing bacteria. The pH of the dispersion was maintained at ~7. Following thorough mixing, the dispersion was kept at 37 °C for 5 min and was cooled thereafter. The dispersion obtained herein was luminescent upon excitation at 320 nm. The luminescent dispersion was centrifuged at a speed of 10,000 rpm for 2 min. The pellet following repeated washing was thereafter redispersed in water and was used for further experiments.

3.3.4. Calculation of quantum yield

The quantum yield of white luminescent bacteria was calculated with reference to quinine sulphate in 0.1 M H_2SO_4. The following equation has been employed to calculate the quantum yield of white luminescent GFP-expressing bacteria:

$$Q_{Bac} = Q_{Ref} \times (I_{bac}/I_{Ref}) \times (A_{Ref}/A_{Bac}) \times (n^2_{Bac}/ n^2_{Ref})$$

Here, Q_{Bac}= Quantum yield of Au NCs synthesised on GFP-expressing bacteria;

Q_{Ref} = Quantum yield of quinine sulphate. It has been reported as 0.54

I_{Bac}= Area under photoluminescence curve of Au NCs synthesised on GFP expressing bacteria

I_{Ref} = Area under photoluminescence curve of quinine sulphate

A_{Ref} = Absorbance of quinine sulphate

A_{Bac}= Absorbance of Au NCs synthesised on GFP-expressing bacteria

n = Refractive Index of Au NCs synthesised on GFP-expressing bacteria and quinine sulphate respectively

The optical density of all the samples was maintained below 0.1. The quantum yield has been calculated to be 2.5 ± 0.7%.

3.4. Characterization

3.4.1. UV-Vis and luminescence measurements

UV–visible spectrophotometer (PerkinElmer Lamda 25) was used for recording the UV-Vis absorbance spectra. Photoluminescence measurements were performed using Fluromax – 4 spectrofluorimeter (Horiba Jobin Yvon).

3.4.2. Transmission Electron Microscopy (TEM) analysis

TEM analysis was performed using Jeol JEM 2100 operating at an accelerating voltage of 200 KV. TEM samples were prepared by drop casting the sample onto a carbon coated copper TEM grid.

3.4.3. X- Ray Photoelectron Spectroscopy (XPS) analysis

To confirm the electronic state of Au NCs synthesized on the surface of bacteria X-ray photoelectron spectroscopy (XPS) analysis was carried out in PHI 5000 Versa Probe II, FEI Inc. scanning XPS microprobe.

3.4.4. Field-Emission Scanning Electron Microscopy (FESEM)

JEOL JSM-7610F was used for FESEM analysis of the samples. The dispersion was drop cast onto an aluminium foil and was dried in a desiccator. Prior to analysis, the samples were coated with platinum using platinum coating sputter coater (JEC-3000FC auto fine coater) JEOL.

3.4.5. Atomic Force Microscopy (AFM)

The prepared samples were drop cast on an aluminium foil and observed under atomic force microscope (Agilent, Model 5500 series).

3.4.6. Confocal Microscopy

White light generation from bacteria was confirmed by detailed confocal studies

using Zeiss LSM 880 microscope. The as synthesized Au NCs on bacteria were drop cast on a glass slide and was covered with a coverslip which was further sealed on both sides by using nail paint. The prepared samples were observed under different emission range e.g. blue, green and red (upon excitation at 405nm). Samples containing control GFP-expressing bacteria were excited using a laser source of 488 nm.

3.4.7. CIE chromaticity coordinates

The "go cie" software was used to calculate the CIE chromaticity coordinates.

3.5. Results and Discussion

Experimentally, the reaction of tetrachloroauric acid ($HAuCl_4$) in the presence of mercaptopropionic acid (MPA) and GFP-expressing bacteria led to the formation of a colloidal dispersion. The details of the reaction procedure are given in the experimental section. The UV-Vis absorption spectrum of the dispersion showed a broad absorption in the region of 200–400 nm with no prominent absorbance peak edge. Importantly, the absorption spectrum was devoid of the characteristic peak due to surface plasmon resonance of Au nanoparticles (which typically appears at about 530 nm), thereby discounting the formation of gold nanoparticles as a product of the reaction between $HAuCl_4$ and MPA in the presence of bacteria **(Figure 3.1 a)**. Also, the UV-Vis spectrum of GFP-expressing bacteria without Au nanoclusters synthesized on it **(Figure 3.1b)** was observed to exhibit an absorbance maximum at 264 nm, which could be attributed to the absorbance of aromatic amino acids constituting the proteins present on the bacterial cell wall. However, following the synthesis of Au nanoclusters on the bacterial surface, the UV-Vis absorbance spectrum was devoid of this peak. This indicates possible involvement of bacterial proteins in cluster synthesis. The dispersion was photoluminescent upon excitation at 320 nm **(Figure 3.1c)**. The emission spectrum was further deconvoluted and the presence of two emission peaks with maxima at 435 nm and 582 nm was thus confirmed **(Figure 3.1d)**. The peak at 435 nm is attributed to the proteins present on the surface of the bacteria.[18] On the other hand; the peak at 582 nm indicated the formation of Au

NCs in the medium. Further, since peaks could still be observed following centrifugation and redispersion of the product, it may be plausible that the so produced NCs could be present in the bacteria. It is interesting to observe that the peak due to GFP (in the bacteria) at 510 nm **(Figure 3.1e)** was no longer prominent in the spectrum of the reaction product.

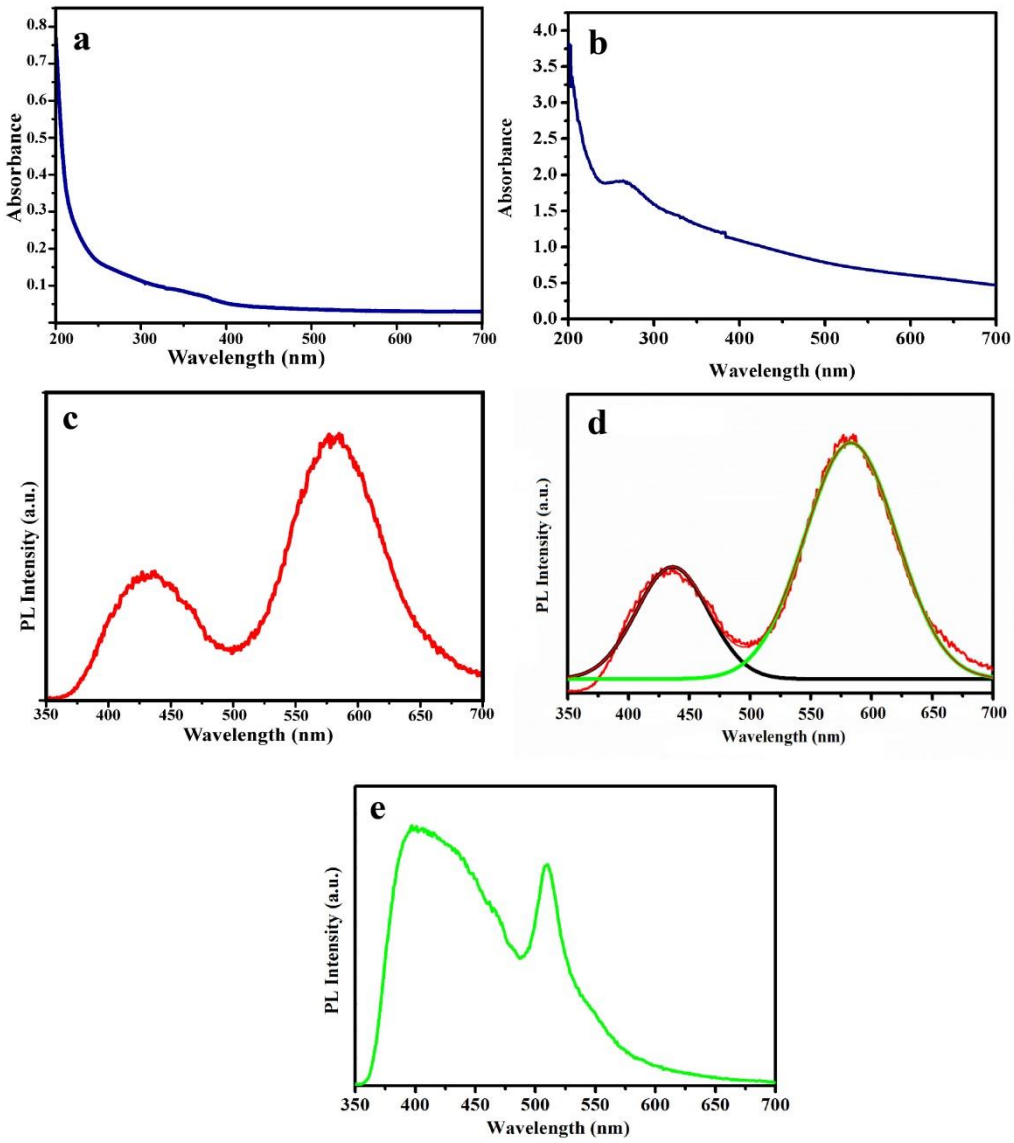

Figure 3.1. (a) UV-Vis spectrum of Au NCs synthesized on GFP-expressing *E.Coli*. (b) UV-Vis absorbance spectrum of GFP-expressing *E.Coli*. (c) Photoluminescence spectrum of Au NCs synthesized on GFP-expressing *E.Coli*. (d) De-convoluted emission spectrum of GFP-expressing *E.Coli* following synthesis of Au nanoclusters. (e) Photoluminescence spectrum of green fluorescent protein expressing *E.Coli*.

That was probably due to the formation of NCs embedded in the bacteria, which led to the quenching of the fluorescence due to the protein (i.e., GFP) inside the

bacterial cell. This is indicative of the formation of luminescent atomic nanoclusters on the surface of bacteria.MPA has been used herein to reduce Au (III) salt to Au (I) thiolates and Au (0) based on an earlier report.[19] Additionally, the amine and thiol groups of amino acid residues constituting the proteins present on the bacterial surface might have been instrumental in reducing Au (III) salt (in conjunction with MPA) as well as in the stabilization of the nanoclusters. Transmission electron microscopy (TEM) analysis revealed that particles with size of 2.02 ± 0.71 nm were formed on the bacteria **(Figure3.2a)**. A closer investigation of the images indicated that the density of particles at the edge of the bacterium appeared to be higher than at the centre. This could be due to the formation of particles on the surface of the bacterial cell. The TEM image of control GFP-expressing bacteria **(Figure 3.2b)** was observed to be distinctly different from the TEM image of GFP-expressing bacteria with gold nanoclusters synthesized on it. While the latter shows the presence of particles of the order of 2 nm on the bacterial surface, the former was devoid of such particles. That these particles formed on the surface of the bacteria were Au (0) was confirmed by X-ray photoelectron spectroscopic measurements. The results **(Figure 3.2c)** showed peaks occurring at 83.88 eV and 87.59 eV, which are due to Au (0). The peak at 84.66 eV also indicated attachment of Au to thiol groups of protein.

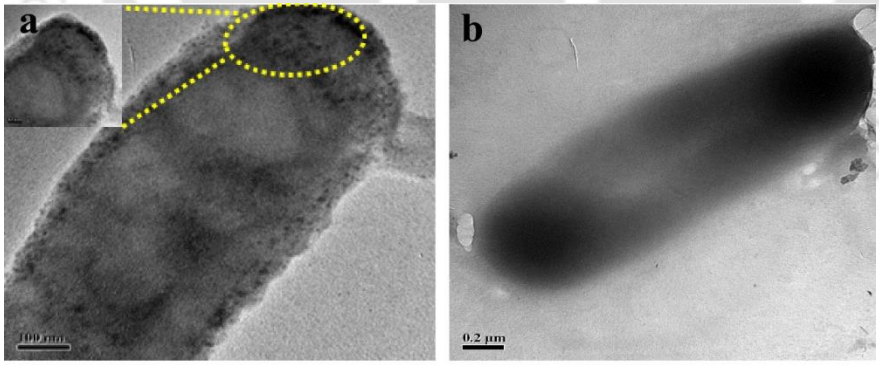

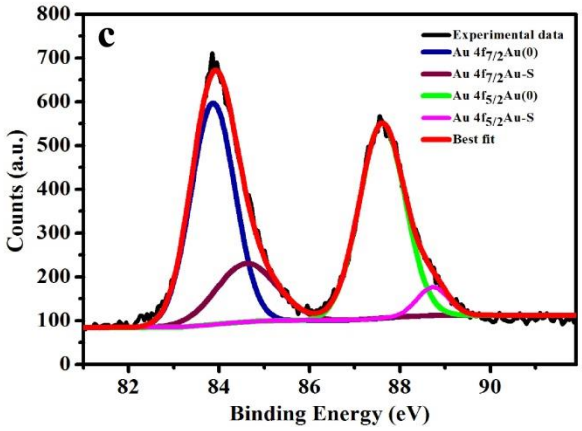

Figure 3.2. (a) TEM image of Au NCs synthesized on GFP expressing *E.Coli*. (b) TEM image of GFP-expressing *E.Coli* (control). (c) XPS analysis of Au NCs synthesized on GFP-expressing *E.Coli*.

It may be mentioned here that Matrix assisted laser desorption ionization (MALDI)-MS is not a suitable technique to calculate the number of atoms in a cluster moiety owing to the possibility of fragmentation of the clusters.[20] Additionally, elucidation of the chemical formula of atomic clusters on the bacterial surface is even more tedious as well as prone to error given the complexity of chemical composition of the latter and was deemed not appropriate. Atomic force microscopy measurements indicated an increase in the roughness of the surface of the bacterium following the synthesis of Au NCs **(Figure 3.3)**. This was further supported by field emission scanning electron microscopy measurements **(Figure 3.4)**.

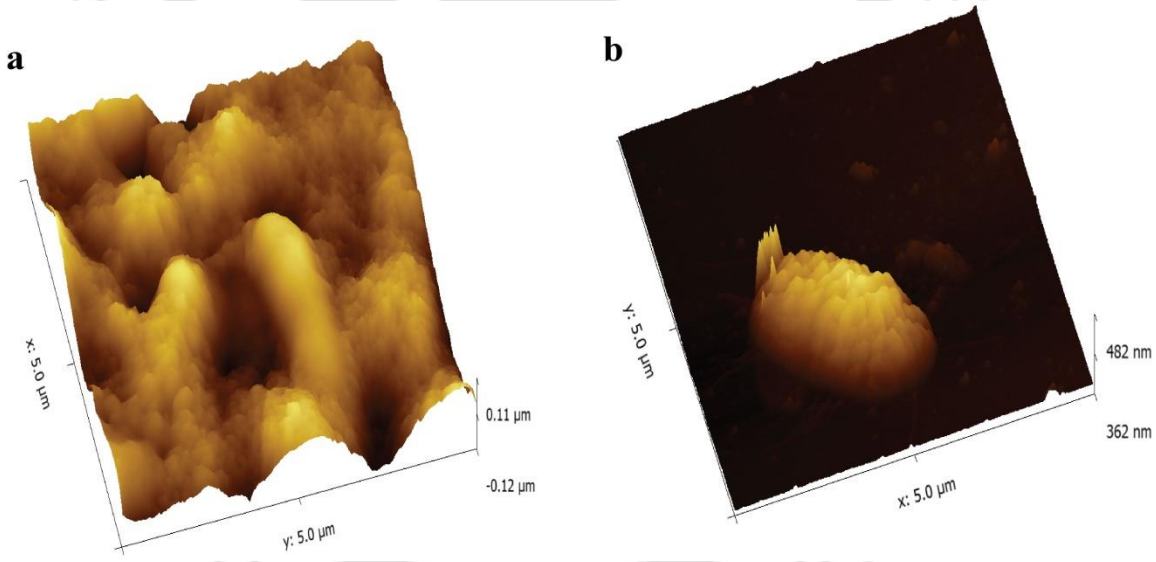

Figure 3.3. Atomic force microscopic (AFM) image of (a) green fluorescent protein (GFP) expressing *E.Coli* following synthesis of Au NCs and (b) control GFP *E.Coli*.

Fortuitously, the presence of two peaks (at 435 nm and 582 nm), due to the surface proteins and Au NCs on the bacterial surface, which spanned the entire visible wavelength region, provided an opportunity to achieve white light emission. This was achieved by varying the ratio of the number of bacteria and $HAuCl_4$ precursor concentration. The photoluminescence spectra for such varying ratios are shown in **(Figure3.5a)**. As is clear from the figure, the ratio of the two

peak intensities could easily be tuned. Also, commission internationale de l'elcairage (CIE) coordinate measurements indicated values of 0.33 and 0.31 for

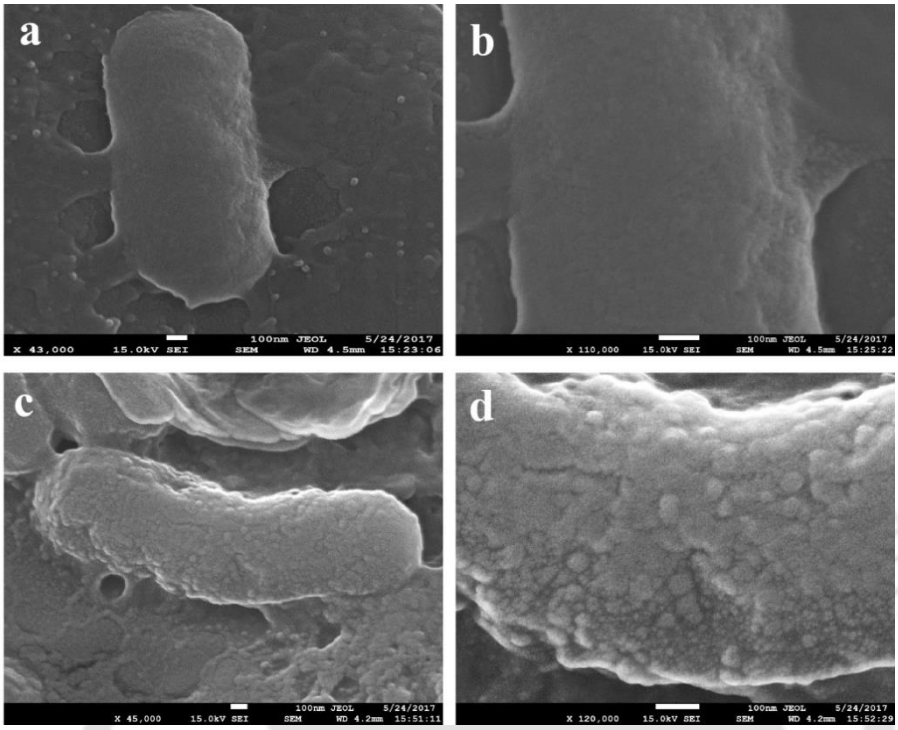

Figure 3.4. FESEM image of (a) control GFP-expressing *E.Coli* (b) High magnification image of (a) FESEM image of (c) GFP-expressing *E.Coli* following synthesis of Au NCs and (d) High magnification image of (c).

the clusters produced from a bacterial number of 10^5, 0.018mL of 10 mM $HAuCl_4$ and 0.006 mL of 0.11 M MPA **(Figure 3.5b)**. The quantum yield associated with this white light-emitting system was calculated to be 2.5 ± 0.7%.

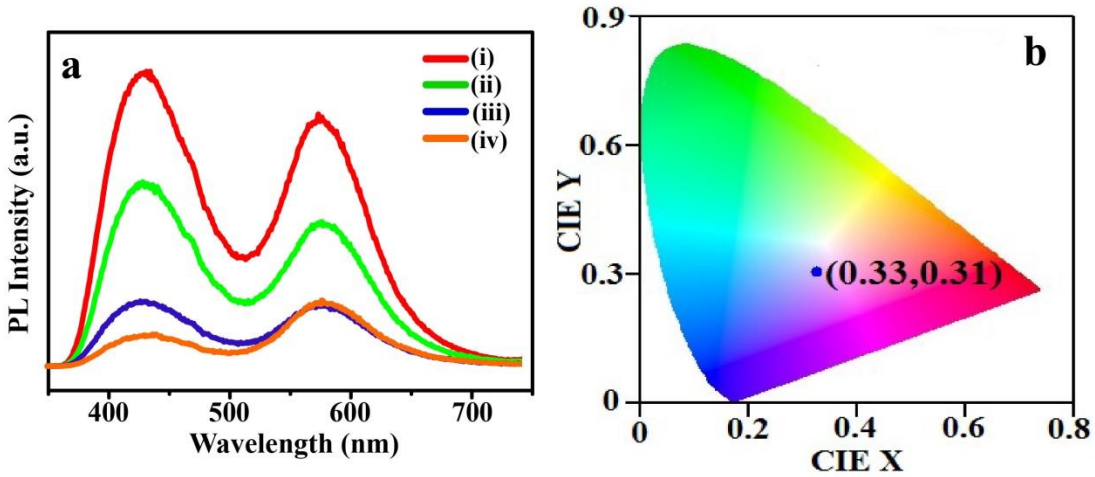

Figure 3.5 (a) Photoluminescence spectra of Au NCs synthesized on GFP-expressing *E.coli* using (i) 2×10^6 (ii) 10^6 (iii) 10^5 and (iv) 10^4 number of bacteria. The concentrations of $HAuCl_4$ and MPA were kept constant in all the cases. (b) CIE chromaticity diagram of Au NCs synthesized on GFP-expressing bacteria-emitting white light. The excitation wavelength was set at 320 nm.

However, as discussed above, the development of single emitting white light species is a key to progress in the field of light-emitting devices. In the present case, the individual bacterial cells containing Au NCs were probed using CLSM with laser excitation at 405 nm. The images in **(Figure 3.6)** clearly reveal white luminescence from single bacterial species. Further analysis demonstrated that the white light emission was composed of blue, green and red emission components. Thus, the characteristic white light emission from a single bacterium consisted of basic colours. It may be noted here that the overall emitting colors of the bacterial cells (containing Au NCs) could be tuned based on the ratio of bacteria, $HAuCl_4$ and MPA. It is to be noted here that CLSM analysis showing white light-emitting bacteria was performed on dried samples of bacterial surface embedded with Au NCs. Hence, it can be concluded that the white light-emitting nature of bacteria remains preserved in the dried state, which is the key to development of bacteria based white light-emitting devices.

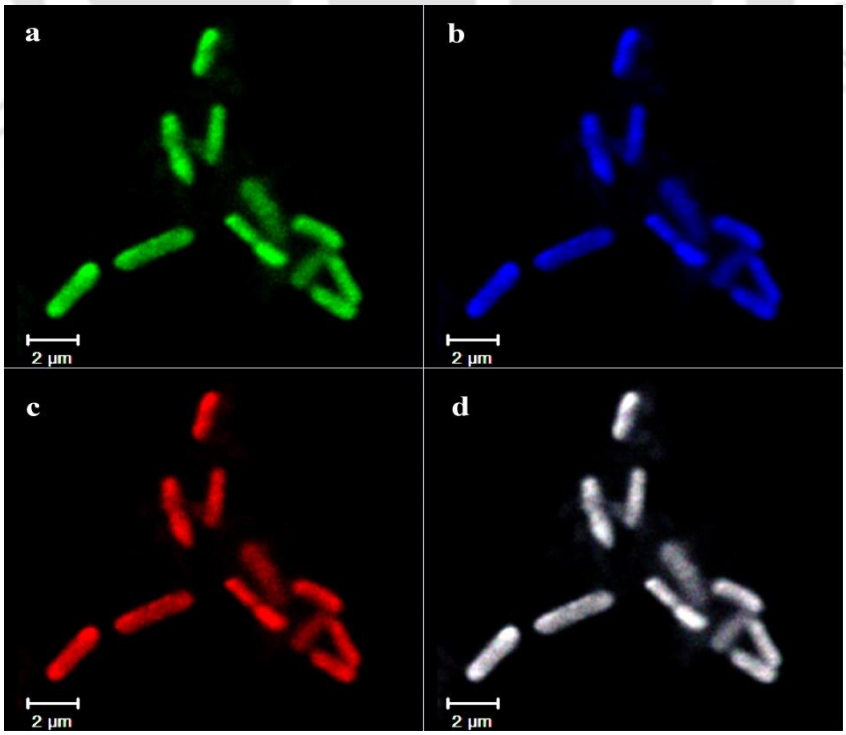

Figure 3.6. CLSM image of Au NCs synthesized on GFP-expressing *E.Coli* upon laser excitation of 405 nm in the (a) green (b) blue and (c) red channels. (d) Merged image of (a), (b) and (c) showing white light emission.

Further, the crucial role of Au NCs in overall white light emission was verified using the CLSM study. Control GFP-expressing bacteria were bright green luminescent under CLSM **(Figure A3.1, Appendix)**. In an allied vein, the mixture of Au NCs synthesized on GFP-expressing bacteria and control GFP bacteria was studied under CLSM. It is to be mentioned here that the luminescence quantum yield of GFP-expressing bacteria following the synthesis of Au NCs is sufficiently low compared to GFP-expressing bacteria. The difference in luminescence between the two, in fact, was used as a parameter to distinguish between Au NC synthesized bacteria and control GFP-expressing bacteria in the mixture of the two. Upon excitation of the sample at an excitation wavelength corresponding to emission of GFP-expressing bacteria (488 nm), the control GFP-expressing bacteria were bright green luminescent while the ones with Au NCs synthesized on them showed attenuated luminescence **(Figure A3.2, Appendix).** On the other hand, upon excitation of the mixture at a wavelength corresponding to Au NC synthesized bacteria (405 nm) – which is far from excitation of GFP-expressing bacteria – those bacteria that showed minimum luminescence upon excitation at a wavelength corresponding to emission of GFP-expressing bacteria now showed considerable white luminescence, while GFP-expressing bacteria devoid of Au NCs were almost nonluminescent under this excitation wavelength **(Figure A3.3, Appendix).**These results further confirmed the potential role of Au NCs synthesized on GFP bacteria in white light emission.

Additionally, to emphasize the candidature of bacterial cells as a versatile template for cluster synthesis and thereby a white light-emitting material, Au NCs were synthesized on various other bacterial strains including Gram negative *Escherichia coli* MTCC 433, Gram positive *Bacillus cereus* MTCC 1305 and *Enterococcus faecalis* MTCC 439 bacteria. In a manner much similar to GFP-expressing bacteria, upon tuning the ratio of the number of bacteria and precursors for cluster synthesis (i.e. gold precursor and MPA), white light emission was achieved **(Figure 3.7-3.9)**. Interestingly, keeping the concentration of the precursors (Au (III) and MPA) unaltered for all the strains, the number of

bacteria required for white light emission was different for different strains. For example, in the case of *Escherichia coli* MTCC 433 and *Bacillus cereus* MTCC 1305, 10^6 bacteria were required to generate white luminescence for a particular concentration of $HAuCl_4$ and MPA. However, keeping the concentration of $HAuCl_4$ and MPA unaltered, 10^4 bacteria were required for the generation of white luminescence for *Enterococcus faecalis* MTCC 439. This further indicated the crucial role of proteins (the content of which is different in each strain) present on bacterial cells in white light emission.

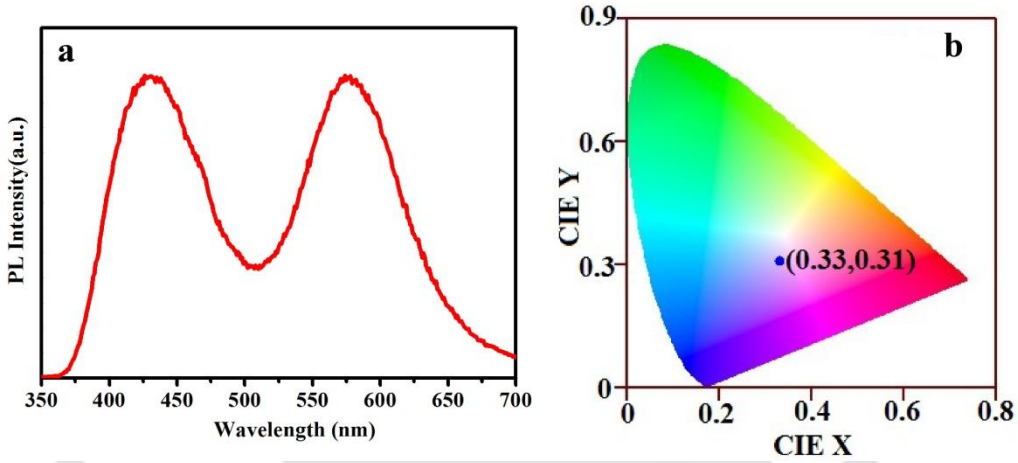

Figure 3.7. (a) Photoluminescence spectrum of non GFP-expressing *Escherichia coli* MTCC 433 following synthesis of Au NCs, (b) Corresponding CIE chromaticity diagram showing chromaticity index of 0.33, 0.31.

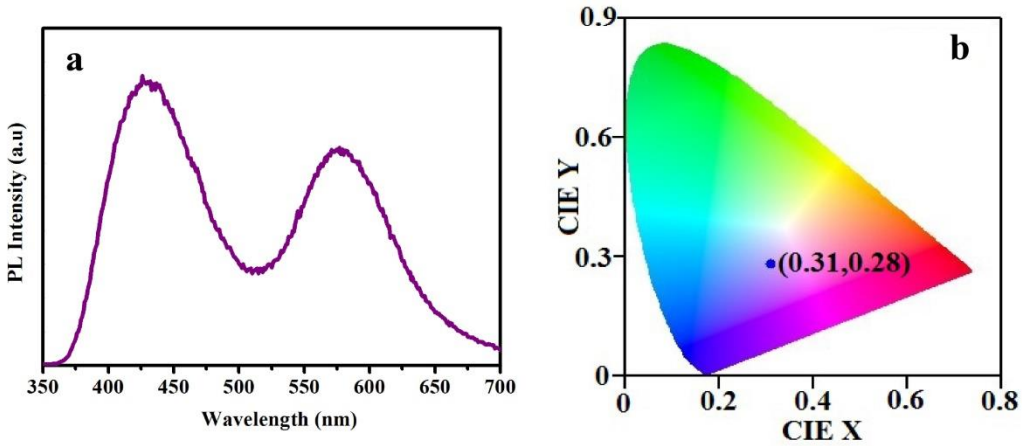

Figure 3.8. (a) Photoluminescence spectrum of *Bacillus cereus* MTCC 1305 bacterial strain following synthesis of Au NCs, (b) Corresponding CIE chromaticity diagram showing chromaticity index of 0.31, 0.28.

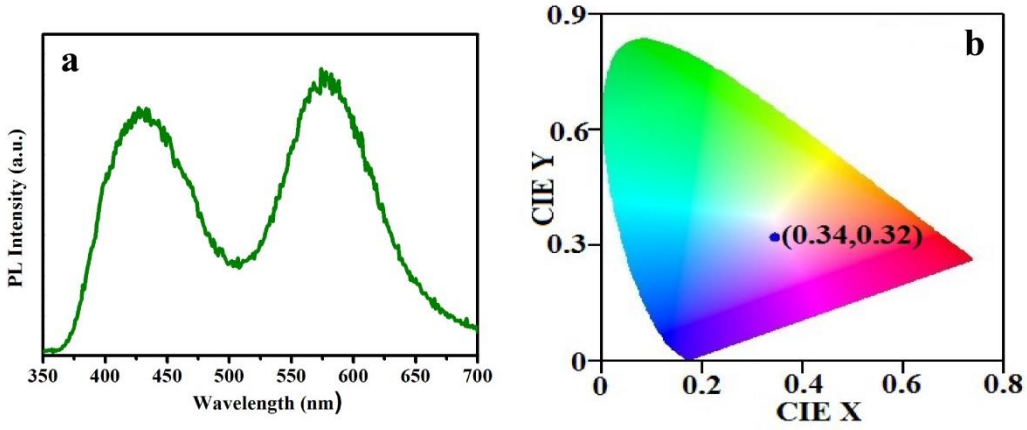

Figure 3.9. (a) Photoluminescence spectrum of *Enterococcus faecalis* MTCC 439 *bacterial strain* following synthesis of Au NCs, (b) Corresponding CIE chromaticity diagram showing chromaticity index of 0.34, 0.32.

With regard to white light-emitting materials, correlated color temperature (CCT) and color rendering index (CRI) are the key factors that decide the potential of the former as a futuristic light-emitting device. In the present study, CCT and CRI for Au NC synthesized white light-emitting GFP-expressing bacteria have been computed to be 77 and 6380 K, respectively. Importantly, the CCT value obtained herein corresponds to that of bright bluish white light, which is analogous to daylight and is well suited for display applications. Similarly, the CRI value suggests that the bacterial white light reported herein is appropriate for commercial purposes with fine resolution. On a similar note, Gram negative *Escherichia coli* MTCC 433, Gram positive *Bacillus cereus* MTCC 1305 and *Enterococcus faecalis* MTCC 439 bacteria have also been found to provide white light emission associated with CRI and CCT values suitable for commercial applications (as tabulated in **Table A3.1**, **Appendix**). Further, to justify the candidature of the white light-emitting bacteria as a potential LED device, the temperature-dependant stability of the same has been studied. The microscopic slide containing GFP-expressing bacteria embedded with gold nanoclusters has been maintained at 30 °C for 2–3 min and thereafter the confocal laser scanning microscopy (CLSM) images showing the presence of single white light-emitting bacteria were acquired. The same slide was then maintained at a temperature of 50 °C for 2–3 min and then brought to room temperature. Thereafter, the CLSM images were recorded again, which still showed the presence of white light-

emitting bacteria. This cycle was repeated. Interestingly, it was observed that the white light emission from single GFP-expressing bacteria with gold nanoclusters synthesized on them, though attenuated to some extent possibly owing to the effect of heat, was still preserved following repeated heating and cooling cycles **(Figure 3.10)**. In an allied vein, the time-dependant stability of white light emitting bacteria was also studied. Time-dependent CLSM analysis of GFP-expressing bacteria with gold nanoclusters synthesized on them (fixed on a microscopic slide) was done at an interval of 24 h for 2 days. The white light emission from cluster-containing bacteria was found to be almost unaffected **(Figure 3.11).**

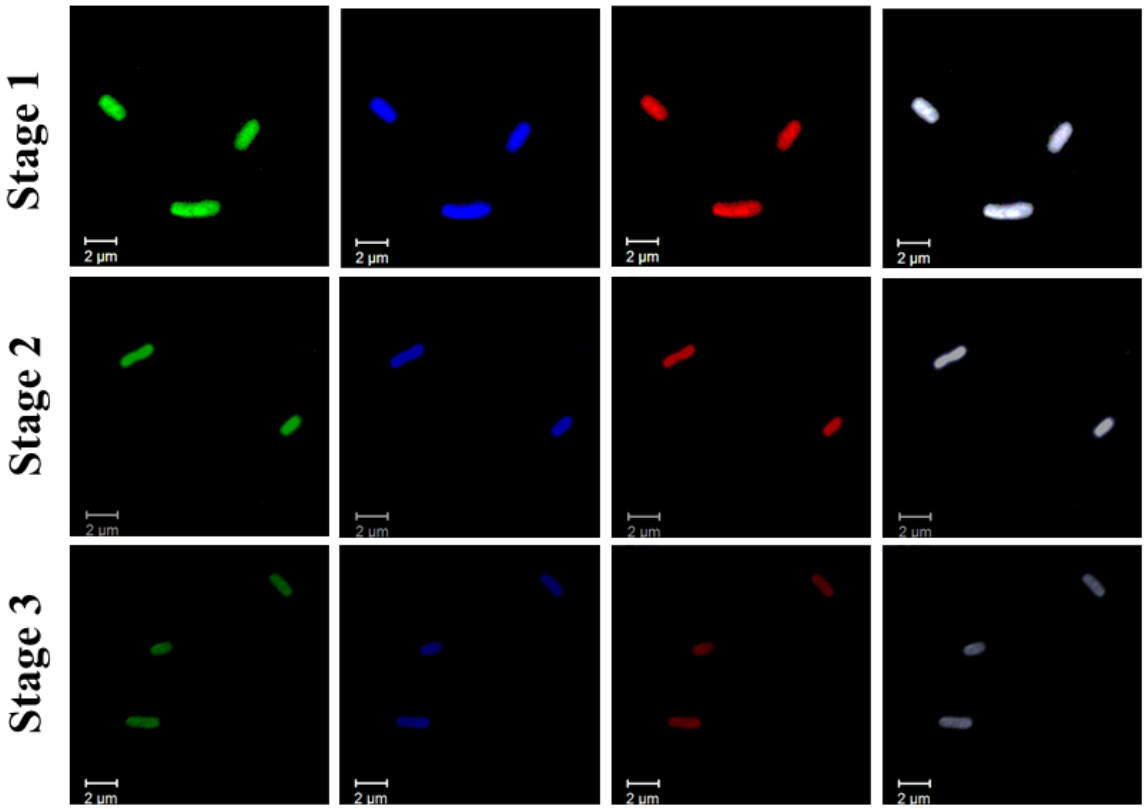

Figure 3.10. CLSM images of GFP-expressing bacteria following synthesis of Au nanoclusters acquired at various thermal conditions. Stage 1: 30 ˚C, Stage 2: heated at 50 ˚C followed by cooling at room temperature, Stage 3: Again heated at 50 ˚C followed by cooling at room temperature.

It is encouraging to note that the fabrication of biomolecules such as protein-based hybrid white light-emitting LED devices has been demonstrated recently.[21] It would also be interesting to fabricate similar devices using bacteria, which would require extensive studies involving the stability of the species under

different environmental conditions. An important candidate in this regard could be thermophilic bacteria, [22] which may provide stability to the device even at considerably higher temperatures.

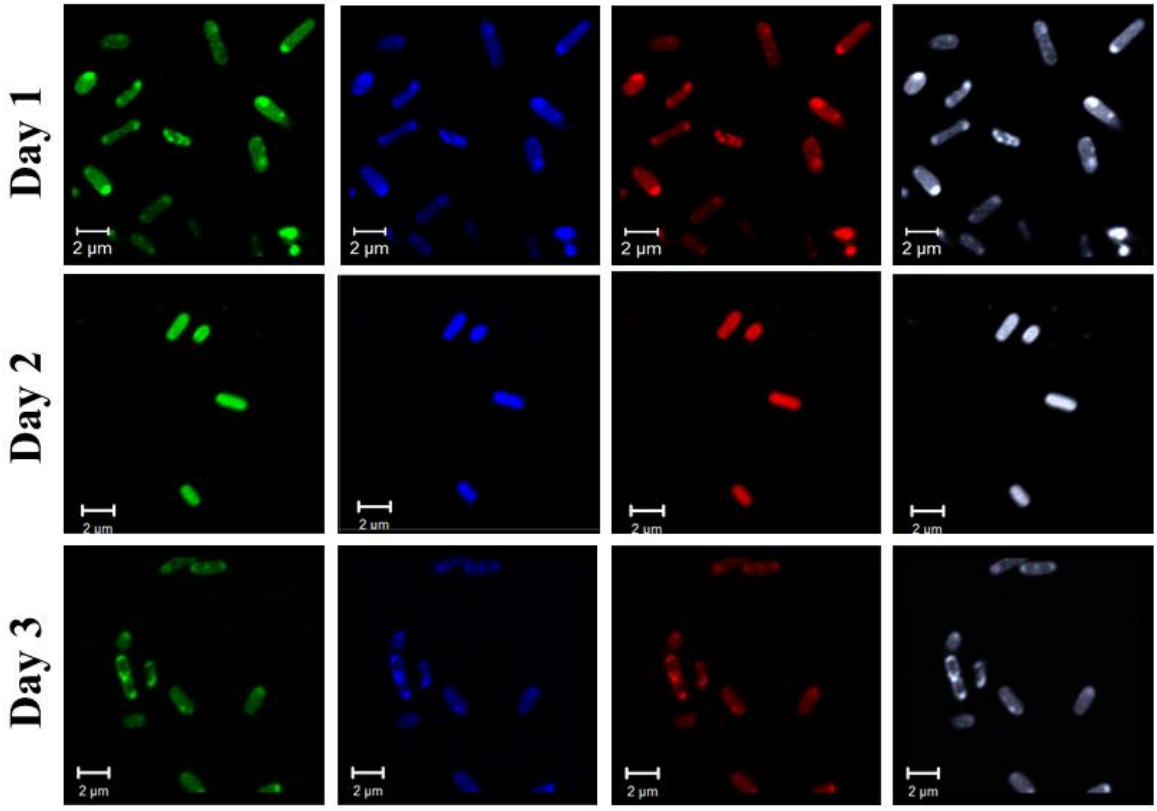

Figure 3.11. CLSM images of GFP-expressing *Escherichia coli* following synthesis of Au nanoclusters acquired at various time intervals.

3.6. Conclusion

In a nutshell, proteins present on unicellular bacteria have been used as a template for the synthesis of atomic clusters. Orange luminescent quantum clusters in conjunction with the blue-emitting proteins constituting the bacterial cell wall led to overall white light emission. It is believed that the concept of white light emission introduced herein based on living organisms opens up a new avenue for the development of cost effective and sustainable light-emitting materials. The study reported introduces a novel concept of using non-pathogenic and non-toxic bio-organisms as templates for the synthesis of clusters to achieve perfect white light emission with appreciable CRI and CCT values.

3.7. References

1. D. K. Maiti and A. Banerjee, *Chem. Commun*., **2013**, *49*, 6909–6911.

2. N. Guan, X. Dai, A. Messanvi, H. Zhang, J. Yan, E. Gautier, C. Bougerol, F. H. Julien, C. Durand, J. Eymery and M. Tchernycheva, *ACS Photonics*, **2016**, *3*, 597–603.

3. G. Haider, M. Usman, T.-P. Chen, P. Perumal, K.-L. Lu and Y.-F. Chen, *ACS Nano*, **2016**, *10*, 8366–8375.

4. S. Pathak, N. Sakai, F. Wisnivesky Rocca Rivarola, S. D. Stranks, J. Liu, G. E. Eperon, C. Ducati, K. Wojciechowski, J. T. Griffiths, A. A. Haghighirad, A. Pellaroque, R. H. Friend and H. J. Snaith, *Chem. Mater*. **2015**, *27*, 8066–8075.

5. C.-W. Sher, C.-H. Lin, H.-Y. Lin, C.-C. Lin, C.-H. Huang, K.-J. Chen, J.-R. Li, K.-Y. Wang, H.-H. Tu, C.-C. Fu and H.-C. Kuo, *Nanoscale*, **2016**, *8*, 1117–1122.

6. F. Wang, Y. Chen, C. Liu and D. Ma, *Chem. Commun*. **2011**, *47*, 3502.

7. D. K. Maiti, S. Roy, A. Baral and A. Banerjee, *J. Mater. Chem. C*, **2014**, *2*, 6574.

8. B. Xu, H. Wu, J. Chen, Z. Yang, Z. Yang, W. Wu, Y. Zhang, C. Jin, P.-Y. Lu, Z. Chi, S. Liu, J. Xu and M. Aldred, *Chem. Sci*. **2016**, *8*, 1–6.

9. S. Bhandari, S. Pramanik, R. Khandelia and A. Chattopadhyay, *ACS Appl. Mater. Interfaces*, 2016, **8**, 1600–1605.

10. S. Pramanik, S. Bhandari, S. Roy and A. Chattopadhyay, J. *Phys. Chem. Lett*., **2015**, *6*, 1270–1274.

11. T. Ghosh and E. Prasad, J. Phys. Chem. C.**2015**, *119*, 2733–2742.

12. Z. Xie, C. Chen, S. Xu, J. Li, Y. Zhang, S. Liu, J. Xu and Z. Chi, *Angew. Chem*., Int. Ed., **2015**, *54*, 7181–7184.

13. I. E. Serdiuk, *J. Phys. Chem. C*, **2017**, *121*, 5277–5286.

14. P. Li, M. Mu¨ller, M.W. Chang, M. Frettlo¨h and H. Scho¨nherr, *ACS Appl. Mater. Interfaces*, **2017**, *9*, 22321–22331.

15. F. Marcellin, *New Scientist: Technology* News, **2016**, 3063.

16. M. Dandapat and D. Mandal, *Phys. Chem. Chem. Phys*., **2016**, *18*, 2564–2573.

17. Z. Wu, J. Liu, Y. Gao, H. Liu, T. Li, H. Zou, Z. Wang, K. Zhang, Y. Wang, H. Zhang and B. Yang, *J. Am. Chem. Soc*., **2015**, *137*, 12906–12913.

18. M. S. Ammor, *J. Fluoresc*., **2007**, *17*, 455–459.

19. A. K. Sahoo, S. Banerjee, S. S. Ghosh and A. Chattopadhyay, *ACS Appl. Mater. Interfaces*, **2014**, *6*, 712–724.

20. R. Jin, *Nanoscale*, **2015**, *7*, 1549–1565.

21. M. D. Weber, L. Niklaus, M. Pro¨schel, P. B. Coto, U. Sonnewald and R. D. Costa, *Adv. Mater*., **2015**, *27*, 5493–5498.

22. B. M. Zeldes, M. W. Keller, A. J. Loder, C. T. Straub, M. W. W. Adams and R. M. Kelly, Front. Microbiol., **2015**, ***6***, 1209.

Appendix of Chapter- 3 :A3

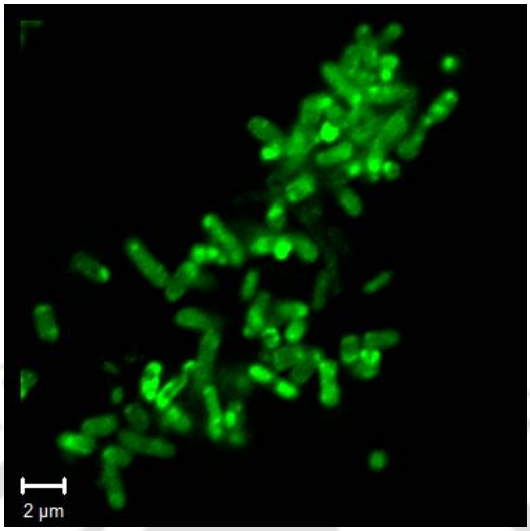

Figure A3.1. CLSM image of GFP expressing bacteria.

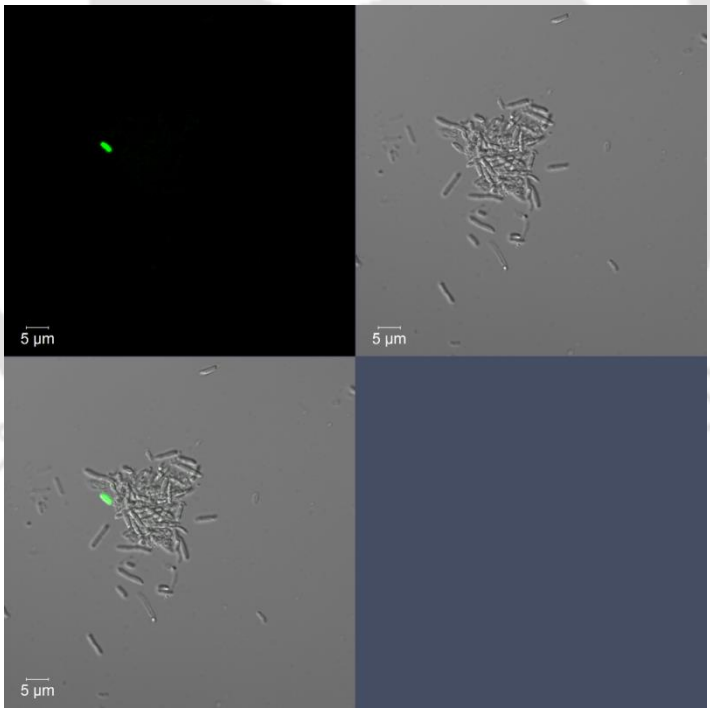

Figure A3.2. CLSM image of a mixture of control GFP expressing bacteria and Au NCs synthesised on the former at a laser excitation of 488 nm.

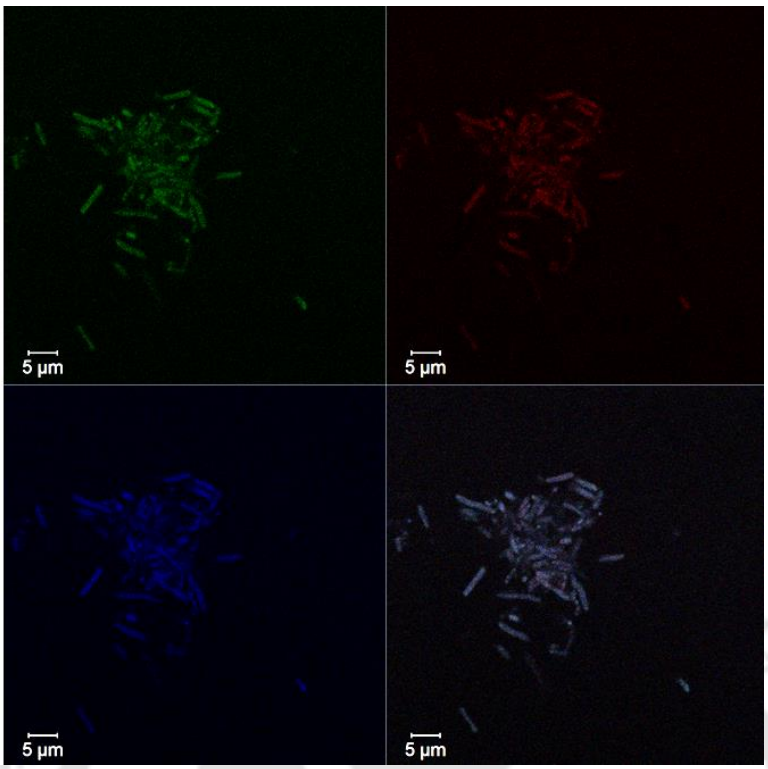

Figure A3.3. CLSM image of a mixture of control GFP expressing bacteria and Au NCs synthesised on the former at a laser excitation of 405 nm.

Table A3.1. Correlated color temperature (CCT) and Colour rendering index (CRI) calculated on various strains of bacteria emitting white light.

Bacterial strain	CCT	CRI
Bacillus Cereus MTCC 1305	7329	81
Escherichia Coli MTCC 433	5589	74
Enterococcus Faecalis MTCC 439	4936	72

Chapter-4

PEG-Encapsulated HDACi Drug-Composite Nanoparticles for Combination Therapy with Artesunate

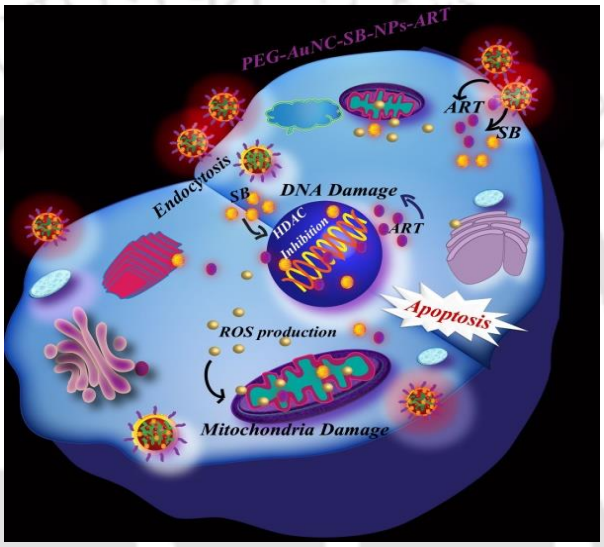

In Chapter 4, *Luminescent Au nanoclusters (Au NCs) were formulated into spherical PEG –Au NC encapsulated drug -sodium butyrate (NaB) composite nanoparticles (PEG-Au NC-NaB-NPs) in presence of PEG and NaB. Their effect on cancer cells were investigated using bio imaging, unravelling the mechanism of endocytosis pathway and combination therapeutic interventions with a plant based antimalarial drug artesunate (ART). Combination of PEG-Au NC-NaB-NPs with ART displayed enhanced therapeutic activity at a reduced dose compared to its individual doses and reveals heightened synergistic activity. In vivo activity of the NPs was evaluated on Daltons lymphoma ascites (DLA) bearing mice, which exhibited significant reduction of tumor volume and viable tumor cells with prolonged life span.*

https://pubs.acs.org/doi/10.1021/acsomega.8b02105

Chapter -4

4.1. Introduction

With various treatment options such as surgical intervention, chemotherapy, radiotherapy for cancer, the most widely used single chemotherapeutic activity (monotherapy) has become less attractive for clinical applications due to its association with many drawbacks, such as high toxicity, nonspecificity and drug resistance.[1-9] This is mainly because of the physiological heterogeneity of cancers with complex tumor microenvironment, which harbour abnormalities in multiple signal pathways and are often associated with drug resistance.[8-11] Along with this, the conventional chemotherapeutic drugs like doxorubicin, paclitaxel and cisplatin are associated with adverse side effects, which induced paradigm shift towards alternative drugs or combination drug therapy. Combination therapy is the co-administration of two different drugs with different pharmacological mechanism, which achieves therapeutic synergy efficacy, reduced toxicity and long term prognosis.[12-16] Thus, the suitable combinations of drugs are essential to overcome the drug resistance and enhanced therapeutic activity for preclinical and clinical cancer treatment.[6,7,9,13,16] At the same time use of alternative drugs for combinational therapy as new effective therapeutics for cancer treatment remains an important endeavour to reduce overall cytotoxicity associated with standard chemotherapeutic drugs.[1,17-19] The shortcomings associated with general administration of different therapeutics (drugs) for combination therapy lies in its distinct pharmacokinetic profiles leading to inconsistent bio distribution and thus an inefficient therapy. In addition, therapeutic drugs are not directly delivered into targeted tumor sites, which induce adverse effects on normal cells and result in killing of normal cells as well.[4, 20, 21] Therefore, novel approaches that can overcome the biological barriers and work upon the malignant cells selectively without affecting the normal cells by delivering the optimal dosage of the therapeutics in the complex tumor environment competently is desired.

In the last few years, with advanced understandings of development of cancer, remarkable breakthroughs were unveiled for its diagnosis and treatment in the field of nanomedicine.[4, 14, 22-25] For the nanoparticle based therapeutics, nanocarriers and nanodrugs were poised to significantly improve the aforementioned shortcomings as revealed by some prominent reports, where some were already approved for clinical practices.[4,5,6,26] The nanoparticle based therapeutics and nanocarriers of various metallic nanoparticles like gold, silver, copper and silica have many advantages like better solubility, advanced delivery, protection from tumor microenvironment and controlled release associated with it.[6,23,27,28] In addition, surface modification of nanoparticles with poly ethylene glycol (PEG) can augment these activities and have improved drug delivery properties, prolonged circulation life time with enhanced protection from clearance by mononuclear phagocytic systems.[29,30,31] In fact PEG and many other polymers are formulated into drug containing nanoparticles[29,32] and have longer *in vivo* circulation time as well. In this regard, the use of biocompatible luminescent metal nanoclusters (NCs), which has been growing as a promising tool for theranostic purposes was mostly anticipated where their luminescence property could also be explored for probing and understanding of mechanism of uptake and activity.[25,27,28] Metal NCs of Au, Ag and Cu have been extensively used for drug delivery purposes where Au NCs because of its stability, potentially less toxicity or noncytoxicity, significant luminescence properties and low photobleaching arose as new option, overcoming the limits associated with organic dyes and quantum dots .[25,27,33] Thus, polymer PEG coated nanodrug has been synthesized by slightly modifying chitosan based Au NCs as reported earlier [33] with the help of negatively charged drug sodium butyrate (NaB). As mentioned earlier, because of the drug resistance and side effects associated with standard chemotherapeutic drugs, novel drugs for cancer therapeutics are of intense interest.

As many epigenetic pathways are associated with cancer, one of the prime regulatory mechanisms is the acetylation status of genes controlled by histone acetyltransferases (HAT) and histone deacetylases (HDAC) for monitoring gene expression and chromatin structure.[34] At the same time, development of histone

deacetylase inhibitors (HDACi) has been received as a promising new class of antineoplastic therapy for anticancer targets, which works by reactivation of tumor suppressor genes.[35,36] One of the common HDACi drugs is sodium butyrate (NaB), which is a short fatty acid chain. NaB is present in the human colon as a product of carbohydrate metabolism and is produced by bacterial fermentation naturally.[37] Moreover, the promising results of NaB as an anti-tumour drug, possibly through inhibition of histone deacetylase (HDAC), have led to phase I and phase II clinical trials.[38] NaB acting as an HDACi, is known to exhibit anticancer effects via differentiation of carcinoma cells and instigate apoptosis in cancer cells both *in vivo* and in several pre-clinical models.[35,38] However, HDACi, although being a potent anti-cancer drug, has limitation of short half-life i.e., easily metabolised and therefore it has better activity in combination with other therapeutic drugs in clinical studies.[36,39] Moreover, there are reports of NaB delivery by solid lipid nanoparticles to overcome the constraints associated with fast metabolism of NaB.[38] Hence NaB was used for nanodrug formulations for its enhanced delivery and is intended for combination therapy for which a plant based drug was chosen.

Due to the adverse side effects associated with standard chemotherapeutic drugs, plant based and naturally available active anti-cancer drugs provide better alternatives and their use for anti-cancer treatment is in demand .[40] In the last few decades, Artemisinin, which is a plant derivative from Chinese medicinal plant *Artemisia annua L.* (sweet wormwood) have been used as an well-established antimalarial drug.[41] Its semisynthetic derivatives are dihydroartemisinin, artesunic acid, and artemether where artemisinin and sodium artesunate are water soluble salt of artesunic acid. World Health Organization (WHO) have recently recommended use of artemisinin and sodium artesunate for chemotherapy of humans (Artemisinin-based combination therapy - ACT) in combination with conventional drugs for malaria.[41] Many reports suggests DNA fragmentation leading to DNA damage as a prime reason for anticancer activity of artesunate (ART).[42] As ART is a prescribed remedy for malarial treatment without any adverse effects and have potent anticancer activity, combination therapy will aid to reduce the overall dose of ART and show enhanced activity along with NaB.

There is a report of using ART and NaB together but detailed understanding of their fate and anticancer mechanism were not well studied.[39] Thus, for combination therapy with ART, a smart theranostic material was desired, having cytotoxic activity with reduced side effects and which can be probed to elucidate the mechanism.

4.2. Outline of the present work

Herein, a polymer PEG coated luminescent nanoparticles were synthesized with Au NCs and negatively charged drug NaB. NaB and PEG reacted with Au NCs and formulated into spherical polymer drug encapsulated composite nanoparticle, which is referred as (PEG-Au NCs-NaB-NPs). The luminescent nanoparticles were used as a probe for uptake studies. Here to reduce the side effects associated with regular chemotherapeutic drugs, a plant based drug (ART) with anticancer property and a naturally available short chain fatty acid (NaB) were chosen for combinational cancer therapy. This resulted in enhanced synergistic therapeutic activity and the mechanism of synergy was elucidated in details. To the best of information for the first time a polymer coated HDACi drug encapsulated composite nanoparticles synthesized herein were studied in detail for combination therapy with ART. The synergy of action of both the drugs i.e., NaB and ART was studied and the mechanism has been studied meticulously. *In vivo* studies were also conducted for its efficacy in Swiss albino mice with Dalton's lymphoma Ascites (DLA) to endorse it for real life applications.[28]

4.3. Experimental Section

4.3.1. Materials

Chitosan (degree of deacetylation >75%), $HAuCl_4$ (Au, 17 wt % in dilute HCl; 99.99%), mercapto propionic acid(MPA), sodium butyrate (NaB), (3-(4, 5-dimethylthiazolyl-2)-2,5-diphenyltetrazolium bromide) (MTT), sinapinic acid, propium iodide, (5,5',6,6'-tetrachloro-1,1',3,3'- tetraethylbenzimi-dazolylcarbocyanine iodide (JC-1), chloropromazine methyl-β-cyclodextrin and HDAC Activity Assay Kit were obtained from Sigma-Aldrich, U.S.A. Artesunate was procured from commercial source. AnnexinV-7AAD kit used for apoptosis and APO-DIRECT™ Kit i.e., for TUNEL assay were acquired from BD lifescience. For

lysosomal staining, lysopainter green was used, which was purchased from Abcam. For all experiments, Milli-Q grade water (18.2 MΩ cm) was used. HeLa (human cervical carcinoma) cells were procured from National Centre for Cell Sciences, India (NCCS) Pune.

4.3.2. Synthesis of PEG coated composite NPs of Chitosan -Au NCs-NaB

For the synthesis of PEG coated composite NPs, first Au NCs were synthesized by slightly modifying previous protocol. Thus 1.5 mL of 0.5% (w/v) chitosan was added in 8 mL of H_2O in a reaction vessel under constant stirring. Into this 180 µL of 10 mM $HAuCl_4$ and 60 µL of 0.11 M MPA were added and stirred for 10 min. Chitosan used as the template was first prepared by dissolving 0.5% (w/v) of chitosan in 0.1% (v/v) acetic acid and kept for overnight stirring, which was then filtered by using Whatman filter paper to eliminate the residuals. The pH of the chitosan solution was adjusted at 6.2 prior to synthesis of Au NCs. For the synthesis of the composite NPs, 50 mM NaB (negatively charged drug), which served as ion gelating agent was added into 2 mL of Au NC solution. For the coating of PEG, 200 µL of PEG-400 was taken in 1 mL of chloroform and added drop wise into as synthesized Au NC solution under probe sonication (50 amplitude) in an ice cold condition for 10 min. Thus PEG coated drug encapsulated composite NPs (PEG-Au NC-NaB NPs) was formed in the aqueous phase, which was collected carefully and centrifuged at 12,000 rpm for 10 minutes. Finally, the precipitate was re-dispersed in 2 mL PBS buffer (pH 7.4) and store at 4 °C for further use.

4.3.3. Drug Encapsulation Efficiency

The encapsulation efficiency of the drug was calculated based on the luminescence of Au NCs.[27] For this in a fixed concentration of Au NCs (v/v) varied concentrations of NaB drug (10, 20, 30, 40, 50 and 60 mM) were added and incubated for 3 h. This was followed by PEG coating and drug encapsulated nanoparticle synthesis with the help of probe sonicator as already mentioned. The aqueous phase was collected followed by centrifugation and the precipitate was

re-dispersed in water. To find out drug encapsulation efficiency the luminescence of Au NCs was probed using fluorescence spectrophotometer LS55 Perkin-Elmer, at excitation and emission wavelengths of 320 nm and 610 nm, respectively. Therefore, the luminescence of control Au NCs (without drug) was measured and Au NCs (with different concentration of drugs) was calculated as follows:

$$E.E\,\% = \frac{AuNCs_i - AuNCs_f}{AuNCs_i}$$

4.3.4 *In vitro* experiments (Mammalian Cell Culture)

The human cervical cancer cell lines (HeLa), were chosen for all the experiments which were procured from National Centre for Cell Sciences, Pune. Cells were cultured in Dulbecco's Modified Eagle's Medium (DMEM, high glucose) supplemented with 10% FBS, 10,000 units of penicillin and 10 mg/mL streptomycin. The cultured cells were maintained in CO_2 incubator with 5% carbon dioxide in humidified atmosphere.

4.3.4 a. *Cell Viability Assay*

The cytotoxic activity of composite nanoparticles along with various controls were carried out with the help of MTT (3-(4,5-dimethylthiazolyl-2)-2,5-diphenyltetrazolium bromide) assay. For this the treatments with the respective composites and individual drugs were given for 48 h followed by MTT assay. Briefly, 96 well plates were seeded with 10× 10^3 cells/well and were allowed to attach for 24h. Treatments were given for 48 h, in triplicates with varied concentrations of Au NCs, NaB (50 mM), PEG -Au NC-NaB-NPs (32.5 mM with respect to NaB, ART (200 µM) and PEG-AuNC-NaB-NPs-ART (where NaB concentration is fixed i.e., 1.8 mM and varied ART concentration i.e., 100 µM). MTT was added after the completion of the treatment period in each well and incubated at 37 °C for 3 h which resulted in formazon formation. The formed formazon corresponds to the number of living cells and was formed due to reduction of MTT in respiratorial mitochondria which was dissolved in DMSO. The measurements were taken at 550 nm with background reference measured at 655

nm in multiplate reader (Tecan) and were calculated based on the following formula:

$$\%\ of\ cell\ viability = \frac{(A_{550} - A_{655})_{sample}}{(A_{550} - A_{655})_{control}} \times 100$$

4.3.4 b. *Determination of Reactive Oxygen Species Generation with FACS*

The reactive oxygen species generated on treatment with Au NCs, NaB, PEG Au NC-NaB-NPs, ART and PEG-AuNC-NaB-NPs-ART were investigated in CytoFLEX flow cytometer (Beckman Coulter) by staining the samples with 2,7-dichlorofluoresceindiacetate (DCFH-DA; Sigma-Aldrich, USA). For this 10×10^3 cells/well were seeded in 6 well plates and were allowed to grow overnight. After acquiring required confluency, the cells were treated with IC_{50} dose of Au NCs, NaB, PEG Au NC-NaB-NPs, ART and PEG-AuNC-NaB-NPs-ART for 3 h. Thereafter, the respective wells along with the control were incubated with 10 µM of DCFH-DA at 37 °C for 30 min. DCFH-DA, which is a flurogenic dye, diffuses into the cell through plasma membrane and is converted to a non-fluorescent compound DCFH by cellular esterase. The DCFH in presence of ROS generated by the cell is oxidized into highly fluorescent compound 2', 7' –dichlorofluorescein (DCF) having green fluorescence (λ_{ex}=488 nm and λ_{em}=530 nm). Thus the obtained green fluorescence was analyzed in FITC channel (530/30nm), which corresponds to green emission. For this the cells were collected after 30 min treatment and were analysed using CytoFLEX flow cytometer (Beckman Coulter).

4.3.4 c. *JC-1 staining*

Apoptosis involves series of events like release of caspase activators such as cytochrome C, alterations in electron transport, and loss of mitochondrial transmembrane potential, which ultimately resulted in cell death. For early stages of programmed cell death, many changes happen in mitochondria like variations in its membrane potential. For this a membrane-permeant cationic lipophilic dye (5,5',6,6'-tetrachloro-1,1',3,3'- tetraethylbenzimi-dazolylcarbocyanine iodide (JC-1) is widely used for effective distinction between apoptotic and healthy cells based on mitochondrial health. In normal healthy cells (high mitochondrial transmembrane potential) JC-1 naturally forms complexes known as J-aggregates

in mitochondrial matrix and gives intense red fluorescence. But in apoptotic or unhealthy cells JC-1 remains in the monomeric form as low mitochondrial transmembrane potential prevents its accumulation in the mitochondria. Therefore, the dye is disseminated throughout the cell, which leads to shifting from red (J-aggregates) to green fluorescence (JC-1 monomers) and thus gives green fluorescence. For this, the cells (10×10^3) were grown in life cell imaging plates (from Thermofisher) and treatments with IC_{50} dose of NaB (10.52 mM), PEG Au NC-NaB-NPs (8.69 mM), ART (51.40 µM) and PEG-AuNC-NaB-NPs-ART (concentration of NaB is 1.8 mM and ART is 17.32 µM) for 48 h were given. The cells were washed and phenol red free DMEM medium was added along with incubation with JC-1 dye (2.7 µM) for 10 min and then life cell imaging was conducted. CLSM was carried out in simultaneous mode for red (λ_{ex} = 525 nm) and green emission (λ_{ex} = 480 nm), respectively.

4.3.4 d. *HDAC Inhibition Assay*

HDAC inhibition was estimated using flurometric HDAC Activity Assay Kit (Sigma), which offers a simple method for the detection of HDAC activity based on a enzymatic reaction. For this, cells were incubated with NaB (10.52 mM), PEG Au NC-NaB-NPs (8.69 mM with respect to NaB), ART (51.40 µM) and PEG-AuNC-NaB-NPs-ART where NaB concentration is fixed i.e., 1.8 mM and ART concentration is 17.32 µM) for 4 h. Following treatment, the cells were lysed with buffer containing 50 mM HEPES, 150 mM NaCl, and 0.1% Triton X-100 supplemented with protease inhibitor cocktail. The obtained cell lysates were then sonicated and further experiments were performed as per the protocol provided with the kit. Tecan plate reader (Infinite® 200 PRO, Tecan, Switzerland) was used to measure the luminescence intensity with λ_{ex} = 350 nm and λ_{em} = 440 nm.

4.3.4 e. *Cell Cycle Analysis*

Propidium iodide (PI) based cell cycle analysis for DNA content measurement was carried out in CytoFLEX flow cytometer (Beckman Coulter), which distinguishes cells in different phases of the cell cycle. Here PI stains DNA quantitatively after permeabilisation. Cells (10×10^3 cells / well) were seeded in a 6 well plate and treatment with IC_{50} dose of Au NCs, NaB, PEG Au NC-NaB-NPs, ART and PEG-

AuNC-NaB-NPs-ART were given for 48 h. Thereafter cells were collected and fixed with ice cold (1 mL) 70% ethanol. Ethanol was added slowly while vortexing and cells were then stored at -20 °C for 1 h. Then 70% ethanol was removed by centrifugation by discarding the supernatant and the pellet was redispersed in PBS followed by incubation in 0.4 mg/mL RNase solution for 1 h at 37 °C. At last cells were incubated with PI (10 µg/mL) for 30 min under dark condition and thereafter analysis was carried in PE-A channel (band-pass filter, 585/42 nm) of CytoFLEX flow cytometer (Beckman Coulter) using an excitation wavelength of 488 nm. The ModFit LT software 5.0 was used for data analysis.

4.3.4 f. *TUNEL Assay*

Terminal deoxynucleotidyl transferase dUTP nick end labeling (TUNEL) is an established method for determination of DNA fragmentation, which is a characteristic hallmark of apoptosis. In TUNEL assay, bromolated deoxyuridine triphosphates (Br-dUTPs) were added to the 3'-hydroxyl (OH) termini of double- and single-stranded DNA, which is catalysed by terminal deoxynucleotidyl transferase (TdT) enzyme. Thereafter the sites are stained with FITC labeled anti-BrdU mAb and is identified with the help of flow cytometer. For this, 10×10^3 cells were seeded in 6 well plates and were allowed to grow for 24 h followed by treatment with Au NCs, sodium butyrate, PEG Au NC-NaB-NPs, ART and PEG-AuNC-NaB-NPs-ART for 48 h. The cells were collected and fixed with 1% paraformaldehyde and incubated in ice for 30-60 min. For further steps, protocols provided by the manufacturer were followed.

4.3.4 g. *PE Annexin V- 7-AAD Apoptosis Detection Assay*

For detection of early and late apoptotic cells, PE Annexin V detection kit (BD Biosciences) in conjunction with 7-amino-actinomycin (7-AAD) dye was used. In a similar way, 10×10^3 cells were seeded in 6 well plates and were allowed to grow for 24 h. This was followed by treatment with Au NCs, Sodium Butyrate, PEG Au NC-NaB-NPs, ART and PEG-AuNC-NaB-NPs-ART for 48 h. In dead cells, due to membrane damage, 7-AAD is permeable as opposed to intact membrane in viable cells. Thus viable cells are both PE Annexin V and 7-AAD negative; early apoptotic cells are PE Annexin V positive and 7-AAD negative and dead cells are both PE

Annexin V and 7-AAD positive. The samples were prepared based on the protocol provided by the company (BD Lifescience) and were analysed in CytoFLEX flow cytometer (Beckman Coulter).

4.3.5 Confocal Laser Scanning Microscopy

Confocal laser microscopy studies were carried out for uptake studies along with inhibition and mitochondrial damage assay using Zeiss LSM 880 microscope. For the uptake studies 10×10^3 cells were seeded on a coverslip in 35 mm culture plates and were incubated in CO_2 incubator for 24 h. After attaining the required morphology and confluency, cells were treated with IC_{50} dose of PEG-AuNC-NaB-NPs (8.69 mM with respect to NaB) for 4 h. Following incubation, the cells were thoroughly washed with PBS and thereafter fixed with 4% formaldehyde (10 min at 37°C). The coverslips were slowly taken out from the plate with the help of tweezers and were placed on a glass slide (upside down). The sides of the coverslips were sealed. The prepared samples were observed under Zeiss microscope LSM 880 with λ_{ex} = 405 nm and λ_{em} = 610 nm. For DAPI staining after incubation with PEG-AuNC-NaB-NPs (8.69 mM) for 4 h, cells were thoroughly washed and incubated with DAPI (2 µg/mL) for 10 min followed by fixing. To carry out imaging simultaneous mode was used (λ_{ex} = 405 nm and λ_{em} = 460 for DAPI) and (λ_{ex} = 405 nm and λ_{em} = 610 nm for PEG-Au NC-NaB-NPs).

4.3.5a. *Co-Localization Study*

To confirm the prevalence of PEG-Au NC-NaB-NPs on lysosomes, cytopainter green lysosome staining kit (Abcam) was used. Similarly, the cells were grown in a coverslip and following treatment with composite nanoparticles for 4 h, 1 mL of cytopainter green was added and incubated for 1 h. Thereafter the cells were washed with PBS twice followed by fixing and transferring into glass slides, where the edges were sealed before analysis. The samples were then analyzed (λ_{ex} = 405 nm) and (λ_{ex} = 488 nm) for the composite NPs and cytopainter green, respectively.

4.3.6 Mechanism of Cellular Uptake in Presence of Inhibitors

To understand the endocytosis mechanisms of composite nanoparticles clathrin

and claveolar inhibitors were used and luminescence based assays were carried out on multiple plate reader (Tecan) and confocal laser scanning microscopy (CLSM). The inhibitors used for studying the endocytosis mechanism were chlorpromazine (50 μM) and methyl-β-cyclodextrin (10 mM) for clathrin based endocytosis and caveolae mediated endocytosis, respectively. For Tecan based assay 10× 10^3 cells were grown in 96 well plates whereas for CLSM studies cells were grown on coverslip in 35 mm culture plates for 24 h at 37 °C. After attachment, first the cells were incubated with the inhibitors for 1 h followed by treatment with nanocomposites for 4 h. Then the cells were washed with PBS and readings were taken in Tecan (λ_{ex} = 320 nm and λ_{em} = 610 nm) whereas for CLSM studies after washing, the samples were fixed on glass slides and were analysed (λ_{ex}= 405 nm and λ_{em}= 610 nm).

4.3.7 *In Vivo* Experiments

For animal studies adult male Swiss albino mice weighing 22-25 g were used, which were obtained from Chakraborty enterprise (1443/PO/b/11/CPCSEA), Kolkata, India. The mice were retained in polypropylene cages at room temperature and relative humidity maintained at 22 ± 2 ºC and 60–70%, respectively with 12–12 h light–dark cycle. They were sheltered at Central Animal Facility, Institute of Advanced Study in Science and Technology (IASST), Guwahati, Assam and standard Rodent pellet diet (Provimi Animal Nutrition India Pvt. Ltd., India) with water ad libitum was provided. The mice were closely monitored for a week to acclimatize. The protocols for various experiments were designed and implemented as per guidelines of Committee for the Purpose of Control and Supervision of Experiments on Animals (CPCSEA), Government of India and was approved (IASST/IAEC/2016–17/2301) by the Institutional Animal Ethics Committee (IAEC) of IASST.

4.3.7a. *In vivo tumor (Dalton's Lymphoma Ascites Cells) development*

Dalton's lymphoma ascites (DLA) cells were acquired from IASST Central Animal Facility and maintained in Swiss albino mice through intraperitoneal (I.P.) injection of viable cells (1×10^6 cells/mice). Abnormal belly swelling and increased

body weight were observed within 8–10 days post induction, confirming the growth of tumor.

4.3.7b. *Acute toxicity studies*

Following the guidelines of Organization for Economic Co-operation and Development (OECD) acute toxicity studies were conducted to test the chemicals on mice. Swiss albino mice of either sex (n=6) were chosen for the experiments to perform. Before administration of test drugs the selected mice were fasted overnight and were given only water. To check the mortality a single dose of PEG-Au NC-NaB-NPs-ART at 50 mg/kg was administered separately to three mice each. Following treatment if mortality was observed in 2 out of 3 mice then the given dose was regarded as toxic and the experiment was repeated. Even if mortality was observed in 1 mice then also the experiments were repeated where treatments were given with lower doses (20, 10, 5 & 2 mg/kg body weight). Thus, based on the result of mortality doses were decided. Irwin scale parameters - like presence or absence of lethality, convulsions, straub tail, sedation, excitation, jumps, loss of balance, abnormal writhes, piloerection, stereotypies (sniffing, chewing or head movements), head twitches, scratching, abnormal respiration, aggressiveness towards the experimenter, loss of righting reflex, loss of corneal reflex, defecation, salivation and lacrimation were followed for initial assessment. Thereafter to check the mortality, mice were kept under observation for 14 days in order.

4.3.7c. *Animal Grouping and in vivo experimental design*

For *in vivo* experiments, first the acute toxicity of PEG-Au NC-NaB-NPs-ART was carried out and the doses of NaB and ART were selected from already established results. DLA cells (1×10^6 cells/mL in 0.2 ml of PBS/mice) were injected intraperitoneally on day 0 for the growth of tumor keeping aside the normal group. After growth of tumour drug treatments were started (9^{th} day) and were given in the interval of 24 h for 8 days. For the present work mice were divided in 7 groups with 10 mice in each group as follows:

- Group-I: Mice with no DLA tumour + No drug treatment

- Group-II: DLA bearing mice + 0.2 ml PBS (I.P) for 8 days
- Group-III: DLA bearing mice + Au NCs at 2 mg/kg (I.P) for 8 days
- Group-IV: DLA bearing mice + NaB at 2mg/kg (I.P) for 8 days
- Group-V: DLA bearing mice + PEG-Au NCs-NaB-NPs at 2mg/kg (I.P) for 8 days
- Group-VI: DLA bearing mice + ART at 2mg/kg (I.P) for 8 days
- Group-VII: DLA bearing mice + PEG-Au NCs-NaB-NP-ART at 2mg/kg (I.P) for 8 days

4.3.7d. *Effect of treatment on tumor Growth*

The mice were monitored and measured daily for body weight changes during the experimental period (30 days). For cell viability assay cells from all the groups were collected at the end of the drug treatment period (16 days). For biochemical and histopathological analysis on 17th day five mice from each group were sacrificed by decapitation to collect the blood, liver and kidney. To estimate the mean survival time (MST) and % increase in life span (% ILS) all the remaining 5 mice from each group were monitored up to 50 days.

4.3.7e. *Trypan Blue Test*

The cell viability assays following treatment were analysed using trypan blue. Trypan blue is a diazo dye used to stain compromised or dead cells and is not taken by live cells because of their intact cell membrane. For this, briefly, 0.1 mL of DLA cells were mixed with 0.1 mL of trypan blue (0.4 %) solution and were counted using cell counter (Countess II FL, Life Technologies, USA). The (%) of cell cytotoxicity was calculated by the following formula:

$$\%\,of\ cell\ cytotoxicity = 100 - \frac{No.of\ viable\ cells\ in\ the\ treated\ group}{No.of\ viable\ cells\ in\ the\ untreated\ control\ group} \times 100$$

4.3.7f. *Haematological profiling*

Following treatment the blood from various treatment groups were taken and were stored in vials coated with ethylenediamine tetra acetic acid (EDTA). For

haematological profiling the levels of blood components like red blood cells (RBC), white blood cells (WBC) and haemoglobin (Hb) were analyzed using haematology analysers (Sysmex, Japan).

4.3.7g. *Biochemical Parameters*

To find out the serum levels of aspartate transaminase (AST), alanine transaminase (ALT) and alkaline phosphatase (ALP) a part of blood was collected in non-anticoagulant vials after completing the drug treatment period. The collected bloods were centrifuged at 1500 rpm for 10 min at 4 °C and from which supernatant (serum) was taken and experiments were performed using biochemical kits obtained from Accurex, India following the instructions given by the manufacturer.

4.3.7h. *Histopathological Analysis*

At the end of drug treatment period i.e., on 17th day five animals from each group had been sacrificed to collect blood, liver and kidney to conduct biochemical and histopathological analyses. For histopathology analysis, livers and kidney from all the treatment groups had been collected in 10 % buffered formaldehyde and stored for at least 24 h before analysis. Further tissue samples were dehydrated through alcohol (70- 100%), cleared in xylene and embedded in paraffin blocks. Thin tissue sections (5 µm) were prepared through microtome and then stained with hematoxylin and eosin. The pathological changes were observed under light microscope and pictures were captured at 10X magnification.

4.3.7i. *Measurement of Mean Survival Time (MST) & Increase in Life Span % (ILS)*

To determine the effect of drug treatment on mortality rate of the cancer (DLA) mice, five mice from each treated groups were monitored for 50 days. Kaplan-Meier curve was established to represent the survivability of mice following drug treatment. MST and % ILS determined with the following formulas:

$$Mean\ survival\ time = \frac{[first\ death + last\ death]}{2}$$

$$Increase\ in\ life\ span(ILS)\% = \left[\frac{Mean\ survival\ time\ of\ treated\ group}{Mean\ survival\ time\ of\ untreated\ group} - 1\right] \times 100$$

4.4. Characterization

4.4.1. TEM Analysis

TEM analysis was carried out to find out the size and morphology of as-synthesized gold nanoclusters (Au NCs) and PEG-Au NC encapsulated drug nanoparticles (PEG-Au NC-NaB-NPs) by using JEOL, JEM 2100 TEM (Peabody, MA, USA), which operates at maximum accelerating voltage of 200 kV. For analysis, the as synthesized Au NCs were diluted in 1 mL of water and TEM was conducted. For PEG-Au NC-NaB-NPs first 1 mL of it was taken and centrifuged at 10,000 rpm for 5 min. The supernatant was discarded and the pellet was dispersed in autoclaved Milli-Q water (1mL). Thereafter, it was diluted in 1:10 ratio with autoclaved Milli-Q water from which 8 μL of the Au NC-NPs was drop cast onto copper coated TEM grid. The sample was left overnight for drying before analysis.

4.4.2. UV-Visible and Fluorescence Spectroscopic Measurements

UV-vis spectra of the composite NPs were recorded using Perkin Elmer Lamda 25 UV-vis spectrophotometer. For fluorescence measurements, Fluorolog-3, Horiba Jobin Yvon, Edison, NY, USA was used.

4.4.3 Dynamic Light Scattering Based Measurements

Malvern Zeta Size Nano ZS-90 instrument was used to measure the hydrodynamic diameter of the PEG Au NC-NaB-NPs and their net surface charges before and after drug encapsulation. All experiments were performed at a temperature of 25 °C and with a fixed run time of 11 s where scattering angle was fixed at 90°. For sample preparations ratio of 1:10 (Au NC-NPs: H_2O) was maintained and experiments were conducted in

triplicates in three different sets. Data analysis was carried out using the Malvern DTS 5.10 software.

4.4.4. Quantum Yield Measurements

The fluorescence quantum yield of as-synthesized PEG-Au NC-NAB-NPs was determined with quinine sulphate as reference sample where quinine sulphate was dissolved in 0.1 M H_2SO_4. To calculate the quantum yield of PEG-AuNC-NAB-NPs the following equation has been used:

$$QY_S = QY_R \times \frac{A_S}{A_R} \times \frac{Abs_R}{Abs_S} \times \frac{\eta_S^2}{\eta_R^2}$$

Where,

QY_S = quantum yield of as synthesized PEG-AuNC-NAB-NPs (sample)

QY_R = quantum yield of quinine sulphate, which was dissolved in 0.1 M H_2SO_4 (reference). The standard quantum yield of the reference (QY_R) is 0.54.

A_S = area under the emission spectrum of PEG-AuNC-NaB-NPs obtained at λ_{ex} = 320 nm at slit-width = 2 nm

A_R = area under the emission spectrum of reference

Abs_R = absorbance of the reference

Abs_S = absorbance of the sample

η_S = refractive index of solvent of sample

η^2_R = refractive index of solvent of reference

4.4.5. Confocal Laser Scanning Microscopy

Confocal laser scanning microscopy was conducted using LSM 880 Carl Zeiss microscope. All the experiments were performed after following the respective protocols required for specific experiments and mostly fixed cells were used for imaging. In case of JC-1 staining live cell imaging was carried out.

4.5. Results and Discussions

The polymer coated drug encapsulated nanoparticles were fabricated with red emitting chitosan stabilized Au NCs by slightly modifying the previous protocol.[33] The schematic representation of formulation of luminescent PEG-Au NC coated drug encapsulated composite nanoparticles and their synergistic combinational therapeutic activity *in vitro* as well as *in vivo* highlighting the probable mechanism are elucidated in **(Figure 4.1)**.

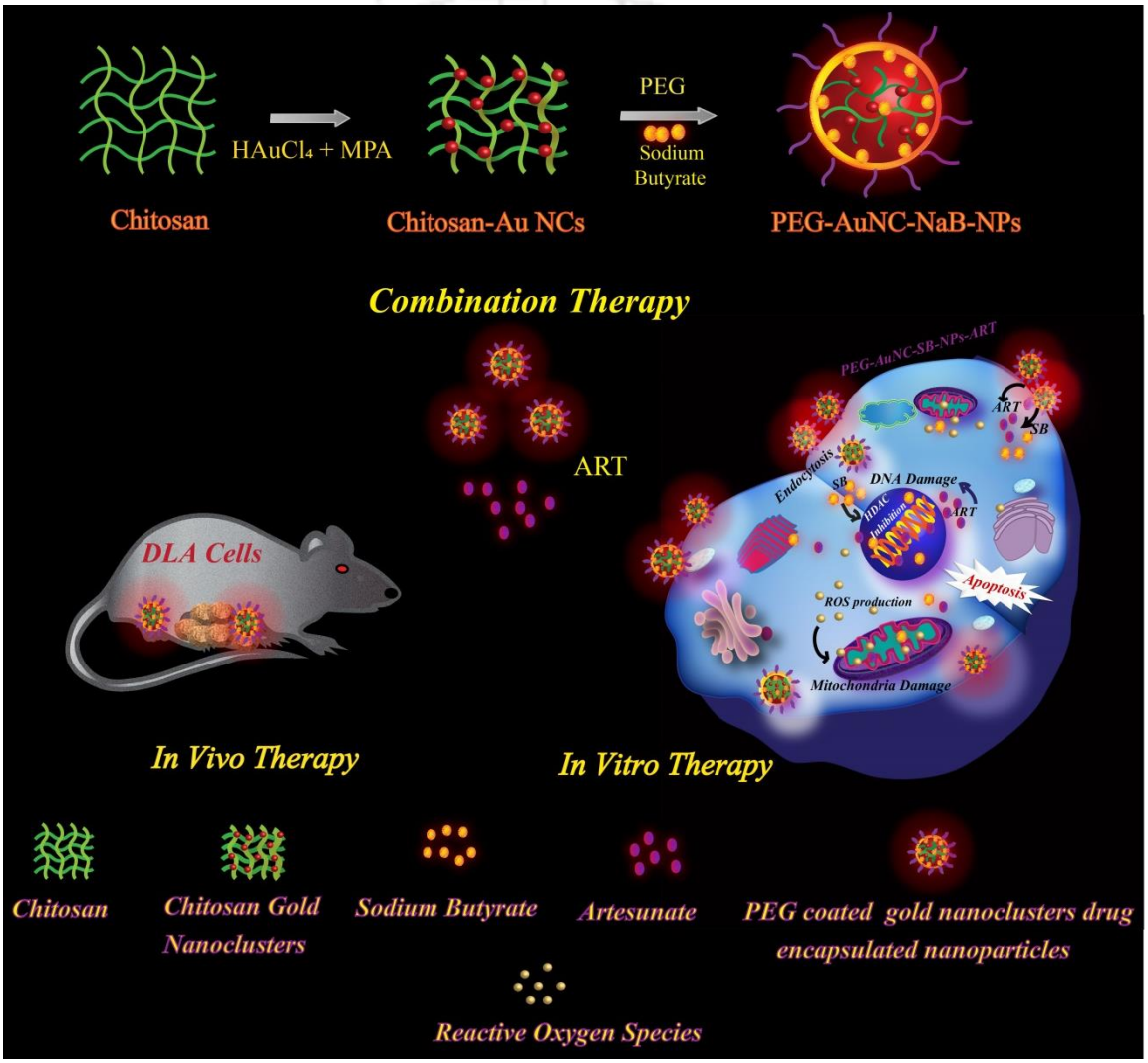

Figure 4.1. Schematic representation of formulation of luminescent PEG-Au NCs drug encapsulated composite nanoparticles (PEG-Au NCs-NaB-NPs) and their synergistic combinational therapeutic activity *in vitro* and *in vivo* systems.

The transmission electron microscopy (TEM) image revealed formation of average of 1.4 ± 0.4 nm of Au NCs **(Figure 4.2)**, as calculated from 100 particles, which were transformed into polymer coated drug encapsulated nanoparticles with the help of negatively charged drug sodium butyrate and nominally charged PEG molecules.

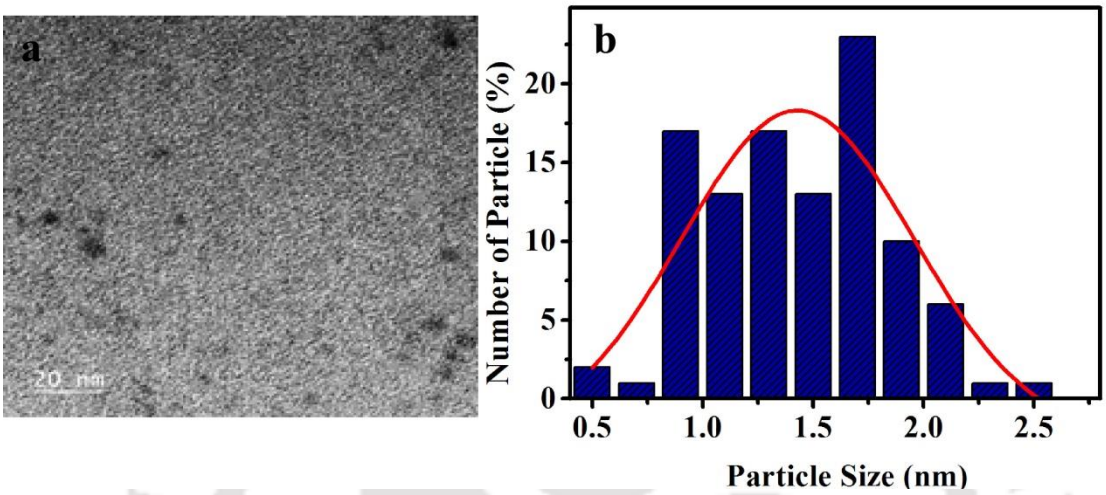

Figure 4.2. (a) TEM image of Au NCs (scale bar 20 nm) and (b) particle size distribution of Au NCs.

Moreover, the absence of any surface plasmon resonance (SPR) peak in the visible region rules out the formation of gold nanoparticles **(Figure 4.3)**.

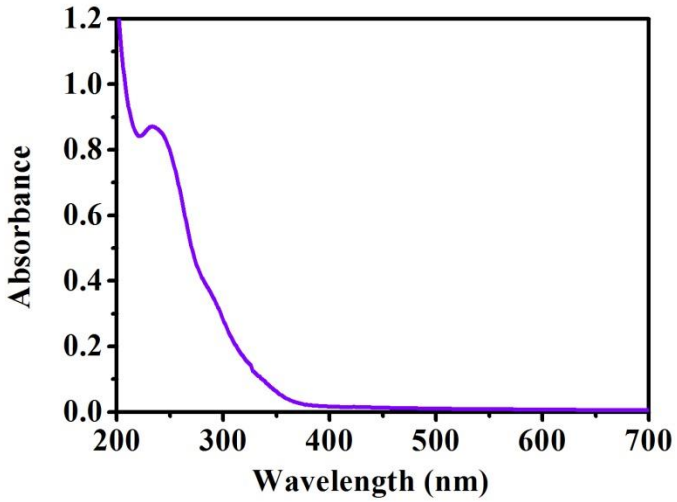

Figure 4.3. UV-vis spectrum of as-synthesized chitosan stabilized Au NCs.

The formation of spherical polymer coated drug encapsulated composite nanoparticle (PEG-Au NC-NaB-NPs) has been confirmed with TEM image **(Figure 4.4a)** with Au NCs embedded on its surface **(Figure 4.4b)**, while no characteristic selected area electron diffraction (SAED) pattern for Au metal **(Figure 4.4c)** was observed. The average particle size of the composite nanoparticles was calculated to be 99.62 ± 18.25 nm (**Figure 4.4d)** using Image J software. The particle size obtained herein is greater than established chitosan tripolyphosphate nanocarrier with Au NCs (72.1 ± 21.8) mainly because of PEG coating as PEGylation increased the size along with its colloidal stability and reduced the surface charge density.[29,30,31]The nanoparticle formation would take place due to the electrostatic

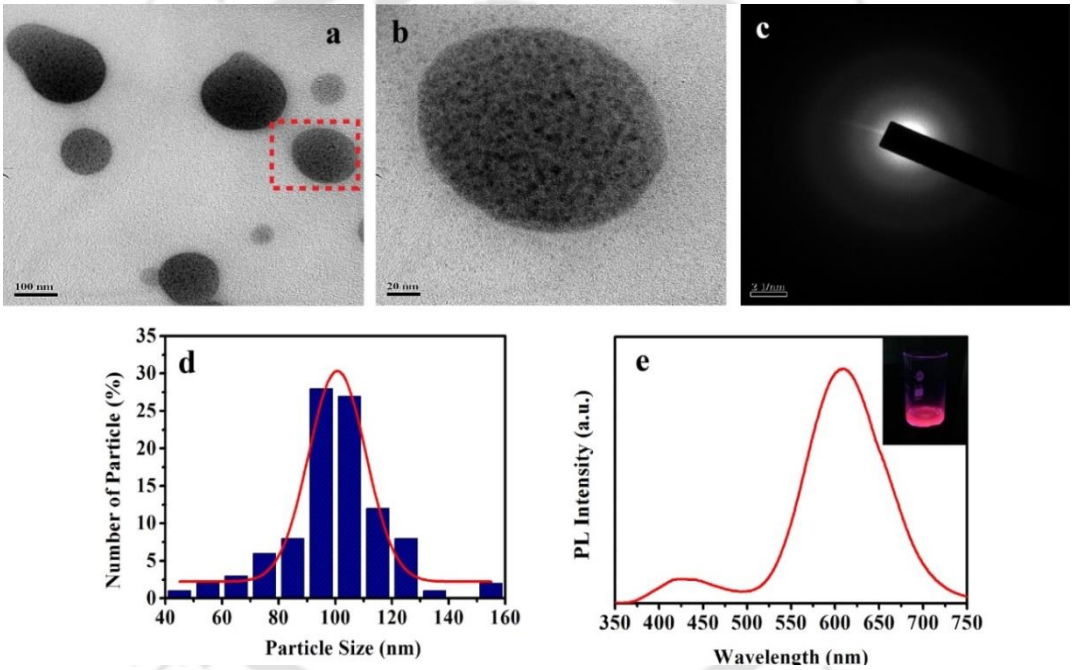

Figure 4.4. (a) TEM image of PEG-Au NC-NaB-NPs (scale bar 100 nm) with the portion to be magnified is marked in red. (b) Magnified image of the same sample clearly showing embedded Au NCs on its surface. (c) SAED pattern obtained from image in (b) showing no characteristic peaks of Au metal. (d) Histogram showing the particle size distribution of PEG-Au NC-NaB-NPs (as calculated from Figure 1b and from the others images taken from different sets of experiments). (e) Photoluminescence spectrum of as synthesized PEG-Au NC-NaB-NPs (λ_{ex} =320 nm) and the digital photograph in the inset showing bright red luminescence of PEG-Au NC-NaB-NPs under UV trans-illuminator.

interaction between positively charged chitosan Au NCs and negatively charged sodium butyrate and PEG might have helped in modifying its surface. To corroborate this, zeta potential studies were conducted, which revealed surface of charge of 34.65 ± 8.35 mV and – 5.10 ± 3.24 mV for Au NCs and NaB, respectively,

the value of which was 8.97 ± 5.8 mV **(Figure 4.5)** after polymeric nanoparticle formation. Synthesis of polymeric nanoparticle with chemotherapeutic drug is

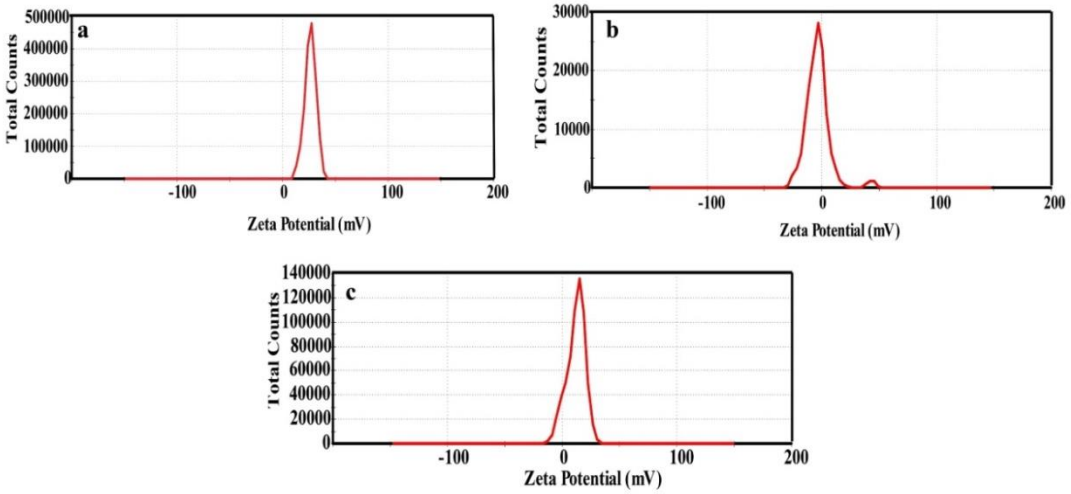

Figure 4.5. Zeta potential of (a) Au NCs, (b) NaB and (c) PEG-Au NC-NaB-NPs.

well established where PEG has been extensively used for nanoparticle formation with some of the known standard drugs (e.g., doxorubicin).[29,32] Polymeric nanocomposites are known to have better drug encapsulation capacity and delivery and help in sustained drug release with prolonged circulation half-life.[43] The as synthesized PEG-Au NC-NaB-NPs displayed strong red emission at 610 nm (λex = 320 nm) as shown in **(Figure 4.4e)** and in its inset image. The quantum yield of the composite nanoparticle was calculated to be 6.8%, using quinine sulphate as the standard and thus can be used for theranostic. The hydrodynamic size of the PEG-Au NC-NaB-NPs was found to be 147.62 ± 10.21, measured with the help of dynamic light scattering (DLS) based studies **(Figure A 4.1, Appendix).**This increment in size with respect to the size measured from TEM may be due to the presence of chitosan and PEG polymer surrounding the composite NPs.

To determine the % of drug encapsulated on PEG-Au NC-NaB-NPs, binding assay was carried out by probing the luminescence of the as synthesized composite NPs. Probing the luminescence of the composite NPs is one of the common methods used for enumerating drug binding (%).[27] Here a negatively charged drug NAB served as ion gelating agent for nanoparticle synthesis and PEG helped in its encapsulation, which was carried out based on solvent exchange

method and precipitation.[44,45] For this various concentrations (10 - 60 mM) of drugs were used for nanoparticle synthesis as mentioned in the experimental section. After synthesis, the aqueous phase was collected and centrifuged at 10,000 rpm for 10 min. The pellet was redispersed in 2 mL Milli-Q water and pH was maintained at ~7 and the luminescence was measured (λ_{ex} = 320 nm and λ_{em} = 610 nm). It was found that nanoparticle synthesis with 50 mM of concentration NaB retained 65% of drug in the nanocomposite after which it became saturated **(Figure A 4.2, Appendix).** Thus, dispersion of PEG-Au NC-NaB-NPs (50 mM) has 32.5 mM of NaB in it after encapsulation.

For effective application of this composite NP in theranostics the size and its luminescence plays a pivotal role. First the bright luminescence of the PEG-Au NC-NaB-NPs was probed. There are many reports of use of metal nanoclusters for theranostics because of their intense luminescence, good quantum yields, tunable fluorescence emission, large Stokes shift and high photostability as opposed to conventional dyes, which undergo photo bleaching.[27,28] To elucidate its role in internalization and real time imaging of cancer cells, PEG-Au NC-NaB-NPs were incubated with cervical cancer cell line (HeLa cells) for 4 h and confocal laser scanning microscopic (CLSM) studies were carried out. Bright red luminescence was clearly observed inside the cells as shown in **(Figure 4.6b)**, substantiating their uptake by HeLa cells. This was further confirmed by depth projection (Z-stack) studies, which validated their successful internalization inside the cells **(Figure 4.6c)**. The control cells i.e., cells without treatment with PEG-AuNC-NaB-NPs did not reveal any luminescence **(Figure A 4.3, Appendix)**. This shows the potential of use of PEG-Au NC-NaB-NPs in cancer theranostics.

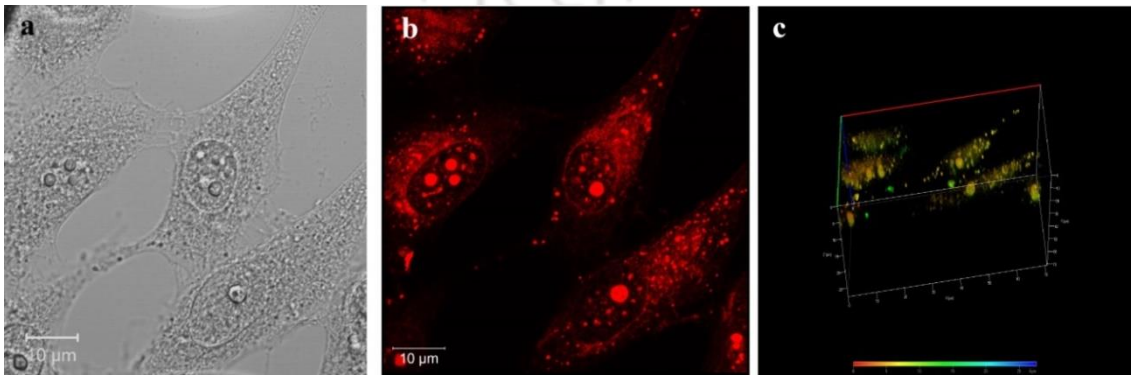

Figure 4.6. Confocal laser scanning microscopy images of HeLa cells after incubation with PEG-Au NC-NaB-NPs for 4 h. (a) Bright field of image HeLa cells. (b) HeLa cells showing distinct red emission due to uptake of luminescent PEG-Au NC-NaB-NPs and (c) Z-stack projection of the cell imaged in (b) confirming the uptake of the NPs.

We have also explored the intracellular localization of the synthesized composite NPs on HeLa cells to find out whether they penetrated the nuclear membrane and entered the nucleus or were localised in the lysosomes. For this the treated cells were incubated with 2 μg/mL of DAPI (for 10 min) and cytopainter green (for 2 h). Lack of co-localization of the composite NPs (PEG-Au NC-NaB-NPs) with nucleus marker DAPI was observed after 30 min of incubation as can be seen in the merged image **(Figure 4.7d)**, whereas **(Figure 4.7a and b)** , shows red and blue luminescence of the probe and DAPI, respectively. This was carried out in CLSM with simultaneous mode where λ_{ex} and λ_{em} of the composite NPs and nuclear marker were fixed in different channels (λ_{ex} = 405 nm and λ_{em} =620 nm and 460 nm).

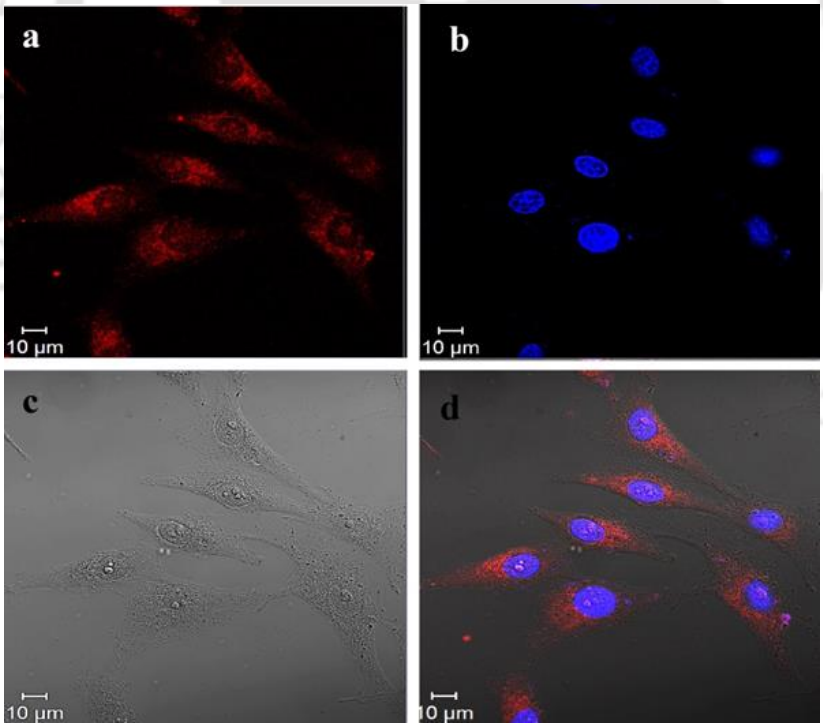

Figure 4.7. Confocal laser scanning microscopy images of HeLa cells after 4 h of treatment with PEG-Au NC-NaB-NPs and with nucleus staining marker DAPI (10 min). (a) Luminescence of PEG-Au NC-NaB-NPs as observed in red channel (λ_{ex} = 405 nm and λ_{em} = 610 nm), (b) luminescence of cells labelled in nuclear marker DAPI (λ_{ex} = 355 nm and λ_{em} = 460 nm), (c) bright field image and (d) merged image of a, b and c.

Comparatively noticeable colocalistaion was observed with cytopainter green that specifically stains the lysosomes. It is to be mentioned here that the cells (i.e., those treated with the composite NPs and without cytopainter green) showed only red luminescence **(Figure 4.8b)** and nothing was observed in the green channel **(Figure 4.8c).** But the cells treated with the PEG-AuNC-NaB-NPs and cytopainter green clearly revealed colocalisation of the probe with cytopainter green in the merged image **(Figure 4.8h)** confirming its presence in the lysosomes. In **Figure 4.8f**, red luminescence represents internalisation of the composite NPs and green luminescence in **Figure 4.8g** is due to staining of only lysosomes with cytopainter green. Thus the internalized PEG-Au NC-NaB-NPs were randomly distributed in the perinuclear region and the lysosomal compartments. The samples were analysed in CLSM with (λ_{ex} = 405 nm) and (λ_{ex} = 488 nm) for the composite NPs and cytopainter green, respectively. Chitosan used as a template for synthesis of Au NCs in our system has N-acetylglucosamine units, which have an affinity towards N-linked glycans present on lysosomal membrane and this might be the prime reason for its localisation in the lysosomes.[46]

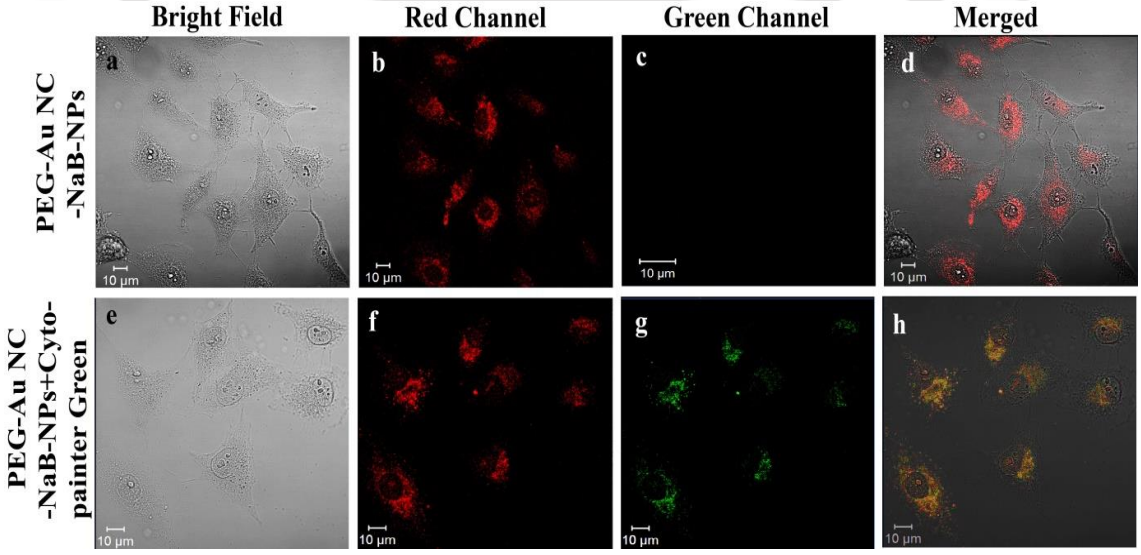

Figure 4.8. Confocal Laser Scanning Microscopy images of HeLa cells showing intracellular distribution of PEG-Au NC-NaB-NPs after 4 h of incubation. (a) Bright-field image of the cell, (b) luminescence observed under red channel (λ_{ex} = 405 nm and λ_{em} = 610 nm), (c) luminescence observed under green channel (λ_{ex} = 488 nm and λ_{em} = 520 nm) and (d) merged image of (b) and (c). CLSM images of HeLa cells incubated along with counter stain cytopainter green. (e) Bright field image, (f) luminescence observed under red channel (λ_{ex}= 405 nm and λ_{em} = 610 nm), (g) luminescence observed under green

channel (λ_{ex}= 488 nm and λ_{em} = 520 nm) and (h) merged imaged of (f) and (g) showing yellow colour confirming its localization in lysosome.

Localistaion of PEG-Au NC-NaB-NPs on lysosomes mainly suggests their internalisation through endosomal pathway as transfer to the lysosomes validates the characteristic transport pathway of nanoparticles internalised by endocytotosis.[47] As mentioned earlier, the size of the nanoparticle also plays an crucial role in its uptake. Nanoparticles with size < 200 nm are usually taken by the endocytic pathway, which is mainly divided into clathrin-dependent, caveolae, macropinocytosis, and phagocytosis pathways.[48] To shed light in the cellular uptake mechanism of PEG-AuNC-NaB-NPs, two inhibitors were used, namely, chlorpromazine (50 μM) and methyl-β-cyclodextrin (10 mM), which are known clathrin and claveolae mediated endocytosis inhibitors. In this context, HeLa cells were incubated with the respective inhibitors for 1 h prior to their treatment with PEG-AuNC-NaB-NPs for 4 h. Quantitative analysis revealed significant decrease in the luminescence intensity to 15.85 ± 2.9 % and 61.22 ± 3.4 % with chlorpromazine and methyl-β-cyclodextrin, respectively, from that of control **(Figure 4.9)**. This was further corraborrated with CLSM studies where less uptake of PEG-Au NC-NaB-NPs was observed in chlorpromazine **(Figure 4.10 iii)** treated cells as compared with that of PEG-Au NC-NaB-NP treated cells without inhibitor **(Figure 4.10 i).** Negligible luminescenc was observed in methyl-β-cyclodextrin treated cells **(Figure 4.10 iv)**, which emphasized that the uptake of PEG-Au NC-NaB-NPs was primarily through claveolae mediated endocytosis.

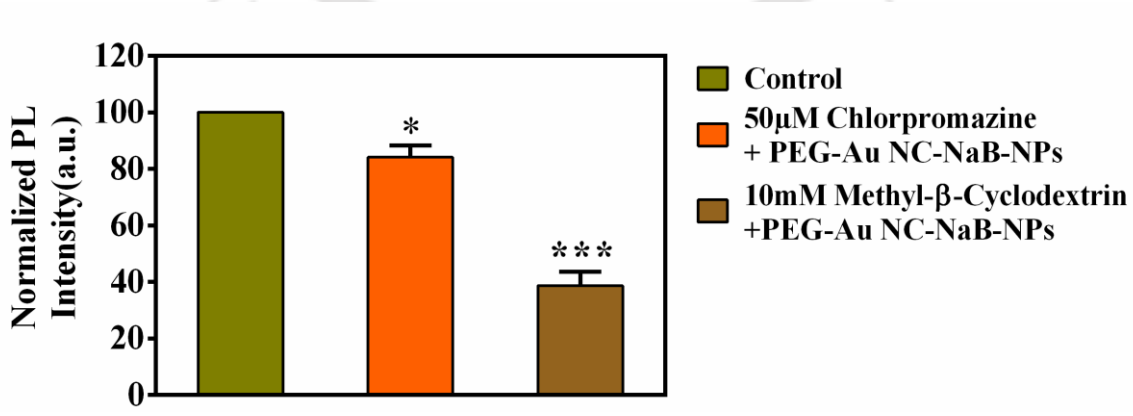

Figure 4.9.(a) Quantitative analysis of cellular uptake of PEG-Au NC-NaB-NPs by HeLa cells after 1 h incubation with chlorpromazine (50 μM) and methyl-β-cyclodextrin (10 mM) inhibitors. All the measurements were carried out in triplicates and luminescence

was measured in Tecan (λ_{ex} = 405 and λ_{em} = 610 nm). Here control stands for HeLa cells treated with PEG-Au NC-NaB-NPs (without inhibitors) for 4 h.

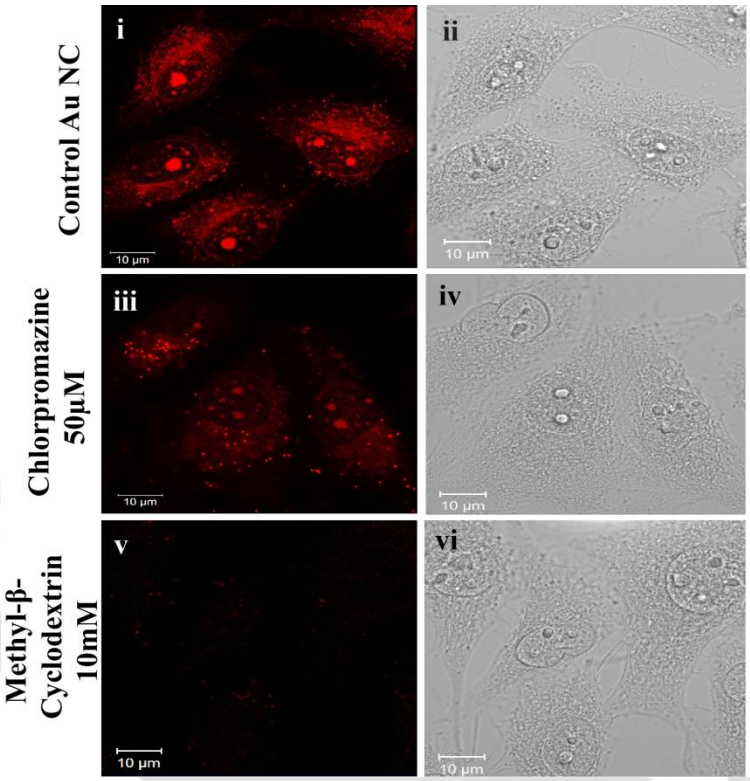

Figure 4.10. Inhibition assay of HeLa cells treated with PEG-Au NC-NaB-NPs (i) Luminescence of the cells in red channel without any inhibitors (λ_{ex} = 405 and λ_{em} = 610 nm), (ii) bright field image of (i), (iii) Luminescence of the cells after pre-treatment with chlorpromazine (50 µM for 1h), (iv) bright field of (iii), (v) Luminescence of the cells after pre-treatment with methyl-β-cyclodextrin (10 mM for 1h) and (vi) bright field image of (v).

To evaluate the potential therapeutic impact of PEG-Au NC-NaB-NPs and combination therapy with drug (ART), MTT based cell viability assay was carried out. The cytotoxic activity was tested on cervical cancer cells (HeLa) with 48 h of treatment. The drug involved herein for combination therapy was NaB, which was encapsulated on the composite NPs (32.5 mM) and in conjunction with ART (100 µM) added separately. First the cytotoxic effect of NaB and ART were checked invidually. After 48 h of treatment with NaB and ART, MTT assay exhibited cell viability of 43.7 % and 40.23% at 11.1 mM and 51.3 µM concentration of NaB and ART, respectively **(Figure 4.11a and b).** The IC_{50} values, calculated by nonlinear regression curve fit using Graphpad Prism Software, were found to be 10.52 mM for NaB and 51.40 µM for ART. The cytotoxic activity of control Au NCs showed

viability of 87.38% **(Figure A4.4, Appendix)**, whereas after synthesis of PEG-Au NC-NaB-NPs the viability was found to be 22.24 % at concentration of 11.1 mM of NaB, which is possibly due to encapsulation of the drug. The IC_{50} value for PEG-Au NC-NaB-NPs was found to be 8.69 mM with respect to NaB, which is lower than IC_{50} dose of control NaB (10.52 mM) as observed in **(Figure 4.11c).** For combinational therapy different ratios of PEG-Au NC-NaB-NPs (32.5 mM) and ART (100 µM) were used and it was found to have enhanced activity. It is to be mentioned here that after several trials PEG-Au NC-NaB-NPs of fixed concentration (1.8 mM) was given to all the cells. With fixed concentration of PEG-Au NC-NaB-NPs varied concentrations of ART (4.4, 8.8, 13.3, 17.7 and 22.2 µM) were added. The results after 48 h of treatment exhibited significant reduction in the cell viability % **(Figure 4.11d).** The IC_{50} value for the combination therapy of PEG-Au NC-NaB-NPs with ART was calculated to be 1.8 mM and 17.32 µM for NaB and ART, respectively, which were prominently less than individual IC_{50} doses of NaB (10.52 mM) and ART (51.40 µM). Thus the combination therapy helped to use drugs at lower dose, which reduces the cytotoxic activity of its individual doses; however, it enhances the efficacy suggesting the augmentation of synergistic activity. To establish the synergistic effect between PEG-Au NC-NaB-NPs and ART, the isobologram and combination index (CI) were calculated by using the CalcuSyn software (Biosoft, Version 2.1). The isobologram plot can be explained based on Median-Effect Equation (Chou) and the Combination Index Theorem (Chou-Talalay). The combination index values (CI values) were used to characterize as synergy (CI < 1), additivity (CI=1) and antagonism (CI > 1).[49] The isobologram plot of combination therapy of PEG-AUNC-NaB-NPs and ART (Figure 5d) revealed that the obtained values of all the data points were < 1 (CI <1), which signify drug-drug interactions **(Figure 4.11e)**. The CI values for all the combinations were given in **(Table A4.1, Appendix)**. Hence, combination therapy with NaB and ART augmented the efficacy with heightened synergistic activity, outweighing the benefits of monotherapy and a prevalent combination therapy associated with many side effects and paves a new way for plant based combinational therapy with naturally available drug.

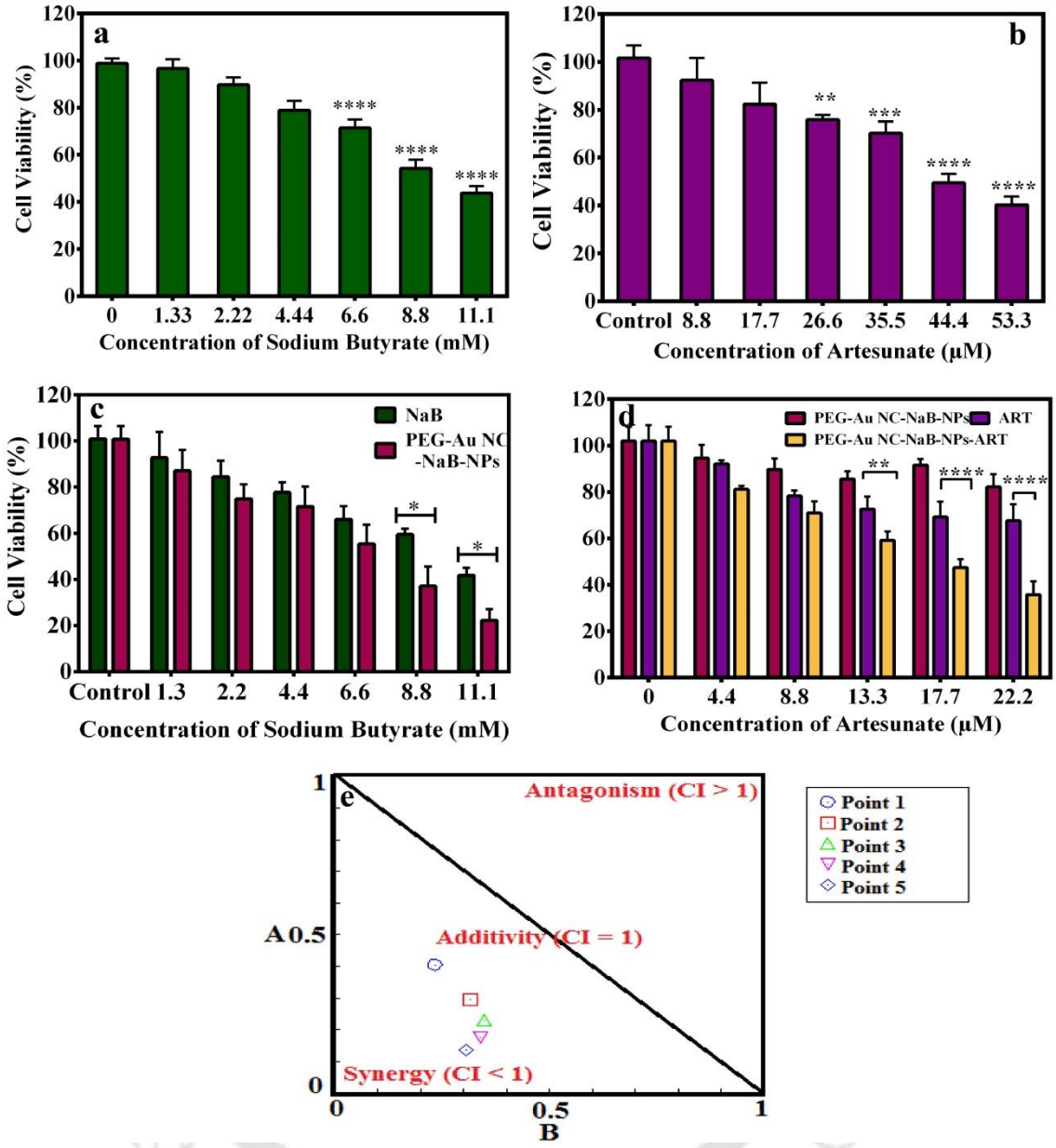

Figure 4.11. Cell viability based MTT assay of HeLa cells after 48 h of treatment. All sets of experiments were carried out in triplicates and are represented as the mean ± SD. The ANOVA test was also carried out for each set where '*' ($p < 0.05$), '**' ($p < 0.005$), '***' ($p < 0.001$) and '****' ($p < 0.0001$) represent statistical significance. (a) Cell viability assay of NaB (50 mM), (b) Cell viability assay of artesunte (200 µM), (c) Cell viability assay of PEG-Au NC-NaB-NPs(32.5 mM with respect to sodium butyrate), (d) Cell viability assay of combination therapy of PEG-Au NC-NaB-NPs –ART) and (e) Isobologram analysis and combination index (CI) values of combination therapy doses. All the values were obtained below the line of additivity to indicate synergistic effect. Isobologram analysis was calculated using Calcusyn software.

To investigate the mode of impact exerted by combination therapy of PEG-Au NC-NaB-NPs-ART and possible mechanism of synergistic therapeutic activity fluorescence- activated cell sorting (FACS) based assays were carried out. First

generation of reactive oxygen species were evaluated by measuring the DCF fluorescence in HeLa cells following treatments with Au NCs, NaB, ART, PEG-AuNC-NaB-NPs and PEG-AuNC-NaB-NPs-ART. It was found that trivial amount of ROS was generated with Au NCs only but significant enhancement of the florescence of DCF was observed with NAB, ART, PEG-AuNC-NPs and PEG-AuNC-NaB-NPs-ART treated cells from that of the control **(Figure 4.12).** It is to be mentioned here that the maximum shift of peak for PEG-AuNC-NaB-NPs-ART treated cells was mainly because of synergistic action of NaB and ART where both the drugs are known to generate ROS.[37,41,42]

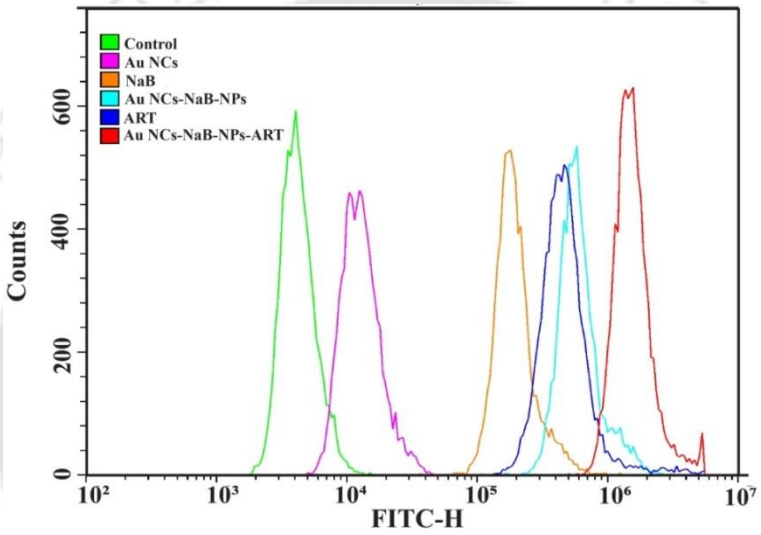

Figure 4.12. FACS analysis of ROS production evaluated by DCF fluorescence in HeLa cells investigated in FITC-H channel, which corresponds to the green emission of the DCF. Cells were treated with IC_{50} dosage of Au NCs, NaB, ART, PEG-AuNC-NaB-NPs and PEG-AuNC-NaB-NPs-ART, which exhibited prominent shifts as compared to that of control cells.

In artesunate treated cells, oxidative cleavage occurs leading to ROS production.[41] Elevated ROS production with NaB and ART might be associated with dysfunction of the mitochondria.[37,50] To enlighten the fact, mitochondrial membrane potential damage was measured with 5,5',6,6'-tetrachloro-1,1',3,3'-tetraethylbenzimi-dazolylcarbocyanine iodide JC-1 dye and observed under CLSM. It was found that the merged image of HeLa cells treated with PEG-AuNC-NaB-NPs-ART primarily showed green luminescence **(Figure 4.13 t)** as opposed to that of control that showed red luminescence **(Figure 4.13d).** The primary reason was due to high mitochondrial membrane potential of the control cells (without

treatment) that allowed to form J-aggregates and exhibited red emission, whereas in the cells treated with PEG-AuNC-NaB-NPs-ART they failed to undergo aggregation (due to low mitochondrial membrane potential) and remained in monomeric form to show green emission. As clearly observed from the merged images that enhanced green luminescence was observed with ART and PEG-AuNC-NaB-NPs-ART treated cells **(Figure 4.13 p and t)** were mainly due to mitochondrial dysfunction. In cells treated with NAB and PEG-AuNC-NaB-NPs less dysfunction of mitochondria had occurred **(Figure 4.13h and i)** and hence, the effect of ART in mitochondrial damage was evident. At the same time histone

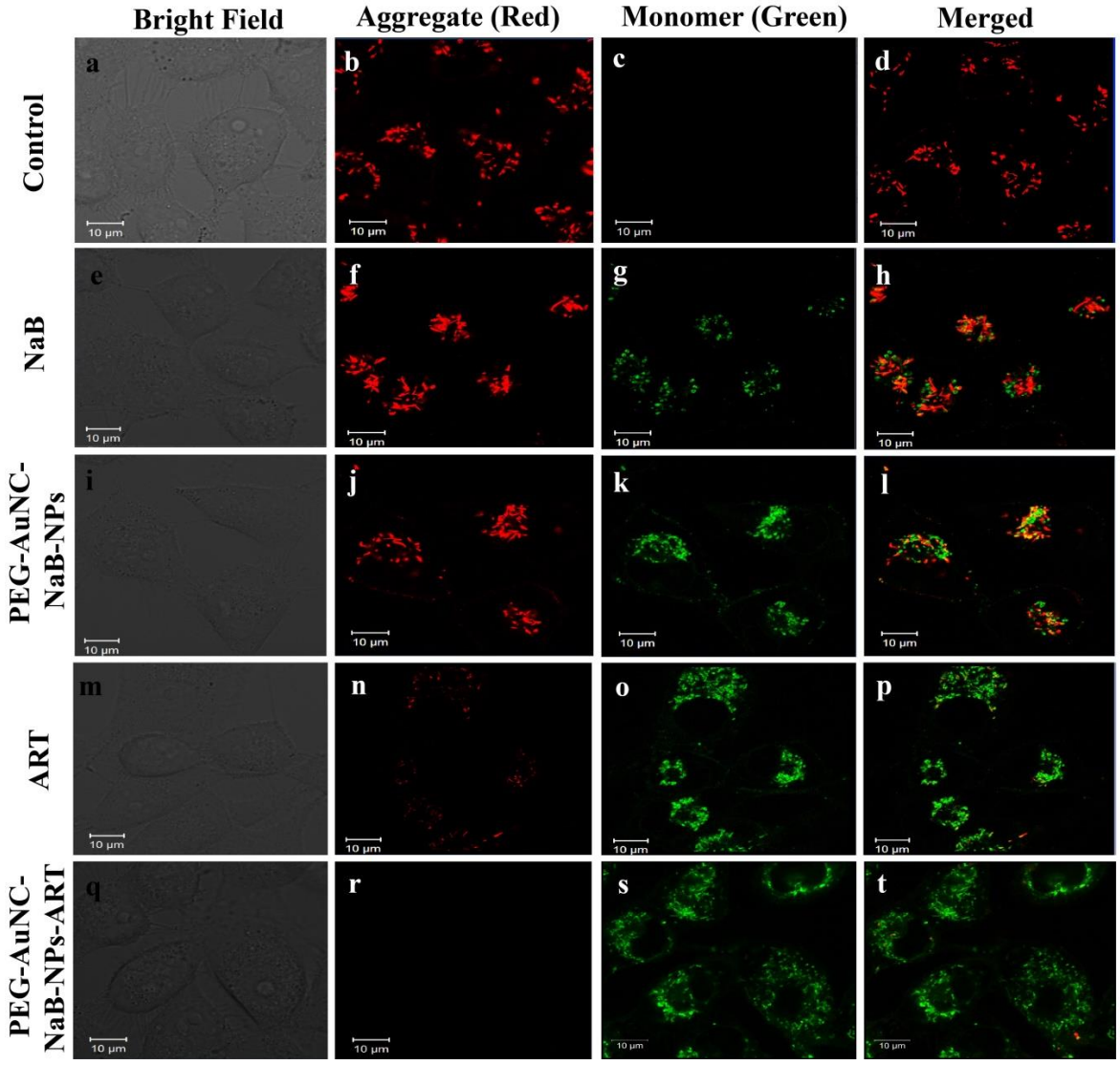

Figure 4.13. Confocal laser scanning microscopy (CLSM) images of control HeLa cells with JC-1 dye. 1st row: (a) Bright field image, (b) red channel, (c) green channel, (d) merged image of a, b and c. 2nd row: Hela cells treated with NaB (10.52 mM),(e) Bright

field image, (f) red channel, (g) green channel, (h) merged image of e, f and g. 3rd row: Hela cells treated with PEG-AuNC-NaB-NPs (8.69 mM). (i) Bright field image, (j) red channel, (k) green channel, (l) merged image of i, j and k. 4th row: Hela cells treated with ART (51.40 µM). (m) Bright field image, (n) red channel, (o) green channel, (p) merged image of m, n and o. 5th row: HeLa cells treated with PEG-AuNC-NaB-NPs-ART. (q) Bright field image, (r) red channel, (s) green channel and (t) merged image of q, r and s.

deacetylases activity (HDAC) were also checked as NaB is known to induce HDAC inhibition, which is an upcoming treatment domain of cancer inhibition.[37,38] For this HDAC assay kit, fluorometric was used for detection of HDAC activity. HDAC activity analysis of HeLa cell lysates treated with NaB (10.52 mM), PEG-A NC-NaB-NPs (8.69 mM with respect to NaB) and PEG-Au NC-NaB-NPs-ART (1.8 mM of NaB and 17.32 µM of ART) revealed significant decrease in the luminescence intensity as compared with that of untreated HeLa cell lysates luminescence **(Figure 4.14)**. Hence the role of NAB in HDAC inhibition might have contributed in enhanced synergistic activity.

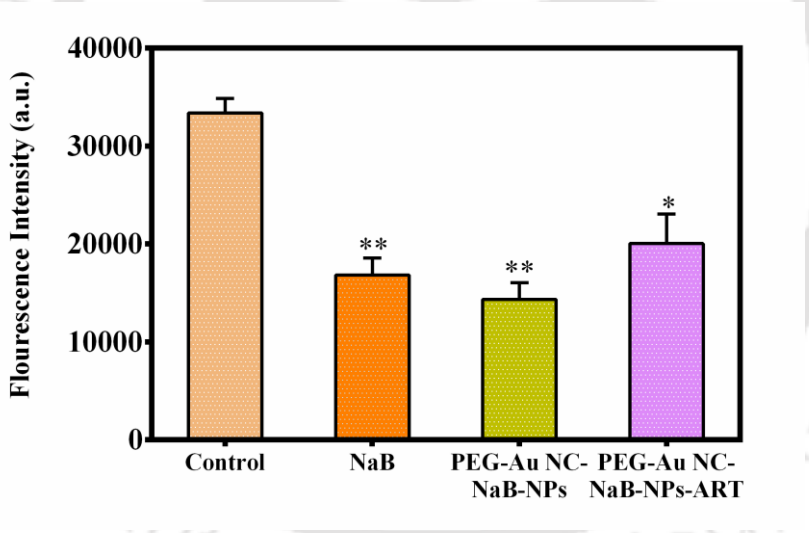

Figure 4.14. Flurometry based HDAC activity of cell lysates of HeLa cells, following treatments with NaB (10.52 mM), PEG-AuNC-NaB-NPs (8.69 mM) and PEG-AuNC-NaB-NP-ART (1.82 mM with respect to NaB and 17.7 µM ART).

Further the effect of combination therapy on cell cycle progression of HeLa cells, were also examined by flow cytometric analysis with PI staining, where arrest in the G0/G1 phase of the cell cycle was observed in case of cells treated with PEG-AuNC-NaB-NPs-ART. The cell population (%) in the G0/G1 phase after treatment with PEG-AuNC-NaB-NPs-ART was considerably higher (76.7%) than

that of the cells treated with individual drugs NaB (53.64%) and ART (68.47%) **(Figure 4.15)**. This can be attributed to DNA damage caused by ART, which was

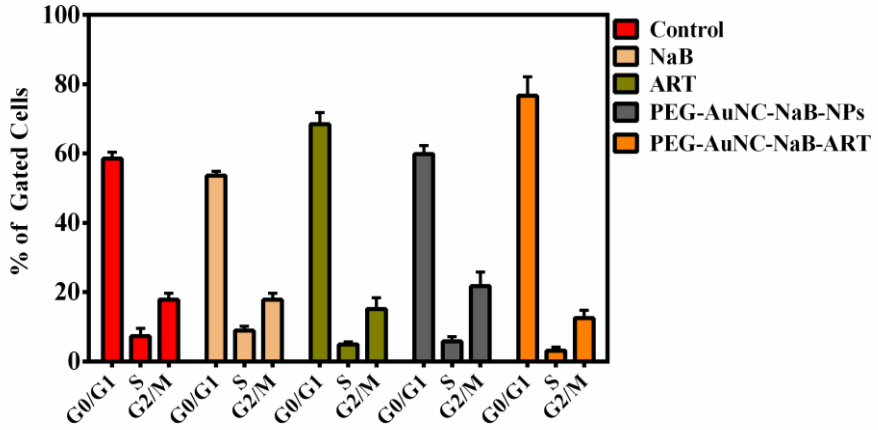

Figure 4.15. FACS based cell cycle analysis of HeLa cells treated with NaB, ART, PEG-AuNC-NaB-NPs and PEG-AuNC-NaB-NPs-ART along with its control.

more in case of combinational therapy. Additionally, terminal deoxynucleotidyl transferase dUTP nick end labelling assay (TUNEL assay) was also performed, which is a method for detecting apoptotic DNA fragmentation and is a hallmark of late apoptosis. In this, addition of bromolated deoxyuridine triphosphates (Br-dUTP) takes place on the broken or fragmented 3'-hydroxyl (OH) termini of DNA and is catalysed by terminal deoxynucleotidyl transferase (TdT) enzyme. These were analysed by staining the cells with a FITC-labeled anti-BrdU mAb and was observed under flow cytometry in green channel. From the histogram obtained **(Figure 4.16)** it was evident that there was a shift in green fluorescence intensity in the PEG-AuNC-NaB-NP treated cells, which is proportional to fragmented DNA. After 48 h of treatment with PEG-AuNC-NaB-NPs, 25.46% of TUNEL positive cells

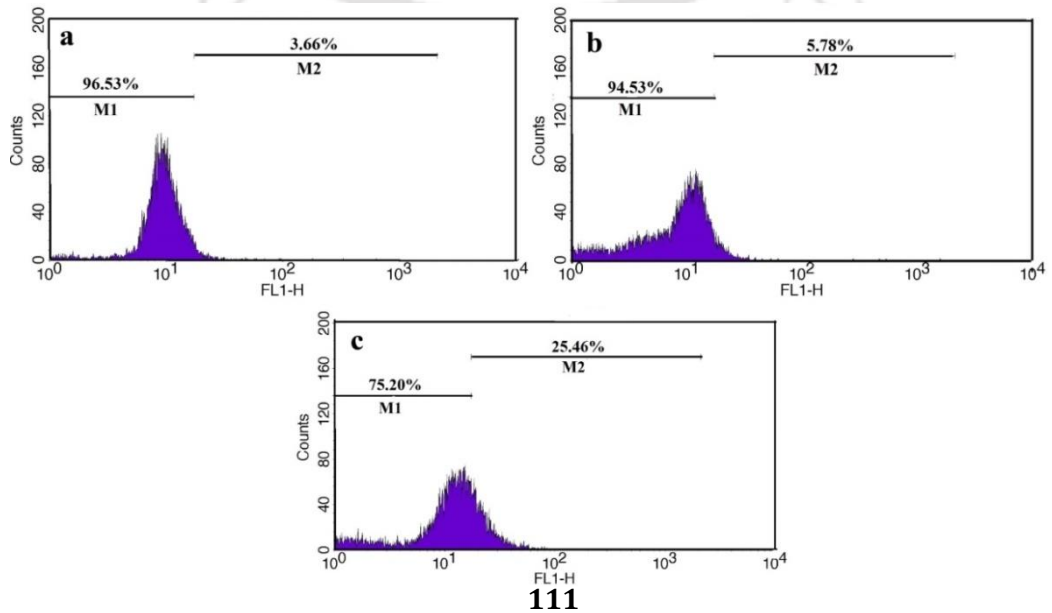

Figure 4.16. Flow cytometry histograms of TUNEL assay showing the shifting of population towards FL1-H green channel, which is due to DNA fragmentation. The luminescence intensity after treatment: (a) control (without treatment), (b) sample treated with PEG-Au NC-NaB-NPs (8.69 mM) and (c) treated with PEG-Au NC-NaB-NPs-ART (1.8 mM NaB and 17.7 μM ART).

were found, whereas negligible amount of TUNEL positive cells of 5.78% was found in case of PEG-AuNC-NaB-NPs that indicates the role of ART on DNA damage. To ensure apoptosis as the mechanism of cell death, FACS based Annexin V-7AAD assay was performed where significantly greater percentage (52.73%) of apoptotic cells were obtained after treatment with IC_{50} dose of PEG-Au NC-NaB-NPs-ART followed by observation of 34.64%, 27.18% and 14.24% of apoptotic cells following treatment with ART, PEG-Au NC-NaB-NPs and NaB, respectively **(Figure 4.17)**.

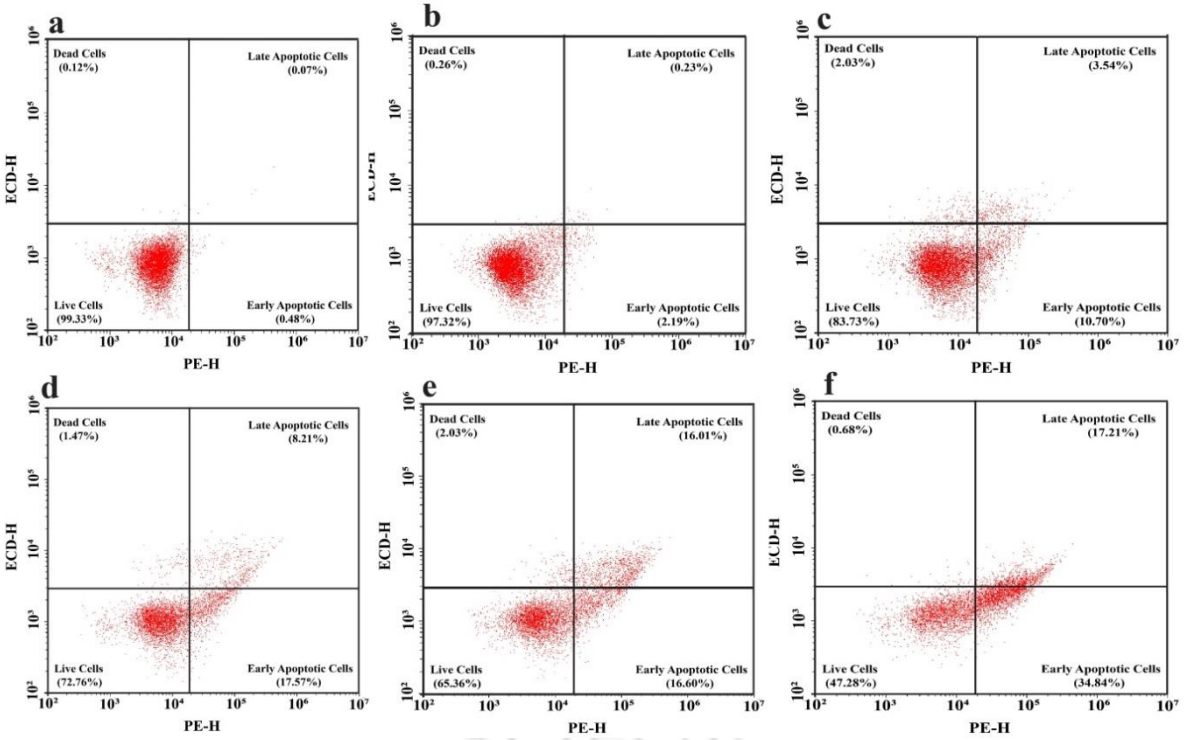

Figure 4.17. Flow cytometric analyses of annexin-V-7-AAD stained HeLa cells. The dot plots are divided into 4 quadrants, where second and third quadrants denote early apoptotic (E.A.), and late apoptotic (L.A.) cell population. (a) Control cells. Annexin-V-7-AAD stained HeLa cells after treatment with (b) Au NCs, (c) NaB, (d) PEG-Au NC-NaB-NPs, (e) ART and (f) PEG-AuNC-NaB-NPs-ART.

Finally, the efficacy of combination therapy observed *in vitro* was tested in *in vivo* mice bearing Dalton's lymphoma ascites (DLA) tumour. For induction of tumour, adult male Swiss albino mice were used where subcutaneous inoculations of DLA cells were performed in mice belonging to group G-II to group G-VII. Following inoculation, the size of tumour growth (belly swelling) was monitored for 8 days that were used for various experiments. First the uptake of PEG-AuNC-NaB-NPs on DLA cells was measured for the use of these materials on DLA model. The CLSM studies revealed the uptake of PEG-AuNC-NaB-NPs (red luminescence) upon incubation for 4 h **(Figure 4.18)** and thus, DLA model was chosen for determining the potent therapeutic activity with combination therapy. The

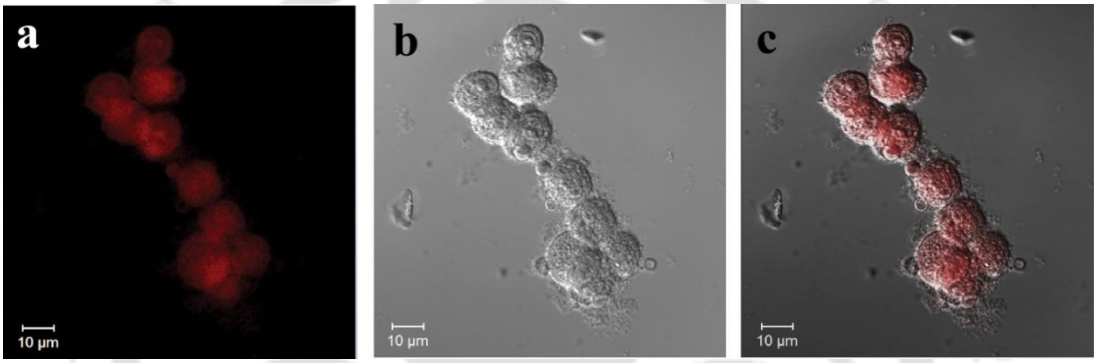

Figure 4.18. Confocal microscopic fluorescence images of DLA cells after 4 h of incubation demonstrating the uptake of Peg-Au NC-NaB-NPs. The excitation wavelength was 405 nm.

toxicity effects of PEG-AuNC-NaB-NPs and ART were pursued, which showed the absence of deleterious effects on animal health at 20 mg/kg (NaB and ART) till 14 days without any mortality. As no observed adverse effect level (NOAEL) of PEG-AuNC-NaB-NPs and ART were observed, 1/10th of its doses (2 mg/kg for NaB and 2 mg/kg for ART) were used for cytotoxic assessment and tumour suppression activities for *in vivo* experiments. The Swiss albino mice used for the experiments were divided into seven groups (n = 10), where the 1st group was assigned as control followed by groups with various treatments. As already mentioned for DLA tumorogenesis (tumour growth with swollen belly) i.e., after 8 days of inoculation, treatment with the non-lethal dose was given in the peritoneal cavity of the mice at scheduled intervals (every 24 h). The non-lethal dose of Au NC (2

mg/mL), NaB (2 mg/kg), PEG-AuNC-NaB-NPs (2 mg/kg), ART (2 mg/kg) and PEG-AuNC-NaB-NPs-ART (2 mg/kg) were given and after 8 days of drug treatment period, trypan blue cell viability test was conducted for the cells collected from the mice (on 16th day). The results as shown in **(Table A 4.2, Appendix)** revealed that combination therapy with PEG-AuNC-NaB-NPs and ART treatment significantly reduced the percentage of viable DLA cells. Interestingly, PEG-AuNC-NaB-NPs have shown enhanced therapeutic activity as compared to that of other treatment groups (NaB and ART only). The viable numbers of DLA cells were similar in case of Au NC treated cells to those of control cells showing almost no toxic effects of Au NCs. At the same time, prominent reduction in tumour volume was observed in both PEG-Au NC-NaB-NPs and PEG-Au NC-NaB-NPs-ART treated mice, which was confirmed by the body weights measured on respective days (0, 8th and 15th day) as represented in **Figure 4.19a**. It can be inferred from (**Figure 4.20)**, that

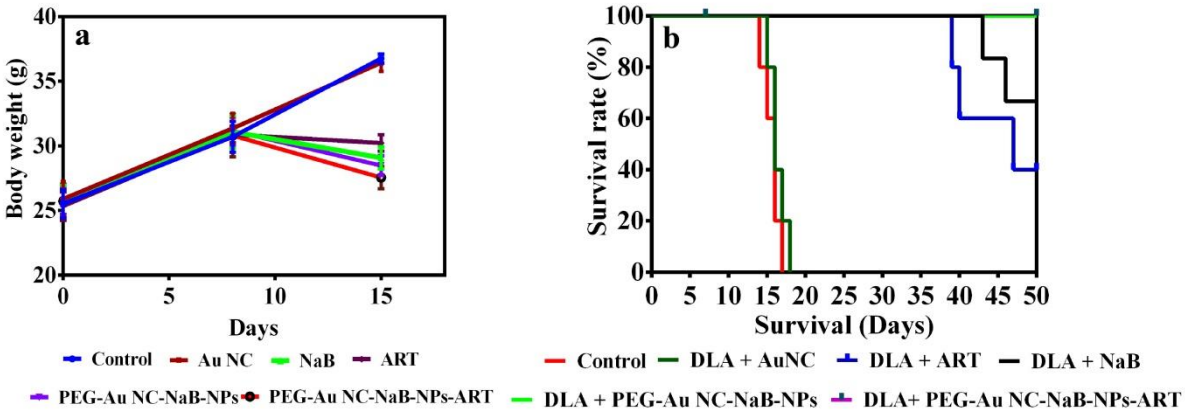

Figure 4.19. (a) Change in the body weight of tumor bearing mice as monitored till 16 days following treatment with Au NC, NaB, PEG-AuNC-NaB-NPs, ART and PEG-AuNC-NaB-NPs-ART, respectively. (b) Survival rate of DLA induced mice monitored up to 50 days after treatment with Au NC, NaB, PEG-AuNC-NaB-NPs, ART and PEG-AuNC-NaB-NPs-ART, as represented by Kaplan–Meir curve.

treatment with PEG-Au NC-NaB-NPs and combination therapy of PEG-Au NC-NaB-NPs with ART showed clear potential in tumor volume reduction **(Figure 4.20 d and f)**. Among all the treatments with PEG-Au NC-NaB-NPs and in combination therapy of PEG-Au NC-NaB-NPs with ART showed less increment in body weight 2.44 ± 0.36*g and 1.85 ± 0.31*g, respectively, as calculated from the initial body weight of the mice. There was an upsurge in body weight of DLA induced mice

(11.28 ± 1.62*g) and Au NCs treated group (10.52 ± 1.52). The results were illustrated in **Table A4.2, Appendix**.

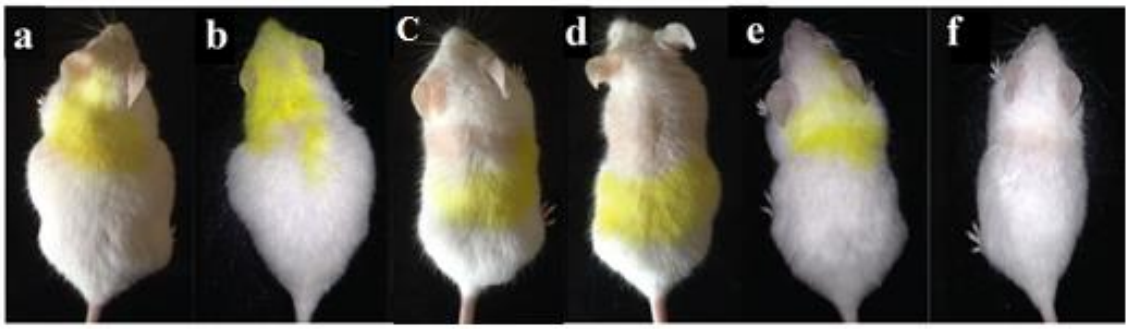

Figure 4.20. Photographs of DLA induced mice: (a) control i.e., without treatment (belly swollen) taken on 14th day and those treated with (b) Au NC on 14th day, (c) NaB taken on 25th day; and (d) PEG-AuNC-NaB-NPs taken on 30th day, (e) ART taken on 30th day and (f) PEG-AuNC-NaB-NPs-ART taken on 30th day.

The enhanced therapeutic activity with combinational therapy can be attributed to synergistic activity of NaB and ART, where PEG encapsulated drug composite nanoparticles provide steric barrier, which prevents nanoparticles opsonisation thereby increasing the blood circulation time and avoiding nonspecific cellular uptake. Thus it helps in EPR and sustained drug release. The increased life span of DLA mice was found in PEG-AuNC-NaB-NPs-ART treated groups that emphasized superior therapeutic activity in combinational treatment **(Figure 4.19b).** All the mice died within 17th and 18th days of post tumour development in case of control and Au NC treated group **(Figure 4.19b)**. It is to be noted that significant increase in mean survival time was observed as compared to that of control and Au NC treated group in case NaB and ART treated groups, where mice died on 39th, 40th and 47th day (3 out of 5) and on 43rd and 46th day (2 out of 5), respectively. In an allied vein, interestingly having potent therapeutic activity PEG-Au NC-NaB-NPs and PEG-Au NC-NaB-NPs-ART led to survival of mice up to 50 days of study, where systemic toxicity of NaB and ART was greatly reduced as observed in **(Figure 4.19b).**

For haematological parameters, increase in WBC counts was observed in DLA induced mice with reduced RBC and Hb counts **(Table A 4.3, Appendix)**. At the same time, similar effects were observed on Au NC treated groups. Treatment with NAB, PEG-Au NC-NaB-NPs and ART also showed elevated WBC counts, but

less than only DLA induced mice (i.e., without treatment). The RBC and Hb counts though had improved in these groups, but still were in lower range. Importantly, treatment with PEG-AuNC-NaB-NPs-ART indicated superior results and revealed counts almost near to the normal levels of WBC, RBC and Hb as shown in **(Table A 4.3, Appendix)**. To evaluate the hepatotoxicity in DLA mice after various treatment conditions, the liver functions tests (LFT) were carried out. It was found that there was a rapid elevation of liver function marker enzymes (SGOT, SGPT & ALP) in case of DLA induced mice as compared to that of normal mice **(Table A 4.4, Appendix)**.The treatment with Au NCs also revealed enhanced liver function marker enzymes. Though treatment with NaB and ART assisted in reduction of these enzymes to some extent but it was still in a higher range. But treatments with PEG-Au NC-NaB-NPs and PEG-Au NC-NaB-NPs-ART showed substantial reduction and were almost near to the levels of control animals (without DLA). The details of the obtained liver function marker enzymes after various treatments are included in **(Table A 4.4, Appendix)**.

Further histopathological studies were also carried out where in kidney of DLA induction mice resulted in tubular congestion, glomerular atrophy and deformed epithelial cells along with inflammatory cell infiltrate **(Figure 4.21 a).** Administration of Au NCs failed to ameliorate the pathological condition to that of DLA animals **(Figure 4.21b)**. Intraperitoneal administration of NaB and ART exhibited pronounced improvement in renal pathology where reduced occurrences of glomerular and blood vessel congestion were recorded **(Figure 4.21c and e)**. PEG-Au NC-NaB-NPs and PEG-AuNC-NaB-NPs-ART treatment ensued the significant protection from DLA induced renal deformities **(Figure 4.21d and f)**, where pronounced reduction of epithelial desquamation, tubular congestion and hyperaemia of medullary part of kidney resembling the normal renal physiology of mice were observed. Additionally, liver histology analysis portrayed the pathological changes of liver in DLA mice. Abnormal hepatocytes along with hepatic fibrillation, hemorrhage, polymorphic neutrophil infiltration, and perinuclear clumping of cytoplasm were observed in DLA mice, whereas similar changes were observed on Au NC treatment **(Figure 4.21 g and h).** In contrast, NaB, ART, PEG-AuNC-NaB-NPs and PEG-AuNC-NaB-NPs-ART **(Figure**

4.21 i, k, j and l) treatment demonstrated significant protection with normal hepatocellular ultra-structures. Among all the treatments, the PEG-AuNC-NaB-NPs-ART **(Figure 4.21 l)** was found to be the best in combating hepatic damage during DLA condition.

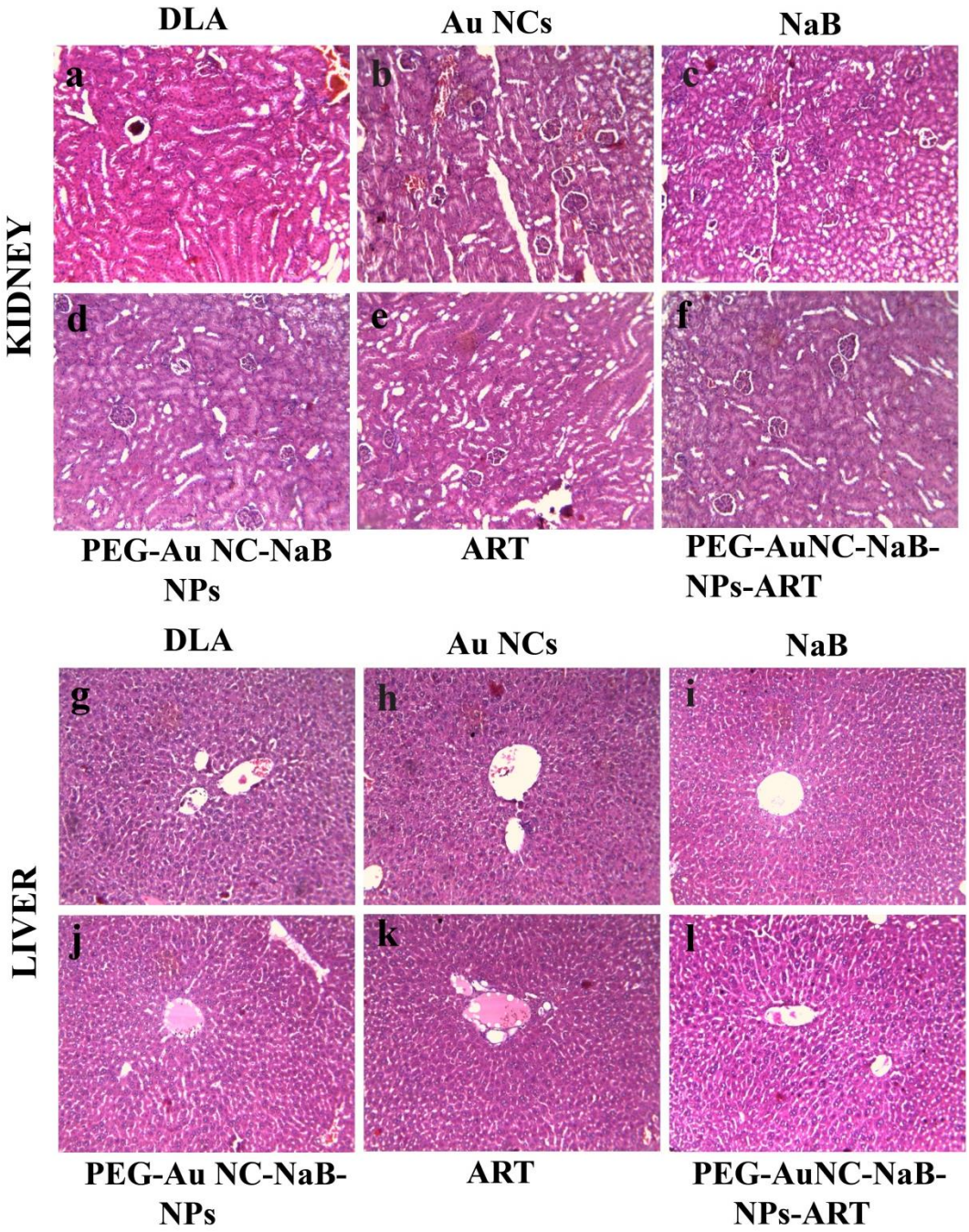

Figure 4.21. Hematoxylin and Eosin stained tissues of kidney collected on 17th day to monitor the histopathological changes. (a) Sections of kidney of DLA mice without any treatment. Following are the images after treatment with (b) Au NCs, (c) NaB, (d) PEG-Au NC-NaB-NPs, (e) ART and (f) PEG-Au NCs-NaB-NPS-ART. Similarly, tissues of liver were also collected and stained where (g) represents liver of DLA mice without any treatment

whereas (h-l) were histopathological data of liver following treatment with Au NCs, NaB, PEG-AuNC-NaB-NPs, ART and PEG-AuNC-NaB-NPs-ART, respectively.

4.6. Conclusion

In brief, spherical PEG coated luminescent drug encapsulated composite nanoparticles (PEG-Au NC-NaB-NPs) were synthesized in presence of negatively charged sodium butyrate as an ion gelating agent. The internalisation of the luminescent (PEG-Au NC-NaB-NPs) in Hela cells occurred through receptor mediated endocytosis as was evident from the experiments with specific inhibitors. The work emphasized the use of combination therapy with a plant based antimalarial drug ART and small fatty acid chain (NaB) to enhance therapeutic activity. The detailed studies on mechanism of synergy of ART and NaB revealed enhanced generation of ROS, which resulted in depolarization of mitochondria. At the same time the work highlighted the role of ART and NaB in DNA damage and HDAC inhibition resulting in cell death. The findings were well supported with *in vivo* studies to decipher synergistic therapeutic activity and provided a promising combination platform for an effective cancer therapy.

4.7. References

(1) Menna, P.; Salvatorelli, E.;Minotti, G. Perspecti V E. *Chem. Res. Toxicol.* **2008,** *21,* 978–989.

(2) Jin, D.; Ma, X.; Luo, Y.; Fang, S.; Xie, Z.; Li, X.; Qi, D.; Zhang, F.; Kong, J.; Li, J.; Lin, B.; Liu, T. *RSC Adv.* **2016**, *6* (35), 29598–29607.

(3) Senapati, S.; Mahanta, A. K.; Kumar, S.; Maiti, P.*Signal Transduction and Targeted Therapy* **2018**, *3* (1), 7.

(4) Sun, T.; Zhang, Y. S.; Pang, B.; Hyun, D. C.; Yang, M.; Xia, Y. *Angew. Chem. Int. Ed.* **2014**, *53* (46), 12320–12364.

(5) Peer, D.; Karp, J. M.; Hong, S.; Farokhzad, O. C.; Margalit, R.; Langer, R. *Nat. Nanotechnol.* **2007**, *2* (12), 751–760.

(6) Meng, H.; Mai, X,W.; Zhang, H.; Xue, M.; Xia,T.; Lin, S.; Wang, X.; Zhao, Y.; Ji, Z.; Zink, I,J.; Nel, E. *ACS Nano* **2008**, *1* (2), 1–22.

(7) Xie, X.; Shao, X.; Ma, W.; Zhao, D.; Shi, S.; Li, Q.; Lin, Y. *Nanoscale* **2018**, *10* (12), 5457–5465.

(8) Li, F.; Mahato, R. I. *Mol. Pharm.* **2014**, *11* (8), 2539–2552.

(9) Holohan, C.; Van Schaeybroeck, S.; Longley, D. B.; Johnston, P. G. *Nat.Rev.Cancer* **2013***, 13 (10),* 714–726*.*

(10) Li, F.; Zhao, C.; Wang, L. *Int. J. Cancer* **2014**, *134* (6), 1257–1269.

(11) Manstein, M, V.; Groner, B. *Med. Chem. Commun.* **2017**, *8* (1), 96–102.

(12) Jiang, T.; Mo, R.; Bellotti, A.; Zhou, J.; Gu, Z.. *Adv. Funct. Mater.* **2014**, *24* (16), 2295–2304.

(13) Yan, X.; Yu, Q.; Guo, L.; Guo, W.; Guan, S.; Tang, H.; Lin, S.; Gan, Z. *ACS Appl. Mater. Interfaces* **2017**, *9* (8), 6804–6815.

(14) Ma, L.; Kohli, M.; Smith, a. Nanoparticles for Combination Drug Therapy. *ACS nano* **2013**, *7* (11), 9518–9525.

(15) Mignani, S.; Bryszewska, M.; Klajnert-Maculewicz, B.; Zablocka, M.; Majoral, J. P. *Biomacromolecules* **2015**, *16* (1), 1–27.

(16) Wu, H.; Jin, H.; Wang, C.; Zhang, Z.; Ruan, H.; Sun, L.; Yang, C.; Li, Y.; Qin, W.; Wang, C. *ACS Appl. Mater. Interfaces* **2017**, *9* (11), 9426–9436.

(17) Licata, S.; Saponiero, A.; Mordente, A.; Minotti, G. *Chem. Res. Toxicol.* **2000**, *13* (5), 414–420.

(18) Jean, S. R.; Tulumello, D. V.; Riganti, C.; Liyanage, S. U.; Schimmer, A. D.; Kelley, S. O. *ACS Chem. Biol.* **2015**, *10* (9), 2007–2015.

(19) Zhang, L.; Cooper, A. J. L.; Krasnikov, B. F.; Xu, H.; Bubber, P.; Pinto, J. T.; Gibson, G. E.; Hanigan, M. H. *Biochemistry* **2006**, *45* (29), 8959–8971.

(20) Dai, L.; Liu, J.; Luo, Z.; Li, M.; Cai, K. *J. Mater. Chem. B* **2016**, *4* (42), 6758–6772.

(21) Wang, S.; Konorev, E. A.; Kotamraju, S.; Joseph, J.; Kalivendi, S.; Kalyanaraman, B. *J. Biol.Chem.* **2004**, *279* (24), 25535–25543.

(22) Xu, X.; Ho, W.; Zhang, X.; Bertrand, N.; Farokhzad, O. *Trends Mol Med*. **2016**, *21* (4), 223–232.

(23) Webb, J. A.; Bardhan, R. *Nanoscale* **2014**, *6* (5), 2502.

(24) Bjornmalm, M.; Thurecht, J, K.; Michael, M.; Scott, M. A.; Caruso,F. *ACS Nano* **2017***, 11,* 9594–9613.

(25) Fan, Z.; Fu, P. P.; Yu, H.; Ray, P. C. T *J. Food Drug Anal.* **2014**, *22* (1), 3–17.

(26) Bobo, D.; Robinson, K. J.; Islam, J.; Thurecht, K. J.; Corrie, S. R. *Pharm. Res.* **2016**, *33* (10), 2373–2387.

(27) Ghoshal, A.; Goswami, U.; Raza, A.; Chattopadhyay, A.; Ghosh, S. S. *RSC Adv.* **2016**, 6,85763–85772.

(28) Goswami, U.; Dutta, A.; Raza, A.; Kandimalla, R.; Kalita, S.; Ghosh, S.S and Chattopadhyay, A. *ACS.Appl. Mater.Interfaces*, **2018**, 10(4), 3282-3294.

(29) Jokerst, V, J.; Lobovkina, T.; Zare ,N, R.; Gambhir, S,S. *Nanomedicine* **2012**, *6* (4), 715–728.

(30) Hak, S.; Helgesen, E.; Hektoen, H. H.; Huuse, E. M.; Jarzyna, P. A.; Mulder, W. J. M.; Haraldseth, O.; Davies, C. D. L. *ACS Nano* **2012**, *6* (6), 5648–5658.

(31) Pelaz, B.; Del Pino, P.; Maffre, P.; Hartmann, R.; Gallego, M.; Rivera-Fernandez, S.; de la Fuente, J. M.; Nienhaus, G. U.; Parak, W. J. *ACS Nano* **2015**, *9* (7), 6996–7008.

(32) Wei, W.; Zhang, X.; Chen, X.; Zhou, M.; Xu, R.; Zhang, X. *Nanoscale* **2016**, *8* (15), 8118–8125.

(33) Sahoo, A. K.; Banerjee, S.; Ghosh, S. S.; Chattopadhyay, A. *ACS.Appl. Mater.Interfaces* **2014**, *6* (1), 712–724.

(34) Strahl, B. D.; Allis, C. D. The Language of Covalent Histone Modifications. *Nature* **2000**, *403* (6765), 41–45.

(35) Entin-Meer, M.; Rephaeli, A.; Yang, X.; Nudelman, A.; VandenBerg, S. R.; Haas-Kogan, D. A. *Mol Cancer Ther.* **2005**, *4* (12), 1952–1961.

(36) Steliou, K.; Boosalis, M. S.; Perrine, S. P.; Sangerman, J.; Faller, D. V. *Biores Open Access* **2012**, *1* (4), 192–198.

(37) Salimi, V.; Shahsavari, Z.; Safizadeh, B.; Hosseini, A.; Khademian, N.; Tavakoli-Yaraki, M. *Lipids Health Dis.* **2017**, *16* (1), 1–11.

(38) Minelli, R.; Occhipinti, S.; Gigliotti, C. L.; Barrera, G.; Gasco, P.; Conti, L.; Chiocchetti, A.; Zara, G. P.; Fantozzi, R.; Giovarelli, M.; Dianzani, U.; Dianzani, C. *Br.J.Pharmacol.* **2013**, *170* (2), 233–244.

(39) Singh, N. P.; Lai, H. C. *Anticancer Res.* **2005**, *25* (6 B), 4325–4331.

(40) Ren, Y.; Yu, J.; Kinghorn, A. D. *Curr. Med. Chem* **2016**, *23* (23), 2397–2420.

(41) Frohlich, T.; Karagoz, A. Ç.; Reiter, C.; Tsogoeva, S. B. *J. Med. Chem.* **2016**, *59* (16), 7360–7388.

(42) Raza, A.; Ghoshal, A.; Chockalingam, S.; Ghosh, S. S. *Sci. Rep* **2017**, *7* (1), 1–13.

(43) Luk, B. T.; Zhang, L. *ACS.Appl. Mater.Interfaces* **2014**, *6* (24), 21859–21873.

(44) Tong, S.; Hou, S.; Ren, B.; Zheng, Z.; Bao, G. *Nano Lett.* **2011**, *11* (9), 3720–3726.

(45) Miladi, K.; Sfar, S.; Fessi, H.; Elaissari, A. *Polymer Nanoparticles for Nanomedicines*; 2016.

(46) Chen, X.; Bi, Y.; Wang, T.; Li, P.; Yan, X.; Hou, S.; Bammert, C. E.; Ju, J.; Gibson, K. M.; Pavan, W. J.; Bi, L. *Sci.Rep.* **2015**, *5*, 1–10.

(47) Yang, L.; Shang, L.; Nienhaus, G. U. *Nanoscale* **2013,** *5*, 1537–1543.

(48) Canton,I.; Battaglia,G. *Chem. Soc.Rev.* **2012**, ***41***, 2718–2739.

(49) Foucquier, J.; Guedj, M. *Pharmacol. Res. Perspect.* **2015**, *3* (3), e00149.

(50) Wang, J.; Zhang, J.; Shi, Y.; Xu, C.; Zhang, C.; Wong, Y. K.; Lee, Y. M.; Krishna, S.; He, Y.; Lim, T. K.; Sim, W.; Hua, Z. C.; Shen, H. M.; Lin, Q. *ACS Cent. Sci.* **2017**, *3* (7), 743–750.

Appendix of Chapter- 4 :A4

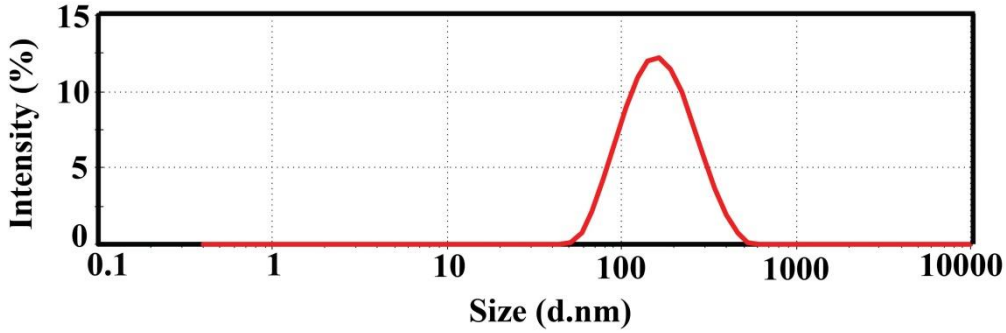

Figure A4.1. DLS results representing the hydrodynamic size of as-synthesized PEG-Au NC-NaB-NPs.

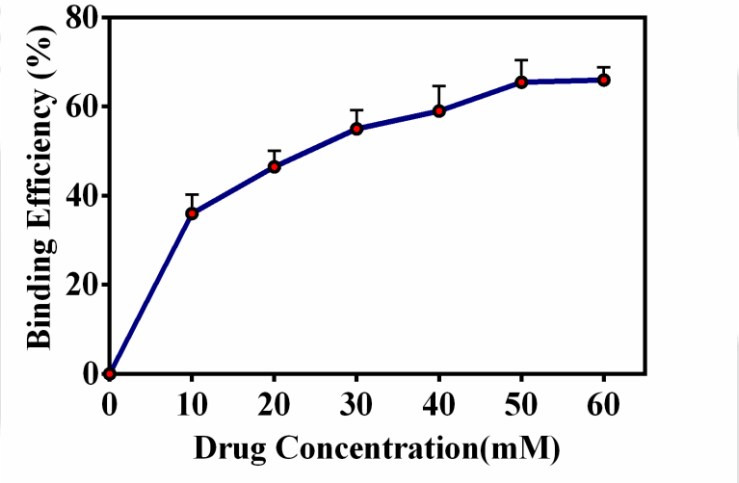

Figure A4.2. Binding efficiency of drug (NaB) with its varied concentration (10 - 60 mM). For this fixed concentration of Au NCs with the respective drug concentrations were used for the synthesis of composite nanoparticles. Maximum binding of 65% was achieved at 50 mM concentration, after which saturation was attained.

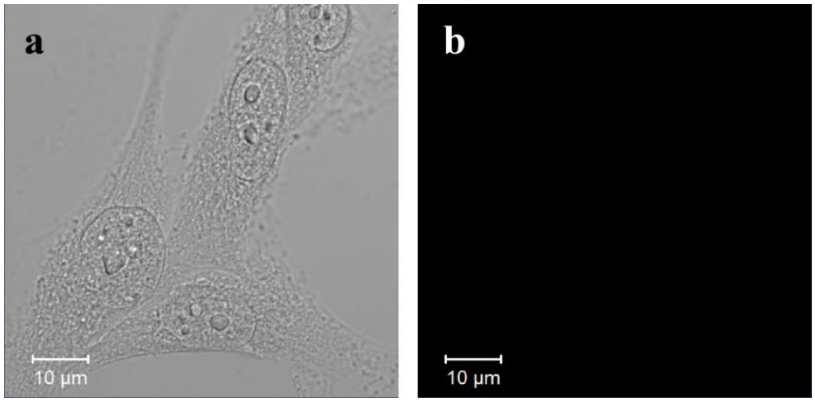

Figure A4.3. Confocal laser scanning microscopy images of control HeLa cells (without any treatment). (a) Bright field image. (b) Red channel showing no luminescence.

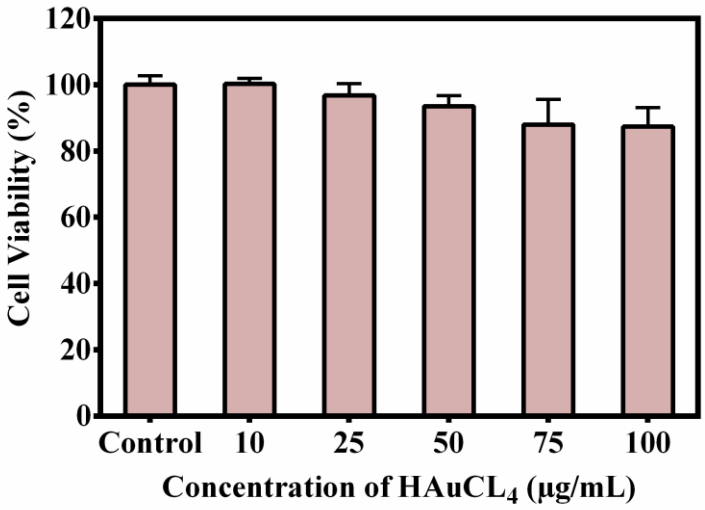

Figure A4.4. Cell viability based on MTT assay after 48 h of treatment with only Au NCs.

Table A4.1. Table showing CI (combination index) values for combination therapy of PEG-AuNC-NaB-NPs (1.8 mM) with varied concentration of ART (100 µM) on Hela cells. The CI values were found to be <1 for all concentrations and hence synergism was considered to have been present.

PEG-Au NC-NaB-NPs (mM)	ART (µM)	Effect (%)	CI value < 1 (Synergism)
1.8	4.4	0.84	0.63
1.8	8.8	0.72	0.61
1.8	13.3	0.59	0.58
1.8	17.7	0.47	0.51
1.8	22.2	0.35	0.44

Table A 4.2. Effect of drug treatment on tumor volume.

S. No	Treatment	Weight change (gm)	Viable cell count (10^5 cells/ml)
1	DLA + Saline	11.28 ± 1.62	418.4 ± 19.7
2	DLA + AuNC	10.52 ± 1.52	402.26 ± 17.8
3	DLA + NaB	3.37 ± 0.52*	9.47 ± 1.7*
4	DLA + PEG-AuNC-NaB-NPs	2.44 ± 0.36*	4.97 ± 1.02*
5	DLA + ART	4.87 ± 0.48*	10.35 ± 1.5*
6	DLA + AuNC-NaB-NPs-ART	1.85 ± 0.31*	2.51 ± 0.78*

All the results were expressed in mean ± S.D. * $p < 0.05$ in comparison of drug treated groups with untreated group.

Table A4.3. Effect of drug treatment on hematological parameters.

S.No	Treatment	RBC (cells/ml X 10^6)	WBC (cells/ml X 10^3)	Hb g/dl
1	Normal animals	5.24 ± 0.43	10.14 ± 0.32	12.7 ± 0.53
2	DLA + Saline	2.73 ± 0.21$	20.35 ± 1.04$	6.6 ± 0.27$
3	DLA + AuNC	2.84 ± 0.31	18.91 ± 1.47	6.9 ± 0.32
4	DLA + NaB	3.82 ± 0.34*	15.35 ± 1.24*	8.6 ± 0.41*
5	DLA + PEG-AuNC-NaB-NPs	4.17 ± 0.56*	13.75 ± 0.77*	9.6 ± 0.38*
6	DLA + Artesunate	3.58 ± 0.38*	16.62 ± 1.12*	8.4 ± 0.46*
7	DLA + PEG-AuNC-NaB-NPs-ART	4.52 ± 0.52*	12.45 ± 0.86*	11.04 ± 0.42*

All the results were expressed in mean ± S.D. $^{\$}$p< 0.05 in comparison of saline treated DLA animals with normal animals. * p < 0.05 in comparison of drug treated DLA animals with untreated group DLA animals.

Table A4.4. Effect of drug treatment on serum biochemical enzymes.

S. No	Treatment	SGOT	SGPT	ALP
1	Normal animals	46.3 ± 2.74	38.2 ± 2.43	114.6 ± 5.26
2	DLA + Saline	92.8 ± 4.26$^{\$}$	68.7 ± 3.64$^{\$}$	226.7 ± 9.42$^{\$}$
3	DLA + Au NC	87.6 ± 5.26	63.8 ± 4.18	219.6 ± 11.53
4	DLA + NaB	63.4 ± 3.67*	55.2 ± 2.84*	151.4 ± 7.35*
5	DLA + PEG-AuNC-NaB-NPs	55.7 ± 3.48*	46.5 ± 3.22*	134.8 ± 6.71*
6	DLA + ART	67.2 ± 4.14*	59.1 ± 3.36*	157.2 ± 8.27*
7	DLA + PEG-AuNC-NaB-NPs-ART	51.2 ± 3.21*	40.4 ± 2.91*	122.5 ± 7.14*

All the results were expressed in mean ± S.D. $^{\$}$ p< 0.05 in comparison of saline treated DLA animals with normal animals. * p < 0.05 in comparison of drug treated DLA animals with untreated group DLA animals.

Chapter-5

Transferrin–Copper Nanocluster Doxorubicin Nanoparticles as Targeted Theranostic Cancer Nanodrug

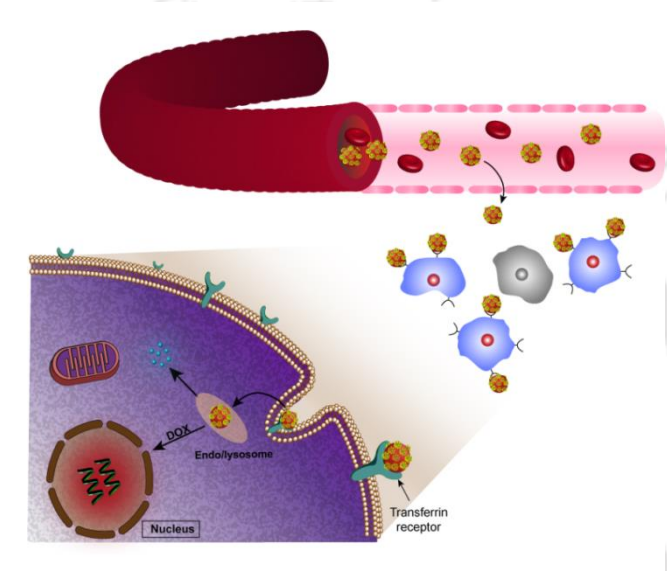

In Chapter 5, *Transferrin (Tf)-templated luminescent blue copper Nanoclusters (Tf-Cu NCs) were synthesized and were formulated into spherical Tf-CuNC−doxorubicin nanoparticles (Tf-Cu NC−Dox NPs). The as-synthesized Tf-Cu NC−Dox NPs were explored for bioimaging and targeted drug delivery to delineate high therapeutic efficacy on TfR overexpressed cells (HeLa and MCF-7) as compared to the cells expressing less TfR (HEK-293 and 3T3-L1). Combination index (CI) revealed synergistic activity of Tf-Cu NCs and Dox in Tf-Cu NC−Dox NPs. In vivo assessment of the NPs on TfR positive Daltons Lymphoma Ascites (DLA) bearing mice revealed significant inhibition of tumor growth rendering prolonged survival of the mice.*

https://pubs.acs.org/doi/abs/10.1021/acsami.7b15165

Chapter 5

5.1. Introduction

In parallel to the conventional radiotherapy,[1] chemotherapy,[2] and surgery for cancer treatments, contemporarily preferred modes include photothermal therapy,[3] immunotherapy,[4,5] hormone therapy,[6] recombinant protein therapy,[7,8] and stem cell therapy[9] which are based on the incidence and progression of cancer. Importantly, nonspecificity and low solubility with reduced retention time of majority of the chemotherapeutic drugs lead not only to severe side effects but also to eventual development of multidrug resistance.[10–14] Thus, in clinical practice along with surgery, combining other therapies with chemotherapy helps curtail such inadequacies to some extent with better therapeutic outcome.[15–17] However, nanotechnology- based composite drug delivery systems have been reported to improve loading capacity, detection, and specific release at the site of the disease, circulation time and bioavailability of drugs, and thus help reduce untoward side effects.[18–21] In this regard, molecule-like properties with discrete electronic states and size-dependent photoluminescence (PL) of metal Nanoclusters of size near to the Fermi wavelength of electrons, i.e., <2 nm (for Ag, Au and Cu), are useful in the fields of bioimaging, biosensing, and drug delivery.[22–27] The ability to evaluate the treatment by introducing multiple functions into a single nanoplatform (as a part of theranostics) can be achieved with nanoclusters to advance the therapeutic paradigm of cancer treatment.[8,22,23] Additionally, interaction of the designed luminescent nanoclusters with cellular species or any external molecule like drug or enzyme, guided by changes in their luminescence based on available mechanisms such as Förster resonance energy transfer (FRET), photoinduced electron transfer (PET), and others may allow monitoring of intracellular interactions, stimuli-responsive behavior, imaging, drug localization, and enhanced release with ease.[28–32] Although Au and Ag nanoclusters are widely reported to have been incorporated into nanocarriers for imaging and therapy,[8,21,23] use of Cu nanoclusters (Cu NCs) has been limited due to lack of

stability even in a mildly oxidizing environment.[26] However, Cu NCs in a hydrogel nanocarrier have shown enhanced activity of cisplatin and synergy of action.[33] Thus, the advantage of photoluminescent drug carrier lies in real-time monitoring of drug localization and release; however, the application has been limited due to nonspecificity.[7,8,33] Nanoparticle-based drugs like Doxil/Lipoplatin (PEGylated liposome), Abraxane (paclitaxel albumin-stabilized nanoparticle), DepoCyt (liposomal cytarabine), Oncaspar (PEG-asparaginase), CAELYXTM (PEGylated liposomal doxorubicin), Genexol-PM (polymeric micellar nanoparticle), and NK105 (Paclitaxel loaded polymeric micelles) are in clinical trials for cancer therapy,[21,24] but options for targeted imaging and diagnosis are not available in these compositions. Mostly, therapeutic agents are released in the perivascular cells of tumor where the nanoparticles tend to accumulate in spleen and liver as captured by reticuloendothelial system. However, the tumor targeting could be achieved by incorporating specific receptor protein(s) in the carriers.[34−37] Transferrin (Tf), a plasma protein, which plays a critical role in homeostasis of iron, is overexpressed in many cancers due to augmented iron requirements in cell proliferation. Tf easily enters the Tf receptor (TfR)-overexpressing cells through active receptor-mediated endocytosis.[38] Thus, the use of Tf in a carrier could help targeted delivery of drugs in cancer tissues.[39] Doxorubicin (Dox) is one of the most widely used drugs for cancer therapy, but its use is associated with side effects, unalterable cardiac toxicity, and occurrence of drug resistance.[10,13−15] Thus, minimization of its use, in combination with other less toxic candidates, would be beneficial for enhanced therapeutic values.

5.2. Outline of the present work

Herein, a formulation of nanodrug containing blue-emitting Tf-stabilized Cu NCs (Tf-Cu NCs) and Dox as hydrophobic drug, referred to henceforth as Tf-Cu NC−Dox −nanoparticles (NPs), is reported. Following UV light excitation, FRET from the blue-emitting Tf-Cu NCs as donor to the Dox acting as acceptor led to the NPs emitting in the red thus acting as a probe. Interestingly, the blue emission of Tf-Cu NCs could be effectively recovered in the cytoplasm of transferrin receptor (TfR) overexpressed cancer cells, allowing observation of simultaneous and gradual

release of Dox into the nucleus following internalization. This allowed real-time monitoring of intracellular drug release based on FRET. At the same time, synergistic anticancer activity could also be achieved involving Tf-Cu NCs and Dox present in Tf-Cu NC–Dox NPs. To the best of our knowledge for the first time a nanodrug incorporating Tf-Cu NCs and Dox has been developed for targeted imaging and therapeutic action in conjunction with synergy of the components. In addition to the in vitro studies, the nanodrug was tested for efficacy by investigating in vivo using Dalton's lymphoma ascites (DLA) cells, a T-cell lymphoma first identified in thymus of DBA (H2D) mice and later adapted to a closely inbred strain of the Swiss albino mice, which mimics characteristics similar to human lymphoma. It is one of the most convenient and widely used models for peritoneal carcinoma to screen the activity of various anticancer agents within a short period of time.[34,40]

5.3. Experimental Section

5.3.1. Materials

Copper sulphate ($CuSO_4$) and hydrazine hydrate (N_2H_4) were procured from Merck Specialties Private Limited, India. Transferrin, (3-(4, 5-dimethylthiazolyl-2)-2,5-diphenyltetrazolium bromide) (MTT), sinapinic acid, calcein acetoxymethyl, ethidium bromide, propium iodide, chlorpromazine and NaN_3 were purchased from Sigma-Aldrich, U.S.A. Chlorazole black E was procured from HIMEDIA. Doxorubicin was bought from a commercial source. AnnexinV-7AAD kit was acquired from BD lifescience. For all experiments, Milli-Q grade water (18.2 MΩ cm) was used. Four different cell lines, namely, HeLa (human cervical carcinoma) and MCF-7 (human breast adenocarcinoma cell line), which overexpress transferrin receptors on the cell surface and HEK-293 (human embryonic kidney cell), 3T3-L1 (mouse embryo fibroblast cell lines (Balb/3T3, control) were procured from National Centre for Cell Sciences, India (NCCS) Pune.

5.3.2. Synthesis of Tf-Cu NCs

In a typical synthesis, 0.2 mL (25 mM) of aqueous solution of copper sulfate ($CuSO_4$) was added dropwise to 2 mL of aqueous solution of transferrin (5 mg/mL) under vigorous stirring at 37 °C. After stirring for 10 min, pH was adjusted to ~12 by adding freshly made 1 M NaOH solution during which the reaction mixture turned purple from colorless solution. After 1 h of stirring, 80μL of N_2H_4 (80%), was introduced into the reaction mixture dropwise and was further allowed to stir for 10 h at 37 °C. The color of the reaction mixture gradually changed from purple to light brown ensuring the completion of reaction. The as-synthesized Tf-Cu NC was then further stored at 4 °C for further use.

5.3.3. Formulation of Tf-Cu NC–Dox NPs

First, 0.017 mL (2.5 mM with respect to copper) of as synthesized Tf-Cu NCs was added to 0.8 mL of aqueous solution in a reaction vial and temperature was set at 37 °C. Under stirring condition, 50 μL of Dox solution (from 400 μM stock) was added successively after a gap of 15 min each, and fluorescence spectrum was recorded simultaneously. After final addition of 250 μL of Dox solution, the reaction mixture attained a pinkish red color. The final resulting mixture, was then allowed to age for ~2 h at 37 °C. The as-synthesized Tf-Cu NC–Dox NPs was then collected by centrifugation at 10 000 rpm for 30 min. The pellet so obtained was redispersed in 1 mL of Milli-Q water for further use.

5.3.4. Encapsulation Efficiency and Release Study of Doxorubicin

In order to calculate the amount of Dox present in the Tf-Cu NC– Dox NPs, the as-synthesized Tf-Cu NC–Dox NPs were centrifuged at 10 000 rpm for 30 min at 15 °C. The supernatant was then collected, and the emission spectrum was recorded with λex = 480 nm. Similarly, emission spectrum of control Dox, i.e., the initial concentration used during NP synthesis was recorded (λ_{ex} = 480 nm). The emission intensities of the supernatant of Tf-Cu NC–Dox NPs and Dox only at λ_{em}= 590 nm were then measured. The encapsulation efficiency (EE%) was then calculated using the following equation:

$$E.E\% = \frac{Dox_i - Dox_f}{Dox_i}$$

where Dox_i refers to emission intensity of Dox corresponding to initial concentartion of Dox used in composite formulation and Dox_f refers to emission intensity of Dox in the supernatant of the composite after synthesis.

For release study, the drug-loaded NPs were incubated in two different buffers (acetate buffer pH 4.5 and PBS pH 7) at 37 °C and release was then monitored for 48 h by UV–vis spectroscopy. At different time intervals, supernatant was collected after centrifugation at 10 000 rpm for 15 min and the absorbance was measured at 480 nm for Dox.

5.3.5. Expression Analysis of Transferrin Receptors

The total RNA was isolated from HeLa, MCF-7, HEK-293, and 3T3-L1 cells using GenElute Mammalian Total RNA Miniprep Kit (Sigma-Aldrich). Furthermore, 1 μg of total RNA was used to generate cDNA pool of the respective cell lines with the help of the Verso cDNA Kit (Thermo Scientific, MA). A semiquantitative polymerase chain reaction (PCR) was performed with TfR primers using cDNA pool of the respective cell lines. β-actin gene was taken as endogenous control. The products of PCR were run on a 1.3% agarose gel prestained with ethidium bromide

5.3.6. *In Vitro* Experiments (Mammalian Cell Culture)

Human cervical cancer cell line (HeLa TfR-positive), human breast cancer cell line (MCF-7 TfR positive), human embryonal kidney cell line (HEK-293 TfR partially positive), and mouse embryo fibroblast cell line (Balb/3T3, control TfR-negative) were procured from National Centre for Cell Sciences, Pune. Cells were grown in CO_2 incubator with 5% carbon dioxide in humidified atmosphere and cultured in Dulbecco's modified Eagle's medium (DMEM, high-glucose) containing 10% FBS, 10 000 units of penicillin, and 10 mg/mL streptomycin.

5.3.6.a. Cell viability assay

To study the effect of Tf-Cu NC–Dox NPs on different types of cell lines with varied TfR expressions, MTT (3- (4,5-dimethylthiazolyl-2)-2,5-diphenyltetrazolium bromide) assay was carried out after 48 h of treatment. Briefly, 5× 10^3 cells were seeded in each well of 96-well plate and were left for 24 h for attachment. Furthermore, varying concentrations of Tf-Cu NCs (10 μg/mL), Dox (10 μg/mL), and Tf-Cu NC–Dox NPs (10 μg/mL) were used for treatment for 48 h, in triplicates. After the completion of the treatment duration, MTT was added in each well, and the resulting formation of formazon was dissolved in DMSO. The absorbance of formazan, which corresponds to the number of living cells, was then measured at 550 nm with background reference measured at 655 nm in Multiplate Reader (Tecan). The normalized percentage cell viability was calculated as where A_{570} corresponds to absorbance of formazan and A_{690} arises due to background.

$$\%\ of\ cell\ viability = \frac{(A_{550} - A_{655})_{sample}}{(A_{550} - A_{655})_{control}} \times 100$$

5.3.6.b. Studying the Mode of Cell Death

To probe the mode of cell death, FACS-based assays were carried out including ROS generation assay, live and dead cell analysis with PI, and cell cycle and PE AnnexinV-7AAD analyses for apoptosis.

5.3.6.c. Calcein AM / Ethium Bromide (EtBr) Staining

To distinguish between live and dead cells, calcein AM and EtBr staining were performed. Calcein AM is a hydrophobic non-fluorescent compound, which can penetrate through live cells and is converted to calcein, a hydrophilic green fluorescent compound by hydrolysis. In contrast, EtBr an intercalating dye, which can pass through the compromised cell membrane. For this, HeLa cells were seeded with 5×10^3 cells/well concentration in six well plates and after 80%–90% confluency was attained, the cells were treated with Tf-Cu NC, Dox and Tf-Cu NC-Dox-NPs. After 48 h of treatment, media were discarded and cells were washed with PBS twice and calcein AM (1 μM) and EtBr solutions (4 μM) in PBS were

added. The cells were incubated for 30 min at 37 °C with 5% CO_2 and were observed under a fluorescence microscope (Nikon ECLIPSE) after thorough washing.

5.3.6.d. FACS Analysis for Reactive Oxygen Species Generation

Generation of reactive oxygen species was analysed by using 2,7-dichlorofluoresceindiacetate (DCFH-DA; Sigma-Aldrich, USA) staining method and is measured in fluorescence activated cells sorter (Beckman Coulter). In brief, cells were plated in 6 well plates at 5×10^3 cells/well confluency and left overnight, which was followed by treatment with Tf-Cu NC, Dox and Tf-CuNC-Dox-NPs at MTT IC50 dose for 3 h. Subsequently, 10 µM of DCFH-DA was added in each well along with the control and they were then kept at 37 °C for 30 min. The nonfluorescent dye DCFH-DA diffuses into the cell through plasma membrane and is deacetylated by cellular esterases to a non-fluorescent compound DCFH. Hereafter, DCFH is oxidized by ROS into 2', 7' –dichlorofluorescein (DCF) giving green fluorescence (λ_{ex}=488 nm and λ_{em}=530 nm). The cells were then collected after trypsinization and are re-dispersed in DMEM before being analyzed in a flow cytometer FITC channel (530/30nm), which corresponds to green emission. 15000 cells were acquired and analyzed using CytoFLEX flow cytometer (Beckman Coulter).

5.3.6.e. Cell Cycle Analysis

To evaluate the DNA content of the cells at different stages of cell division, propidium iodide (PI) based cell cycle analysis was carried out in CytoFLEX flow cytometer (Beckman Coulter). 5×10^3 cells/well was seeded in 6 well plates and kept overnight for attachment followed by treatment with Tf-Cu NCs, doxorubicin or Tf-Cu NC-Dox-NPs for 48 h. From the plates, both media and PBS were collected and the trypsinised cells were harvested followed by centrifugation at 650 rcf for 6 min. Afterwards, under constant vortexing of trypsinized cells, chilled 1 mL of cold 70% ethanol was added to fix the cells, which were then stored at -20 °C for 1 h and again centrifuged. The pellet was then redispersed in PBS before being incubated in 0.4 mg/mL RNase solution for 1 h at 37 °C. Finally PI at a concentration of 10 µg/mL was added into this and kept for 30 min under dark

condition before analysis was carried out. The cells were acquired in PE-A channel (band-pass filter, 585/42 nm) of CytoFLEX flow cytometer (Beckman Coulter) using an excitation wavelength of 488 nm and emission was recorded in PE-A channel. The data were then analysed using ModFit LT software 5.0.

5.3.6.f. PE Annexin V- 7-AAD Apoptosis Detection Assay

PE Annexin V detection kit (BD Biosciences) in conjunction with 7-amino-actinomycin (7-AAD) dye was used to detect early and late apoptotic cells. Viable cells are PE Annexin V and 7-AAD negative; whereas early apoptosis are PE Annexin V positive and 7-AAD negative. The cells that are in late apoptosis or dead are both PE Annexin V and 7-AAD positive. 7-AAD is permeable to dead cells because of membrane damage, whereas viable cells with intact membrane exclude 7-AAD. Therefore, viable cells are negative for both PE Annexin V and 7-AAD. Early apoptotic cells where membrane integrity is present are PE Annexin V positive and 7-AAD negative; and cells that are in late apoptosis or already dead are both PE Annexin V and 7-AAD positive. In this quest, the cells were grown in a similar way as mentioned above, which was followed by treatment with Tf-CuNCs, Dox and Tf-CuNC-Dox-NPs for 48 h. The prescribed protocol was followed for sample preparation and the cells were analysed by the FACS.

5.3.7. Confocal Microscopy

To study the difference in uptake, based on the TfR expression, confocal microscopy studies were carried out in 4 different cell lines (HeLa, MCF-7, HEK-293, and 3T3-L1) using Zeiss LSM 880 microscope. A total of 5×10^3 cells were grown on a coverslip in 35 mm culture plate for 24 h under integral condition of CO_2 incubator. The uptake study was carried out after 4 h incubation with Tf-Cu NC–Dox NPs followed by PBS washing and fixing with 4% formaldehyde. Thereafter, the coverslips were gently handled with the help of tweezers and were placed upside down on the glass slide, and the sides were sealed. For time-dependent uptake, the same procedure was followed where the cells were fixed at appropriate time interval. The control cells without any treatment were prepared in a similar manner for all sets of experiments. The prepared samples were

observed under simultaneous mode (with λ_{ex} 405 nm for Tf-Cu NCs and λ_{ex} 488 nm for Dox) under Zeiss microscope LSM 880.

5.3.8. Mechanism of Cellular Uptake with Inhibitors

The uptake study was carried out with fluorescence based assays on both Tecan and CLSM. For Tecan-based assay 5× 10^3 cells were grown in 96-well plate for 24 h at 37 °C, and cells were grown on coverslip in 35 mm culture for CLSM study. For active and passive transport, the cells were incubated at 4 °C for 4 h and with 10 mM NaN_3 for 30 min at 37 °C. These pretreated cells were then incubated with composite (Tf-Cu NC–Dox NPs) for 4 h. To confirm the mode of uptake, two inhibitor assays were performed with Chlorazole Black E which is a TfR inhibitor and chlorpromazine which inhibits clathrin mediated endocytosis. Before the treatment with composite for 4 h, the cells were pre-treated with Chlorazole Black E (50 μM for 6h) and chlorpromazine (50 μM for 4 h).

5.3.9. *In Vivo* Experiments

Adult male Swiss albino mice weighing 22– 25 g were procured from Chakraborty enterprise (1443/PO/b/11/CPCSEA), Kolkata, India. All mice were housed at Central Animal Facility, Institute of Advanced Study in Science and Technology (IASST), Guwahati, Assam. The mice were maintained in polypropylene cages and the room conditions was maintained at 22 ± 2°C, 60–70% relative humidity, and a 12 h–12 h light–dark cycle. All mice were fed a standard Rodent pellet diet (Provimi Animal Nutrition India Pvt. Ltd., India) and water ad libitum. Mice were allowed to acclimate for a week and after close monitoring for a week all the experiments were conducted. Before commencing the work, the protocols were designed and approved (IASST/IAEC/2016–17/ 2301) by the Institutional Animal Ethics Committee (IAEC) of IASST and implemented as per guidelines of Committee for the Purpose of Control and Supervision of Experiments on Animals (CPCSEA), Government of India.

5.3.9.a. Development of in Vivo Tumor (Dalton's Ascites Lymphoma Cells)

Dalton's ascites lymphoma (DLA) cells were acquired from IASST Central Animal

Facility, and 1 × 10^6 viable tumor cells were transplanted through intraperitoneal (I.P.) route to each mouse. The growth of tumor was ascertained by abnormal belly swelling and increased body weight, which were visible in 8–10 days, post induction.

5.3.9.b. Acute toxicity studies

Acute toxicity studies were conducted as per the Organization for Economic Co-operation and Development (OECD) guidelines to test chemicals. Swiss albino mice of either sex (n=6) were selected randomly to perform the experiment. All the mice were fasted overnight with free access to water before administration of test drugs. A single dose of Tf-C NC-Dox -NPs at 50 mg/kg was administered separately to three mice each. The dose was regarded as toxic if mortality was observed in 2 out of 3 mice. The experiment was repeated again and if mortality was observed in 1 out of 3 mice then again the experiment is conducted. If the mortality was observed, the experiment was continued with lower doses (20, 10, 5 & 2 mg/kg body weight). Initial observations were made based on the Irwin scale parameters - like presence or absence of lethality, convulsions, straub tail, sedation, excitation, jumps, loss of balance, abnormal writhes, piloerection, stereotypies (sniffing, chewing or head movements), head twitches, scratching, abnormal respiration, aggressiveness towards the experimenter, loss of righting reflex, loss of corneal reflex, defecation, salivation and lacrimation. Further, mice were kept under observation for 14 days in order to observe the mortality.

5.3.9.c. Animal Grouping and in Vivo Experimental Design

Dox doses were selected for in vivo experiments on the basis of the acute toxicity studies on Tf-Cu NC–Dox NPs and from previous literature data. For the tumor progression, DLA cells (0.2 mL of 1 × 10^6 cells/ mice) were injected intraperitoneally on day 0 leaving aside the normal group. The drug treatments were started from day 8 post tumor transplantation in the interval of 24 h for 8 days. The work involved 46 mice, which were taken and separated into 5 groups with 10 mice in each group, besides group I having 6 mice.

• Group-I: Mice with no DLA tumor + No drug treatment

• Group-II: DLA-bearing mice +0.2 mL of PBS (I.P.) for 8 days

• Group-III: DLA-bearing mice + Tf-Cu NC 2 mg/kg (I.P.) for 8 days

• Group-IV: DLA-bearing mice + Dox 2 mg/kg (I.P.) for 8 days

• Group-V: DLA-bearing mice + Tf-Cu NC–Dox NP 2 mg/kg (I.P.) for 8 days

5.3.9.d. Effect of Treatment on Tumor Growth

During the experimental period, the body weight changes were measured daily, and cells from all the groups were collected at the end of the drug treatment period (16 days) to determine the cell viability and morphological changes (FESEM analysis). At day 17, five mice from each group were sacrificed by decapitation to collect the blood, liver, and kidney for biochemical and histopathological analysis. The remaining 5 mice were observed for up to 50 days to estimate the mean survival time (MST) and % increase in life span (% ILS).

5.3.9.e. Trypan Blue Test

To determine the cell viability from various treatment groups trypan blue assay was conducted. Briefly, 0.1 mL of DLA cells was mixed with 0.1 mL of trypan blue (0.4 %) solution - which is impermeable to the healthy cell because of its intact cell membrane - and thus stains the cytoplasm of compromised cells. The cells were counted using cell counter (Countess II FL, Life Technologies, USA). Cytotoxicity (%) was measured by using the following formula:

$$\%\,of\ cell\ cytotoxicity = 100 - \frac{No.of\ viable\ cells\ in\ the\ treated\ group}{No.of\ viable\ cells\ in\ the\ untreated\ control\ group} \times 100$$

5.3.9.f. FESEM analysis

To observe the cell morphology FE-SEM analysis of DLA cells was perfomed. After

the treatment, the cells from various treatment groups were fixed in 3 % glutaraldehyde solution for 4 h. After incubation with 0.2 mM PBS for 6 h the cells were subjected to dehydration with gradiant acetone (30, 50, 70, 90 & 100 %) followed by critical point dehydration by tetramethyl silane. Further, cells were observed under FE-SEM to observe the morphological changes.

5.3.9.g. Haematological profiling

The blood from various treatment groups were collected in ethylenediaminetetra acetic acid coated (EDTA) vials. The blood components like red blood cells (RBC), white blood cells (WBC) and haemoglobin (Hb) levels were estimated using haematology analyser (Sysmex, Japan). All the results were expressed in mean ± S.D.

5.3.9.h. Biochemical Parameters

After the drug treatment period, a part of blood was collected in non-anticoagulant vials. Blood was centrifuged at 1500 rpm for 10 min at 4 °C and supernatant (serum) was separated. The serum levels of aspartate transaminase (AST), alanine transaminase (ALT) and alkaline phosphatase (ALP) were measured using biochemical kits obtained from Accurex, India as per the instructions given by the manufacturer.

5.3.9.i. Histopathological Analysis

To observe the pathological changes in liver and kidney tissues from all the treatment groups; the organs were immediately isolated and fixed with 10% formalin. Further, tissues were processed for dehydration using alcohol (50, 70, 90 & 100 %), xylene and then embedded in paraffin blocks. Sections of 5 µm were prepared using microtome and stained with hematoxylin and eosin to observe under light contrast microscope (10×).

5.3.9.j. Measurement of Mean Survival Time(MST) & Increase in Life Span % (ILS)

Five mice from all the treatment groups were observed for 50 days to determine

the effect of drug treatment on motality rate of the cancer (DLA) mice. Kaplan meier curve was established to represent the death of mice on respective days. MST and % ILS were calculated by using the following formula:

$$Mean\ survival\ time = \frac{[\ first\ death + last\ death]}{2}$$

$$Increase\ in\ life\ span(ILS)\% = \left[\frac{Mean\ survival\ time\ of\ treated\ group}{Mean\ survival\ time\ of\ untreated\ group} - 1\right] \times 100$$

5.3.9.k. Statistical Analysis

Statistical analysis was carried out for each group to find out significant difference. Mean values and standard deviation were calculated by one way ANOVA, where statistical significance is denoted by '*' ($p < 0.05$), '**' ($p < 0.005$), '***' ($p < 0.001$) and '****' ($p < 0.0001$) followed by Tukey's multiple Comparison test between all the groups with $P < 0.05$ was considered as significant. Graph Pad Prism 6 software was used for standard statistical analysis and Kaplein–Meier method was followed for survival study.

5.4. Characterization

5.4.1. UV-Visible and Fluorescence Spectroscopic Measurements

UV-vis spectra were recorded using Perkin Elmer Lamda 25 UV-vis spectrophotometer and fluorescence spectra were recorded using HORIBA Jobin Yvon FluoroMax-4 spectrofluorimeter.

5.4.2. Transmission Electron Microscopy (TEM)

The size and morphology of as synthesized Tf-Cu NC and Tf-CuNC-Dox-NPs were probed using JEOL, JEM 2100 TEM (Peabody, MA, USA), which operates at maximum accelerating voltage of 200 kV. For analysis, first 1 mL of as-synthesized particle was taken and centrifuged at 15 000 rpm for 30 min. The pellet was then redispersed in 1 mL of Milli-Q water and from which 200 µL of Tf-

Cu NC–Dox NPs were taken and diluted in 1 mL of water. Briefly, 8 µL of the composite from the above dispersion was drop-cast onto copper-coated TEM grid. The sample was allowed to dry at room temperature for 6 h before analysis.

5.4.3. Dynamic Light Scattering Based Measurements

Hydrodynamic diameter and net surface charge of the composite nanoparticles were measured using Malvern Zeta Size Nano ZS-90 instrument. The change in dynamic light scattering (DLS) hydrodynamic size and surface zeta potential of Tf-Cu NCs before and after drug binding were performed at a temperature of 25 °C. In each case, 50 µL of the dispersion was diluted in 950 µL of water, and then measurements were performed. For each sample dispersion, three DLS measurements were made with a fixed run time of 11 s with scattering angle set at 90°. The Malvern DTS 5.10 software was used for data analysis.

5.4.4. Time Resolved Photoluminescence (TRPL) Study

Time-resolved photoluminescence (TRPL) intensity decay of the NCs were recorded using time-correlated single photon counting (TCSPC) set up (Horiba). The laser diode 375 (Delta Diode) was used as a source with excitation wavelength of 375 nm. The fluorescence decays were fitted using DAS6 software.

5.4.5. Matrix-Assisted Laser Desorption Ionization Time-of–Flight Mass Spectrometric (MALDI-TOF-MS) Measurements

Bruker 4800 Plus MALDI TOF/TOF Analyzer was used to measure the mass spectra of the composite nanoparticles. Sinapinic acid was used as matrix, which was prepared by dissolving sinapinic acid (10 mg) in a mixture of 1 mL of 50 % acetonitrile (ACN) and 0.05% of trifluroacetic acid (TFA). Composite nanoparticles and matrix were mixed in the ratio of 1:2 (volume ratio) carefully and then spotted.

5.4.6. Circular Dichroism Study

Circular dichroism spectra were recorded using JASCO-815 spectrometer (Jasco,

Japan).

5.4.7. Field-Emission Scanning Electron Microscopy (FESEM)

FESEM analyses of the composites and the cells were carried out in a JEOL JSM-7610F instrument. For FESEM, the prepared samples were drop cast on glass slide covered with aluminium foil and kept overnight for drying. Before analysis, the samples were coated with platinum using sputter coater JEC-3000FC auto fine coater, JEOL. Cells treated with IC_{50} dose of the composite for 48 h were washed with PBS and subsequently collected after trypsinization. The trypsinized cells were then fixed with 4 % formaldehyde. The same procedure was followed for untreated cells (control).

5.4.8. Quantum Yield Measurements

The fluorescence quantum yield of as-synthesized Tf-Cu NCs was determined relative to a reference sample - quinine sulphate (dissolved in 0.1 M H_2SO_4). It was calculated by using the following formula, where both Tf-Cu NCs and reference sample i.e., quinine sulphate were excited at same wavelength.

$$QY_S = QY_R \times \frac{A_S}{A_R} \times \frac{Abs_R}{Abs_S} \times \frac{\eta_S^2}{\eta_R^2} \qquad (S1)$$

where QY_S and QY_R refers to measured quantum yield of as synthesized Tf-CuNCs and quinine sulphate in 0.1 M H_2SO_4 as reference respectively; A_S and A_R refers to area under the emission spectrum obtained at λ_{ex} = 375 nm at slit-width = 2 nm for sample and reference, respectively; Abs_R and Abs_S refer to absorbance of the reference and sample, respectively; η_S and η_R refer to refractive indices of solvents for the sample and reference, respectively. For experiments, same solutions with respect to sample and reference were used to record UV-vis absorbance and fluorescence emission. The quantum yield of the reference (QY_r) is 0.54, whereas refractive index of solvent (water) is 1.33.

5.5. Results and Discussion

The nanodrug formulation was achieved using a blue-emitting Tf-Cu NCs and well-known hydrophobic drug, Dox, with the availability of FRET-based energy transfer between the components. Blue-emitting Tf-Cu NCs was synthesized by an aqueous method with hydrazine hydrate as the reducing agent at pH 12. (Refer to Experimental Section **5.3.2**). The schematic depiction of formulation of nanodrug for FRET assisted bioimaging, targeted delivery and synergistic therapeutic activity in vitro as well as in vivo has been elucidated in **(Figure 5.1)**.Here, Tf acted as a stabilizer by forming strong metal–ligand bond between Cu ions and cysteine residues along with contribution from N atom of histidine and O atom of tyrosyl residues[41] apart from acting as functional ligand for targeting TfR overexpressed in cancer cells. The 26 tyrosine residues of Tf (at pH > 10) along with N_2H_4 imparted the reducing environment, whereas some of the 38 cysteine sulfur residues might have acted as stabilizing ligands to the copper core in the cluster.[39,42]

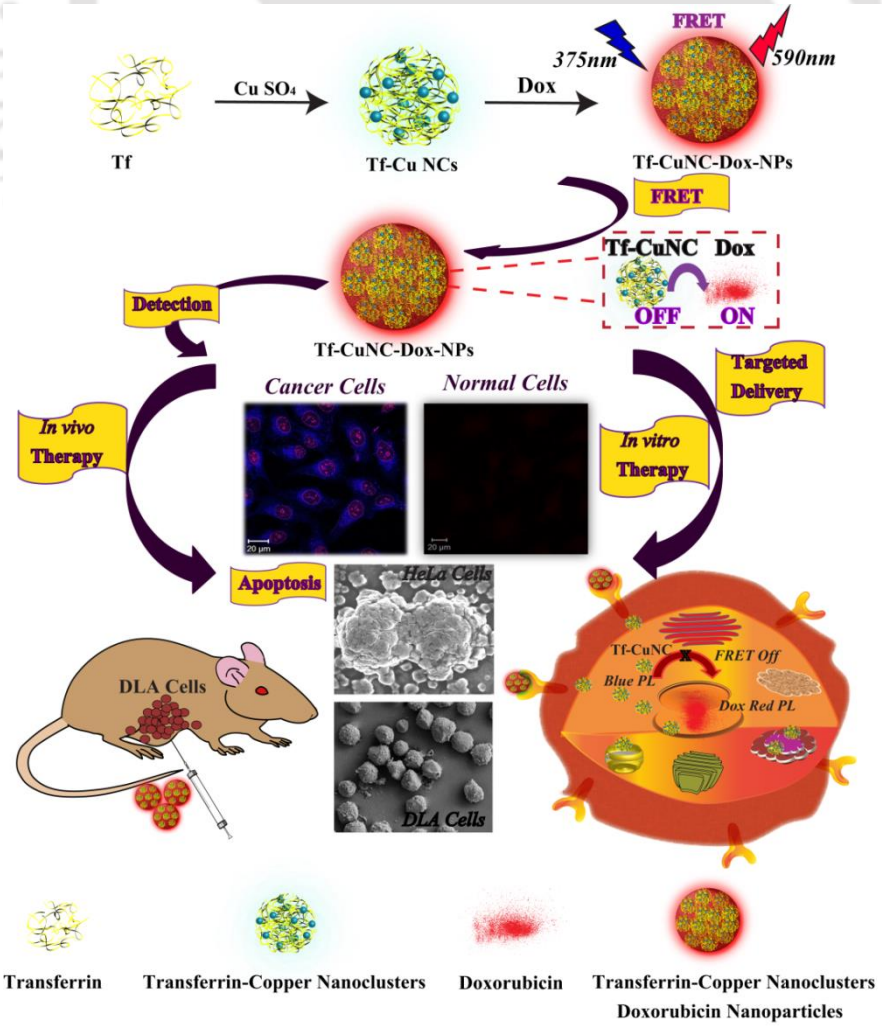

Figure 5.1. Schematic Depiction of Formulation of Targeted Nanodrug for FRET-Assisted Bio-Imaging, Targeted Delivery, and Synergistic Therapeutic Activity *In Vitro* as well as *In Vivo.*

The as synthesized Tf-Cu NCs exhibited strong blue emission band at 460 nm (λ_{ex} = 375 nm) as shown in **(Figure 5.2a)**. Additionally, the absence of any surface plasmon resonance (SPR) peak in the visible region discounted the presence of large sized copper nanoparticles **(Figure A 5.1, Appendix)**. The PL quantum yield of the as synthesized Tf-Cu NCs was quantified as 7.5%, using quinine sulfate as the standard. This is analogous to the reported emission efficiency of Cu NCs and therefore supported their suitability to be used as bioimaging probe.[26,33] The formation of Tf-Cu NCs was further validated from TEM image as shown in **(Figure 5.2b)** with average particle size distribution of 2.08 nm ± 0.84 **(Figure 5.2c)**. The average size was calculated from about 100 particles in TEM images recorded with different sets of experiments and with the help of Image J software. The characterization of the as-synthesized Tf-Cu NCs was further pursued by both matrix assisted laser desorption/ionization time-of-flight (MALDI-TOF) based mass spectrometric measurements (using sinapinic acid as the matrix) and X-ray photoelectron spectroscopy (XPS), which signified the number of atoms responsible for cluster formation and the oxidation state of the concerned atoms, respectively. MALDI TOF mass spectrum showed a base peak due to singly charged Tf at m/z = 80 027, whereas mass spectrum of Tf-Cu NCs as recorded showed a weak peak at m/z = 80 207 and two prominent peaks at m/z = 80 312 and m/z = 80 496 indicating the presence of 3, 5, and 7 Cu atoms in the as-synthesized Tf-Cu NCs **(Figure 5.2d)**. XPS spectrum showing two peaks at 932.2 and 952.2 eV, corresponding to Cu $2p_{3/2}$ and Cu $2p_{1/2}$, respectively **(Figure 5.2e)**, indicated the Cu(0) state of copper in the as-synthesized Tf-Cu NCs along with Cu(I), which differs from Cu(0) binding energy by 0.1 eV. Thus, both Cu(0) and Cu(I) species might have been present in the clusters. Additionally, absence of peak at 942 eV ruled out the possibility of Cu(II) in the system. Furthermore, circular dichroism (CD) measurements were carried out to probe the targeting ability of the protein by evaluating the degree of conformational change in transferrin following the synthesis of Tf-Cu NCs. It was found that after Tf-Cu NC synthesis there was a slender decrease in the α-helix conformation from 28.6 to

26.2% and β-sheet from 21.3 to 20.3% respectively **(Figure 5.2f)**. This indicated that the targeting efficiency of Tf might have remained unaffected after Tf-CuNCs synthesis.

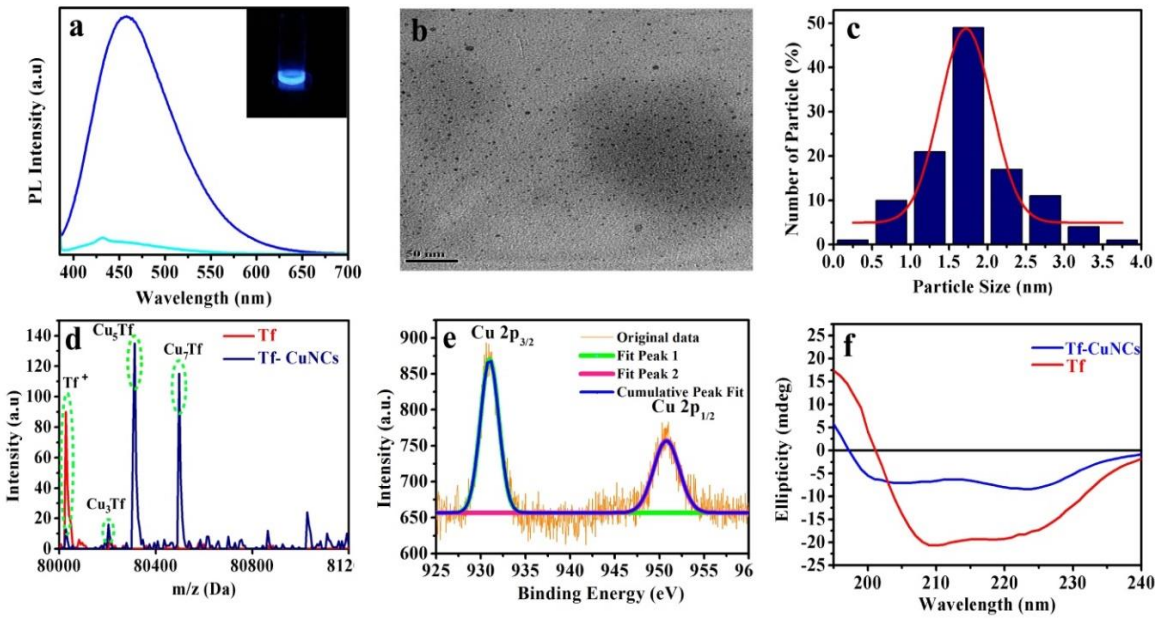

Figure 5.2. (a) Photoluminescence intensity of as synthesized Tf-Cu NCs (blue curve, λ_{ex} = 375 nm) and transferrin (cyan curve) with the inset showing digital image of Tf-Cu NCs under UV trans-illumination. (b) TEM image of Tf-Cu NCs (scale bar 50 nm). (c) Histogram showing size distribution of Tf-Cu NCs (as obtained from panel b). (d) MALDI-TOF spectra of Tf (red) and Tf-Cu NCs (blue) due to singly charged species. Peaks assigned to respective number of Cu atoms are circled in green. (e) XPS spectrum of as synthesized Tf-Cu NCs showing two peaks corresponding to Cu2p electrons. (f) CD spectra of Tf (red) and Tf-Cu NCs (blue).

For the formulation of organic–inorganic nanodrug composite, freshly prepared Dox was added to a dilute aqueous dispersion of the as-synthesized Tf-Cu NCs, under constant stirring at ambient temperature, which was followed by aging for 2 h. Details of synthesis have been described in the **Experimental Section 5.3.3**. The Tf-Cu NC–Dox NPs were then collected after centrifugation at 10 000 rpm for 30 min. The formulation of organic–inorganic nanodrug was monitored using steady-state fluorescence spectroscopy. The inorganic moiety of Tf-Cu NCs showed a characteristic emission at 460 nm (λ_{ex} = 375 nm), whereas Dox employed as organic drug has characteristic absorption at 480 nm, which emits at 590 nm. Thus, prominent spectral overlap between Tf-Cu NCs (donor, λ_{ex}

= 375 nm and λ_{em}= 460 nm) and Dox (acceptor, λ_{ex}= 480 nm and λ_{em}= 590 nm) allowed us to realize the existence of a FRET mechanism between them **(Figure 5.3a)**. Additionally, the excitation spectra recorded for Dox only (acceptor) and

composite NPs at λ_{em}= 590 nm provided further evidence of the energy transfer process from donor Tf-Cu NCs **(Figure 5.3b)**. A good spectral overlap between the excitation spectrum of composite NPs **(Figure 5.3b (ii))** and emission spectrum of Tf-Cu NCs can be observed in **Figure 5.3b (iii)**, whereas **Figure 5.3b (iv)** shows the emission spectrum of final composite NPs (nanodrug).

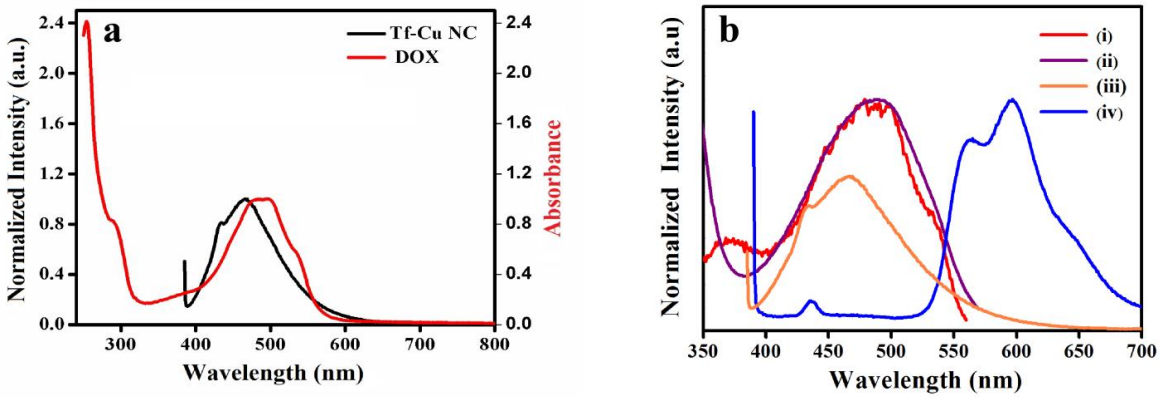

Figure 5.3. (a) Photoluminescence (PL) spectrum of Tf-CuNCs (λ_{ex} at 375 nm) and absorption spectrum of Dox. (b) Normalized excitation spectra of (i) Dox (λ_{em} = 590 nm) and (ii) composite (λ_{em} = 590 nm), and emission spectra of (iii) Tf-CuNCs (λ_{ex}= 375 nm) and (iv) the composite nanoparticle Tf- Cu NC-Dox-NPs (λ_{ex}= 375 nm).

To understand the FRET process, emission characteristic change of Tf-Cu NCs was monitored by addition of varying concentration of Dox at fixed intervals of time (λ_{ex} = 375m). Briefly, a fixed concentration of Tf-Cu NCs **(Experimental Section 5.3.4)** was taken, and Dox was added under stirring condition after an interval of 15 min each. The fluorescence spectrum of the composite dispersion was then recorded after each successive addition of 50 µL of Dox (from 400 µM stock). As is evident in **Figure 5.4a**, the emission intensity at 460 nm due to Tf-Cu NCs showed gradual drop with concomitant rise in emission intensity at 590 nm due to Dox (when excited by 375 nm light). The results indicated the energy transfer from the Tf-Cu NCs to Dox based on FRET mechanism. At a final Dox concentration of 93.7 µM in the composite (which is equal to 50.92 µg of dox), the blue fluorescence of Tf-Cu NCs was completely quenched showing maximum emission at 590 nm due to Dox thereby reaching a saturation and hence finally

giving rise to pink color dispersion that exhibited red emission. To get better insight into the occurrence of FRET between Tf-Cu NCs and Dox, time resolved photoluminescence (TRPL) spectroscopic measurements were carried out. **Figure 5.4b** shows the PL decay profile of Tf-Cu NCs and Tf-Cu NC–Dox NPs with λ_{ex} = 375 nm. The drop in average PL lifetime of Tf-Cu NCs from 3.3 to 1.2 ns in the Tf-Cu NC–Dox NPs **(Figure 5.4b)** gave evidence of the steady state emission quenching of the donor in the presence of the acceptor (Dox) and its active participation in the FRET process. On the basis of this, the energy transfer efficiency from Tf-Cu NCs to Dox in the NPs was calculated to be 63.6% following **equation A5.2 ii, Appendix**. The degree of energy transfer was further determined from spectral overlap integral value calculated following **eq A5.2 iii appendix** which was found to be 3.71×10^{14} M^{-1} cm^{-1} Förster radius (R_0) equal to 2.83 nm (using **eq A5.2 iv,Appendix**), which was found to be in the desired range (1–10 nm) of an ideal FRET pair. Therefore, using the values obtained for R_0 and E, the actual distance between the FRET pair (using **eq A5.2 v, Appendix**) was calculated to be 2.55 nm. (Refer to the Section **5.2 Appendix** for FRET parameters and calculation details.)

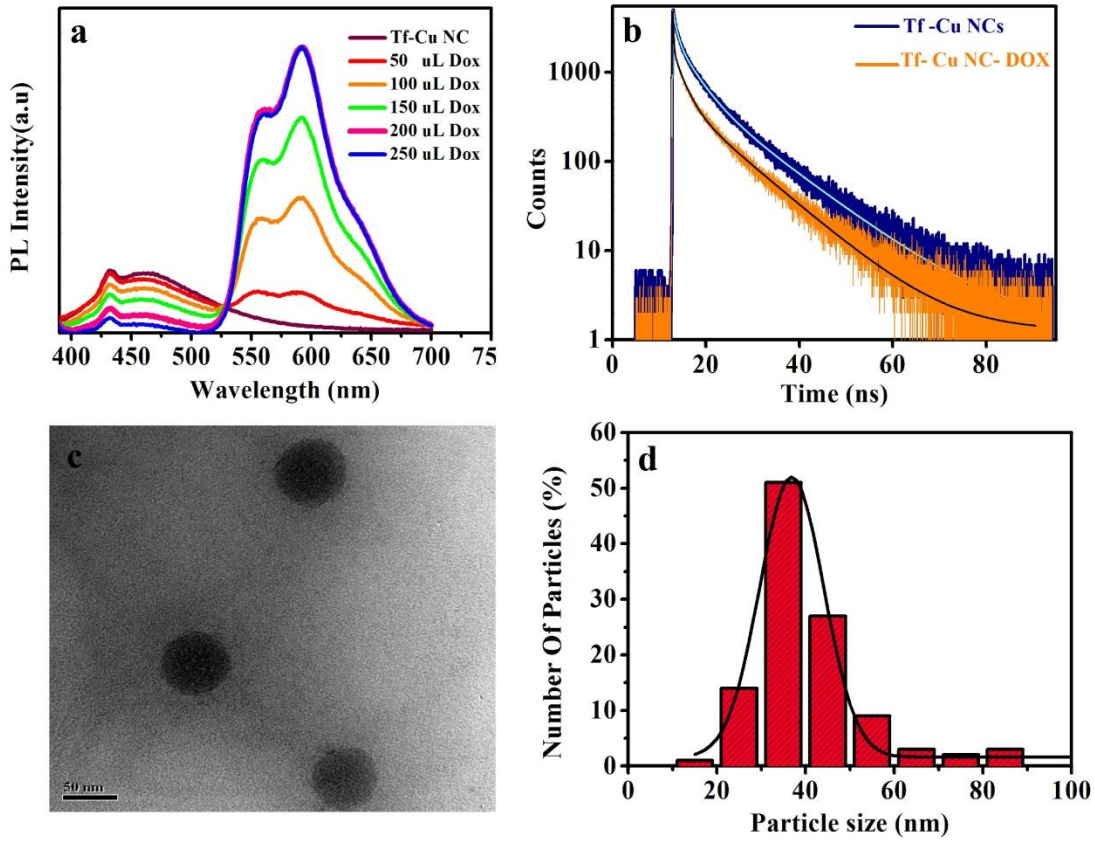

Figure 5.4. Change in PL emission intensity of Tf -Cu NCs recorded at varying concentrations of Dox (400 μM stock) as mentioned in the legends (λ_{ex} = 375 nm).(b)Time-resolved photoluminescence decay curve of as-synthesized Tf-Cu NCs (blue) and Tf-Cu NC–Dox NPs (red) monitored at λ_{em} = 460 nm (and λ_{ex} = 375 nm). (c) TEM image of Tf-Cu NC–Dox NPs. (d) Corresponding particle size distribution of as synthesized Tf-Cu NC–Dox NPs.

Furthermore, to shed light into the mechanism of NP formation, DLS-based zeta potential measurements were performed. The zeta potential data revealed a negative charge of −13.2 ± 5.02 mV for the as-synthesized Tf-Cu NCs. The increase in zeta potential of the Tf-Cu NCs in the final composite to a value of 2.74 ± 1.59 mV, upon addition of positively charged doxorubicin suggested the electrostatic mode of interaction between the two species. However, H-bond interaction as well as π–π stacking interaction between Dox and hydrophilic and hydrophobic sites in protein could also be the basis of interaction.[32] Thus, after the formation of NPs, the net surface charge of the composite NPs was found to be 2.74 ± 1.59 mV, indicating the propensity of electrostatic and hydrogen bond interaction toward strong association between as synthesized Tf-Cu NCs and Dox **(Figure A5.3, Appendix)**. The resulting Tf-Cu NC–Dox NPs dispersion (pH 6.5) was centrifuged at 10 000 rpm at 15 °C and supernatant was collected. The drug encapsulation efficiency was then obtained by measuring the emission intensity (λ_{ex}= 480 nm) for Dox present in supernatant, following centrifugation of Tf-Cu NC–Dox NPs, with respect to the emission intensity of Dox used for synthesis **(Figure A5.4,Appendix)**. Further details of the procedure are available in the **Experimental Section 5.3.4**. On the basis of this, the encapsulation efficiency was found to be ~89% in the final composite collected after centrifugation, which was equivalent to 44.5 μg/mL of Dox in the dispersion. For successful drug delivery through passive targeting of tumor cells using enhanced permeability and retention (EPR) effect, fulfilment of size criterion remains an essential feature. Studies revealed that particles with diameter <200 nm are effective for easy extravasation through leaky tumor cells via EPR effect.[24] Therefore, the as-synthesized NPs were characterized by transmission electron microscopy (TEM), field-emission scanning electron microscopy (FESEM), and DLS-based studies. TEM study revealed spherical nature of the as- synthesized Tf-Cu NC–Dox NPs **(Figure 5.4c)** with an average particle size 42.14 nm ±16.83 nm, which represents

the thermodynamically most stable structure and hence shape under the given reaction condition. In addition, kinetic stability of the particles during the observation period may also have contributed to such particular size range. Additionally, the histogram plot of the as-synthesized Tf-Cu NC–Dox NPs is shown in **Figure 5.4d**. The Cu NCs of size <2 nm in Tf-Cu NC– Dox NPs are noticeable in the TEM image **(Figure A5.5c,Appendix),** while no characteristic SAED pattern for Cu metal was observed **(Figure A5.5d, Appendix)**. The FESEM image **(Figure 5.6b, Appendix)** of Tf-Cu NC– Dox NPs revealed an average particle size of 47.79 ± 8.53, which matched closely with the TEM results. However, DLS based measurement of the hydrodynamic size of the Tf-Cu NC–Dox NPs revealed size of 117.35 ± 10.15 nm, which may be due to the protein in the liquid medium and the hydration layer surrounding the NC core **(Figure A5.5e, Appendix).** Thus, the present composite NP system fulfils the size criterion required for passive targeting based on EPR effect. To further explore the cellular internalization and real-time imaging of cancer cells, confocal microscopy imaging experiments were carried out on TfR overexpressed cells. Confocal microscopy image along with depth projection image of HeLa cells after 4 h of treatment with Tf-Cu NCs revealed their successful internalization in the cells. The cells exhibited bright blue luminescence in the cytoplasm **(Figure A5.7b, Appendix)** signifying their uptake, which was corroborated by Z-stack image as shown in **(Figure A5.7d, Appendix)**.

However, a similar phenomenon was not observed in 3T3-L1 cells, which have low expression of TfR **(Figure A5.8b, Appendix)**. It has been reported that TfR is overexpressed in HeLa and MCF-7 cells, whereas HEK-293 and 3T3-L1 cells have low expression of them as shown by semi quantitative polymerase chain reaction (PCR) using TfR gene primers **(Figure 5.5a)**. Relative expression level of the TfR was measured by extracting the RNA of the respective cells followed by transformation into cDNA by reverse transcription polymerase chain reaction (RTPCR). Semi quantitative PCR analysis and agarose gel electrophoresis of cDNA gave an insight into the expression level of TfR in all the cells. To confirm the receptor-mediated active endocytosis, fluorescence-activated cell sorting (FACS)-based experiments were performed with transferrin inhibitor Chlorazole Black E (50 μM), which was added to the cells 6 h prior to the treatment (in order to block

the TfR). The overgrown HeLa cells on treatment with transferrin inhibitor blocked the uptake of Tf-Cu NC–Dox NPs. The same amount of Tf-Cu NC–Dox NPs without inhibitor showed a higher shift in fluorescence intensity plot than the cells treated with inhibitor after 4 h of treatment **(Figure 5.5b)** as analysed by FACS. Without inhibitor, the uptake of Tf-Cu NC–Dox NPs was more facile compared to that of control Dox used for the treatment **(Figure A5.9, Appendix)**.

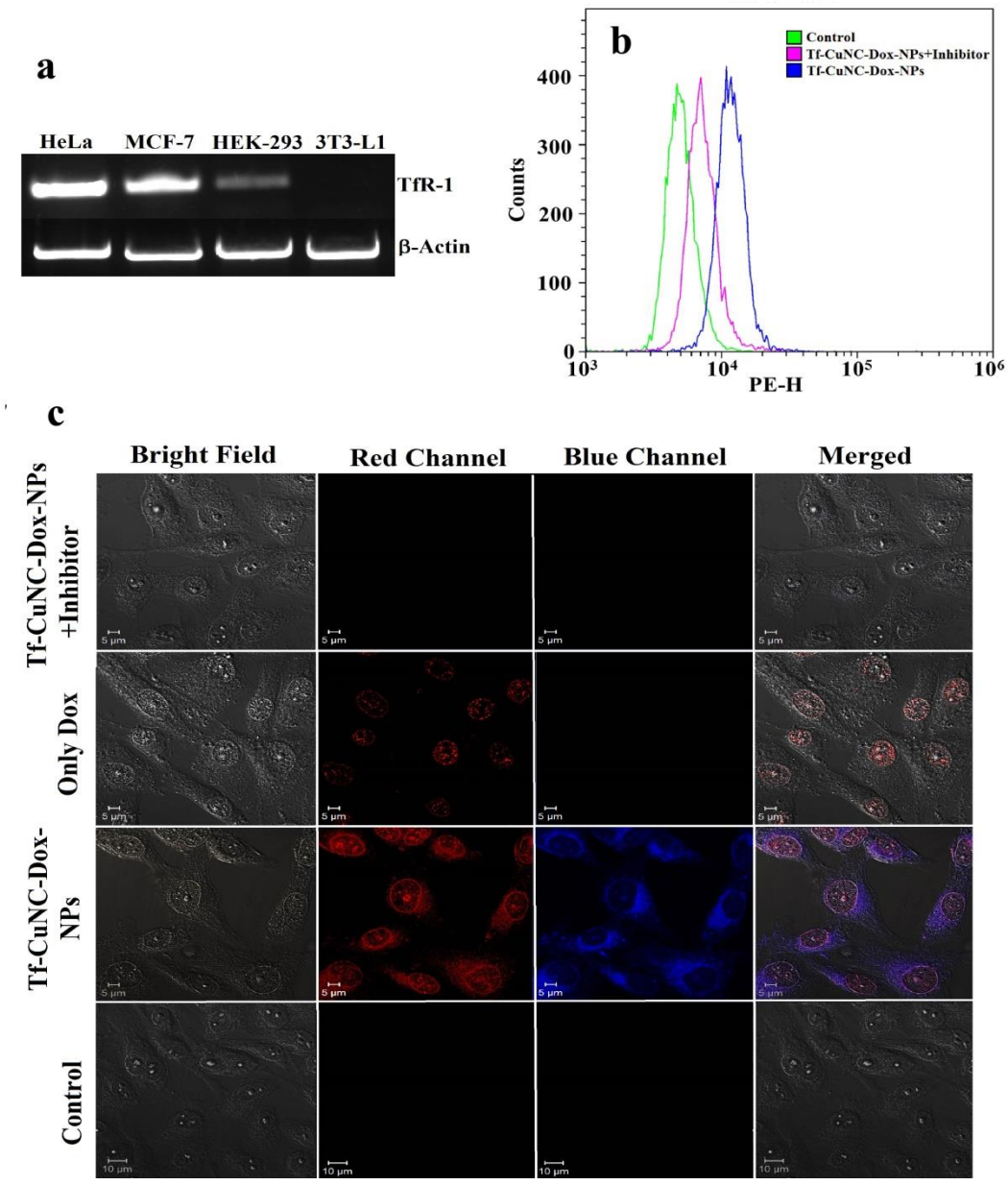

Figure 5.5 (a) Agarose gel electrophoresis results (image) showing different expressions of TfR on HeLa, MCF-7, HEK-293, and 3T3-LI cells, and β- actin, which was taken as endogenous control. (b) FACS analysis confirming the uptake of the composite by cells without Tf inhibitor as observed by shift in fluorescence intensity profile in PE-H channel than the cells treated with inhibitor. (c) Confocal fluorescence microscopic images of

HeLa cells treated with Tf-Cu NC−Dox NPs for 4 h, and then with inhibitor for 6 h, only Dox and cells treated with Tf-Cu NC−Dox NPs without inhibitor. First column represents the bright-field images; the second and third columns represent fluorescence image collected in the emission windows of 580−700 and 380−490 nm at excitation wavelengths of 405 and 488 nm, respectively. The fourth column is the merged image. The scale bar is 5 μm for first 3 columns, whereas the image representing the control has a scale bar of 10 μm.

It is apparent from the FACS data that there was an observable shift of fluorescence intensity plot of HeLa cells after 4 h of treatment with Tf-Cu NC−Dox NPs than only Dox as depicted in **(Figure A5.9, Appendix)**. To evaluate whether the uptake was an active or passive process, the cells were preincubated (i) at 4 °C for 4 h and (ii) in an ATP-depleted environment (using 10 mM NaN_3 for 30 min). This is followed by incubation with (Tf-Cu NC−Dox NPs) for 4 h. The control was also maintained at 37 °C following treatment for 4 h. These exposures resulted in prominent reduction of fluorescence intensity by 67.45 and 58.96%, respectively **(Figure 5.6)**. The results were further supported by CLSM studies **(Figure A5.10, Appendix)**, hence suggesting the prevalence of active transport mechanism.

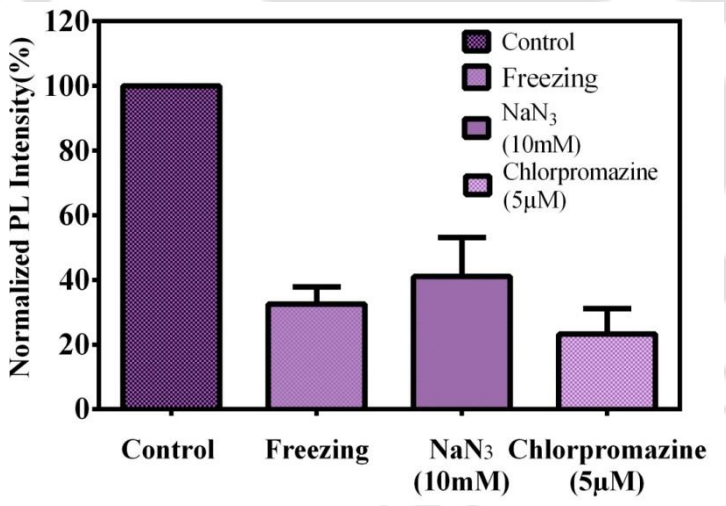

Figure 5.6. Quantitative analysis of cellular uptake of Tf-CuNC-Dox-NPs by HeLa cells after 4°C incubation, in presence of sodium azide (NaN_3) and chlorpromazine inhibitors. All the measurements were carried out in Tecan (in triplicates). Here control means HeLa cells treated with Tf-CuNC-Dox-NPs for 4h at 37°C.

Furthermore, to validate the pathway involved in endocytosis, the cells were preincubated with chlorpromazine (5 μM for 4h), which is a known clathrin mediated endocytosis inhibitor. Experimental results indicated drastic reduction

of fluorescence intensity (76.67%) compared with that of control **(Figure 5.6)**. The reduced luminescence as seen in CLSM images **(Figure A5.10, Appendix)** also revealed less uptake of Tf-Cu NC–Dox NPs in chlorpromazine treated cells thus confirming the clathrin mediated endocytosis pathway.

Additionally, the confocal microscopy studies also supported the inhibitory action of Chlorazole Black E, as no activation of luminescence was observed on HeLa cells treated with Chlorazole Black E for 6 h followed by 4 h treatment with Tf-Cu NC–Dox NPs **(Figure 5.5c)**. This observation was possibly due to blocking of TfR receptor mediated endocytosis pathway by the inhibitor. Furthermore, the internalization of Tf-Cu NC–Dox NPs after 4 h of treatment was clearly observed in case of HeLa and MCF-7 cells as opposed to HEK- 293 and 3T3-L1 cells, which have low expression levels of TfR (**Figure A5.11, Appendix)**. To get a better insight into the manifestation of FRET in the as-synthesized NPs, vis-a`-vis, being inside cells, time-dependent confocal microscopy studies was carried out in HeLa cells.

Interestingly, receptor-mediated endocytosis of Tf-Cu NC– Dox NPs in TfR-overexpressing cells led to gradual activation of blue luminescence of Tf-Cu NCs in the cytoplasm as is clear from Figure 4. The time-dependent confocal laser scanning microscopic studies revealed no luminescence at 0 h of treatment by the as-synthesized NPs **(Figure 5.7)**. However, after 2 h of treatment, slender blue luminescence was observed in the cytoplasm, which was gradually enhanced over the time possibly due to gradual disruption of donor–acceptor interaction between Tf-Cu NCs and Dox following internalization. This led to gradual recovery of blue fluorescence in cytoplasm and hence simultaneous release of Dox in the nucleus. **Figure 5.7** clearly revealed the blue luminescence observed in cytoplasm after 4 h of treatment with red fluorescence of the Dox in the nucleus, the intensity of both of which was augmented at the end of 6 h of study. In contrast, no significant recovery of blue luminescence was observed in 3T3-L1 cells, which have relatively low TfR expression, when treated with the Dox loaded composite **(Figure 5.8a)**.

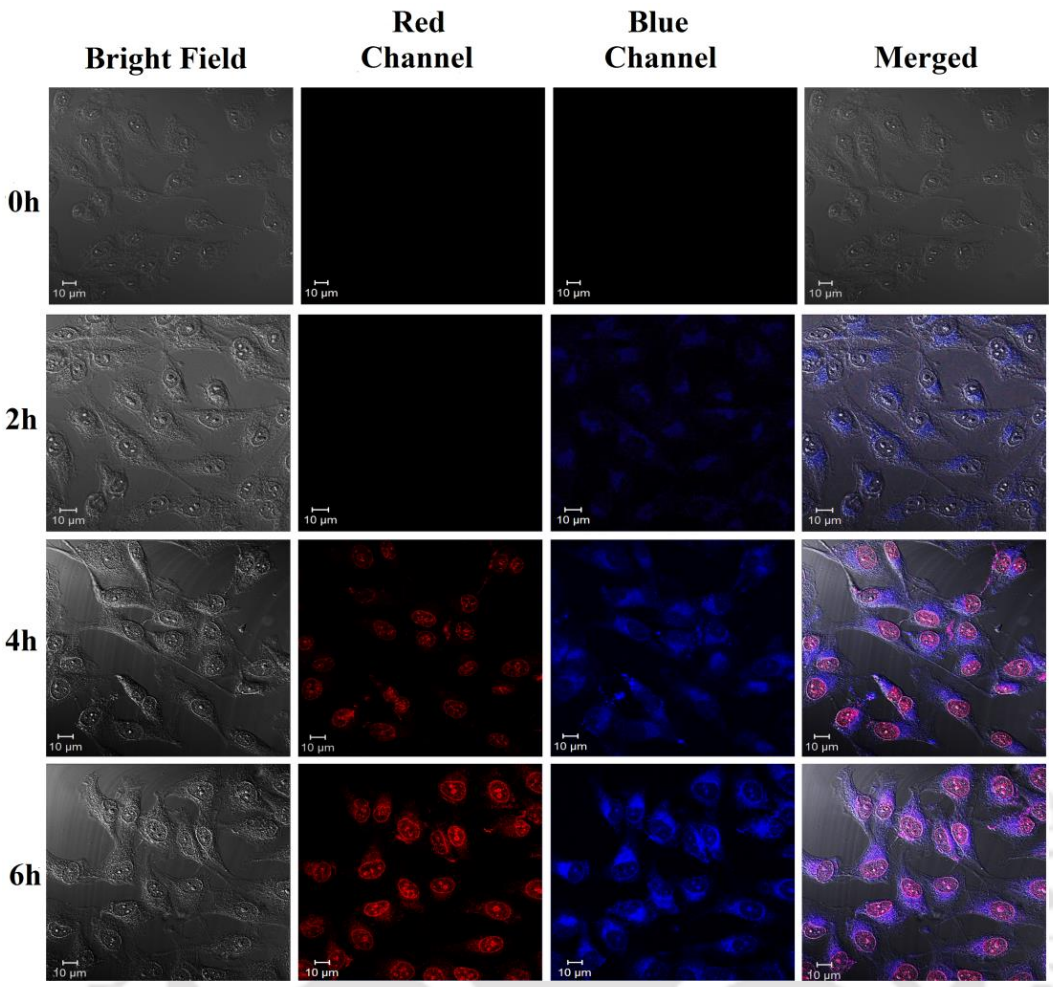

Figure 5.7. Fluorescence confocal microscopy images of HeLa cells at different time intervals −0 h, 2 h, 4 and 6 h of treatment, indicating the gradual uptake of Tf-Cu NC−Dox NPs. The excitation wavelength was 405 and 488 nm. First column is the bright-field image, for the second and third columns the fluorescence images were collected in the range of 580−700 and 380−490 nm, respectively. Fourth column is the merged image. The scale bar is 10 µm.

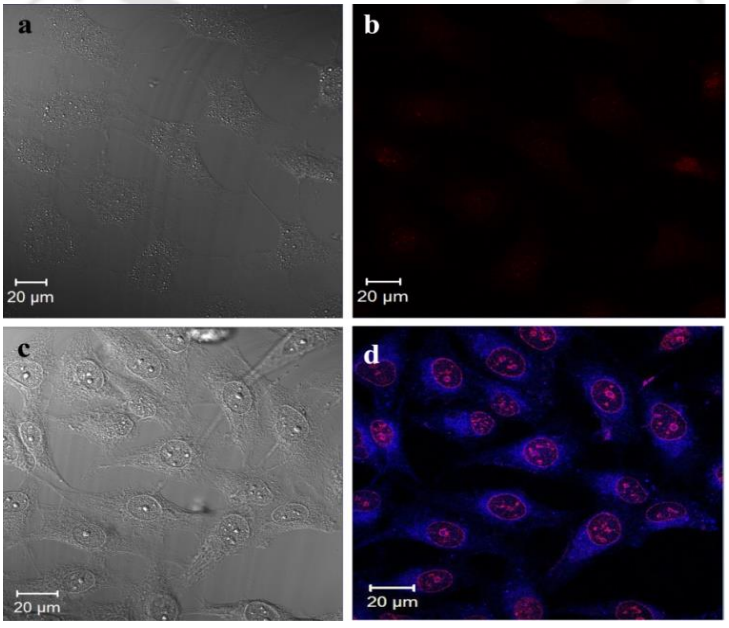

Figure 5.8. Bright field (a and c) and confocal microscopy (b and d) images of 3T3-L1 and HeLa cells treated with Tf-Cu NC-Dox-NPs recorded after 4 h of treatment.

To evaluate the intracellular drug release and its therapeutic activity, MTT-based cell viability assay was carried out. The HeLa cells were incubated at different concentrations of Tf-CuNCs, free Dox, and Tf-Cu NC−Dox NPs for 48 h at 37 °C. The final concentrations of copper and Dox in the Tf-Cu NC−Dox NPs was 1.82 and 44.5 μg/mL, respectively. The copper concentration in the Tf-Cu NC−Dox NPs was determined by AAS. Furthermore, 75% of HeLa cells were found to be viable when treated with Tf-Cu NCs only at a concentration of 0.44μg/mL (with respect to copper) as shown in **(Figure A5.12a, Appendix)**. Furthermore, MTT assay carried out in HeLa cells at Dox concentrations in the range of 0.2−1.33 μg/mL showed viability of around 50% at 1.23 μg/mL as shown in Figure **5.9a**. Interestingly, the same concentration of Dox on cells treated with Tf-Cu NC−Dox NPs displayed viability of only 22%. The IC_{50} values, calculated by nonlinear regression curve fit (using Graphpad Prism Software), were found to be 0.65 μg/mL for Dox and 0.32 μg/mL for copper **(Figure 5.9a)**, suggesting the occurrence of synergistic effect. To establish the synergy of Cu and Dox in Tf-Cu NC−Dox NPs, the isobologram and combination index (CI) were calculated based on the median effect principle of Chou and Talalay,43 using the CalcuSyn software (Biosoft, Version 2.1). The line of additivity of isobologram plot can be interpreted in terms of synergy (CI <1) placed below the line, additivity (CI = 1) on the line and antagonism (CI > 1) above the line. The isobologram plot of MTT data shown in **Figure 5.9b** depicts that all the data points were below the line of additivity, which represented drug−drug interactions, i.e., synergy. The details of the CI values are given in **(Table A5.1)**. Similar dose-dependent cytotoxicity of nanodrug was also observed in MCF-7 cells **(Figure A5.12b, Appendix)**, where cell viability was decreased to 20% at 1.33 μg/mL of Dox. The IC_{50} value was found to be at 0.6 μg/mL of Dox and 0.24 μg/mL of copper. However, in case of HEK-293 and 3T3-L1 cells, around 80−90% of cells were viable at the IC_{50} dose of HeLa cells (**Figure A5.12 c,d, Appendix)**. In fact, at the highest concentration of Dox (1.33 μg/mL) of our experiment, the viability of cells was more than 70% in the case of 3T3-L1 cells. This is essentially because of the selective targeting of the Tf-Cu NC−Dox NPs,

based on TfR expression that promoted increased uptake by HeLa and MCF-7 cells as opposed to HEK-293 and 3T3-L1 cells. Thus, the significant decrease of cell viability with nanodrug (composite NPs) as opposed to free drug molecule evidenced synergistic therapeutic efficacy herein. The anti-cell proliferative effect of Dox was remarkably enhanced in HeLa cells when incorporated in Tf-Cu NCs. Hence, the subsequent intracellular release of anticancer drug, with synergistic therapeutic activity, was observed in case of overexpressed TfR cells (HeLa and MCF-7). To support the cytotoxicity of Tf-Cu NC–Dox NPs, *in vitro* release profile of Dox was pursued at pH 4.5 (acetate buffer) and pH 7.0 (phosphate buffer), which resemble the physiological conditions of tumor cells and normal cells, respectively. The time-dependent release profile shown in **Figure 5.9c** indicates that at pH 4.5 nearly 65% of Dox was released after 48 h, whereas around 40% of drug was released at pH 7.0. This outcome was attributed to enhanced disintegration of the inorganic–organic composite NP system at acidic pH.

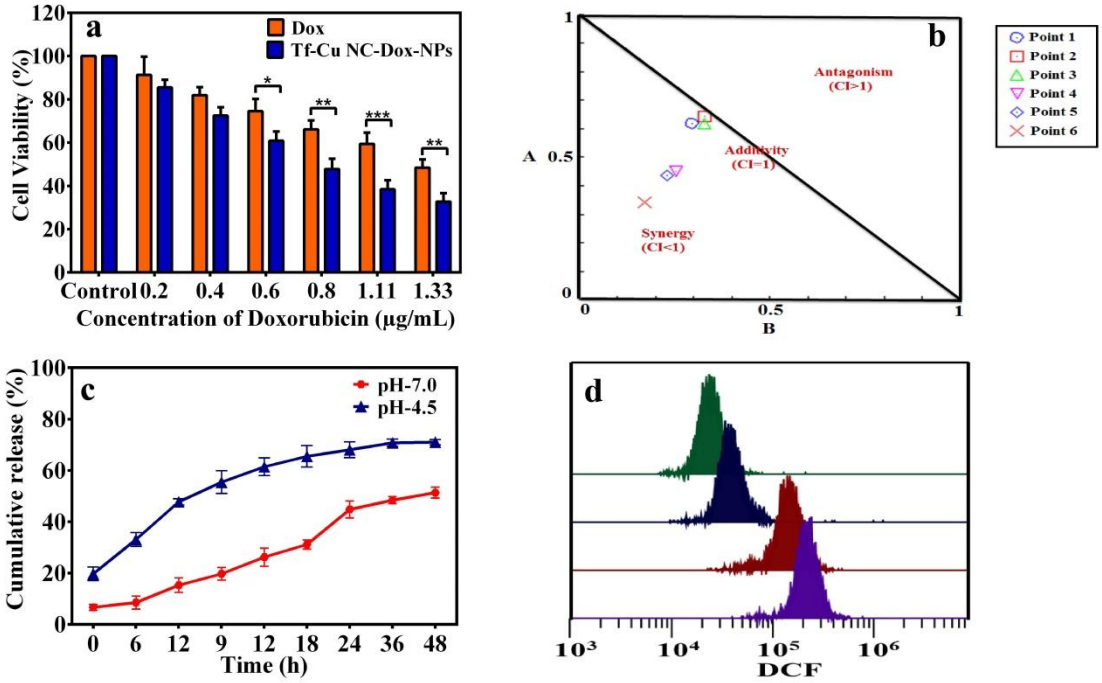

Figure 5.9. (a) Cell viability based on MTT assay after 48 h of treatment with varying concentrations of Dox and Tf-Cu NC–Dox NPs in HeLa cells. The experiments were carried out in triplicate and are represented as the mean ± SD. The ANOVA test revealed the statistical significance between Dox and Tf-Cu NC–Dox NPs which is denoted by * ($p < 0.05$), ** ($p < 0.005$), and *** ($p < 0.001$). (b) Isobologram analysis showing all points below additive line indicating synergistic effect. Combination index (CI) values calculated

using Calcusyn software. (c) Time-dependent in vitro release profile (in %) of Dox from Tf-Cu NC–Dox NPs in the PBS (pH 7.0) and acetate buffer (pH 4.5). Experiments were carried out at 37 °C and are represented as the mean ± SD from three individual experiments. (d) FACS analysis results of the generation of reactive oxygen species (ROS) in HeLa cells investigated in DCF channel (FITC) corresponds to the green emission of the DCF. Cells treated with Tf-Cu NC–Dox NPs exhibited prominent shift as compared to the control cells.

To further examine the cytotoxicity of Tf-Cu NC–Dox NPs, analyses of live and dead cells were performed using Calcein AM and EtBr. For this, HeLa cells were treated with IC_{50} dose of Tf-Cu NC–Dox NPs with respective Tf-Cu NC and Dox concentrations as mentioned above. Observation under epifluorescence microscope revealed heightened EtBr-stained apoptotic cells, which signified the preferential uptake of Tf- Cu NC–Dox NPs as compared with Dox by the treated cells **(Figure 5.10)**.

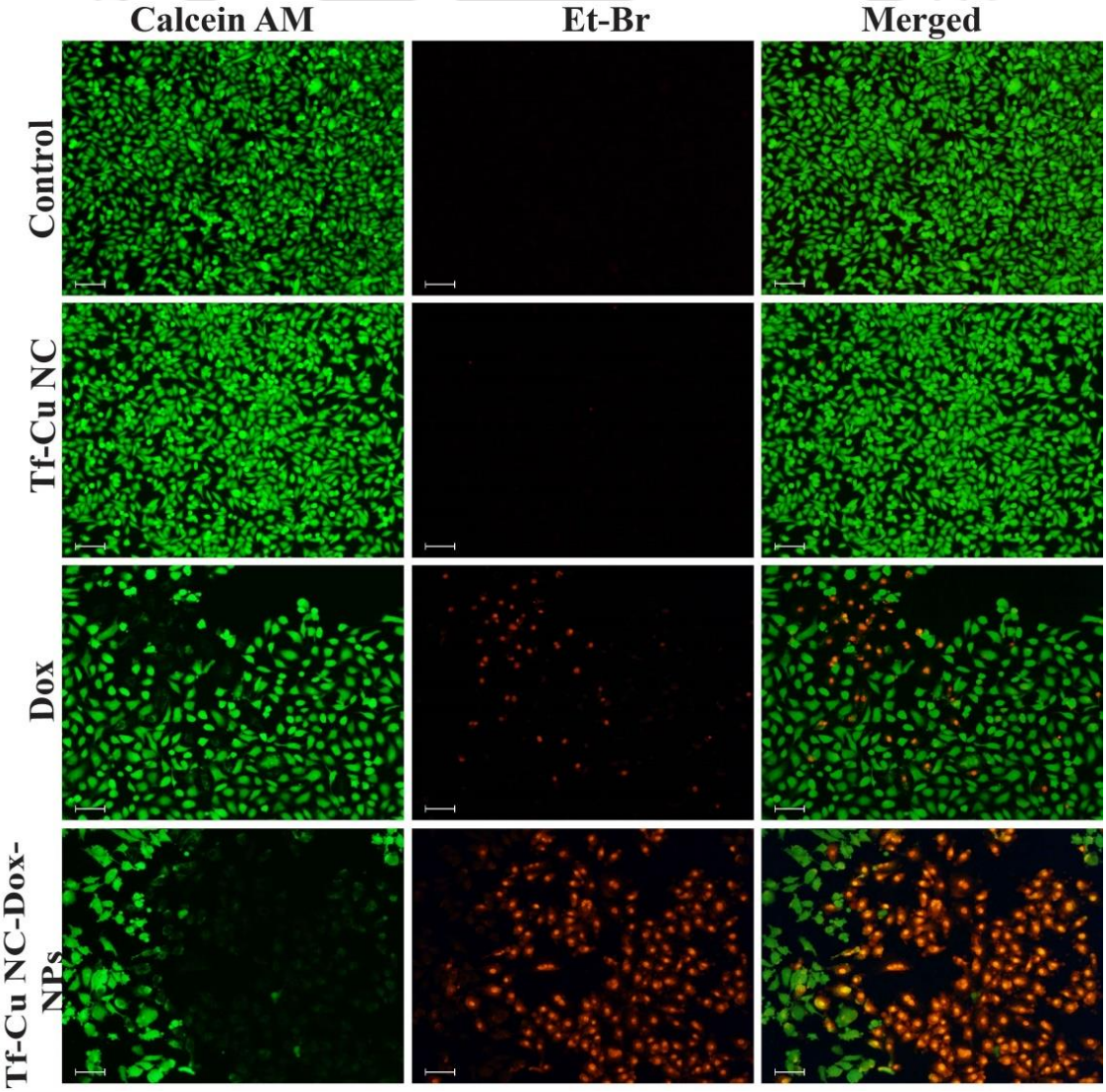

Figure 5.10. Calcein AM/Et-Br dual staining of live and dead HeLa cells (control) and cells treated with Tf-CuNCs, Dox, and Tf-CuNC-Dox-NPs, respectively. Scale bar represents 100 µm.

Additionally, the onset of apoptosis was documented in FESEM images, after 48 h of treatment with Dox and Tf-Cu NC–Dox NPs. Initiation of apoptosis was illustrated by gradual indentation and irregularity in the cell morphology treated with Dox **(Figure 5.11b)** than control **(Figure 5.11a)**. In contrast, more blebbing and distortion were observed in case of cells treated with Tf-Cu NC–Dox NPs **(Figure 5.11c)**.

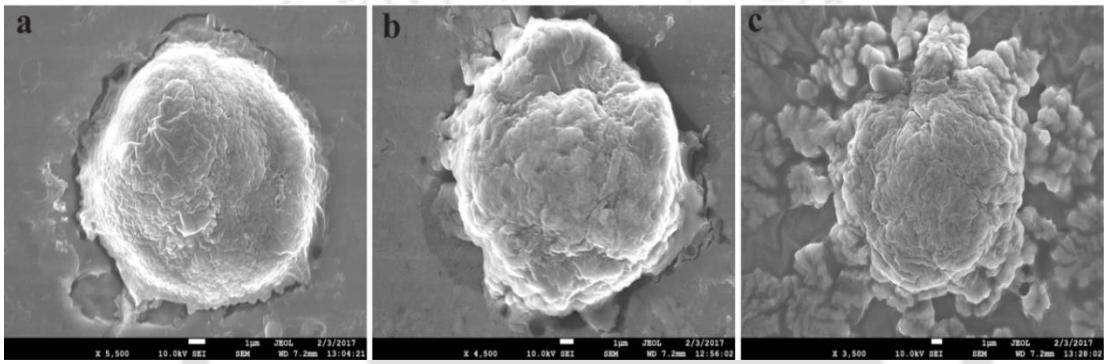

Figure 5.11. FESEM images of HeLa cells for (a) control, (b) cells after 48 h treatment with Dox showing initiation of blebbing and (c) cells after 48 h treatment with Tf-CuNC-Dox NPs showing blebbing and cell distortion. Scale bar is 1µm.

Moreover, the presence of apoptosis was also confirmed using propidium iodide (PI) assays after 48 h of treatment at IC_{50} dose of Tf-Cu NC–Dox NPs along

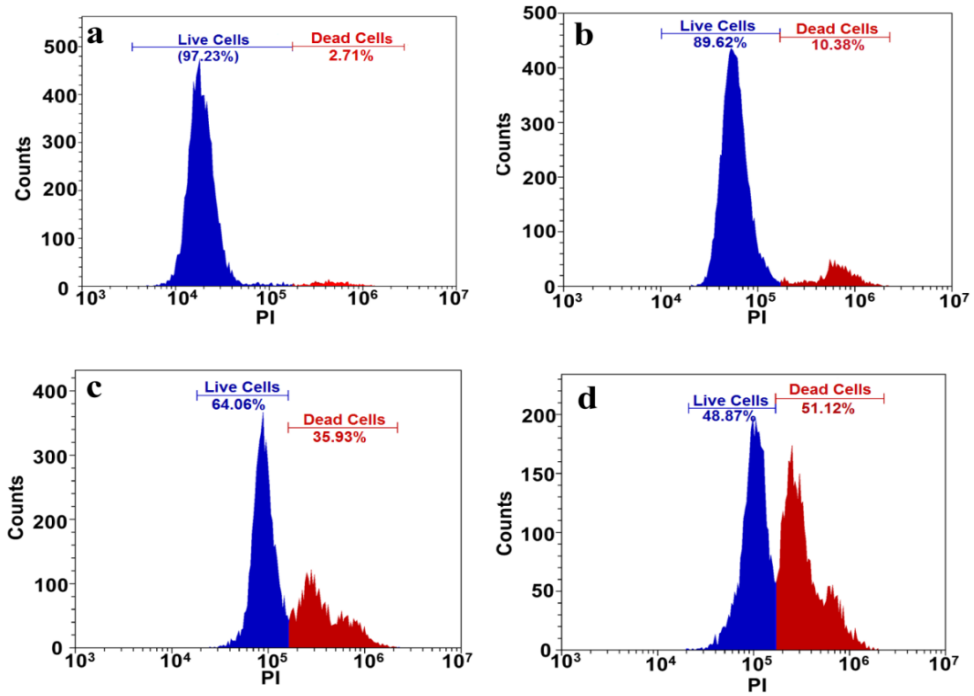

Figure 5.12. FACS based PI staining analyses for live and dead HeLa cells after 48 h (a) control (without treatment), and after treatment with (b) Tf-CuNCs, (c) Dox and (d) Tf-CuNC-Dox-NPs.

with the control Tf-Cu NCs and Dox. The results suggested upsurge of dead cells population to 51.12, 10.38, and 35.93%, for cells treated with composite NPs, Tf-Cu NCs, and Dox respectively **(Figure 5.12)**, which corroborated the cell viability results.

To elucidate the mode of cell death exerted by the nanodrug (Tf-Cu NC–Dox NPs), fluorescence-activated cell sorting (FACS) based assays were carried out. First, reactive oxygen species (ROS) generation was investigated using the 2',7'-dichlorofluorescin diacetate (DCFDA) staining method where DCFH is to be oxidized to green fluorescent 2',7'-dichlorofluorescein (DCF) in the presence of ROS. It can be inferred from **Figure 5.9d** that there was shift in fluorescence intensity in cells treated with nanodrug (Tf-Cu NC–Dox NPs), which correlated with the amount of ROS production inside the cells. Tf-Cu NCs and Dox on the other hand induced less oxidative stress than Tf-Cu NC–Dox NPs. Cell cycle analysis revealed the arrest of G2/M phase in cells treated with Dox, whereas S-phase arrest was observed in the case of cells treated with Tf-Cu NC–Dox NPs **(Figure 5.13)**. Additionally, FACS based Annexin V-7AAD assay confirmed apoptosis mode of cell death, where significantly greater percentage of apoptotic cells (17.47%) was observed for Tf-Cu NC–Dox NPs treated cells than control (2.59%), Tf-Cu NCs (4.56%) and Dox (10.15%) treatment **(Figure 5.14)**.

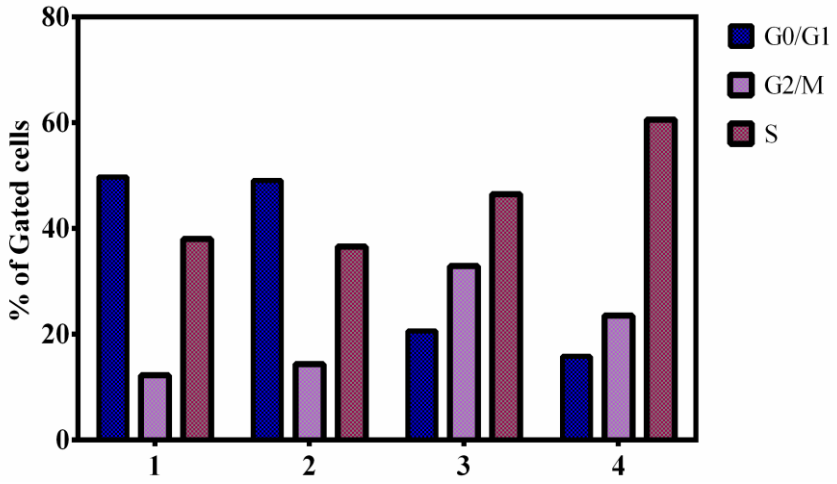

Figure 5.13. (a) Propidium iodide based cell cycle analysis using FACS where 1 represents the control and 2–4 are the cells treated with Tf- Cu NCs, Dox, and Tf-Cu NC–Dox NPs, respectively.

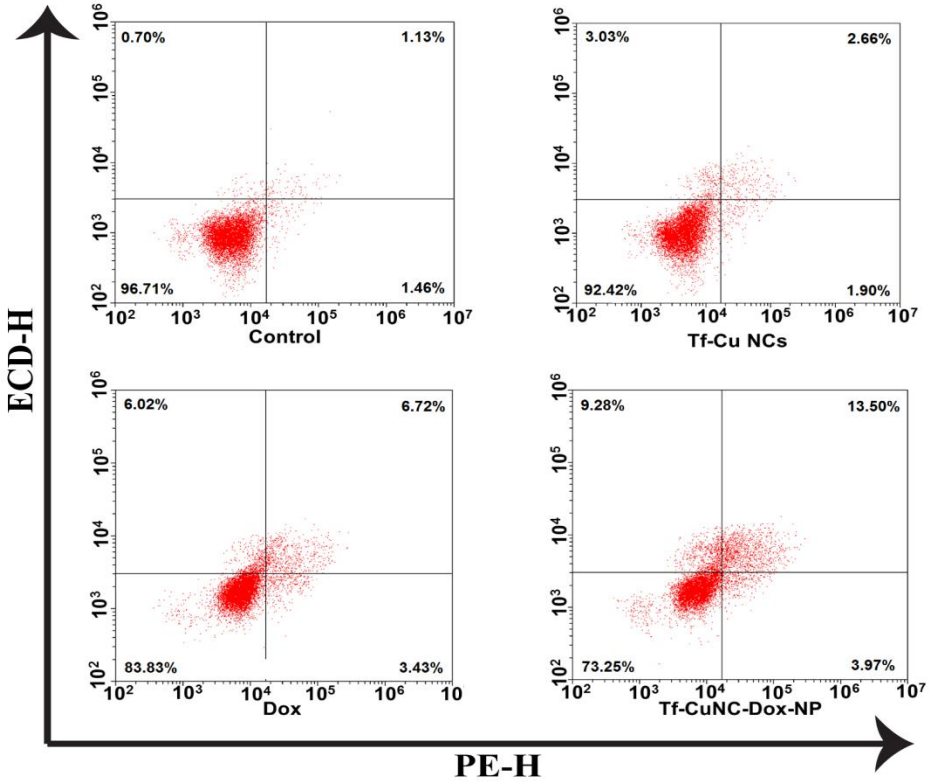

Figure 5.14. Flow cytometric analyses via annexin-V-7-AAD staining in order to find out the apoptotic and necrotic populations (%). In the dot plots the second, and third quadrants denotes early apoptotic (E.A.), and late apoptotic (L.A.) population of control cells and the cells treated with Tf-Cu NCs, Dox, and Tf-Cu NC–Dox NPs, respectively.

Finally, *in vivo* efficacy of Tf-Cu NC–Dox NPs was examined on mice bearing tumors of Dalton's lymphoma ascites (DLA). Adult male Swiss albino mice were used to induce DLA by subcutaneous inoculation of DLA cells in groups II–V for respective experiments; subsequently, the size of tumor growth was monitored. The DLA cells collected from the mice harboring tumor showed adequate expression of TfR **(Figure 5.15a)**; hence, the transferrin-carrying NPs could be employed on DLA mice model for selective targeting in vivo. The uptake of Tf-Cu NC–Dox NPs on DLA cells was confirmed by confocal microscopy **(Figure 5.15b)**. The toxicity studies of Tf- Cu NC–Dox NPs suggested that Tf-Cu NC–Dox NPs at 20 mg/kg did not produce any deleterious effects on animal health, and no mortality was seen up to 14 days of observation period. Therefore, 1/10th of the no observed adverse effect level (NOAEL), i.e., 2 mg/kg, was selected for cytotoxic

evaluation and tumor suppression activities of Tf-Cu NC–Dox NPs, Tf-Cu NCs, and free Dox.

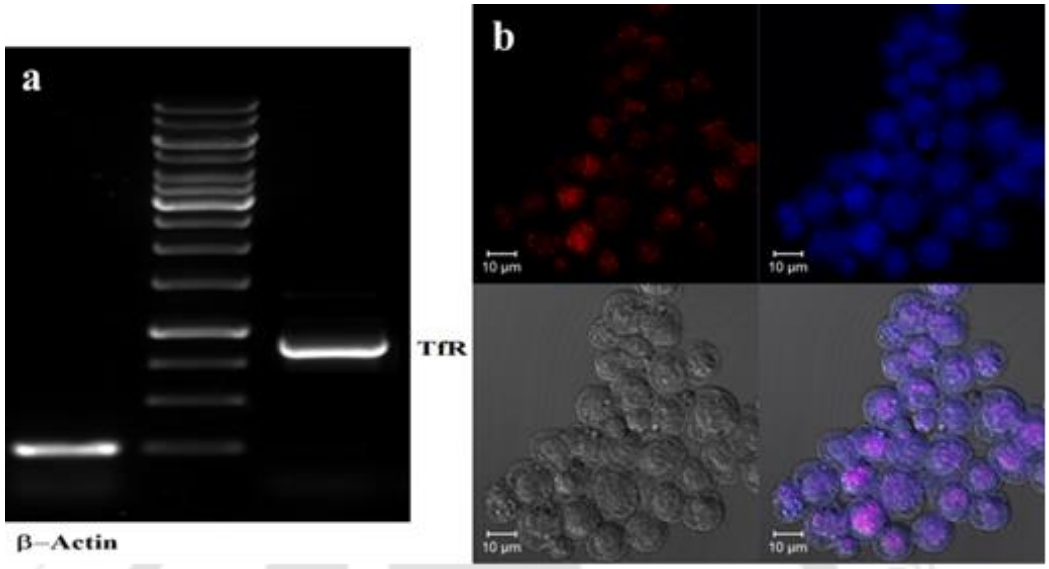

Figure 5.15. (a) Expression analysis of transferrin receptors protein in DLA cells using semi quantitative PCR. (b) Confocal microscopic fluorescence images of DLA cells after 3 h of incubation indicating the uptake of Tf-CuNCs-Dox-NPs. The excitation wavelength was 405 and 488 nm.

The experiments were conducted in Swiss albino mice bearing DLA tumorogenesis. The mice were divided into four groups (n = 10) where the first group was assigned as control followed by groups treated with Tf-Cu NCs (2 mg/kg), free Dox (2 mg/kg), and Tf-Cu NC–Dox NPs (2mg/kg). After 8 days of tumor growth (with the belly swollen due to accumulation of ascitic fluid), the nonlethal dose of Tf- Cu NC–Dox NPs (2 mg/kg) was injected into the peritoneal cavity of the mice at scheduled intervals for 8 days as illustrated in the experimental **Figure 5.16 a**. After 8 days of drug treatment period, the cells from all mice were tested for cell viability. Results of trypan blue **(Table A5.2,Appendix)** assay revealed that Tf-Cu NC–Dox NPs treatment significantly reduced the percentage of viable DLA cells compared to the other treatment groups (free Dox and Tf-Cu NCs). It can be inferred from **Figure 5.16b** that reduction in tumor volume was observed in both free Dox and Tf-Cu NC–Dox NPs treated mice, as confirmed by body weight reduction compared to control and Tf-Cu NC treated groups. Among all the treatments, the Tf-Cu NC–Dox NPs treatment

showed the highest potential in tumor volume reduction. At the end of the treatment (day 16), mice treated with Dox and Tf-Cu NC–Dox NPs showed a lesser increase in body weight (4.32 ± 0.86* g and 1.55 ± 0.42* g, respectively) compared to control and Tf-Cu NCs treated mice (11.28 ± 1.62 g and 10.14 ± 1.14 g, respectively) to that of initial body weight **(Figure 5.16b)**.

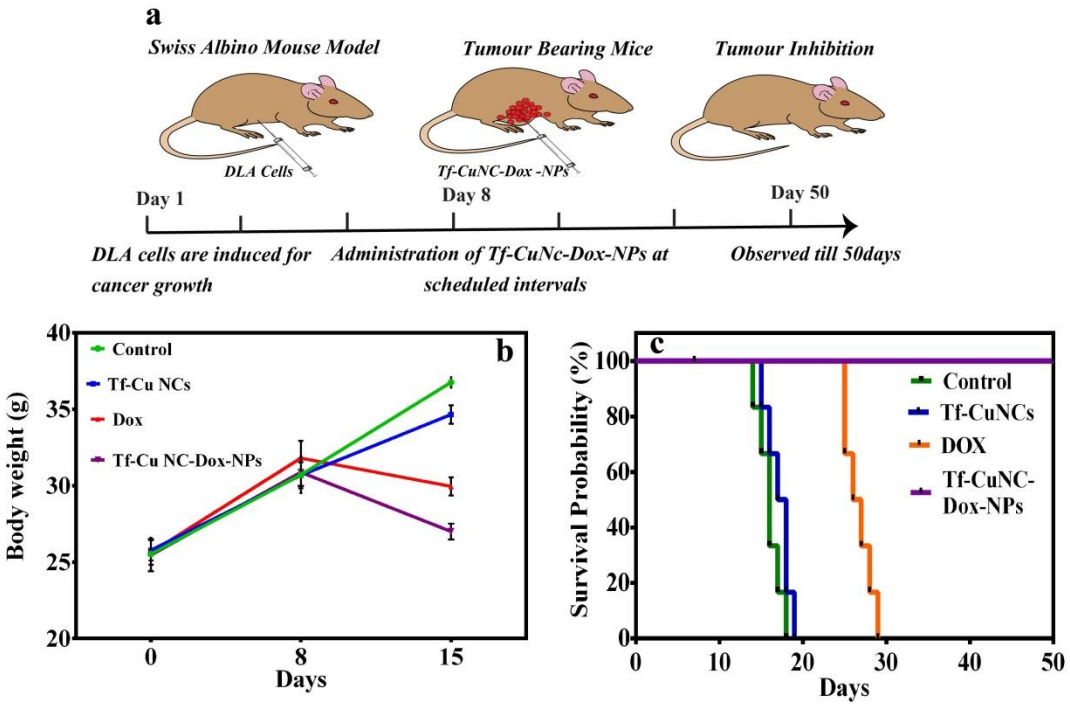

Figure 5.16. (a) Experimental scheme representing the effect of Tf-Cu NC–Dox NPs in tumor bearing Swiss albino mice monitored for 50 days. (b)Change in the body weight of tumor bearing mice after treatment with Tf-Cu NCs, Dox, and Tf-Cu NC–Dox NPs, respectively, until 16 days of treatment. (c) Survival probability of DLA induced mice monitored up to 50 days after treatment with Tf-Cu NCs, Dox, and Tf-Cu NC–Dox NPs, as represented by Kaplan–Meir curve.

The changes in body weight, cell viability, and tumor volume in various treatment groups are illustrated in **Figure 5.17** and **Table A5.2, Appendix**.

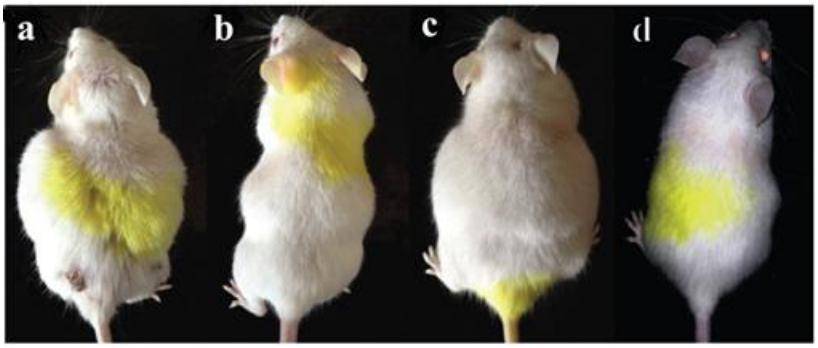

Figure 5.17. Photographs of DLA induced mice (a) control i.e., without treatment (belly swollen) taken on 14th day and those treated with (b) Dox taken on 25th day, (c) Tf-CuNC taken on 14th day; and (d) Tf-CuNC-Dox-NPs taken on 30th day.

The superior activity of Tf-Cu NC–Dox NPs compared to that of free Dox can be attributed to the targeted internalization and longer circulation time of Tf-CuNC–Dox NPs resulting in enhanced EPR effect. This superior therapeutic efficacy of Tf-Cu NC–Dox NPs has a direct impact on the increased life span of DLA mice as compared to other treatment groups. In control and Tf-Cu NCs treated groups, all mice died by 18 days of post tumor development as shown in **Figure 5.17c**. Most importantly, though free Dox treatment showed promising therapeutic effect on tumor size reduction, due to systemic toxicity issues the life span of DLA mice were reduced as compared to that of Tf-Cu NC–Dox NPs treated mice. The free DOX treated mice showed a significant increase in mean survival time compared to those of control and Tf-CuNC groups, but periodical death of mice was observed by day 28 **(Figure 5.17c)**. Selective targeting efficacy of Tf-Cu NC–Dox NPs led to survival of mice until 50 days of study, where systemic toxicity of Dox was greatly reduced as can be viewed from **Figure 5.17c**. Furthermore, morphological observation of DLA cells from various treatment groups confirmed that Tf-CuNC–Dox NPs induced maximal destruction of DLA cells over treatment with other group, viz., free Dox or Tf-Cu NCs **(Figure 5.18)**.

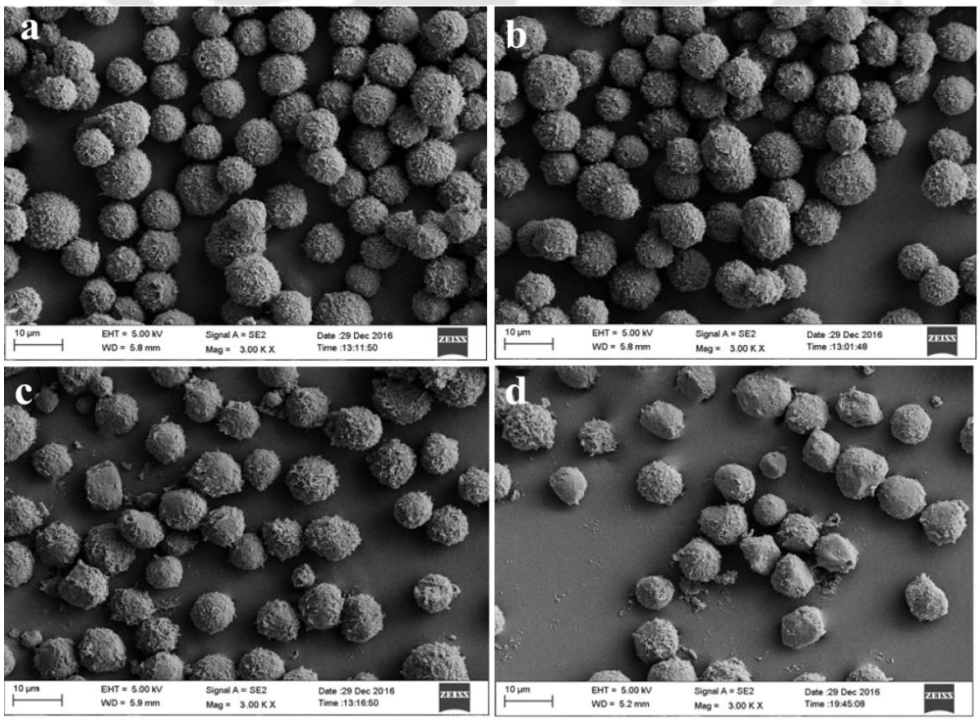

Figure 5.18. FESEM images of (a) control DLA cells without treatment and DLA cells after 16 days of treatment with (b) Tf-Cu NCs, (c) Dox, and (d) Tf-Cu NC–Dox NPs.

In addition, DLA transplanted untreated mice showed increased levels of WBC and decline of Hb and RBC counts **(Table A5.3, Appendix)**. Tf-Cu NCs administration showed almost similar counts of those found in DLA transplanted untreated mice, whereas free Dox treatment showed an increase in RBC and Hb count toward the normal, and in parallel decrease in WBC count. Interestingly, treatment with Tf-Cu NC–Dox NPs showed superior results and displayed counts almost near to normal levels of WBC, RBC and Hb as shown in **Table A5.3**, **Appendix**. Furthermore, liver functions tests (LFT) were performed to assess the hepatotoxicity in DLA mice under different treatment conditions. DLA induction in mice significantly raises all the liver function marker enzymes (SGOT, SGPT, and ALP) compared to those of normal mice **(Table A5.4, Appendix)**. Tf-Cu NC administration did not show any appreciable variation in these levels. However, free Dox treatment reduced these enzyme levels compared to those of DLA mice, while the Tf-CuNC–Dox NPs treatment showed their significant reduction, which were close to normalcy. Histopathological examination of kidney of untreated DLA mice **(Figure 5.19b)** showed glomerular atrophy, tubular congestion, infiltration of cells, and deformed epithelial cells. Tf-Cu NC administration (Figure 9c) failed to improve the condition and showed pathological observations similar to that of DLA mice. Free Dox treatment **(Figure 5.19d)** demonstrated significant improvement in the condition with decreased occurrence of tubular, glomerular, and blood vessel congestion. However, Tf-Cu NC–Dox NPs treated mice **(Figure 5.19e)** exhibited significant reduction of tubular cast and congestion, epithelial desquamation, and hyperaemia of medullary part with normal glomerular structures, which resemble the normal renal physiology of mice. Similarly, liver tissue sections of DLA mice **(Figure 5.19f)** showed abnormal hepatocytes with polymorphic neutrophil infiltration, hepatic fibrillation, hemorrhage, and perinuclear clumping of cytoplasm. These histological features were also observed in Tf-Cu NC treated mice **(Figure 5.19g)**. On the contrary, free Dox **(Figure 5.19h)** and Tf-Cu NC–Dox NPs treatment **(Figure 5.19i)** significantly reduced the damages with cellular ultrastructure's, which were comparable to normal mice.

Most importantly, hepatic physiology of DLA mice treated with Tf-Cu NC–Dox NPs was comparable with normal mice.

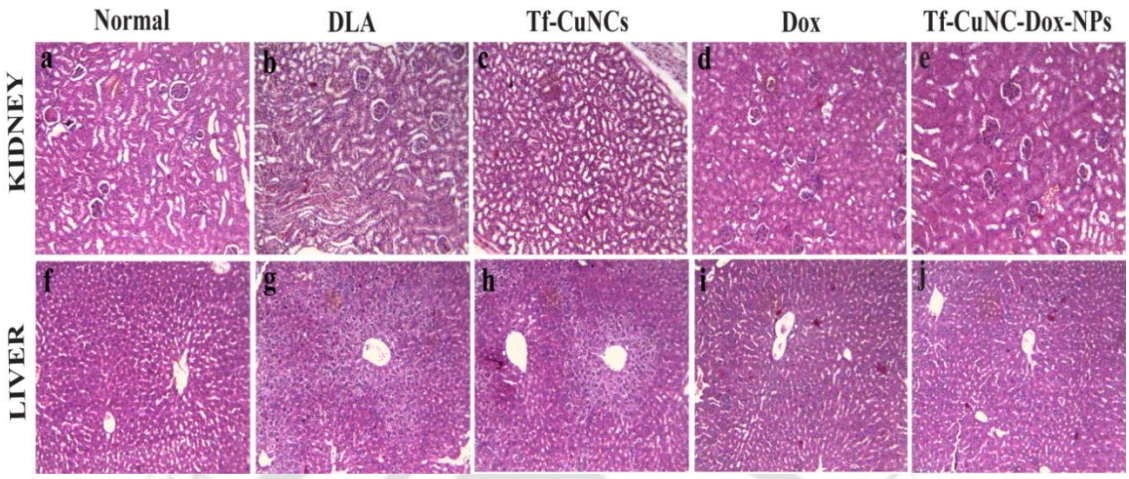

Figure 5.19. Histopathological examination images of main organs kidney (a–e) and liver (f–j), stained with hematoxylin and eosin. The organs were collected on day 17 after treatment with Tf-Cu NCs, Dox, and Tf-Cu NC–Dox NPs, respectively.

5.6. Conclusions

In brief, a green aqueous method of synthesis of a novel nanodrug system in the form of Tf-Cu NC–Dox NPs has been reported. The as-synthesized composite NPs were found to be efficacious in targeted delivery of anticancer drug Dox to TfR receptor expressing cancer cells, where uptake and release of Dox from the nanoparticulate system was monitored by FRET assisted bioimaging. Additionally, inhibitor-based experiments helped understand the cellular uptake of the formulated nanodrug specifically in TfR overexpressed HeLa and MCF-7 cells than the normal healthy cells, thereby elucidating their targeted imaging and therapeutic potential. The work also highlighted the significance of synergistic activity of Tf-Cu NC and Dox in the formulated NPs and their important therapeutic efficacy on TfR positive DLA mice model. To the best of our knowledge, this is the first report with Cu NCs, where high drug-loading capacity, excellent tumor targeting specificity and monitoring of drug release based on a FRET-assisted strategy have been combined for potential clinical applications in cancer theranostics.

5.7. References

(1) Kunjachan, S.; Detappe, A.; Kumar, R.; Ireland, T.; Cameron, L.; Biancur, D. E.; Motto-Ros, V.; Sancey, L.; Sridhar, S.; Makrigiorgos, G. M.; Berbeco, R. I. *Nano Lett.* **2015**, *15* (11), 7488–7496.

(2) DeVita, V. T.; Young, R. C.; Canellos, G. P. *Cancer* **1975**, *35*, 98–110.

(3) Zou, L.; Wang, H.; He, B.; Zeng, L.; Tan, T.; Cao, H.; He, X.; Zhang, Z.; Guo, S.; Li, Y. *Theranostics* **2016**, *6* (6), 762–772.

(4) Shao, K.; Singha, S.; Clemente-casares, X.; Tsai, S.; Yang, Y. *ACS Nano* **2015**, *9*, 16–30.

(5) Vanneman, M.; Dranoff, G. *Nat Rev Cancer* **2012**, *12* (4), 237–251.

(6) Zhang, F. L.; Song, M. R.; Yuan, G. K.; Ye, H. N.; Tian, Y.; Huang, M. D.; Xue, J. P.; Zhang, Z. H.; Liu, J. Y. *J. Med. Chem.* **2017**, *60* (15), 6693–6703.

(7) Ghoshal, A.; Goswami, U.; Sahoo, A. K.; Chattopadhyay, A.; Ghosh, S. S. *ACS Biomater. Sci. Eng.* **2015**, *1* (12). 1256-1266.

(8) Ghoshal, A.; Goswami, U.; Raza, A.; Chattopadhyay, A.; Ghosh, S. S. *RSC Adv.* **2016**, *6* (89), 85763-85772.

(9) Rao, W.; Wang, H.; Han, J.; Zhao, S.; Dumbleton, J.; Agarwal, P.; Zhang, W.; Zhao, G.; Yu, J.; Zynger, D. L.; Lu, X.; He, X. *ACS Nano* **2015**, *9* (6), 5725–5740.

(10) Kamimura, M.; Furukawa, T.; Akiyama, S.; Nagasaki, Y. *Biomaterials Science* **2013**, *1* (4), 361-367.

(11) Wang, F.; Wang, Y.; Dou, S.; Xiong, M.; Sun, T.; Wang, J.; Al, W. E. T. *ACS Nano* **2011**, *5*, 3679–3692.

(12) Kong, F.; Zhang, X.; Zhang, H.; Qu, X.; Chen, D.; Servos, M.; Mäkilä, E.; Salonen, J.; Santos, H. A.; Hai, M.; Weitz, D. A. I *Adv. Funct. Mater.* **2015**, *25* (22), 3330–3340.

(13) Li, W. Q.; Wang, Z.; Hao, S.; He, H.; Wan, Y.; Zhu, C.; Sun, L. P.; Cheng, G.; Zheng, S. Y. *ACS Appl. Mater. Interfaces* **2017**, *9* (20), 16793–16802.

(14) Yu, H.; Cui, Z.; Yu, P.; Guo, C.; Feng, B.; Jiang, T.; Wang, S.; Yin, Q.; Zhong, D.; Yang, X.; Zhang, Z.; Li, Y. *Adv. Funct. Mater.* **2015**, *25* (17), 2489–2500.

(15) Luo, W.; Wen, G.; Yang, L.; Tang, J.; Wang, J.; Wang, J.; Zhang, S.; Zhang, L.; Ma, F.; Xiao, L.; Wang, Y.; Li, Y. *Theranostics* **2017**, *7* (2), 452–465.

(16) Gao, H.; Bi, Y.; Chen, J.; Peng, L.; Wen, K.; Ji, P.; Ren, W.; Li, X.; Zhang, N.; Gao, J.; Chai, Z.; Hu, Y. *ACS Appl. Mater. Interfaces* **2016**, *8* (24), 15103–15112.

(17) Luo, D.; Carter, K. A.; Miranda, D.; Lovell, J. F. *Adv. Sci.* **2017**, *4* (1), 1–24.

(18) Yu, M. K.; Park, J.; Jon, S. *Theranostics* **2012**, *2* (1), 3–44.

(19) Falagan-Lotsch, P.; Grzincic, E. M.; Murphy, C. J.*Bioconjugate. Chem.* **2016**, *28*,135-152.

(20) Lim, E.-K.; Kim, T.; Paik, S.; Haam, S.; Huh, Y.-M.; Lee, K. *Chemical Reviews* **2015**, *115* (1), 327–394.

(21) Su, Y. L.; Fang, J. H.; Liao, C. Y.; Lin, C. T.; Li, Y. T.; Hu, S. H. *Theranostics* **2015**, *5* (11), 1233–1248.

(22) Tao, Y.; Li, M.; Ren, J.; Qu, X. *Chem. Soc. Rev.* **2015**, *44*, 8636–8663.

(23) Sahoo, A. K.; Goswami, U.; Dutta, D.; Banerjee, S.; Chattopadhyay, A.; Ghosh, S. S. *Biomater. Sci. Eng.* **2016**, *2*,1395-1402.

(24) Zhou, F.; Feng, B.; Yu, H.; Wang, D.; Wang, T.; Liu, J.; Meng, Q.; Wang, S.; Zhang, P.; Zhang, Z.; Li, Y. *Theranostics* **2016**, *6* (5), 679–687.

(25) Sun, J.; Jin, Y. *J. Mater. Chem. C* **2014**, *2* (38), 8000–8011.

(26) Zhou, M.; Tian, M.; Li, C. *Bioconjug. Chem.* **2016**, *27* (5), 1188–1199.

(27) Song, X.-R.; Goswami, N.; Yang, H.-H.; Xie, J. F *Analyst* **2016**, *141* (11), 3126–3140.

(28) Chen, N.-T.; Cheng, S.-H.; Liu, C.-P.; Souris, J.; Chen, C.-T.; Mou, C.-Y.; Lo, L.-W. *Int. J. Mol. Sci.* **2012**, *13* (12), 16598–16623.

(29) Wang, S.; Deng, H.; Huang, P.; Sun, P.; Huang, X.; Su, Y.; Zhu, X.; Shen, J.; Yan, D. *RSC Adv.* **2016**, *6* (15), 12472–12478.

(30) Wang, J.; Gao, P. P.; Yang, X. X.; Wang, T. T.; Wang, J.; Huang, C. Z. *J. Mater. Chem. B* **2014**, *2* (27), 4379-4386.

(31) Chattoraj, S.; Amin, M. A.; Jana, B.; Mohapatra, S.; Ghosh, S.; Bhattacharyya, K. *ChemPhysChem* **2016**, 17, 253-259.

(32) Tang, J.; Kong, B.; Wu, H.; Xu, M.; Wang, Y.; Wang, Y.; Zhao, D.; Zheng, G. *Adv. Mater.* **2013**, *25* (45), 6569–6574.

(33) Ghosh, R.; Goswami, U.; Ghosh, S. S.; Paul, A.; Chattopadhyay, A. *ACS Appl. Mater. Interfaces* **2015**, *7,* 209-222.

(34) Laha, D.; Pramanik, A.; Chattopadhyay, S.; Dash, S. kumar; Roy, S.; Pramanik, P.; Karmakar, P. *RSC Adv.* **2015**, *5* (83), 68169–68178.

(35) Wang, Y.; Chen, J.; Yan, X. *Anal.Chem*. **2013**, *85,* 2529-2535.

(36) Pulakkat, S.; Balaji, S. A.; Rangarajan, A.; Raichur, A. M. *ACS Appl. Mater. Interfaces* **2016**, *8* (36), 23437–23449.

(37) Cheng, W.; Nie, J.; Xu, L.; Liang, C.; Peng, Y.; Liu, G.; Wang, T.; Mei, L.; Huang, L.; Zeng, X. *ACS Appl. Mater. Interfaces* **2017**, *9*, 18462-18473.

(38) Choi, C. H. J.; Alabi, C. A.; Webster, P.; Davis, M. E. *Proc. Natl. Acad. Sci. U. S. A.* **2010**, *107* (3), 1235–1240.

(39) Zhao, T.; He, X.-W.; Li, W.-Y.; Zhang, Y.-K. *J. Mater. Chem. B* **2015**, *3* (11), 2388–2394.

(40) Sriram, M. I.; Kanth, S. B. M.; Kalishwaralal, K.; Gurunathan, S.*Int. J. Nanomedicine* **2010**, *5* (1), 753–762.

(41) Aasa, R.; Aisen, P. *J.Biol.Chem.* **1968**, *243* (9), 2399–2404.

(42) Welch, S. Transferrin: The Iron Carrier, CRC Press, Inc.: Florida, **1992**, pp 70-72.

(43) Foucquier, J.; Guedj, M. *Pharmacol. Res. Perspect.* **2015**, *3*, e00149.

Appendix of Chapter- 5 :A5

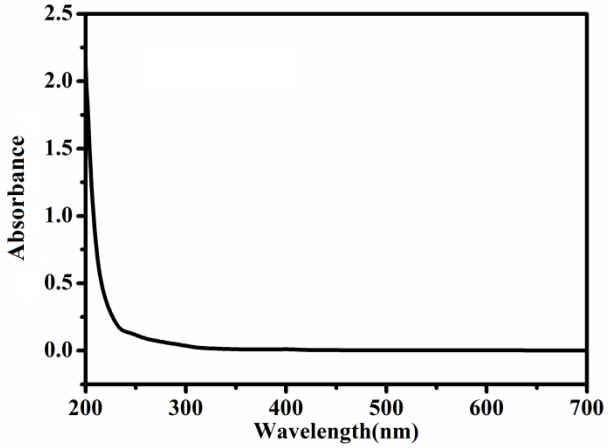

Figure A5.1 . UV-vis spectrum of as-synthesized Tf-CuNCs.

A5.2 Calculation of Energy Transfer Parameters between Tf CuNC-Dox FRET Pair

The efficiency of energy transfer (E) in a FRET pair from donor to acceptor depends upon FRET parameters viz, R_0 and r and is given by equation (i),[1]

$$E = \frac{R_0^6}{R_0^6 + r^6} \qquad (i)$$

where 'R_0' refers to critical binding distance called Förster radius when the efficiency of energy transfer is 50 % and 'r' refers to actual distance between the donor and acceptor pair.

The transfer of energy efficiency can also be calculated from the lifetime of the donor in absence and presence of acceptor using equation below,

$$E = 1 - \frac{\tau_{DA}}{\tau_D} \qquad (ii)$$

Where τ_{DA} and τ_D refer to lifetime of the donor in absence and presence of acceptor, respectively.

Now, the degree of spectral overlap between donor emission and acceptor absorption can be obtained from overlap integral (J(λ)) value calculated by the equation (iii) below,

$$J(\lambda) = \int_0^\infty F_D(\lambda)\varepsilon_A(\lambda)\lambda^4 d\lambda \qquad (iii)$$

where $F_D(\lambda)$ refers to corrected fluorescence intensity of the donor in the wavelength range λ to λ +Δλ with total intensity normalized to unity and $\varepsilon_A(\lambda)$ refers to molar extinction coefficient of the acceptor (in the units of $M^{-1}cm^{-1}$).

Now, the critical FRET distance (R_0) which depends upon the overlap integral value *J* is related by the equation (iv) shown below,

$$R_0 = 0.0211[J(\lambda)\kappa^2\eta^{-4}\varphi] \text{ (in nm)}^{1/6} \qquad (iv)$$

where J(λ) refers to overlap integral value, κ^2 refers to dipole orientation factor usually considered to be 2/3, η refers to refractive index of the medium and φ refers to quantum yield of the donor (Tf-CuNCs).

Now using equation (i), the actual FRET distance between the donor and the acceptor (r) can be calculated as follows:

$$r = R_0 \sqrt[6]{\frac{1-E}{E}} \qquad (v)$$

In the present system Tf-CuNCs is the donor and Dox is acceptor. Considering equation (ii), (iii), (iv) and (v) and using the standard values assigned for κ^2 =0.666, η (water) = 1.33, $\varepsilon_A(\lambda)$ (acceptor, Dox) = 10410 $M^{-1}cm^{-1}$and φ (donor, Tf-CuNCs) = 0.075, we calculated R_0 = 2.83 nm, J =3.71×10^{14} $M^{-1}cm^{-1}nm^4$, E = 63.6 % and r = 2.55 nm.

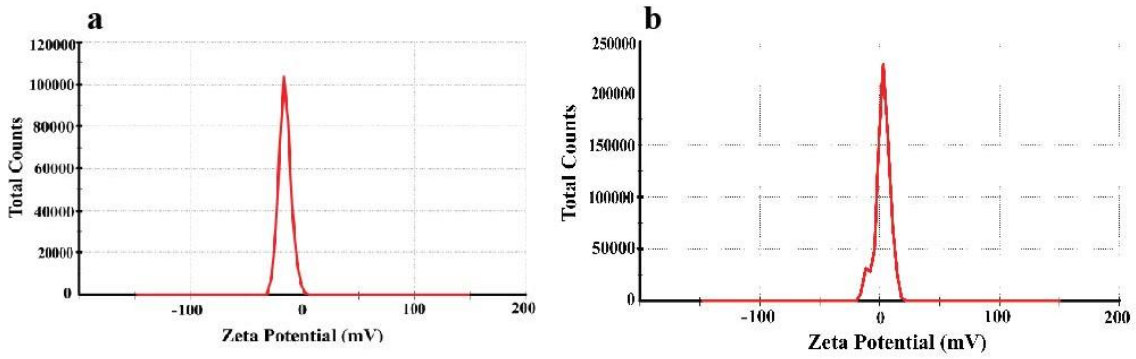

Figure A5.3 . Zeta potential of (a) Tf-Cu NCs and (b) Tf-Cu NC-Dox-NPs.

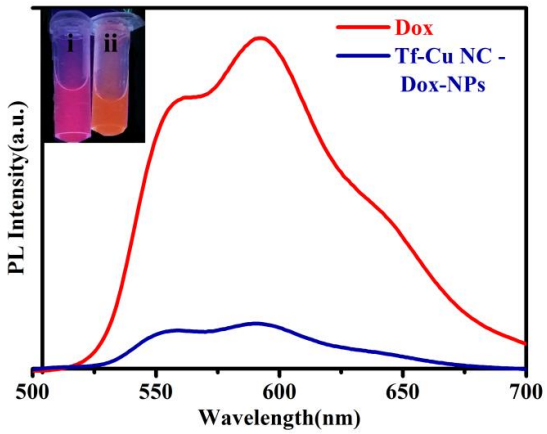

Figure A5.4. Photoluminescence spectra (λ_{ex}= 480 nm) of free Dox (red) and that corresponding to Dox (blue) present in the supernatant, which was obtained following centrifugation of Tf-CuNC-Dox-NPs dispersion at 10000 rpm for 30 min. Inset : Digital photograph of (i) Tf-CuNC-Dox-NPs and (ii) only Dox under UV light excitation. Encapsulation efficiency was calculated from the emission intensity of control Dox and the Dox present in the supernatant obtained from Tf-CuNC-Dox-NPs dispersion.

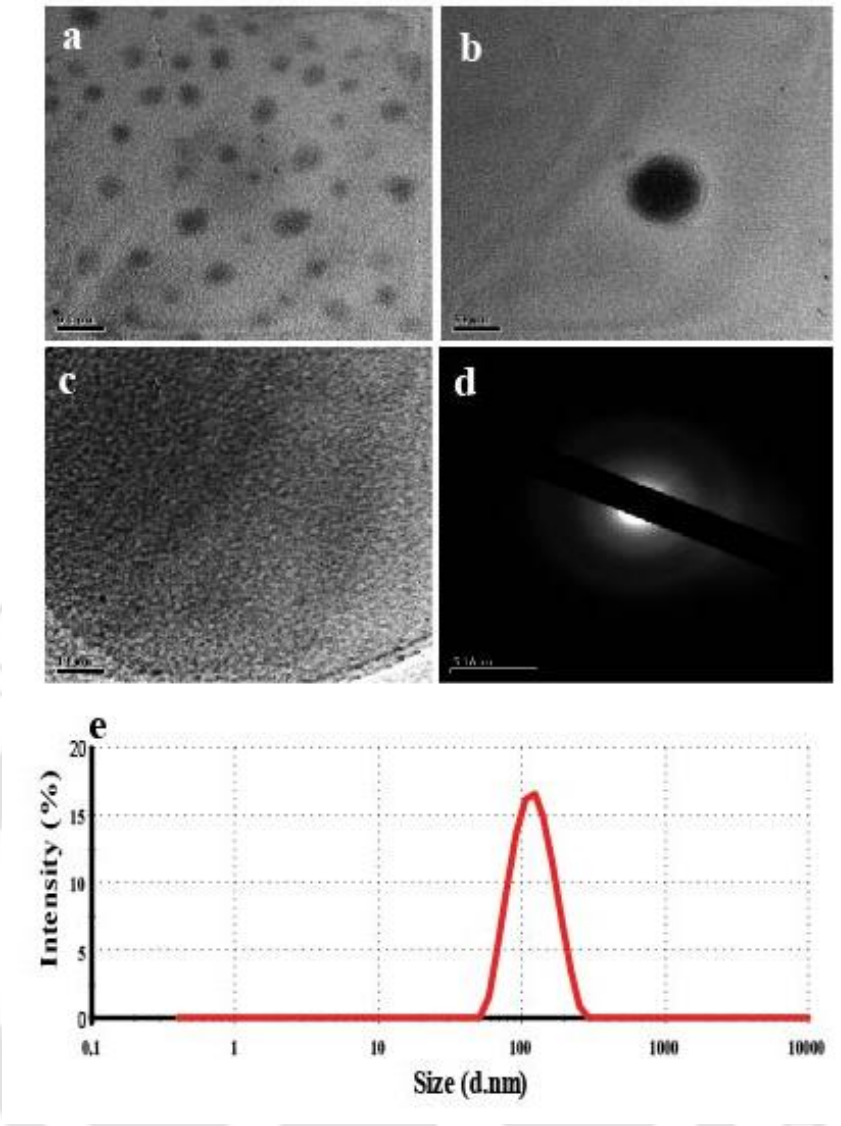

Figure A5.5. TEM image of as-synthesized Tf-Cu NC-Dox-NPs at (a) lower magnification and (b) higher magnification. (c) Magnified view of the TEM image in (b) showing the presence of CuNCs in Tf-CuNC-Dox NPs, (d) Featureless SAED pattern obtained from image in (b) and (e) DLS results representing the hydrodynamic size of as-synthesized Tf-CuNC-Dox-NPs.

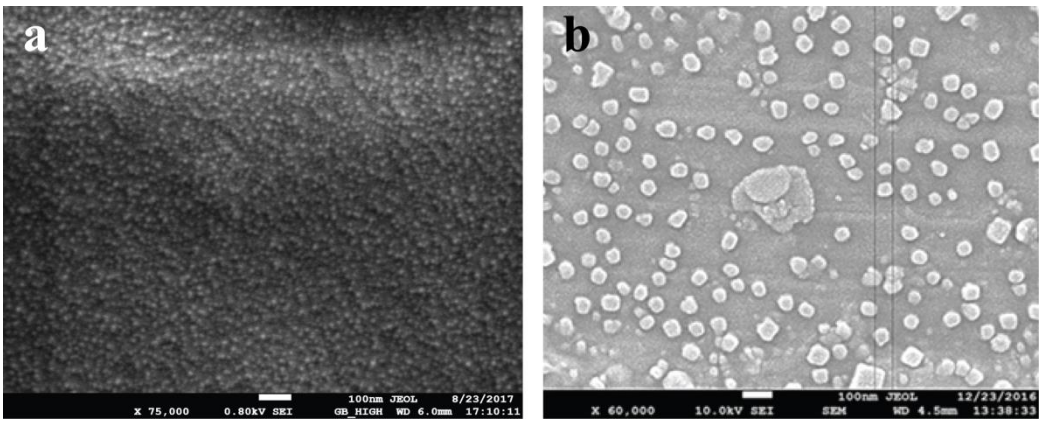

Figure A5.6. FESEM image of (a) Control (only platinum coating without sample) and (b) Tf-Cu NC-Dox-NPs (scale bar =100 nm).

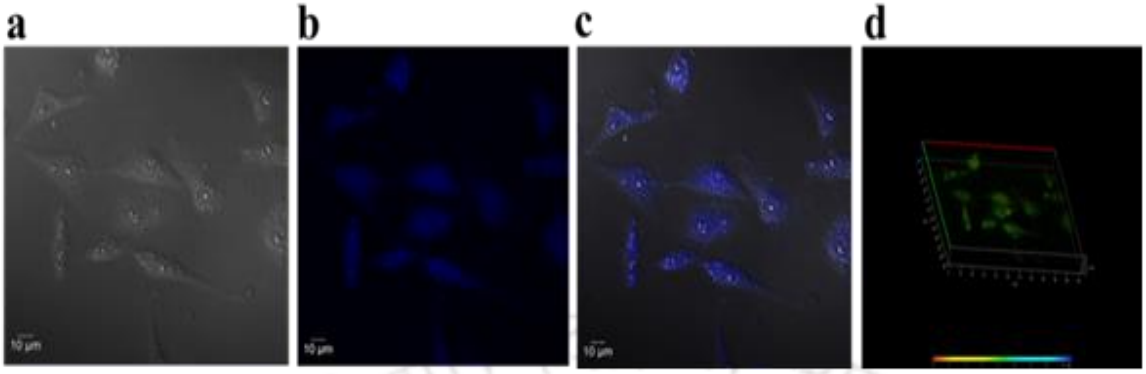

Figure A5.7 . Confocal images of HeLa cell treated with Tf-Cu NCs for 4 h. (a) Bright field image and (b) fluorescence image of the HeLa cells showing distinct blue emission of Tf-Cu NCs,(c) Merged image of both (a) and (b); (d) Z-stack projection of the cell imaged in (a) confirming the uptake of the NPs.

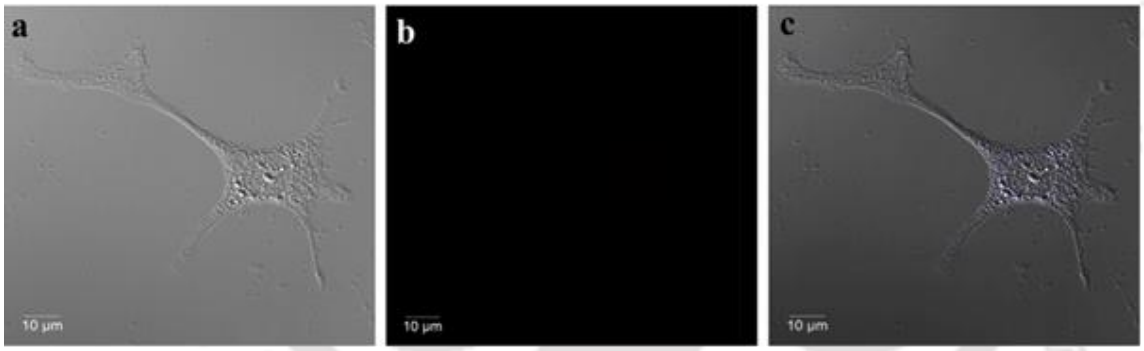

Figure A5.8. Confocal microscopy images of 3T3-L1 cells treated with Tf-Cu NCs for 4 h. (a) Bright field image and (b) fluorescence image of the 3T3-L1 with no emission corresponding to Tf-Cu NCs, (c) Merged image of both (a) and (b).

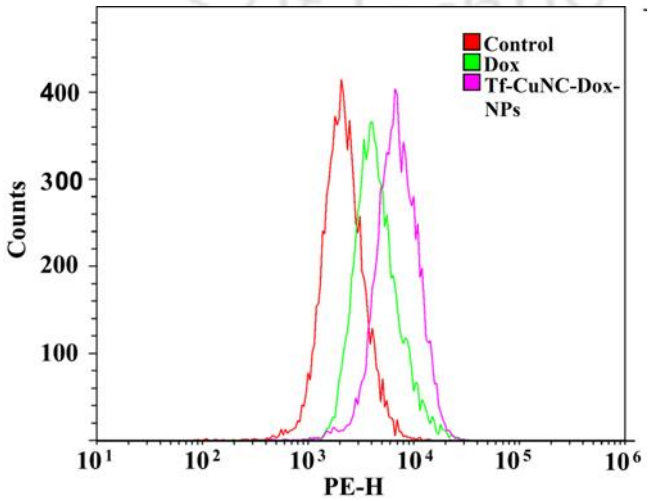

Figure A5.9. FACS results for uptake of Dox and Tf-CuNC-Dox-NPs in HeLa cells after 4 h of treatment, monitored in PE-H channel by tracking the luminescence of Dox.

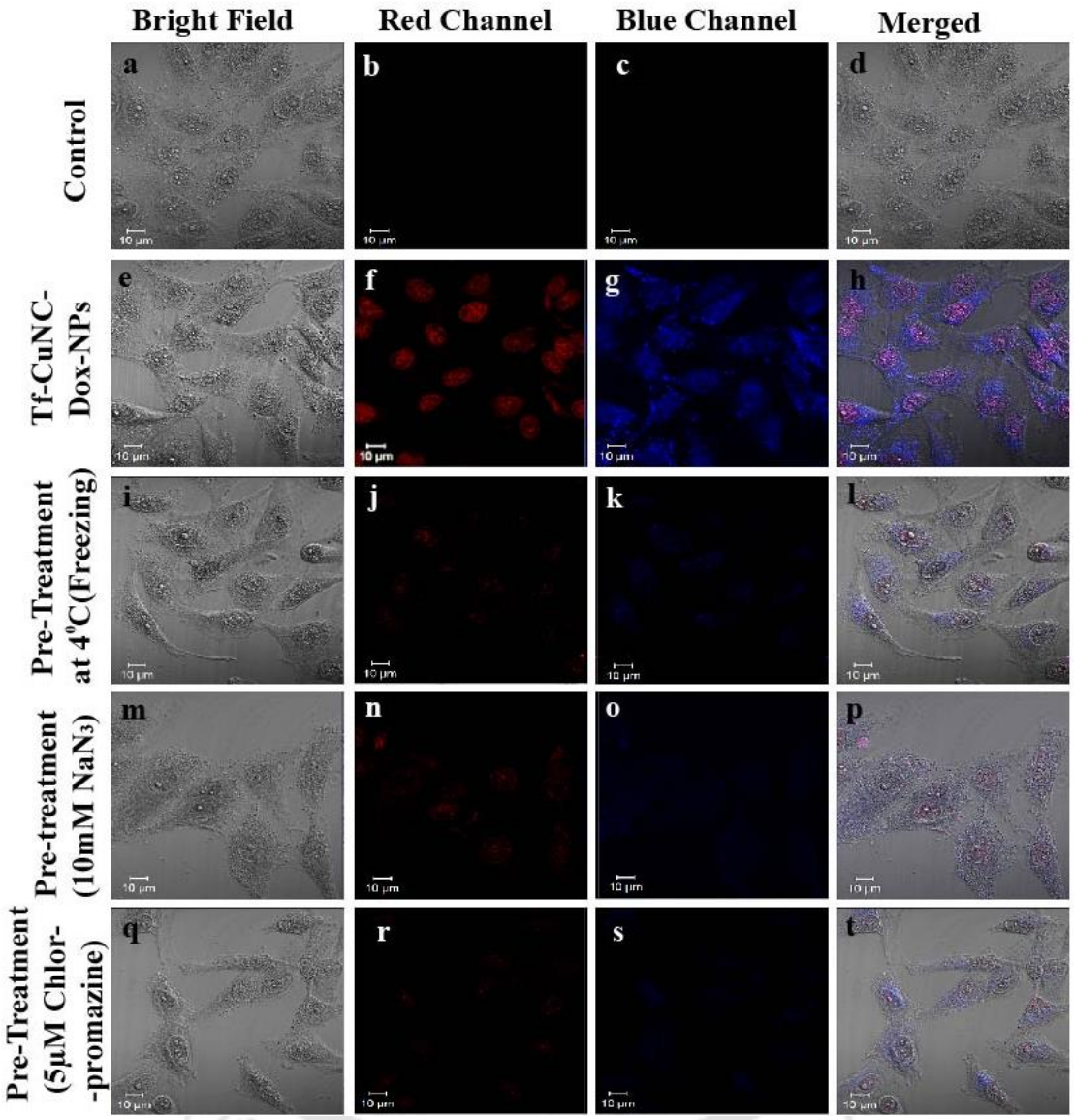

Figure A5.10. Confocal laser microscopy images of control HeLa cells (1st row), HeLa cells treated with Tf-Cu NC-Dox-NPs for 4 h without any inhibitor (2nd row). In the 3rd, 4th and 5th row, HeLa cells were pre-treated at 4°C (4h), 10mM NaN_3 (30 min) and in 5μM chlorpromazine respectively followed by 4h incubation with the nanocomposite. First column represents the bright-field images; second and third column represents fluorescence images collected in emission window 580–700 and 380–490 nm at excitation wavelength 405 and 488 nm, respectively. Fourth column is the merged image. The scale bar is 10 μm.

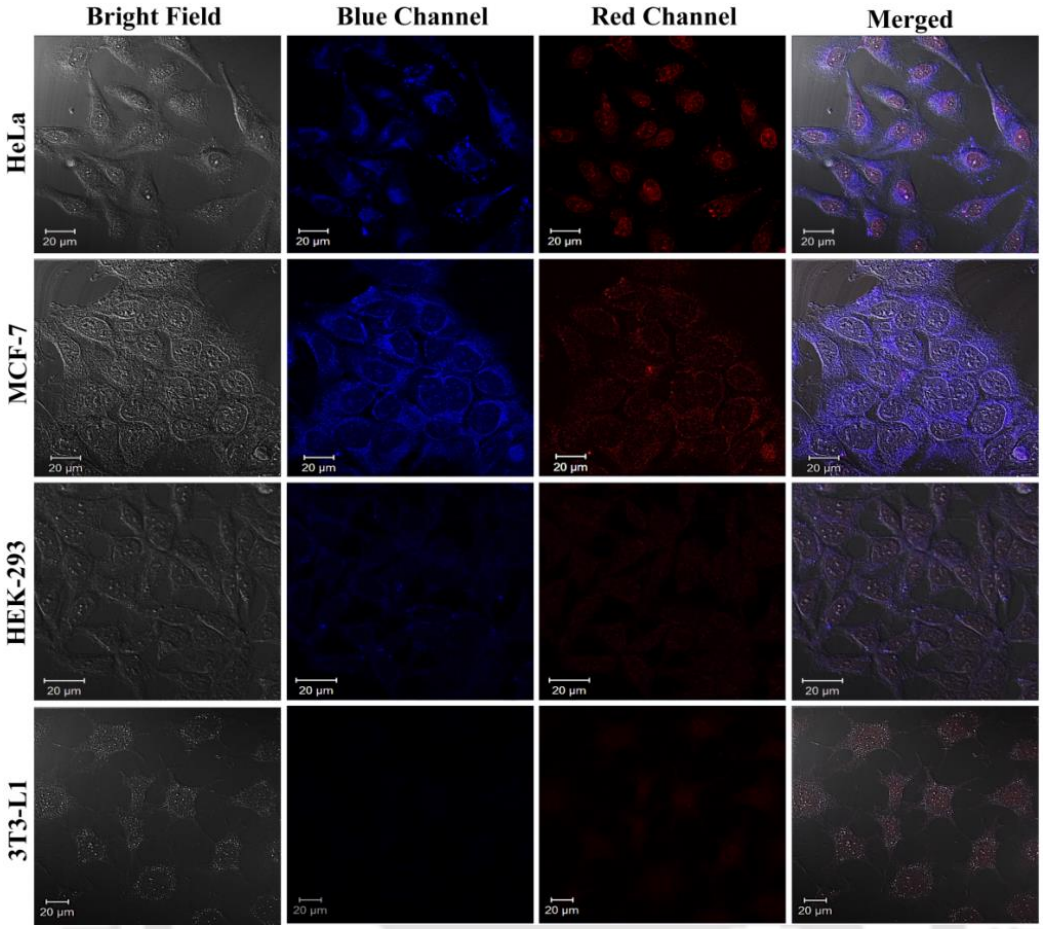

Figure A5.11. Confocal microscopy images of HeLa, MCF-7, HEK-293, 3T3-L1 cells treated with Tf-CuNC-Dox NPs for 4 h. First column is the bright-field image; in the second and third column the fluorescence images were collected at 380–490 nm and 580–700nm under excitation wavelengths 405 and 488 nm, respectively. Fourth column represents the merged images. The scale bar is 20µm.

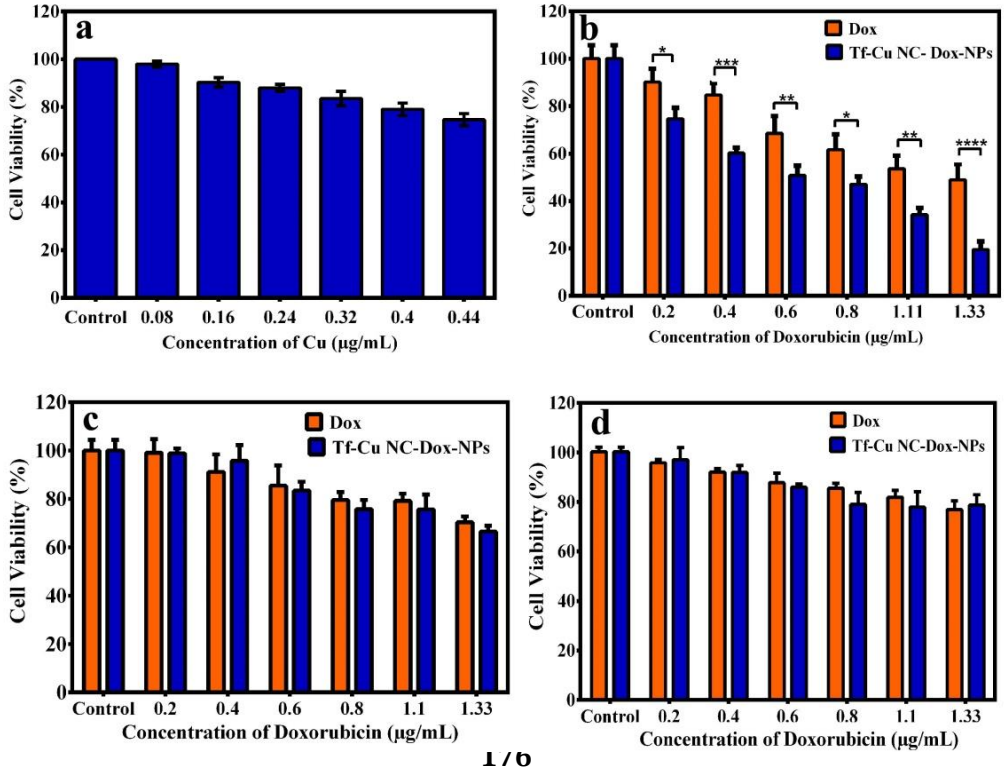

Figure A5.12. Cell viability based on MTT assay after 48 h of treatment with (a) varying concentration of Tf-CuNCs on HeLa cells. MTT assay to check the viability of different cells at variable concentration of Dox only and Tf-Cu NCs-Dox-NPs after 48 h of incubation in (b) MCF-7 cells, (c) HEK-293 cells and (d) 3T3-L1 cells. Experiments were carried out in triplicates.

Table A5.1. CI (combination index) values for varying concentrations of Tf-CuNCs-Dox-NPs treated cells with the viability %. The CI <1 for all concentration thus showing synergism.

Dox (µg/mL)	Tf-CuNC (µg/mL)	Effect(%)	CI Value < 1 Synergism
0.2	0.08	0.85	0.91284
0.4	0.16	0.72	0.97013
0.6	0.24	0.6	0.94584
0.8	0.32	0.42	0.70510
1.11	0.4	0.32	0.66833
1.33	0.44	0.22	0.516

Table A5.2. Effect of drug treatments on cell viability and body weight changes in DLA mice.

Sl. No	Treatment	Increment in body weight (gm)	Viable cell count (10^5 cells/ml)
1	DLA + Saline	11.28 ± 1.62	418.4 ± 19.7
2	DLA + Tf-CuNCs	10.14 ± 1.14	389.3 ± 18.6
3	DLA + Dox	4.32 ± 0.86*	7.1 ± 1.3*
4	DLA + Tf-CuNC-Dox-NPs	1.55 ± 0.42*	3.4 ± 0.7*

All the results were expressed in mean ± S.D. with * $p < 0.05$ for drug treated groups in comparison with untreated group.

Table A5.3. Effect of drug treatments on haematological parameters.

S.No	Treatment	RBC (cells/ml X 10^6)	WBC (cells/ml X 10^3)	Hb g/dl
1	Normal animals	5.24 ± 0.43	10.14 ± 0.32	12.7 ± 0.33
2	DLA + Saline	2.73 ± 0.21$	20.35 ± 1.04$	6.6 ± 0.17$
3	DLA + Tf-CuNCs	2.85 ± 0.26	18.94 ± 1.12	7.1 ± 0.19
4	DLA + Dox	3.64 ± 0.26*	15.75 ± 0.41*	8.9 ± 0.20*
5	DLA + CuNC-Dox-NPs	4.73 ± 0.41*	13.21 ± 0.44*	11.2 ± 0.22*

All the results were expressed in mean ± S.D. $ $p < 0.05$ in comparison of saline treated DLA animals with normal animals. *$p < 0.05$ in comparison of drug treated DLA animals with untreated group DLA animals.

Table A5.4 . Effect of drug treatments on serum biochemical enzymes.

S. No	Treatment	SGOT	SGPT	ALP
1	Normal animals	46.3 ± 2.74	38.2 ± 2.43	114.6 ± 5.26
2	DLA + Saline	92.8 ± 4.26$	68.7 ± 3.64$	226.7 ± 9.42$
3	DLA + Tf-CuNCs	87.4 ± 5.73	66.3 ± 4.04	214.3 ± 8.64
4	DLA + Dox	58.2 ± 5.21*	48.2 ± 3.17*	148.6 ± 7.22*
5	DLA + Tf-CuNC-Dox-NPs	49.7 ± 4.16*	43.6 ± 3.48*	124.2 ± 6.38*

All the results were expressed in mean ± S.D. $ $p < 0.05$ in comparison of saline treated DLA animals with normal animals. * $p < 0.05$ in comparison of drug treated DLA animals with untreated group DLA animals.

Chapter-6

Conclusions and Future Prospects

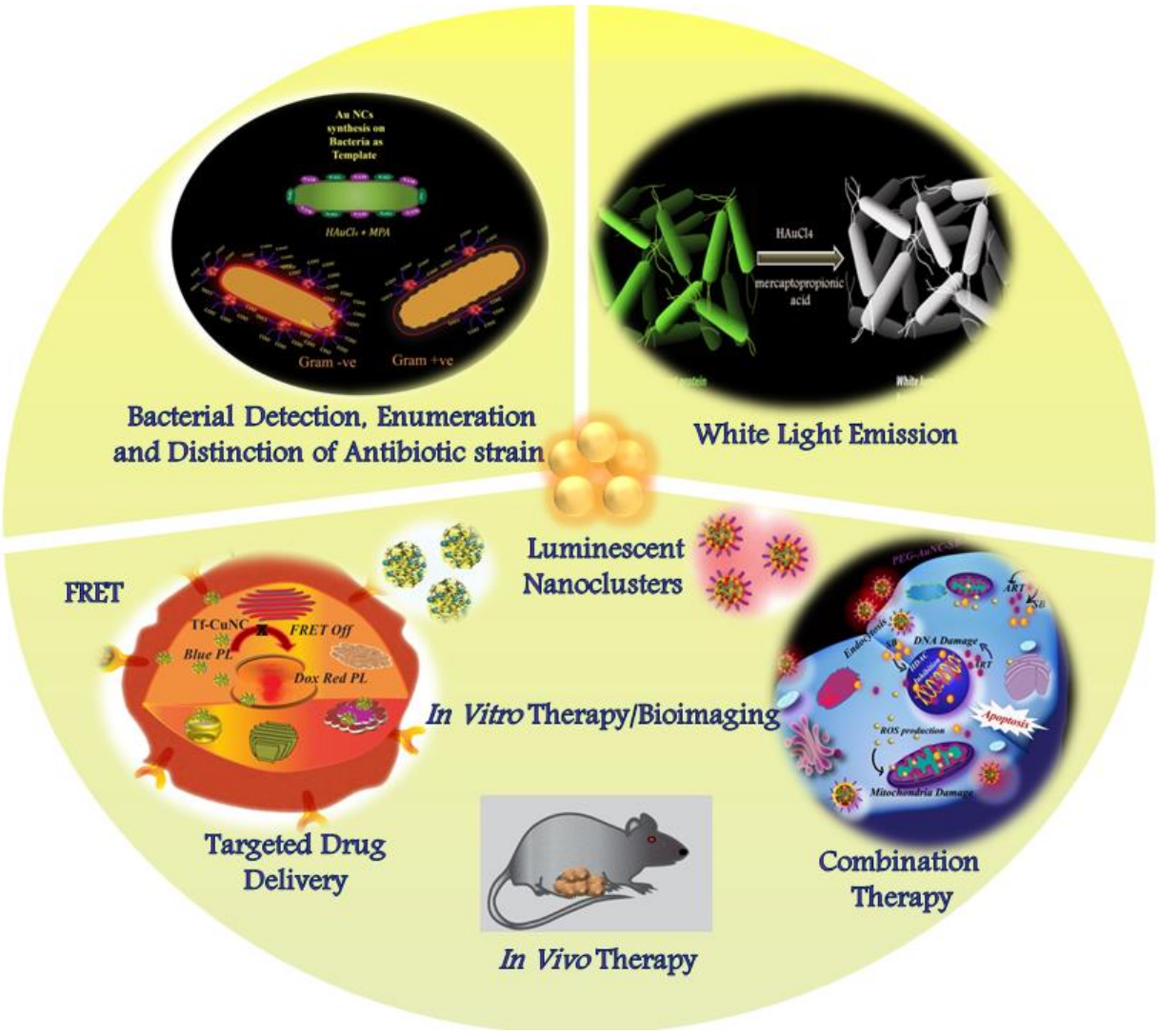

This chapter briefly presents the summary of the current study and scope for future work.

Chapter 6

6.1. Summary of the Thesis

Metal nanoclusters owing to their physicochemical features including distinct molecular-like photoluminescence, high stability, tunable luminescence, ultrasmall size, and high biocompatibility have received notable attention in the different fields of science. Luminescent metal nanoclusters have enormous applications in the field of bioimaging, sensors, detection, energy, medicine and in therapeutics.

The present thesis primarily emphases on synthesis and development of noble luminescent metal nanoclusters (gold and copper) with biomolecules as templates and their formulation into composite nanoparticles with potential applications in bacterial detection and enumeration, detection of antibiotic resistant bacteria, white light emission, bioimaging and cancer therapeutics. For this, a new synthesis method of non-toxic luminescent gold nanoclusters (Au NCs) using bacteria as template was developed, which is easy, rapid, and low cost approach. The luminescence property of the as-synthesized Au NCs was probed for bacterial detection and counting where luminescence intensity of the Au NCs changes with the number of bacteria, offering a quick method to enumerate the number of bacteria present in the test samples. The intrinsic properties of bacterial cell wall were explored for differentiation between the Gram strains. The method was also employed for detection of bacterial contaminants from water sources and kanamycin resistant strains rapidly. In the subsequent study, similar method was employed for synthesis of Au NCs by tuning the number of bacteria along with its precursors. This resulted in generation of white light from a unicellular living organism with high quantum yield and chemical stability. The commission internationale de I'elcairage (CIE) coordinate measurements values were found to be 0.33 and 0.31 with quantum yield of 2.5 ± 0.7%. The correlated color temperature (CCT) and colour rendering index (CRI), which decides the potential of the former as futuristic light emitting device and was found to be

equivalent to bright bluish white light and is quite analogous to day light. Additionally, for potent application in the field of cancer theranostics different bimolecular templates like chitosan and transferrin were used for the synthesis of Au NCs and Cu NCs, respectively. For hallmark of successful cancer treatment, combination therapy was accomplished with Au NCs encapsulated drug sodium butyrate (NaB) nanoparticles and a plant based drug artesunate (ART). The work highlighted the use of alternative chemotherapeutic drugs i.e NaB and ART as effective anticancer agents to elucidate enhanced synergistic activity with detailed molecular mechanisms. NaB and ART plays a vital role in inhibition of histone deacetylase (HDACi) and DNA fragmentation, respectively, leading to cell death. The work is well supported with *in vivo* results. Further, for specific targeting of the cancer cells, transferrin directed luminescent blue Cu NCs were synthesized and transformed into nanodrug with doxorubicin (Dox) for detection, targeted drug delivery and effective therapy. The uptake and release of Dox from the nanodrug was monitored by FRET assisted bioimaging, where blue luminescence of Cu NCs was restored in cytoplasm upon internalisation by transferrin receptor (TfR) due to specific interaction between Cu NCs and TfR receptors. The established nanodrug was biocompatible and displayed superior targeting efficiency on TfR overexpressing HeLa and MCF-7 cells for detection and therapy in both *in vitro* and *in vivo* conditions. The nanodrug evinced synergistic anticancer activity involving Cu NCs and Dox, where mechanism of its action was also elucidated.

6.2. Future Prospects

The future scopes of study based on the current findings are as follows

- Synthesis of metal nanoclusters (Ag, Cu, Pt, Pd) on different types of bacteria may open a wide range of applications in food industry and waste water treatments.
- The luminescence property of metal nanoclusters can be exploited for early detection of bacteria responsible for various diseases e.g. *Salmonella Typhi* responsible for typhoid and to detect antibiotic resistant bacteria.
- Thermophillic bacteria can be used for nanocluster synthesis to produce white light emitting device.
- Surface modification of bacteria followed by synthesis of luminescent nanoclusters can pave a new domain of microbots. The microbots can be used for both bacterial and cancer detection.
- Microbots can be used as a cargo for drug delivery in cancer therapy.
- Block polymers, dendrimers and liposomes nanoclusters can also be employed for nanocluster synthesis for better efficacy of cancer treatment.
- Combination therapy with different drugs and genes along with photothermal activity for cancer theranostics.
- The fate and renal clearance of various metal nanoclusters can be further explored.

PUBLICATIONS

Publications based on the works reported in the thesis

1. **Goswami, U.**; Basu, S.; Paul, A.; Ghosh, S.S.; Chattopadhyay, A.White light emission from gold nanoclusters embedded bacteria. *J. Mater. Chem. C*, **2017**, 5, 12360-12364.

2. **Goswami, U.**; Dutta, A.; Raza, A.; Kandimalla, R.; Kalita, S.; Ghosh, S.S.; Chattopadhyay , A. Transferrin – Copper Nanocluster - Doxorubicin Nanoparticles as Targeted Theranostic Cancer Nanodrug. *ACS. Appl. Mater . Interfaces*, **2018**, 10(4), 3282-3294.

3. **Goswami, U.**; Sahoo, A.; Chattopadhyay, A.; Ghosh, S.S. *In situ* Synthesis of Luminescent Au Nanoclusters on Bacterial Template for Rapid Detection, Quantification and Distinction of Kanamycin Resistant Bacteria. *ACS Omega* **2018**, 3 (6), 6113–6119

4. **Goswami, U.**; Kandimalla, R.; Kalita, S.; Chattopadhyay, A and Ghosh.S.S. Theranostic PEG-Encapsulated Encapsulated HDACi Drug-Composite Nanoparticles for Combination Therapy with Artesunate. *ACS Omega,* **2018,** 3**,** 11504−11516.

Publications from Collaborations

5. Ghosh, R.; **Goswami, U.**; Ghosh, S.S.; Paul, A and Chattopadhyay, A. *ACS Appl. Mater. Interfaces,* **2015**, 7 (1), 209–222.
6. Sk, M.P.; **Goswami, U.**; Ghosh, S.S and Chattopadhyay, A. *J.Mater.Chem. B,* **2015**, 3, 5673-5677.
7. Vanitha, S.; **Goswami, U.**; Chaubey, N.; Ghosh, S.S and Sanpui, P. *Biotechnol Lett,* **2016**, 38, 243–249.
8. Maravi, D. K.; Sahoo, A.; **Goswami, U.**; Prasad, S.; Sahoo, L and Ghosh, S. S. *Int. J. Phar. Bio. Sci.* **2015**, 6(4), 482 – 493.
9. Ghoshal, A.; **Goswami, U.**; Sahoo, K.A.; Chattopadhyay, A and Ghosh, S.S. *ACS Biomater. Sci. Eng*. **2015**, 1 (12), 1256–1266.

10. Sahoo, K.A.; **Goswami, U.**; Banerjee, S.; Dutta, D.; Chattopadhyay, A .; Ghosh, S.S. *ACS Biomater. Sci. Eng.* **2016**, 2 (8), 1395–1402.
11. Ghoshal, A.; **Goswami, U.**; Raza, A.; Chattopadhyay, A and Ghosh, S.S. *RSC Adv*. **2016**, 6, 85763–85772.
12. Khannam, M.; Weyhermüller, T.; **Goswami, U.**; Mukherjee, C. *Dalton Trans*. 2017, 46, 10426–10432.
13. Phukan, B.; Mukherjee, C.; **Goswami, U.**; Sarmah, A.; Mukherjee, S.; Sahoo, K. S and Moi, Ch.S. *Inorg. Chem.*, 2018, 57 (5), 2631–2638.
14. Basu, S.; **Goswami, U.**; Paul, A and Chattopadhyay. *J. Mater. Chem*. *B*, 20**18**, 6, 1650-1657.
15. Dutta, A.; **Goswami, U.**; Chattopadhyay, A. *ACS Appl. Mater. Interfaces* 10.1021/acsami.8b05160
16. Raza, A.; **Goswami, U.**; Shome, R and Ghosh, S.S.Silver Nanocluster Based Nanocarrier Enhances the Activity of 4-Phenylbutyrate synergistically**(2018)** ***Manuscript Under Preparation***
17. Rajender, G.; **Goswami, U.**; Ghosh, S.S and Giri. K.P. Mechanism of Solvent Dependent Synthesis of Highly Photoluminescence Quantum Yield Graphene Quantum Dots and Their Evolution in Bio-Imaging Application. **(2018)** ***Communicated.***
18. Ahmad, K.; Verma, A.; Arshad, F.; **Goswami, U.**; Samanta ,K. S.; Sahoo, A.; and Sk, Md.P. Role of Surface Charge in Enhancing Antibacterial Activity of Fluorescent Carbon Dots. **(2018)** ***Communicated.***
19. Das, S.; Horob, H.; **Goswami ,U.**; Kundu.M.L. Synthesis of a New Peptide Conjugated 5-Fluorouracil Gelator Prodrug for Photo-Controlled Release of the Antitumor Agent. **(2018)** ***Communicated.***
20. Das, M.; **Goswami, U.**; Ghosh,S.S.; Chattopadhyay, A. Fe-Cu bimetallic nanocomposites on the surface of sand-particles for annihilation of drug resistant clinical isolates and point of use water filtration.**(2018)** ***Communicated.***

Patents filed

1. Chattopadhyay, A.; Ghosh, S.S.; Das, M and **Goswami, U**. Sand-Fe-Cu bimetallic -nano-composite based microorganism and metal exterminator system. **(2018)** ***Submitted***

2. Chattopadhyay, A.; Ghosh, S.S.; Das, M and **Goswami, U**. Iron and copper based bimetallic nanocomposite powder and cotton patch for diabetic wound healing. **(2018)** ***Submitted***

Conferences Attended

1. Presented a poster in 4th International Conferences on Advanced Nanomaterials and Nanotechnology, ICANN 2015 held at Indian Institute of Technology Guwahati, Guwahati, India.

2. Participated in a national conference on New Advanced and Horizons in Nanoscience and Nanotechnology, Nano Sci 2014 held at Institute of Advanced Study in Science and Technology (IASST), Guwahati, India.

3. Presented a poster in International Conference on Nanoscience and Technology, ICONSAT 2018 held at Indian Institute of Science (IISc), Bengaluru, India.

4. Oral Presentation in International Conference on Nanomedicine and Nanobiotechnology, ICONAN 2018 held in Rome, Italy.

RSC | Advancing the Chemical Sciences

Royal Society of Chemistry
Thomas Graham House
Science Park
Milton Road
Cambridge
CB4 0WF

Tel: +44 (0)1223 420 066
Fax: +44 (0)1223 423 623
Email: contracts-copyright@rsc.org

www.rsc.org

Acknowledgements to be used by RSC authors

Authors of RSC books and journal articles can reproduce material (for example a figure) from the RSC publication in a non-RSC publication, including theses, without formally requesting permission providing that the correct acknowledgement is given to the RSC publication. This permission extends to reproduction of large portions of text or the whole article or book chapter when being reproduced in a thesis.

The acknowledgement to be used depends on the RSC publication in which the material was published and the form of the acknowledgements is as follows:

- For material being reproduced from an article in *New Journal of Chemistry* the acknowledgement should be in the form:
  - [Original citation] - Reproduced by permission of The Royal Society of Chemistry (RSC) on behalf of the Centre National de la Recherche Scientifique (CNRS) and the RSC
- For material being reproduced from an article *Photochemical & Photobiological Sciences* the acknowledgement should be in the form:
  - [Original citation] - Reproduced by permission of The Royal Society of Chemistry (RSC) on behalf of the European Society for Photobiology, the European Photochemistry Association, and RSC
- For material being reproduced from an article in *Physical Chemistry Chemical Physics* the acknowledgement should be in the form:
  - [Original citation] - Reproduced by permission of the PCCP Owner Societies
- For material reproduced from books and any other journal the acknowledgement should be in the form:
  - [Original citation] - Reproduced by permission of The Royal Society of Chemistry

The acknowledgement should also include a hyperlink to the article on the RSC website.

The form of the acknowledgement is also specified in the RSC agreement/licence signed by the corresponding author.

Except in cases of republication in a thesis, this express permission does not cover the reproduction of large portions of text from the RSC publication or reproduction of the whole article or book chapter.

A publisher of a non-RSC publication can use this document as proof that permission is granted to use the material in the non-RSC publication.

TH-1880_126153007

TH-1880_126153007

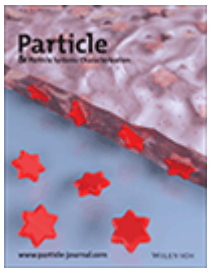

Title:	Noble Metal Clusters: Applications in Energy, Environment, and Biology
Author:	Ammu Mathew, Thalappil Pradeep
Publication:	Particle & Particle Systems Characterization
Publisher:	John Wiley and Sons
Date:	May 26, 2014

Order Completed

Thank you for your order.

This Agreement between IIT Guwahati -- Upashi Goswami ("You") and John Wiley and Sons ("John Wiley and Sons") consists of your license details and the terms and conditions provided by John Wiley and Sons and Copyright Clearance Center.

Your confirmation email will contain your order number for future reference.

printable details

License Number	4357521220207
License date	May 28, 2018
Licensed Content Publisher	John Wiley and Sons
Licensed Content Publication	Particle & Particle Systems Characterization
Licensed Content Title	Noble Metal Clusters: Applications in Energy, Environment, and Biology
Licensed Content Author	Ammu Mathew, Thalappil Pradeep
Licensed Content Date	May 26, 2014
Licensed Content Volume	31
Licensed Content Issue	10
Licensed Content Pages	37
Type of use	Dissertation/Thesis
Requestor type	University/Academic
Format	Print
Portion	Figure/table
Number of figures/tables	1
Original Wiley figure/table number(s)	Figure 1
Will you be translating?	Yes, including English rights
Number of languages	1
Languages	English
Title of your thesis / dissertation	Luminescent gold and copper nanoclusters for theranostic applications
Expected completion date	Jun 2018
Expected size (number of pages)	200
Requestor Location	IIT Guwahati J-Block,IIT Guwahati Guwahati, North Guwahati 781039

TH-1880_126153007

	India Attn: IIT Guwahati
Publisher Tax ID	EU826007151
Total	0.00 USD

Would you like to purchase the full text of this article? If so, please continue on to the content ordering system located here: Purchase PDF

If you click on the buttons below or close this window, you will not be able to return to the content ordering system.

ORDER MORE CLOSE WINDOW

TH-1880_126153007

Title: Antimicrobial Gold Nanoclusters
Author: Kaiyuan Zheng, Magdiel I. Setyawati, David Tai Leong, et al
Publication: ACS Nano
Publisher: American Chemical Society
Date: Jul 1, 2017

PERMISSION/LICENSE IS GRANTED FOR YOUR ORDER AT NO CHARGE

This type of permission/license, instead of the standard Terms & Conditions, is sent to you because no fee is being charged for your order. Please note the following:

- Permission is granted for your request in both print and electronic formats, and translations.
- If figures and/or tables were requested, they may be adapted or used in part.
- Please print this page for your records and send a copy of it to your publisher/graduate school.
- Appropriate credit for the requested material should be given as follows: "Reprinted (adapted) with permission from (COMPLETE REFERENCE CITATION). Copyright (YEAR) American Chemical Society." Insert appropriate information in place of the capitalized words.
- One-time permission is granted only for the use specified in your request. No additional uses are granted (such as derivative works or other editions). For any other uses, please submit a new request.

If credit is given to another source for the material you requested, permission must be obtained from that source.

TH-1880_126153007

Title: Nanomaterials for Theranostics: Recent Advances and Future Challenges

Author: Eun-Kyung Lim, Taekhoon Kim, Soonmyung Paik, et al

Publication: Chemical Reviews

Publisher: American Chemical Society

Date: Jan 1, 2015

PERMISSION/LICENSE IS GRANTED FOR YOUR ORDER AT NO CHARGE

This type of permission/license, instead of the standard Terms & Conditions, is sent to you because no fee is being charged for your order. Please note the following:

- Permission is granted for your request in both print and electronic formats, and translations.
- If figures and/or tables were requested, they may be adapted or used in part.
- Please print this page for your records and send a copy of it to your publisher/graduate school.
- Appropriate credit for the requested material should be given as follows: "Reprinted (adapted) with permission from (COMPLETE REFERENCE CITATION). Copyright (YEAR) American Chemical Society." Insert appropriate information in place of the capitalized words.
- One-time permission is granted only for the use specified in your request. No additional uses are granted (such as derivative works or other editions). For any other uses, please submit a new request.

If credit is given to another source for the material you requested, permission must be obtained from that source.

TH-1880_126153007

Title:	Rational Design of Multifunctional Gold Nanoparticles via Host–Guest Interaction for Cancer-Targeted Therapy
Author:	Wei-Hai Chen, Qi Lei, Guo-Feng Luo, et al
Publication:	Applied Materials
Publisher:	American Chemical Society
Date:	Aug 1, 2015

PERMISSION/LICENSE IS GRANTED FOR YOUR ORDER AT NO CHARGE

This type of permission/license, instead of the standard Terms & Conditions, is sent to you because no fee is being charged for your order. Please note the following:

- Permission is granted for your request in both print and electronic formats, and translations.
- If figures and/or tables were requested, they may be adapted or used in part.
- Please print this page for your records and send a copy of it to your publisher/graduate school.
- Appropriate credit for the requested material should be given as follows: "Reprinted (adapted) with permission from (COMPLETE REFERENCE CITATION). Copyright (YEAR) American Chemical Society." Insert appropriate information in place of the capitalized words.
- One-time permission is granted only for the use specified in your request. No additional uses are granted (such as derivative works or other editions). For any other uses, please submit a new request.

If credit is given to another source for the material you requested, permission must be obtained from that source.

TH-1880_126153007

Title: Engineered Nanoparticles for Drug Delivery in Cancer Therapy
Author: Tianmeng Sun, Yu Shrike Zhang, Bo Pang, et al
Publication: Angewandte Chemie International Edition
Publisher: John Wiley and Sons
Date: Oct 7, 2014

Order Completed

Thank you for your order.

This Agreement between IIT Guwahati -- Upashi Goswami ("You") and John Wiley and Sons ("John Wiley and Sons") consists of your license details and the terms and conditions provided by John Wiley and Sons and Copyright Clearance Center.

Your confirmation email will contain your order number for future reference.

printable details

License Number	4357690898857
License date	May 28, 2018
Licensed Content Publisher	John Wiley and Sons
Licensed Content Publication	Angewandte Chemie International Edition
Licensed Content Title	Engineered Nanoparticles for Drug Delivery in Cancer Therapy
Licensed Content Author	Tianmeng Sun, Yu Shrike Zhang, Bo Pang, et al
Licensed Content Date	Oct 7, 2014
Licensed Content Volume	53
Licensed Content Issue	46
Licensed Content Pages	45
Type of use	Dissertation/Thesis
Requestor type	University/Academic
Format	Print
Portion	Figure/table
Number of figures/tables	1
Original Wiley figure/table number(s)	Table 1
Will you be translating?	No
Title of your thesis / dissertation	Luminescent gold and copper nanoclusters for theranostic applications
Expected completion date	Jun 2018
Expected size (number of pages)	200
Requestor Location	IIT Guwahati J-Block,IIT Guwahati Guwahati, North Guwahati 781039 India Attn: IIT Guwahati
Publisher Tax ID	EU826007151
Total	0.00 USD

TH-1880_126153007

Title: Transferrin–Copper Nanocluster–Doxorubicin Nanoparticles as Targeted Theranostic Cancer Nanodrug

Author: Upashi Goswami, Anushree Dutta, Asif Raza, et al

Publication: Applied Materials

Publisher: American Chemical Society

Date: Jan 1, 2018

PERMISSION/LICENSE IS GRANTED FOR YOUR ORDER AT NO CHARGE

This type of permission/license, instead of the standard Terms & Conditions, is sent to you because no fee is being charged for your order. Please note the following:

- Permission is granted for your request in both print and electronic formats, and translations.
- If figures and/or tables were requested, they may be adapted or used in part.
- Please print this page for your records and send a copy of it to your publisher/graduate school.
- Appropriate credit for the requested material should be given as follows: "Reprinted (adapted) with permission from (COMPLETE REFERENCE CITATION). Copyright (YEAR) American Chemical Society." Insert appropriate information in place of the capitalized words.
- One-time permission is granted only for the use specified in your request. No additional uses are granted (such as derivative works or other editions). For any other uses, please submit a new request.

If credit is given to another source for the material you requested, permission must be obtained from that source.

TH-1880_126153007